Imperial College London

Predicting Trabecular Bone Architecture through Structural Modelling

Branimir Radukic

A dissertation submitted in part fulfilment of the requirements of the degree of Doctor of Philosophy

Imperial College London
Department of Civil and Environmental Engineering

July 2024

I declare that, except where reference is explicitly made to the work of others, this dissertation is the result of my own work and has not been submitted for any other degree at Imperial College London or any other institution.

Branimir Radukic

The copyright of this thesis rests with the author. Unless otherwise indicated, its contents are licensed under a Creative Commons Attribution-Non Commercial-No Derivatives 4.0 International Licence (CC BY-NC-ND).

Under this licence, you may copy and redistribute the material in any medium or format on the condition that; you credit the author, do not use it for commercial purposes and do not distribute modified versions of the work.

When reusing or sharing this work, ensure you make the licence terms clear to others by naming the licence and linking to the licence text.

Please seek permission from the copyright holder for uses of this work that are not included in this licence or permitted under UK Copyright Law.

The author can be contacted at branimir.radukic16@imperial.ac.uk

Acknowledgements

As this Thesis draws to a close I reflect on the inspiration for this work; my late wife's struggle with destructive bone disease brought on by cancer. The serendipity of discovering Andrew Phillips' research soon after Sarah's death is striking. I am very grateful to Andrew for the opportunity to turn all the grief into something constructive. His advice and guidance allowed me to apply my structural engineering skills to a field which borders medicine and may make a very small contribution to people with bone disease in the future.

I would like to thank the Civil Engineering Department for the Dixon Scholarship award.

My colleagues at Arup have shown an interest, supported me, and at times 'picked up the slack': Eleni, Stuart, Jonathan, Giuseppe, David, Juann, Lucy, Suresh, Pietro, Paul, Kim, Tom and Pete. Martin may even read a page or two. My employer has accommodated my leave requirements and provided cover. My holiday balance has been 'in the red' for two years!

I have appreciated the support and camaraderie of my academic colleagues in the department. Office 326 and 317a deserve a special mention; in no particular order: Dan, Claire, Luca, Clément, Laura, Adam, Josh, Luís and Stas. It was very uplifting to be surrounded by young knowledge thirsty people at the start of this project.

I wish to recognise the help I received from Sarah WIllis, who made sure I complied with all the PhD requirements and the encouragement from Anna Hikel whom I first encountered as an undergraduate 40 years ago.

I would like to thank my dad Vladimir, my mum Vlasta and my sister Lana. My dad passed on a life long love of learning to me.

Finally, I would not have been able to complete this thesis without the support from my daughters Christina and Eva and my partner Kate. Their encouragement, proofreading, tolerance and ubiquitous cups of tea and coffee made all the difference. Their love has carried me through!

Abstract

Bone is a complex composite material at both micro and macro-scale. At macro-scale we distinguish between the external shell of bones, the cortex and a series of rods and plates which occupy the internal volume, the trabecular bone.

This thesis focuses on advancing computationally efficient structural modelling methodology for trabecular bone, to achieve close resemblance with micro-CT imaging studies while maintaining agreement in predicted stiffness and relative density with macro-scale continuum studies.

A number of structural forms were examined to improve the understanding of trabecular bone behaviour. Good agreement between previous continuum and structural models and all rigid jointed lattice simulations was found. However, a bending dominated low connectivity lattice, particularly a space filling Voronoi inspired lattice, was found to most closely resemble real bone. The adaptation process, which for the first time, introduces a non-prismatic representation of trabeculae, created efficient robust structures. It is hypothesised that bone development processes leads to irregular structures. Following adaptation, these structures exhibit an even strain distribution in response to loading and a higher resistance to damage than high connectivity structures. Low connectivity Voronoi and high connectivity near neighbour femur models were created. Favourable comparisons with clinical observations and previous studies were made, demonstrating the viability of the structural adaptation approach to generate physiologic models of whole bones which closely represent trabeculae at micro-scale.

Despite advancements, limitations remain, including challenges in predicting trabecular thickness and matching the reported abundance of minimum connectivity nodes.

The developed methodology holds promise in the development of additively manufactured bone scaffolds and implants with a micro-architecture more closely resembling that of trabecular bone. It has the potential to elucidate the development of skeletal conditions such as osteoporosis and osteoarthritis. Finally, this approach can optimise structural engineering designs, improving material efficiency and response to damage and unexpected loading.

Contents

Contents iii

List of abbreviations vii

List of figures viii

List of tables xxii

1 Introduction **1**

1.1 Context of the research 2

1.2 Thesis objectives 3

1.3 Summary of chapters 5

2 Background **7**

2.1 Bone architecture 8

2.2 Review of numerical simulations 11

2.2.1 Introduction 11

2.2.2 Analytical theories 12

2.2.2.1 Tissue differentiation 12

2.2.2.2 Functional adaptation 13

2.2.3 Macro-scale models 15

2.2.4 Micro-scale models 18

2.2.5 Structural models 21

2.2.6 Summary 22

3 Research methodology **25**

3.1 Introduction 26

3.2 Model generation 27

3.2.1 Near neighbour models 27

3.2.2 Modelling workflow 27

3.3 Adaptation algorithm 33

3.4 Summary 38

4 Trabecular bone as a cellular solid: predictions of mechanical properties with near neighbour models **39**

4.1 Introduction 40

4.2 Methodology 44

4.3 Results 50

4.3.1 Predicted trabecular architecture and mechanical properties . . 51

4.4 Discussion 65

4.5 Conclusion 72

5 Trabecular bone at micro-scale: morphological features predictions **75**

5.1 Introduction 76
5.1.1 Overview of morphological characteristics 76
5.1.2 Review of morphological characteristics imaging studies 78
5.2 Methodology 80
5.3 Results 84
5.3.1 Nodal connectivity 84
5.3.2 ITA 93
5.3.3 Trabecular thickness 100
5.4 Discussion 110
5.5 Summary 115

6 Trabecular bone as a Voronoi structure **117**

6.1 Introduction 118
6.2 Methodology 119
6.3 Results 122
6.3.1 Predicted trabecular architecture and mechanical properties . . 122
6.3.2 Predicted trabecular topology 131
6.3.3 Impact of dead zone threshold 137
6.4 Discussion 146
6.5 Summary 155

7 Proximal femur adaptation simulations **157**

7.1 Introduction . . . 158
7.2 Methodology . . . 159
7.2.1 Finite element model . . . 159
7.2.2 Adaptation simulations . . . 163
7.2.3 Data analysis . . . 165
7.3 Results . . . 165
7.3.1 Predicted trabecular architecture and mechanical properties . . . 166
7.3.2 Predicted trabecular topology . . . 177
7.4 Discussion . . . 181
7.5 Conclusion . . . 187

8 Discussion and conclusion **188**

8.1 Summary . . . 189
8.2 Limitations and future work . . . 193
8.3 Field of application . . . 195
8.4 Conclusion . . . 195
References . . . 197
Publications . . . 208

A Additional results appendix **209**

B Digital appendix **225**

List of abbreviations

This list describes abbreviations frequently used in this thesis.

ANC# Adapted NC#. NC after adaptation where # is the number of elements connecting at a node.

ITA Inter trabecular angle, the angle between individual elements meeting at each node.

MSL Mean strut length.

NC# Nodal connectivity, where # is the number of elements connecting at a node.

NN# Near neighbour lattice with NC#.

NNC# Nominal NC#. The minimum number of elements connecting at each node in the initial model prior to adaptation simulations. The mean and maximum connectivity are often larger.

List of Figures

2.1 Bone architecture. 8

2.2 Hydrostatic and octahedral shear stress illustration adapted from Carter et al. (1998). 12

2.3 Hypothesis of bone remodelling based on Carter (1982). 14

2.4 Topology optimisation concept adapted from Boyle & Kim (2011). 19

3.1 Simulation overview. 26

3.2 Diagram showing releases applied to struts to transform models from rigid to pin jointed lattices. B32 elements at strut ends are shown in red and the ones in the middle in cyan. 29

3.3 Strut division into four finite elements. 30

3.4 Grasshopper Model Generation. * the 0.5mm limit was chosen in order to achieve a uniform load distribution, please refer to the narrative related to Figure 3.5. **Figure 3.2 shows how member releases were applied. 31

3.5 Adaptation simulation models boundary conditions. 32

3.6 Comparison of Stress and Strain Yield Behaviour (extract from Pankaj (2013)). 34

3.7 Illustration of the mechanostat principle used in the functional adaptation. 35

3.8 Illustration of strain distribution on a typical strut. 36

4.1 Idealised cube models of bending and stretch dominated cellular solids and closed cell foams adopted from Gibson & Ashby (1982). 41

4.2 Five initial NN04 and NN14 models with MSL=0.7mm. 45

4.3 Five initial NN04 and NN14 models with MSL=1.5mm. 46

4.4 Triaxial and uniaxial loading scenarios used in the simulations. 48

4.5 Radii contour plots for one of five converged models in four typical simulations. The initial radius prior to adaptation simulations was 25μm. Dead elements with radius of 1μm are not shown.The models were subjected to a uniform pressure of 1MPa either on one or three faces as indicated. 52

4.6 Contour plots of the absolute bending strain on LHS, the absolute axial strain in the middle and the radii on the RHS on a 2mm slice through the middle of one of the five NN04 models with MSL and loading as indicated. The initial radius prior to adaptation simulations was 25μm. Dead elements with radius of 1μm are not shown. 53

4.7 Contour plots of the absolute bending strain on LHS, the absolute axial strain in the middle and the radii on the RHS on a 2mm slice through the middle of one of the five NN14 modelswith MSL and loading as indicated. The initial radius prior to adaptation simulations was 25μm. Dead elements with radius of 1μm are not shown. 54

4.8 Mean predicted trabecular volume for (a) triaxial and (b) uniaxial load simulations for 5 randomly generated models of each NNC with MSL as shown. The filled bars are for stretch and hollow for bending models. Error bars for the 95% confidence interval are shown. The bars are plotted for NNC whilst the trendlines are plotted for ANC at the end of simulation as presented in table 4.3. A range of trabecular volume calculated from reported density ranges (Linde et al. (1992), Ashby (2006)) is shown for comparison. 56

4.9 Mean Young's modulus values in three principal direction for uniaxial load simulations for 5 randomly generated models of each NNC with MSL as shown. The filled bars are for stretch and hollow for bending models. Error bars for the 95% confidence interval are shown. A range of E values for real bone reported by Linde et al. (1992) is shown for comparison. . 58

4.10 Mean Young's modulus values in three principal direction for triaxial load simulations for 5 randomly generated models of each NNC with MSL as shown. The filled bars are for stretch and hollow for bending models. Error bars for the 95% confidence interval are shown. A range of E values for real bone reported by Linde et al. (1992) is shown for comparison. . 59

4.11 Structural efficiency Ω, expressed as Young's modulus divided by trabecular volume, plotted against ANC at the end of adaptation simulation. Only the values for 1.0mm MSL simulations as indicated in the legend are shown to provide a visual effect of the relationship between efficiency, ANC and lattice rigidity. Full results are presented in Table 4.4. 60

4.12 Mean relative Young's modulus plotted against mean relative density using 5 model average values prior to adaptation simulations for (a) MSL=1.5mm and (b) MSL=0.7mm. A curve has been fitted to each data set and the equations of these curves are presented next to them bound by a frame of the same colour. Coefficients of determination (R^2) are also shown. 62

4.13 Mean relative Young's modulus plotted against mean relative density using 5 model average values for MSL=1.5mm at the end of adaptation simulation using (a) triaxial loading scenario and (b) uniaxial loading scenario. A curve has been fitted to each data set and the equations of these curves are presented next to them bound by a frame of the same colour. Coefficients of determination (R^2) are also shown. 63

4.14 Mean relative Young's modulus plotted against mean relative density using 5 model average values for MSL=0.7mm at the end of adaptation simulation using (a) triaxial loading scenario and (b) uniaxial loading scenario. A curve has been fitted to each data set and the equations of these curves are presented next to them bound by a frame of the same colour. Coefficients of determination (R^2) are also shown. 64

4.15 Contour plots of the a) absolute bending strain and b) absolute axial strain on a 2mm slice through the middle of one of the five models for NN10, NN08 and NN06 uniaxial loading simulations. The initial radius prior to adaptation simulations was 25μm. Dead elements with radius of 1μm are not shown. The models were subjected to a uniform pressure of 1MPa as indicated. 67

4.16 Contours of displacements in z direction plotted on deflected shapes of idealised open cell foam models inspired by Gibson & Ashby (1997). Each model was subjected to four 1N point loads, two on top and two on bottom face. 70

4.17 Young's modulus versus relative density plots for idealised open foam cells depicted in Figure 4.16. 71

5.1 Mean strut radius distribution data reproduced from Kirby et al. (2020). . 81

5.2 Illustration of ITA angle measurement. 82

5.3 Examples of node geometry for NC3, NC4, NC5 and NC6 in NN04 model with MSL=0.7mm and fixed joints following a uniaxial adaptation simulation with dead zone at 250$\mu\varepsilon$. The mean connectivity following the adaptation of this simulation is 4.0 88

5.4 Geometry of the same nodes presented in Figure 5.3 for a model with the same parameters as in Figure 5.3 except that the dead zone is set at 1000$\mu\varepsilon$. NC4, NC5 and NC6 nodes in Figure 5.3 transform into NC3, NC4 and NC5 nodes whilst NC3 node remains unchanged. The mean connectivity following this simulation is 3.4 88

5.5 Geometry of the same nodes presented in Figure 5.3 for a model with the same parameters as in Figure 5.3 except that it was subjected to a triaxial loading. The NC4, NC5 and NC6 nodes remain with same connectivity but element radius increases. The NC3 node transforms to NC5. The mean connectivity following this simulation is 4.8 89

5.6 Geometry of the same nodes presented in Figure 5.3 for a model with the same parameters as in Figure 5.3 except that it was subjected to a triaxial loading and the dead zone was set at 1000$\mu\varepsilon$. There is no apparent change for example nodes from predictions in Figure 5.5 but the mean NC decreases to 4.4. 89

5.7 Examples of node geometry for NC09 NC10, NC11 and NC12 in NN14 model with MSL of 0.7mm and fixed joints following a uniaxial adaptation simulation with dead zone at 250$\mu\varepsilon$. The mean connectivity following this simulation is 9.6 91

5.8 Geometry of the same nodes presented in Figure 5.7 for a model with the same parameters as in Figure 5.7 except that the dead zone is set at 1000$\mu\varepsilon$. NC09, NC11 and NC12 nodes in Figure 5.7 transform into NC06, NC03 and NC04 nodes whilst elements in NC10 all became inactive. The mean connectivity following the adaptation of this simulation is 3.8. 91

5.9 Geometry of the same nodes presented in Figure 5.7 for a model with the same parameters as in Figure 5.7 except that it was subjected to a triaxial loading. The NC9, NC10, NC11 and NC12 nodes transform into NV14, NC16, NC13 and NC14 nodes respectively. The mean connectivity following this simulation is 15.1 92

5.10 Geometry of the same nodes presented in Figure 5.7 for a model with the same parameters as in Figure 5.7 except that it was subjected to triaxial loading and the dead zone was set at 1000$\mu\varepsilon$. NC09, NC10, NC11 and NC12 nodes in Figure 5.7 transform into NC10, NC09, NC05 and and NC06 nodes. The mean connectivity following the adaptation of this simulation is 7.0. 92

5.11 Relative frequency (RF) of ITA grouped in 4° bins for nodes with ANC of 3, 4, 5 and 6 and over. Combined results from five different models with MSL of 0.7 mm, different NC as shown in the legend and where B signifies fixed joint and S pinned joint simulations. The number following the fixity description defines uniaxial (1) or triaxial (3) loading scenarios. Simulations with dead zone set at the lower limit of the lazy zone are followed by letters NDZ. 98

5.12 Relative frequency (RF) of ITA grouped in 4° bins for nodes with ANC of 3, 4, 5 and 6 and over. Combined results from five different models with MSL of 1.5 mm, different NC as shown in the legend and where B signifies fixed joint and S pinned joint simulations. The number following the fixity description defines uniaxial (1) or triaxial (3) loading scenarios. Simulations with dead zone set at the lower limit of the lazy zone are followed by letters ndz. 99

5.13 Comparison of strut radii distributions for NN04 adaptation simulations. Each diagram presents simulation data combined from 5 randomly generated models and the headings identify the MSL and the loading. Letters NDZ signify that a dead zone threshold pf 1000$\mu\varepsilon$ has been used. Each bar represents a number of strut radii element sets and the number of sets is annotated on diagrams. The histogram in light blue and the red distribution curve represent the full set of data. The distribution curve in green excludes the elements with the smallest radius of 25 μm. 103

5.14 Comparison of strut radii distributions for NN06 adaptation simulations. Each diagram presents simulation data combined from 5 randomly generated models and the headings identify the MSL and the loading. Each bar represents a number of strut radii element sets and the number of sets is annotated on diagrams. The histogram in light blue and the red distribution curve represent the full set of data. The distribution curve in green excludes the elements with the smallest radius of 25 μm. 105

5.15 Comparison of strut radii distributions for NN14 adaptation simulations. Each diagram presents simulation data combined from 5 randomly generated models and the headings identify the MSL and the loading. Each bar represents a number of strut radii element sets and the number of sets is annotated on diagrams. The histogram in light blue and the red distribution curve represent the full set of data. The distribution curve in green excludes the elements with the smallest radius of 25 μm. 107

5.16 Ideal ITAs. The diagrams illustrate the bond angles between the nucleus in blue an electrons in red. 112

5.17 An illustration of how a single plate may replicate the bending stiffness of five circular struts. 115

6.1 Illustration of a Voronoi diagram in 2D. 119

6.2 Illustration of a Voronoi diagram in 3D. 120

6.3 2mm slice through initial NN04 and Voronoi models with MSL=0.7mm showing similar topology. 121

6.4 Absolute maximum axial and bending strains in one of the five Voronoi models with MSL=0.7mm. The initial radius prior to adaptation simulations was 25μm. Dead elements with radius of 1μm are not shown. The models were subjected to a uniform pressure of 1MPa either on one or three faces as indicated. 123

6.5 Absolute maximum axial and bending strains in one of the five NN04 models with MSL=0.7mm. The initial radius prior to adaptation simulations was 25μm. Dead elements with radius of 1μm are not shown.The models were subjected to a uniform pressure of 1MPa either on one or three faces as indicated. 124

6.6 Frequency distributions of axial strain in green and bending strain in red for one of the five models in Voronoi and NN04 simulations with MSL of 0.7mm. Mean values for each distribution are represented by a vertical line and annotated accordingly. 50$\mu\varepsilon$ bin size has been used. 125

6.7 Mean predicted trabecular volume of 5 randomly generated models with MSL as shown for Voronoi and NN04 simulations. 95% confidence interval error bars are shown. A range of trabecular volume calculated from reported density ranges (Linde et al. (1992), Ashby (2006)) is shown for comparison. 126

6.8 Mean predicted Young's Modulus Values of 5 randomly generated models with MSL as shown for Voronoi and NN04 simulations. 95% confidence interval error bars are shown. A range of E values for real bone reported by Linde et al. (1992) is shown for comparison. 127

6.9 Mean Relative Young's Modulus plotted against mean relative density for 5 models prior to adaptation for Voronoi model and NN04 model simulations. A curve has been fitted to each data set and the equations of these curves are presented next to them bound by a frame of the same colour. Coefficients of determination (R^2) are shown. The curves do not fit to data points exactly due to variability of 5 models. The upper and lower bound curves are shown for the worst fit Voronoi 0.7mm MSL results. 129

6.10 Mean Relative Young's Modulus plotted against mean relative density for 5 models at the end of adaptation for Voronoi model and NN04 model simulations. A curve has been fitted to each data set and the equations of these curves are presented next to them bound by a frame of the same colour. Coefficients of determination (R^2) are shown. 130

6.11 Comparison of ITA distribution simulation predictions for ANC3, ANC4 and ANC5 with those reported by Reznikov et al. (2016). Top row presents results of uniaxial and bottom row of triaxial loading simulations. 135

6.12 Mean strut radii distribution for bending simulations for 5 randomly generated Voronoi models. The distribution curve in green excludes the elements with the smallest radius of 25μm. 136

6.13 A 3mm wide by 2mm thick slices through the full 8mm height of one of Voronoi and NN models with initial connectivity 14 at he start and the end of simulations showing the absolute maximum total strain. The Voronoi model additionally shows the strains at the end of the second iteration as the large strain magnitude at the end of the first iteration prevents meaningful differentiation and comparison. 142

6.14 Comparison of strut radii distributions for Voronoi adaptation simulations. Each diagram presents simulation data combined from 5 randomly generated models and the headings identify the MSL and the loading. Letters NDZ signify that a dead zone threshold of 1000$\mu\varepsilon$ has been used. Each bar represents a number of strut radii element sets and the number of sets is annotated on diagrams. The histogram in light blue and the red distribution curve represent the full set of data. The distribution curve in green excludes the elements with the smallest radius of 25μm. 144

7.1 Illustration of the Voronoi femur model Grasshopper definition. For clarity 116 Voronoi seeds generated with 600 random points are shown. The model used in the adaptation simulation used 24,737 Voronoi seeds generated from 128,000 random points which achieved a 0.7mm MSL. . . . 162

7.2 Finite element model of the proximal femur showing the loading and the boundary conditions. JCF is the joint contact force, ABF is the abductor muscle force, and IBF is the iliotibial band force. View A-A on the distal end of the femur shows the boundary conditions. The model is restrained in the z direction at all nodes at the distal end, two nodes are restrained in the y direction and one in the x direction. 164

7.3 A 2mm thick slice through the converged Voronoi model of the proximal femur showing trabecular and cortical architecture. Inactive elements with a radius of 0.5μm are omitted and the elements with the smallest active element radius of 25μm are shown in cyan. 167

7.4 A close up of the converged Voronoi model in Figure 7.3. Trabecular trajectories in the greater trochanter and the femoral head are shown with greater resolution. Ward's triangle is clearly defined. Inactive elements with a radius of 0.5μm are omitted and elements with the smallest active element radius of 25μm are shown in cyan. 168

7.5 A 2mm thick slice through the converged NN14 model of the proximal femur showing trabecular and cortical architecture. Inactive elements with a radius of 0.5μm are omitted and the elements with the smallest active element radius of 25μm are shown in cyan. 169

7.6 A 2mm thick slice through the converged NN14 model of the proximal femur showing trabecular and cortical architecture. Inactive elements with a radius of 0.5μm are omitted and the elements with the smallest active element radius of 25μm are shown in cyan. Elements with radii above 1.7mm are omitted. 170

7.7 A close up of the converged NN14 model of proximal femur in Figure 7.5. Trabecular trajectories in the greater trochanter and the femoral head are shown with greater resolution. Ward's triangle is clearly defined. Inactive elements with a radius of 0.5μm are omitted and the elements with the smallest active element radius of 25 μm are shown in cyan. 171

7.8 A comparison of proximal femur trabecular architecture predicted by the a) NN14 model and c) Voronoi model with the real proximal trabecular architecture in the b) photograph of the slice trough the bone. Inactive elements with a radius of 0.5μm are omitted and the elements with the smallest active element radius of 25 μm are shown in cyan. 172

7.9 Young's modulus and relative density of trabeculae in the femoral head and the greater trochanter based on an 8mm x 8mm x 8mm cube sample extracted from the adapted Voronoi model as indicated in red on the slice. α is the angle between the femur model z axis and the cube model z' axis with anticlockwise direction about y axis being positive. Inactive elements with a radius of 0.5μm are omitted and the elements with the smallest active element radius of 25μm are shown in cyan. The cubes orientated at 30° and -30° from the model z axis were extracted at those orientations from the femur model and rotated to vertical in Abaqus for calculation of stiffness properties. 174

7.10 Young's modulus and relative density of trabeculae in the femoral head and the greater trochanter based on an 8mm x 8mm x 8mm cube sample extracted from the adapted NN14 model as indicated in red on the slice. α is the angle between the femur model z axis and the cube model z' axis with anticlockwise direction about y axis being positive. Inactive elements with a radius of 0.5μm are omitted and the elements with the smallest active element radius of 25 μm are shown in cyan. The cubes orientated at 30° and -30° from the model z axis were extracted at those orientations from the femur model and rotated to vertical in Abaqus for calculation of stiffness properties. 174

7.11 Plots of E values in different orientations in the femoral head and the greater trochanter as presented in Figures 7.9 and 7.10. Values are given at 30° intervals. For clarity greater trochanter plots are 8 times larger as indicated by the scale bars. The smaller plots to the left hand side of each greater trochanter plot are at the same scale as the femur head plots for ease of visual comparison. 175

7.12 Comparison of the Voronoi model predictions of ANC4 node ITA distribution with those reported by Reznikov et al. (2016). Red dots present the raw data, grouped into bins 4° wide, whilst the curves are fitted probability distributions. 179

7.13 Comparison of the Voronoi and NN14 model radius distributions. Voronoi distributions are based on the mean radii of four elements comprising a strut and the NN14 of the radii for each struts as there were no subdivisions. 180

7.14 Evaluation of ellipse element radii to reproduce the capacity of a circular strut at the end of the adaptation simulation. In step 1 the minimum radius of the ellipse is calculated so that a circular strut with such radius is able to resist the axial load applied to the circular strut whilst limiting the strain to the target value. The major radius is then calculated so that combined axial force and moment do not exceed the target strain value. 186

A.1 ITA probability distribution (PD) for actual connectivity (AC) of 3 following adaptations simulations. Distribution plots are derived from mean values of five different models for each nominal connectivity as shown in the legend where b signifies bending and s stretch simulations. Mean ITA for each distribution is indicated by a vertical line and annotated with the corresponding value. (a) and (b) show distributions for simulations using the mean strut length of 0.7mm subjected to triaxial and uniaxial loading scenarios respectively. (c) and (d) show equivalent plots for mean strut length of 1.5mm 216

A.2 ITA probability distribution (PD) for actual connectivity (AC) of 4 following adaptations simulations. Distribution plots are derived from mean values of five different models for each nominal connectivity as shown in the legend where b signifies bending and s stretch simulations. Mean ITA for each distribution is indicated by a vertical line and annotated with the corresponding value. (a) and (b) show distributions for simulations using the mean strut length of 0.7mm subjected to triaxial and uniaxial loading scenarios respectively. (c) and (d) show equivalent plots for mean strut length of 1.5mm 217

A.3 ITA probability distribution (PD) for actual connectivity (AC) of 5 following adaptations simulations. Distribution plots are derived from mean values of five different models for each nominal connectivity as shown in the legend where b signifies bending and s stretch simulations. Mean ITA for each distribution is indicated by a vertical line and annotated with the corresponding value. (a) and (b) show distributions for simulations using the mean strut length of 0.7mm subjected to triaxial and uniaxial loading scenarios respectively. (c) and (d) show equivalent plots for mean strut length of 1.5mm 218

A.4 ITA probability distribution (PD) for actual connectivity (AC) of 6 following adaptations simulations. Distribution plots are derived from mean values of five different models for each nominal connectivity as shown in the legend where b signifies bending and s stretch simulations. Mean ITA for each distribution is indicated by a vertical line and annotated with the corresponding value. (a) and (b) show distributions for simulations using the mean strut length of 0.7mm subjected to triaxial and uniaxial loading scenarios respectively. (c) and (d) show equivalent plots for mean strut length of 1.5mm 219

A.5 ITA probability distribution (PD) for all actual connectivity (AC) of above 6 following adaptations simulations. Distribution plots are derived from mean values of five different models for each nominal connectivity as shown in the legend where b signifies bending and s stretch simulations. Mean ITA for each distribution is indicated by a vertical line and annotated with the corresponding value. (a) and (b) show distributions for simulations using the mean strut length of 0.7mm subjected to triaxial and uniaxial loading scenarios respectively. (c) and (d) show equivalent plots for mean strut length of 1.5mm 220

A.6 Comparison of 5 model mean strut radii distributions for low connectivity stretch simulations with and without dead zone. Each diagram is annotated with the simulation name identifying the mean strut length and the loading scenario. Each bar represents a number of strut radii element sets which are also annotated on diagrams. 222

A.7 Comparison of 5 model mean strut radii distributions for high connectivity bending simulations with and without dead zone. Each diagram is annotated with the simulation name identifying the mean strut length and the loading scenario. Each bar represent a number of strut radii element sets which are also annotated on diagrams. 223

A.8 Comparison of 5 model mean strut radii distributions for high connectivity stretch simulations with and without dead zone. Each diagram is annotated with the simulation name identifying the mean strut length and the loading scenario. Each bar represents a number of strut radii element sets which are also annotated on diagrams. 224

List of Tables

4.1 Simulation models; the symbol * signifies the lattice type portion of the simulation name and the symbol # the strut length portion. The NC4 models with pinned joints were structurally unstable and were thus not considered. 47

4.2 List of models subjected to further simulations to obtain the relationship between relative density and Young's modulus. 49

4.3 Mean and standard deviation of ANC values for simulations with different NNC, MSL and loading. 50

4.4 Structural efficiency Ω, expressed as Young's modulus divided by trabecular volume. key results are highlighted in yellow. 61

4.5 Abstract bone cube samples strains [$\mu\varepsilon$] at macro-scale resulting from the 1 MPa uniformly distributed loading at the end of adaptation simulation. 74

5.1 Samples used in the Reznikov et al. (2016) study. 78

5.2 Proportion of nodes of specified nodal connectivity (NC) in typical trabecular bone and the associated ITA values (Reznikov et al. (2016)). . . 79

5.3 List of additional simulations with no dead zone. 83

5.4 The mean, mode, standard deviation, minimum and maximum NC before and after adaptation tabulated by MSL, loading scenario, lattice type and initial NC. Dead zone of 250$\mu\varepsilon$ has been used except for simulations with * next to the NNC value which indicate that the dead zone of 1000$\mu\varepsilon$ has been used. Key results are highlighted in yellow. 85

5.5 Proportions of nodes with four most prevalent NC following adaptation simulations. Results are tabulated by the loading, initial NC and MSL. Each simulation entry gives NC on top and its proportion below. Dead zone of 250$\mu\varepsilon$ has been used except for simulations with * next to the NNC value which indicate that the dead zone of 1000$\mu\varepsilon$ has been used. Representative results are presented here with full results available in the appendix Table A.1.Key results are highlighted in yellow. 86

5.6 The ITA mean, median, standard deviation (SD), minimum (min) and maximum (max) values for representative fixed joints simulations. ITAs for four most prevalent ANCs are presented. Dead zone of 250$\mu\varepsilon$ has been used except for simulations with * next to the NNC value which indicate that the dead zone of 1000$\mu\varepsilon$ has been used. Full results are available in the Appendix Figures A.2 and A.3.Key results are highlighted in yellow. 94

5.7 The ITA mean, median, standard deviation (SD), minimum (min) and maximum (max) values for representative pinned joint simulations. ITAs for four most prevalent ANCs are presented. Dead zone of 250$\mu\varepsilon$ has been used except for simulations with * next to the NNC value which indicate that the dead zone of 1000$\mu\varepsilon$ has been used. Full results are available in the Appendix Figures A.4 and A.5. Key results are highlighted in yellow. 95

5.8 The prevalence of Nodes with ANC 3, 4, 5 and 6 for simulations with different NNC, MSL and loading. Dead zone of 250$\mu\varepsilon$ has been used except for simulations with * next to the NNC value which indicate that the dead zone of 1000$\mu\varepsilon$ has been used. Key results have been highlighted in yellow. 96

5.9 The mean, 95 % Confidence intervals (CI), median, standard deviation(SD), the minimum (min) and the maximum (max) of active strut radii [mm] for the NN simulations presented in this chapter. Statistical distributions are calculated from 5 randomly generated models of each nominal connectivity with mean strut length (MSL), lattice type and loading as shown. Dead zone of 250$\mu\varepsilon$ has been used except for simulations with * next to the NNC value which indicate that the dead zone of 1000$\mu\varepsilon$ has been used. Key results are highlighted in yellow. 101

5.10 Comparison of the predicted five model mean trabecular volumes [mm^2] for simulations with dead zone thresholds of 250 $\mu\varepsilon$ and 1000$\mu\varepsilon$. Values are presented for high and low NNC simulations using MSL of 0.7 and 1.5mm subjected to either a triaxial or uniaxial loading scenario. 109

5.11 Comparison of the predicted five model mean Young's moduli in the loading direction [MPa] or simulations with dead zone thresholds of 250 $\mu\varepsilon$ and 1000$\mu\varepsilon$. Values are presented for high and low NNC simulations using MSL of 0.7 and 1.5mm subjected to either a triaxial or uniaxial loading scenario. 109

6.1 Structural efficiency, expressed as Young's modulus divided by trabecular volume, for Voronoi and NN nominal connectivity 4 simulations. The 95% maximum confidence intervals of structural efficiency are calculated from the maximum values of E and minimum values of V using the 95% confidence intervals for those values. The opposite was done for the minimum confidence intervals. 128

6.2 Initial connectivity and ANC for Voronoi and NN04 simulations with 0.7mm, 1.0mm and 1.5mm MSL. The table presents mean, mode, standard deviation (SD), minimum and maximum values for uniaxial and triaxial loading simulations. 131

6.3 Abundance of ANC 3, 4, 5 and >5in Voronoi and NN04 models at the end of adaptation simulations. The topological study values reported by Reznikov et al. (2016) are also included. 132

6.4 Comparison of ITA values for Voronoi and NN04 simulations for various values of MSL and two loading scenarios. The mean, 95% Confidence interval (CI), median, standard deviation (SD), minimum (Min) and maximum (Max) values are presented. ITAs are grouped by nodes with the same ANC. Statistical distributions are calculated from 5 randomly generated models of each simulation. Key results have been highlited in yellow. 133

6.5 Comparison of Mean NC at the end of the adaptation between simulations using dead zone threshold of 250$\mu\varepsilon$ and 1000$\mu\varepsilon$. NN04 and Voronoi(V) simulations each with MSL of 0.7mm or 1.5mm are compared. . 137

6.6 Comparison ANC3, ANC4 and ANC5 abundance between simulations using dead zone threshold of 250$\mu\varepsilon$ and 1000$\mu\varepsilon$. NN04 and Voronoi(V) simulations each with MSL of 0.7mm or 1.5mm are compared. In addition to absolute connectivity values the results for dead zone threshold of 1000$\mu\varepsilon$ include the difference ($\triangle$) from the results for dead zone threshold of 250$\mu\varepsilon$. 138

6.7 Comparison of trabecular volume [mm^3] at the end of the adaptation between simulations using dead zone threshold of 250$\mu\varepsilon$ and 1000$\mu\varepsilon$. NN04 and Voronoi(V) simulations each with MSL of 0.7mm or 1.5mm are compared. In addition to absolute trabecular volume values the results for dead zone threshold of 1000$\mu\varepsilon$ include the percentage difference ($\triangle$) from the results for dead zone threshold of 250$\mu\varepsilon$. 139

6.8 Comparison of Young's modulus [MPa] at the end of the adaptation between simulations using dead zone threshold of 250$\mu\varepsilon$ and 1000$\mu\varepsilon$. NN04 and Voronoi(V) simulations each with MSL of 0.7mm or 1.5mm are compared. In addition to absolute trabecular volume values the results for dead zone threshold of 1000$\mu\varepsilon$ include the percentage difference (Δ) from the results for dead zone threshold of 250$\mu\varepsilon$. 139

6.9 Comparison of ITAs for ANC3, ANC4 and ANC5 between simulations using dead zone threshold of 250$\mu\varepsilon$ and 1000$\mu\varepsilon$. NN04 and Voronoi(V) simulations each with MSL of 0.7mm or 1.5mm are compared. ITAs were not shown for ANCs with 5% predominance or less as given in the Table 6.6 140

6.10 The mean, 95% Confidence intervals (CI), median, standard deviation(SD), the minimum (Min) and the maximum (Max) of active strut radii for Voronoi and NN04 simulations. Statistical distributions are calculated from 5 randomly generated models with either 0.7mm or 1.5mm MSL, simulation type and loading as shown. The strut radius has been calculated as the average of 4 element radii making up each strut, in line with methodology of other topological studies (Liu et al. (2008), Kirby et al. (2020)). 145

6.11 Shear modulus [MPa] value predictions for NN04 and Voronoi simulations subjected to uniaxial loading. Mean, standard deviation and confidence intervals are calculated from 5 model results for each simulation. 148

6.12 Direction index for a single model of Voronoi, NN04 and NN14 simulations with 0.7mm and 1.5mm MSL and dead zone thresholds of 250$\mu\varepsilon$ and 1000$\mu\varepsilon$. The values given are element area weighted absolute values of vector components. 153

7.1 Proximal femur relative density (RD) reported in the literature. 176

7.2 Proximal femur Young's modulii [MPa] reported by Liu et al. (2006). E_l denotes the modulus in the direction with the lowest values and E_h denotes the modulus in the direction with the highest values. 176

7.3 Proportion of joint nodes with ANC=3, ANC=4, ANC=5 and ANC>5 in the Voronoi femur model at the end of adaptation simulations. Nodes which subdivide struts are excluded. 177

7.4 Proportion of joint nodes with ANCs which are present in more than 5% of total nodes. 177

7.5 Predicted mean, mode, standard deviation (SD), minimum (Min) and maximum (Max) NC in the adapted Voronoi femur model. 178

7.6 Predicted mean, mode, standard deviation (SD), minimum (Min) and maximum (Max) NC in the adapted NN14 femur model. 178

7.7 Predicted number of nodes, mean, standard deviation (SD), minimum (Min) and maximum (Max) ITA for given NC in the adapted Voronoi femur model. 178

7.8 Predicted number of nodes, mean, standard deviation (SD), minimum (Min) and maximum (Max) ITA for given NC in the adapted NN14 femur model. 179

7.9 Mean and standard deviation of element radii at the end of the adaptation simulation for circular and equivalent elliptical struts. 187

A.1 Proportions of nodes with four most prevalent NC following adaptation simulations. Results are tabulated by the loading, initial NC and MSL. Each simulation entry gives NC on top and its proportion below. Results for simulation with dead zone at 250$\mu\varepsilon$ and 1000$\mu\varepsilon$ are shown in black and red respectively. 210

A.2 The ITA mean, 95 % Confidence intervals (CI), median, standard deviation(SD), minimum (min) and maximum (max) values for fixed joint lattice model simulations subjected to uniaxial loading. ITAs for four most prevalent NCs at the end of adaptation are presented. Dead zone of 250$\mu\varepsilon$ has been used except for simulations with * next to the NNC value which indicate that the dead zone of 1000$\mu\varepsilon$ has been used. 211

A.3 The ITA mean, 95 % Confidence intervals (CI), median, standard deviation(SD), minimum (min) and maximum (max) values for fixed joint lattice model simulations subjected to triaxial loading. ITAs for four most prevalent NCs at the end of adaptation are presented. Dead zone of 250$\mu\varepsilon$ has been used except for simulations with * next to the NNC value which indicate that the dead zone of 1000$\mu\varepsilon$ has been used. 212

A.4 The ITA mean, 95 % Confidence intervals (CI), median, standard deviation(SD), minimum (min) and maximum (max) values for pinned joint lattice model simulations subjected to uniaxial loading. ITAs for four most prevalent NCs at the end of adaptation are presented. Dead zone of 250$\mu\varepsilon$ has been used except for simulations with * next to the NNC value which indicate that the dead zone of 1000$\mu\varepsilon$ has been used. 213

A.5 The ITA mean, 95 % Confidence intervals (CI), median, standard deviation(SD), minimum (min) and maximum (max) values for pinned joint lattice model simulations subjected to triaxial loading. ITAs for four most prevalent NCs at the end of adaptation are presented.Dead zone of 250$\mu\varepsilon$ has been used except for simulations with * next to the NNC value which indicate that the dead zone of 1000$\mu\varepsilon$ has been used. 214

A.6 Goodness of fit between radius and ITA data extracted from simulations and the probability distributions fitted to this data. The table presents goodness of fit for three probability distributions of 2 separate simulations tested with squared error (MSE), normalised root mean squared error (NRSME) and normalised mean squared error (NMSE) cost functions. Lower numbers indicate better fit where 0 is the perfect fit. 215

1

Introduction

1.1 Context of the research

Several clinical conditions are linked to bone health, with osteoporosis and osteopenia being the most prevalent. Reginster & Burlet (2006) estimate that 200 million people worldwide have osteoporosis, whilst Salari et al. (2021) report an 18.3% prevalence of the disease. Osteoporosis and osteopenia are associated with decrease in bone mineral density and cause a change in trabecular bone architecture. Study of vertebral fractures in middle-aged men with osteopenia (Legrand et al. (2000)) strongly suggests that bone trabecular micro-architecture is a major and independent determinant. Harvey et al. (2015) investigated fracture risk in osteoporotic bone. They developed an imaging analytical tool, the trabecular bone score (TBS), which is computed from the total number of trabeculae, trabecular separation and connectivity. A high TBS appears to represent strong, fracture-resistant micro-architecture, whilst a low TBS reflects weak, fracture-prone micro-architecture.

Paget's disease is characterised by increased bone remodelling resulting in disorganised coarse trabeculae (Whyte (2006)). The overall volume of trabecular bone increases, with trabeculae becoming thicker. However, the architecture develops large voids, and cortical bone regions may resemble trabecular bone (Nebot et al. (2019)). Other conditions such as femoral head osteonecrosis, caused by a decrease in the blood supply (Mont & Hungerford (1995), give rise to the thinning of the trabeculae (Arabnia & Tran (2015)). Finally trabeculae are susceptible to fracture and can be affected by cancer.

This thesis focuses on computational model adaptation simulations based on mechanotransduction, rather than on biochemical signalling. Mechanotransduction is the process by which cells convert mechanical stimuli into biochemical signals, with osteocytes playing a key role in detecting mechanical signals and influencing bone modelling and re-modelling. Such models provide valuable insights into trabecular bone mechanics by analysing its response to human activities. They can be used to predict fracture risk, optimise orthopaedic implants, study the effects of changes in trabecular architecture due to osteoporosis and osteopenia and provide visual representations of bone archi-

tecture. Recently, they have been used for additive manufacture of bone scaffolds.

To produce reliable results, these models need accurate representation of bone geometry, material properties, and boundary conditions. However, most current models, apart from micro-scale continuum models, fail to predict trabecular architecture, which accurately represents real bone. Specifically, the nodal connectivity (NC), a number of trabeculae connecting at a node and the inter trabecular angle, the angle between individual trabeculae meeting at each node (ITA), values do not reflect the properties of actual bone. Micro-scale continuum models are computational expensive and there is a clear benefit to a time efficient computational model that provides more accurate representation of real bone. This thesis aims to improve trabecular architecture representation at the micro-scale in computationally low cost structural models. It investigates the significance of the initial model structural layout, focusing on variations in the initial NC.

1.2 Thesis objectives

The aim of this thesis is to improve the micro-scale representation of trabecular bone in structural models. Its primary goal has been to achieve a close correspondence between the adapted model topology and that observed in micro-CT imaging studies, while maintaining agreement in predicted stiffness and relative density with macro-level continuum studies. Structural studies have achieved good agreement with ex-vivo tests (van Lenthe et al. (2006)) and have predicted trabecular architecture with good agreement to real bone (Villette & Phillips (2018),Zaharie & Phillips (2018), Favier et al. (2021)) whilst offering computational efficiency over continuum models. However, the accuracy of trabecular representation achieved by such models at micro-scale is unclear in the context of recent work by authors such as Reznikov et al. (2016, 2020).

There is evidence that prosthetic implants perform better if their material properties are similar to that of the surrounding bone (Lill et al. (2003)). A more biofidelic model would create potential for 3D printing of bone scaffolds and implants which more closely match bone architecture. In addition, this research will improve the understanding of

how well the current meso-scale models predicts bone behaviour.

Structural idealisation of trabecular bone with beam or truss elements in meso-scale models presents a computational efficiency benefit. The trabecular architecture predicted by these models corresponds well with real bone at meso-scale. This thesis examines the biofidelity of structural models at micro-scale by considering the trabecular bone structural form. An assumption that the trabecular bone behaves as a lattice structure is integral to structural models. Lattices consist of strut frameworks which are light and efficient in the use of material. Their strength is a function of the strut material properties, joint fixity and strut organisation. Joint fixity determines whether a lattice structure is bending dominated, where the struts are rigidly connected at nodes to resist rotation, or stretch dominated, where joints are free to rotate (Ashby (2006)). Nodes which are free to rotate are often referred to as pinned joints and to achieve stability, such lattices typically require a larger number of struts connecting at each node than bending dominated ones (Maxwell (1864)).

One way of examining lattice structures is to consider them as cellular solids and the works of Gibson & Ashby (1997), Gibson (2005) and Ashby (2006) provide a framework for trabecular bone to be considered as such. Ashby (2006) introduces a relationship between the relative density of a cellular solid and stiffness as presented by Equation 1.1.

$$E_i^* = \alpha \, E_s \, \bar{\rho}^{\beta} \tag{1.1}$$

where E_i^* is the Young's modulus of the lattice and E_s is the Young's modulus of the material making up the struts and the subscript i can take a value of 1, 2 or 3 defining the three principal directions. $\bar{\rho}$ is the relative density defined by Equation 1.2 and α and β are constants dependant on the lattice form.

$$\bar{\rho} = \frac{\rho^*}{\rho_s} = \frac{v_s}{v_t} \tag{1.2}$$

where ρ^* is the density of the lattice, ρ_s is the density of strut material, v_s is the volume occupied by the struts and v_t is the total volume of the cellular solid including voids.

1.3 Summary of chapters

This thesis is organised in eight chapters, including the Introduction.

In Chapter 2, a background of the research project is presented. The key features of bone architecture are described and numerical simulations of bone adaptation reviewed.

Chapter 3 presents the research methodology focusing on the FE modelling and the adaptation algorithm. This chapter explains how key modelling parameters such as nodal connectivity (NC), mean strut length (MSL) and the trabecular element radii are defined.

Chapters 4 and 5 investigate how modifications to the Structural Biomechanics research group at Imperial (Phillips (2012), Villette & Phillips (2017), Zaharie & Phillips (2018), Favier et al. (2021), Kaufmann et al. (2021)) near neighbour (NN) modelling approach may yield improvements in predicted topology. In particular, it evaluates whether improvements in NC, compared to CT imaging studies, can be achieved whilst retaining continuum level mechanical properties consistent with those reported in experimental studies. A sensitivity study was undertaken to establish the significance of the nominal node connectivity (NNC) and the implication of treating trabecular bone as either a stretch or bending dominated lattice. The effect of MSL is evaluated through a series of studies with equal NNC models. Uniaxial and triaxial loading scenarios are considered and the behaviour under different loading is compared to empirical relationships of Young's modulus and density reviewed by Helgason et al. (2008). Chapters 4 and 5 will consider the effect of variations in these modelling parameters on mechanical property and topology predictions respectively.

The research presented in Chapter 6 evaluates an alternative to NN models considered in Chapters 4 and 5. The effects of MSL and loading for the alternative model are be examined as in Chapter 4. Behaviour of lattice structures under different loading is compared to empirical relationships of Young's modulus and density reviewed by Helgason et al. (2008). As in Chapter 5, comparisons with real bone are made using

the morphological characteristics.

Chapter 7 applies the findings of the previous chapters to an adaptation simulation using two simplified proximal femur models. Chapters 4, 5 and 6 establish which of the simulations considered in this thesis has the potential to most closely predict mechanical and topological properties of trabecular bone. This methodology has been applied to one proximal Femur adaptation simulation. Another simulation, acting as a control, uses the established approach of the Imperial Structural Biomechanics research group with a few minor modifications.

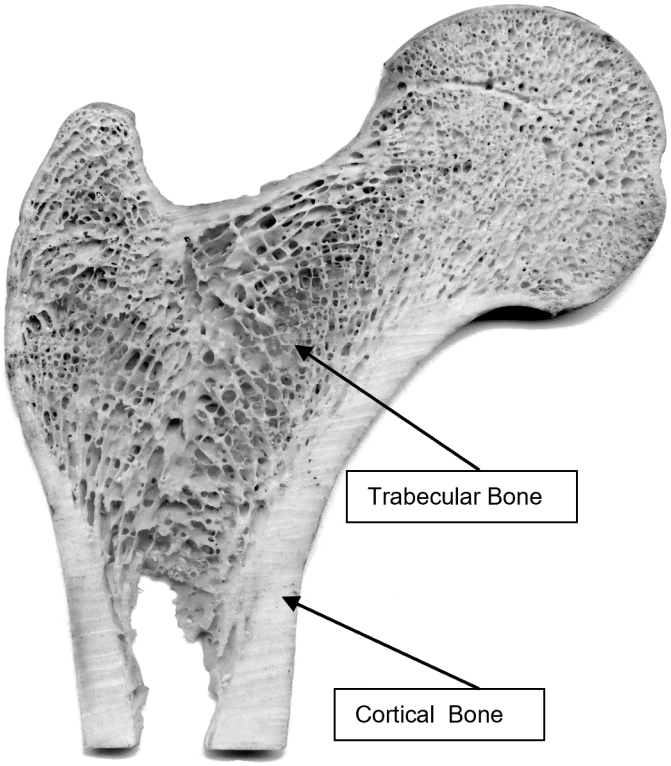
Chapter 8 summarises the work undertaken during the PhD. Assumptions made and model limitations will be reviewed highlighting the areas for potential improvement and further work. Potential for practical implementation will be considered.

2

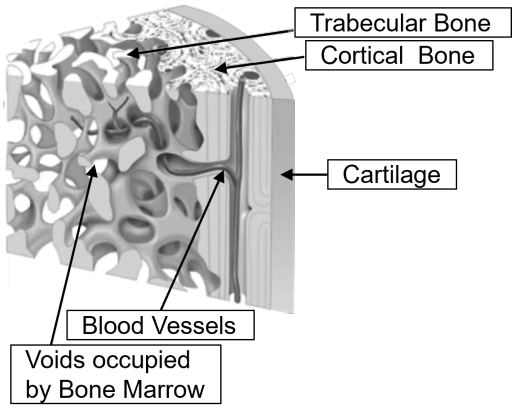
Background

2.1 Bone architecture

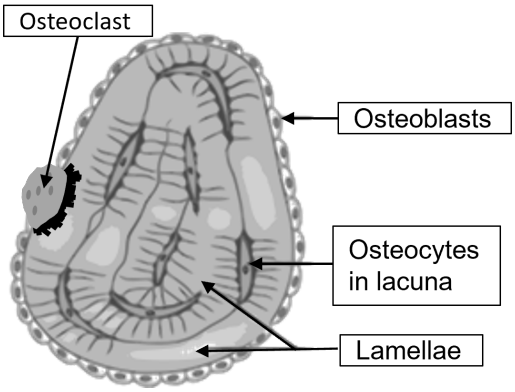
Bone is a complex composite material at both micro and macro-scale. At macro-scale we distinguish between the cortical and trabecular bone (Figure 2.1a). Cortex at this scale is a solid material forming the outer membrane of the bone typically several millimetres thick at the middle of the diaphysis (the central portion of long bones) and only a few hundred microns at epiphysis (the joint ends of long bones). Trabeculae occupy the void created by the cortex and appear as a series of rods and plates (Figure 2.1b) typically 100μm to 300μm thick (Keaveny et al. (2004), Rho et al. (1998)). Trabecular bone is highly porous with blood vessels, nerves and bone marrow occupying the voids (Figure 2.1b) .



(a) Coronal Slice through the proximal femur based on Phillips (2010).



(b) Bone internal structure based on OpenStax (2017).



(c) Section through a trabecula based on OpenStax (2017).

Figure 2.1: Bone architecture.

Both types of bone are made of similar micro-scale structural units called lamellae. Lamellae are thin sheets, typically 6μm thick, made up of mineralized collagen fibrils ($<$50nm in diameter). Fibrils are laid linearly within lamellae, which are themselves arranged in packets to form trabecular bone as shown in Figure 2.1c (Reznikov et al. (2014*a*), Keaveny et al. (2004), Rho et al. (1998)). The most recent lamellar packets are located on the external surface of the trabecula and align with its axis. The axes of the older packets, located in the body of the trabecula, and the axes of the most recent packets form an angle of about 20° to 30° (Reznikov et al. (2015)). Lacunae are small gaps between lamellae which incorporate osteocytes and are spaced a few tens of μm apart and interconnected through canaliculi (Reznikov et al. (2015), Rho et al. (1998)).

The main functions of bone are to provide support to the body, protect internal organs and, together with the muscle system, facilitate movement (Clarke (2008)). Bones also act as a calcium store and the bone marrow produces blood cells. In order to fulfil its functions, bone needs to maintain its strength and integrity. Bone formation and remodelling play a key role in this.

Bone is formed, during embryonic development and fracture healing, from precursor cells which can differentiate into fibrous tissue, such as muscles and tendons, cartilage or bone. Bone formation occurs by two distinct mechanisms: endochondral or intramembranous ossification (Ducheyne (2015)). Endochondral ossification is a two-step process whereby an organic matrix (osteoid/cartilage template) is initially laid down by osteoblasts. This is followed by precipitation of mineral crystals which grow slowly over time to produce the composite material. Intramembranous ossification proceeds without the initial cartilage template and is present in skull bone formation and fracture healing. Both of these processes involve the differentiation of mesenchyme into bone tissue; directly during intramebranous ossification or via cartilage in endochondral ossification. Mesenchyme consists of undifferentiated stem cells suspended in a fluid matrix. As ossification takes place stiff structures emerge from this loosely organised embryonic connective tissue.

Bone tissue is continuously regenerated through a bone remodelling mechanism. This process allows infant bone tissue to be replaced with larger, more mechanically competent material. It is also necessary for repair of micro-cracks which arise dur-

ing daily activity and for functional adaptation to loading. Remodelling takes place in four phases and is regulated by three bone cell types: osteocytes, osteoblasts and osteoclasts. In the activation phase osteocytes sense stimuli due to loading changes and trigger differentiation of bone lining cells into osteoclasts. Once activated, the osteoclasts dissolve bone during the resorption phase before undergoing apoptosis (cell death). During the reversal phase, which follows, debris produced during resorption is removed. Finally, osteoblasts are recruited to the remodelling area to produce a new bone matrix and promote its mineralisation in the formation phase (Rucci (2008), Hill (1998), Parfitt (1994)). During this process, osteoblasts stay trapped in the bone matrix and change into osteocytes (Rucci (2008), Kular et al. (2012)). Time taken from activation to reversal of remodelling is approximately three weeks, while reversal to complete mineralisation is around three months (Parfitt (1994)). Complete turnover of the skeleton occurs approximately every 10 years (Deal (2009)).

The exact mechanism of bone remodelling is unknown, but it is thought that osteocytes sense fluid flow through the canaliculi. Mechanical loading is thought to force the fluid into lacunae where the signal is detected by the osteocytes. Osteoblasts or osteoclasts are then activated to initiate apposition or resorption dependent on the nature of the signal. Recent cell biology theory suggests that all cells may be mechanosensitive through some form of a membrane attachment or a structure such as cilia (Kung (2005)). This opens up the possibility that all bone cells, not just the osteocytes, may detect a mechanical stimulus triggering a complex biochemical response which results in bone remodelling.

Bone remodelling is most prominent in trabecular bone and it is estimated that 80% of bone remodelling activity takes place in trabecular bone, although it only comprises 20% of bone by volume. The relative importance of cortical remodelling increases with age as trabecular bone volume decreases and the remodelling activity in both increases (Seeman (2013)).

In addition to the constant renewal trough remodelling, bone can be shaped and reshaped through modelling by the independent action of osteoblast and osteoclasts (Langdahl et al. (2016), Burr & Allen (2019)). The activities of these cells do not necessarily need to be synchronised anatomically or temporally. Bone modelling defines

skeletal development and growth which continues throughout life. Modelling is often stimulated by physical activity which can be seen in increased bone mass of tennis players' dominant arms (Kontulainen et al. (2003) or by stance change diverting loads through the femur neck and increasing the bone mass at this site (Nawathe et al. (2015)). A strain environment could also be altered by clinical intervention and bone modelling of the tibial bone has been observed after harvesting of the fibula for reconstructive surgery (Taddei et al. (2009)).

2.2 Review of numerical simulations

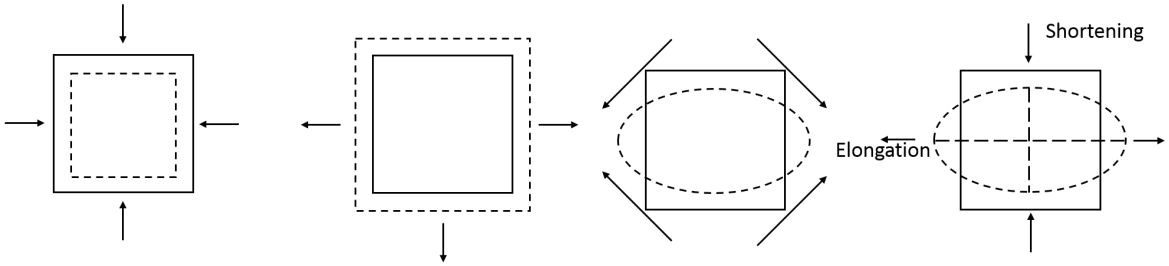
2.2.1 Introduction

It is widely accepted that bone adapts its architecture in accordance with the loading regime it has been subjected to through a process of remodelling. This is particularly true of trabecular bone. This was first documented by Culmann (1866), von Meyer (1867) and Wolff (1869) who observed trabecular bone architecture in the proximal femur. Remodelling also allows infant bone tissue to be replaced by more mechanically competent material and is active during fracture healing, guided by tissue differentiation. A number of analytical theories of tissue differentiation and functional adaptation are reviewed in Sections 2.2.2.1 and 2.2.2.2 respectively. With the advent of computer technology, researchers have attempted to simulate functional adaptation with Finite Element (FE) numerical models. Numerical simulations can be categorised in accordance to the size of the FE mesh size they employ. Macro-scale simulations, reviewed in Section 2.2.3, use elements larger than the individual bone tissue components, namely the trabeculae. In micro-scale studies, reviewed in Section 2.2.4, FE mesh size is smaller than the individual trabeculae. More recently, structural idealisation of trabecular bone with beam and truss elements was used in meso-scale simulations. These are reviewed in Section 2.2.5.

2.2.2 Analytical theories

2.2.2.1 Tissue differentiation

Tissue Differentiation was first studied to gain understanding of fracture healing. Pauwels (1959) used continuum mechanics stress invariants of hydrostatic (volumetric) and octahedral shear (distortional) stresses, in an attempt to explain it (Figure 2.2) . He recognised that octahedral shear stress causes elongation in one direction and observed that collagen fibres in the fracture callus were all aligned. Making simple assumptions on the loading he speculated that the elongation direction coincided with fibre alignment. Pauwels concluded that the octahedral shear stress elongation stimulated fibrous tissue growth whilst hydrostatic compression stimulated cartilage creation. He did not identify specific signals that encouraged bone growth which he stipulated, occurred by cartilage calcification under the influence of hydrostatic pressure.



(a) Hydrostatic pressure. (b) Octahedral shear.

Figure 2.2: Hydrostatic and octahedral shear stress illustration adapted from Carter et al. (1998).

Carter et al. (1998) built on these ideas, adding the stipulation that bone growth was stimulated by low hydrostatic and octahedral shear stresses. They further suggested that the fracture gap initially fills with fibrous material which differentiates into woven bone and eventually, through remodelling, turns into bone tissue. They validated this theory with a finite element simulation of fracture healing which replicated clinical x-ray observations. Claes & Heigele (1999) improved on this work by quantifying invariant value ranges which guided differentiation of cells into specific tissue. Stress invariants have their strain counterparts and Shefelbine et al. (2005) expressed the differentiation limits defined by Claes & Heigele (1999) using hydrostatic and octahedral shear strain values.

2.2.2.2 Functional adaptation

Functional adaptation theories assume a relationship between bone volume changes and either a bone stress or strain state. Pauwels (1965) (english translation Pauwels (1980)), suggested that remodelling u is governed by the difference in stress at any one time σ and the equilibrium stress σ_s as defined by Equation 2.1

$$u = f((\sigma - \sigma_s)^n) \tag{2.1}$$

where n is an unknown constant and f is some undefined function. A positive value of u would indicate bone growth (apposition) and a negative value bone loss (resorption).

Using thermomechanical continuum theory, assuming conservation of mass and treating cortical bone as a porous solid Cowin & Hegedus (1976) and Hegedus & Cowin (1976) developed a theory of adaptive elasticity. They formulated an expression which describes the changes in bone density and is applicable to both cortical and trabecular bone(2.2).

$$\frac{dE}{dt} = A_{ij}(\varepsilon_{ij} - \varepsilon^o_{ij}) \tag{2.2}$$

where E is the modulus of elasticity, ε_{ij} is the actual strain tensor, ε^o_{ij} is the strain tensor at bone remodelling equilibrium and A_{ij} is a set of empirical coefficients. They defined another expression for external remodelling which describes cortical bone changes

$$\frac{dX}{dt} = B_{ij}(\varepsilon_{ij} - \varepsilon^o_{ij}) \tag{2.3}$$

where X is a radial coordinate perpendicular to cortical bone surface and B_{ij} is a set of empirical coefficients.

Carter (1982) combined data from animal studies and FE analysis to develop a cortical bone adaptation theory, illustrated in Figure 2.3. The theory suggests that bone volume changes are regulated by the rate of change of strain history. The rate of change of bone strain history is dependent on the mean strain, the range between the minimum and maximum strain and the rate of loading recurrence. Carter and his colleagues used three different approaches to extend this theory of cortical bone adaptation to trabecular

bone adaptation (Fyhrie & Carter (1986), Carter et al. (1987)). They assumed that bone is optimised with respect to its ultimate strength, that the strain energy density stored in bone is minimised or that fatigue damage accumulation drives adaptation. All three assumptions resulted in Equation 2.4

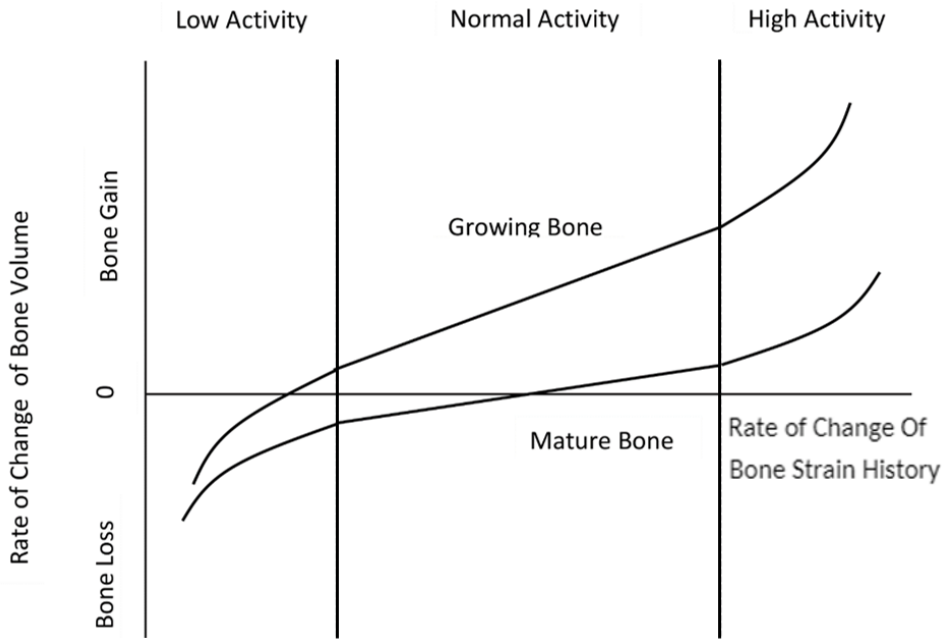


Figure 2.3: Hypothesis of bone remodelling based on Carter (1982).

$$\rho \propto \left(\sum_{i=1}^{n} n_i \bar{\sigma}_i^m \right)^{1/(2m)} \tag{2.4}$$

where ρ is the relative density of trabecular bone, n_i is a number of loading cycles of loading case i, and $\bar{\sigma}_i$ is the maximum effective stress due to load case i. Empirical constant m acts as the weighting factor giving a greater or a lesser importance to the stress magnitude in relation to the number of loading cycles. Effective stress $\bar{\sigma}_i$ is defined by Equation 2.5.

$$\bar{\sigma}_i = \sqrt{EU} \tag{2.5}$$

where E is the average elastic modulus of the bone and U is the strain energy density (SED) defined by Equation 2.6 and is equal to the area under the stress-strain plot.

$$U = \frac{1}{2}(\sigma_{ij}\varepsilon_{ij}) \tag{2.6}$$

where σ_{ij} and ε_{ij} are the stress and strain tensors respectively. Using the ultimate

strength approach Carter et al. (1987) also derived the adaptation stimulus Equation 2.7 used in a number of simulations (Beaupré et al. (1990), Whalen et al. (1988) Garcia-Aznar et al. (2005)).

$$S^* \propto \sum_{day} n_i(\bar{\sigma}_i/\bar{\sigma}_{ult})^m \tag{2.7}$$

where S^* is the daily stimulus and $\bar{\sigma}_{ult}$ is the ultimate bone strength. Studies which used this approach also rely on Equations 2.8 and 2.9 previously empirically developed by Carter & Hayes (1977) to predict the density and elastic modulus

$$\rho = A\bar{\sigma}_{ult}^{1/2} \tag{2.8}$$

$$E = C\rho^3 \tag{2.9}$$

where A and C are empirical constants.

More recently Frost (1996, 2003) proposed the principle of the mechanostat which, like a thermostat, switches bone apposition and resorption on or off depending on whether a mechanical stimulus is above or below a target value. He suggested that the molecular signalling driving the remodelling would not be activated in a small range, the lazy zone, around the target. This allowed bone to remain in equilibrium for small variations in stimulus. The exact action of the mechanostat is unknown, but it is thought that osteocytes take on this role as explained in Section 2.1

Both approaches by Pauwels (1965) and Cowin & Hegedus (1976) rely on the ability to establish changes in strain or stress state from some equilibrium reference state, often referred to as homeostatic state. The optimisation theory proposed by Carter et al. (1987) uses an iterative approach to predict the Young's modulus for the next step from the SED in the current step. As such it does not guide the simulation towards a specific goal whilst the mechanostat theory (Frost (1996)) guides the strain state towards a target.

2.2.3 Macro-scale models

Early studies were motivated by Wolff's, von Meyer's and Cullman's observations of the proximal femur (Carter et al. (1987), Beaupré et al. (1990), Huiskes et al. (1987)).

They used isotropic 2D macro-scale continuum models, choosing a variety of scalars as mechanical signals and simplified loading scenarios to drive the simulations. Inspired by these studies, a number of authors (Prendergast & Taylor (1994), Bitsakos et al. (2005), Geraldes & Phillips (2014)) sought to improve the precision of trabecular architecture predictions through the use of finer FE meshes, application of more detailed loading scenarios, or by using a different mechanical stimulus. They bench-marked their results against the early work.

Huiskes et al. (1987) and Bitsakos et al. (2005) followed the theory of adaptive elasticity developed by Cowin & Hegedus (1976) and assumed the existence of an equilibrium strain state which they calculated from the initial model. In order to reduce the modelling complexity associated with the full strain tensor, Equation 2.2 was modified and SED was used instead. The difference between the SED at an iteration step and the equilibrium value was used to evaluate the Young's modulus. As the simulation is driven towards a constant value of SED, the concept is not dissimilar to the mechanostat principle (Frost (1996, 2003)) used by Geraldes & Phillips (2014) where the simulation converges towards a predetermined target strain.

Carter (1989) used Equation 2.4 in the iterative adaptation simulation. Effective stress was evaluated at every iteration step and elastic modulus updated based on Equation 2.9 previously empirically developed by Carter & Hayes (1977). For simplicity, the number of loading cycles for each of three load cases was taken as 1 and values of m=1 and m=4 were investigated. Beaupré et al. (1990) followed the theory developed by Carter et al. (1987) but used the concept of attractor state stimulus, a bone maintenance signal which preserves healthy bone mass. The simulation was driven by a remodelling signal; the difference between the actual stimulus and attractor state stimulus. The attractor state stimulus was calculated from results of animal and human in vivo studies conducted to measure the required number of loading repetitions to maintain bone mass (Lanyon et al. (1975)). Further assumptions on the relationship between bone growth rate and remodelling signal were made and elastic modulus and relative density updated at each step based on these values.

The loading considered in early simulations of the proximal femur (Carter et al. (1989), Huiskes et al. (1987), Beaupré et al. (1990)) consisted of the single leg stance

hip contact force and the associated muscle forces on the greater trochanter. Bitsakos et al. (2005) recognised the importance of detailed loading definition and examined the effect of three different loading configurations. They found greater precision in predicted bone volume changes with more detailed loading scenarios. Geraldes & Phillips (2014) applied muscle loads from all major groups attached to the femur resulting from a variety of activities and found a good agreement between the study predictions, CT and μCT reconstructed imaging.

As opposed to most of the macro-scale studies, which considered bone as an isotropic material, Geraldes & Phillips (2014) used an orthotropic finite element model. Their study compared the results between this model and an equivalent isotropic model. The orthotropic model material properties orientations were aligned with local principal stress directions. For multiple load cases these directions were determined from the load case which gave rise to the highest absolute normal maximum strain. The modulus of elasticity in each of the principal directions was adjusted in accordance with the strain in that direction following the mechanostat theory. Target strain was set to 1250 $\mu\varepsilon$ with a lazy zone of +/- 250 $\mu\varepsilon$ around the target value. They found that the orthotropic model predictions correlated better with medical imaging data than isotropic predictions.

Each study had a different approach to convergence criteria. Carter et al. (1989) concluded that the relative density distribution pattern appeared to capture the major features of bone morphology after the third iteration. However, after the seventh iteration, density converged toward either the absolute maximum or minimum values, which is clearly unrealistic. This effect could be caused by the feedback loop between stiffness and stress, where a change in stress gives rise to a rapid change in relative density, which in turn causes a stress change. Huiskes et al. (1987), whilst not imposing a convergence criteria, attempted to overcome this by limiting the rate of stiffness change. They achieved monotonic convergence, determined by visual inspection, after 17 iterations . Beaupré et al. (1990) terminated the simulation once the density changes became less than 0.02 g/cm^3 which occurred after 30 iterations. Bitsakos et al. (2005) terminated their simulation after 30 iterations whilst Geraldes & Phillips (2014) assumed convergence when the average change in Young's moduli of all elements was less than

2% between successive iterations.

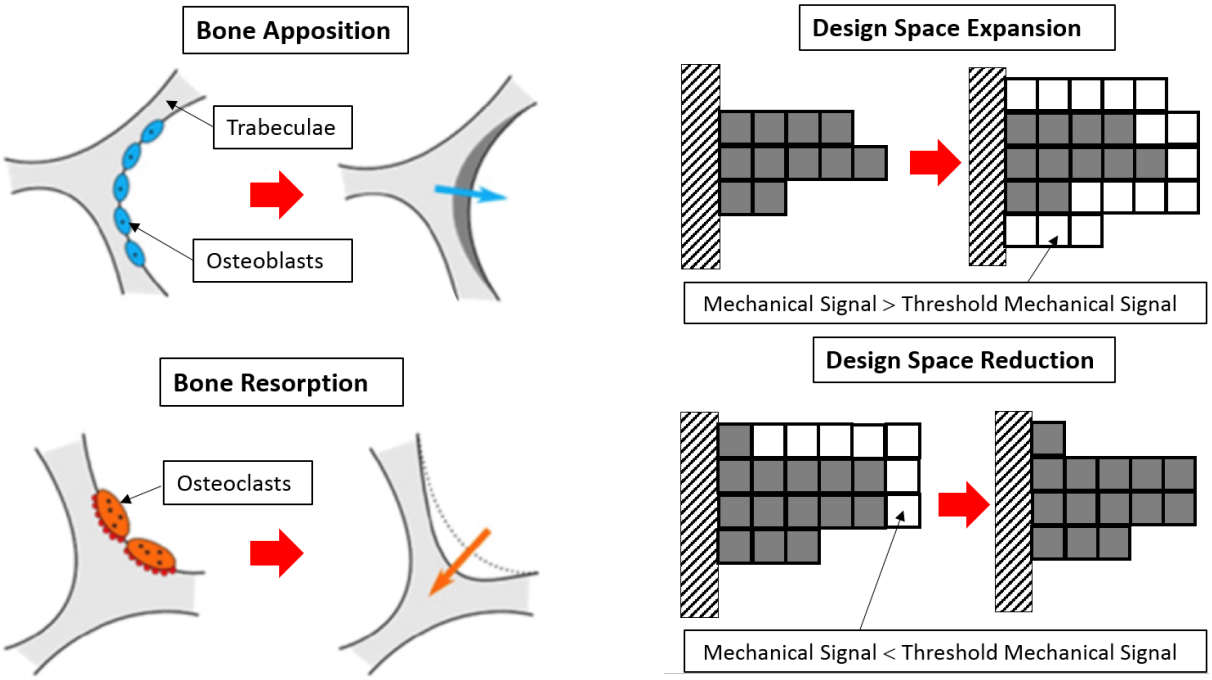
The macro-scale studies reviewed in this section use phenomenological algorithms based on either a stress or a strain stimulus. Early simulations (Carter et al. (1989), Huiskes et al. (1987), Beaupré et al. (1990)) were able to predict variations in bone mass which correlated reasonably well with ex-vivo sections and medical imaging. Greater precision was achieved through the use of 3D models and by adopting a more complete loading envelope (Bitsakos et al. (2005), Geraldes & Phillips (2014)), or by adopting an orthotropic rather than an isotropic constitutive relationship (Geraldes & Phillips (2014)). However, as finite elements were larger than the individual trabecula, simulations were only able to predict global bone stiffness with reasonable accuracy, but were less precise when considering local effects.

2.2.4 Micro-scale models

Variations in bone mineral density predicted by the macro-scale studies reviewed in Section 2.2.3 correlated reasonably well with medical imaging, but with exception of Geraldes & Phillips (2014) did not contain information on trabecular directionality. A number of authors have conducted studies with micro-scale models with the aim of achieving greater precision in trabecular direction predictions.

Micro-scale model simulations (Adachi et al. (2001), Tsubota et al. (2002), Jang & Kim (2008), Boyle & Kim (2011)) provide binary representations of bone tissue with elements in FE models representing either bone or a void. Topology optimisation algorithms add material in areas of high mechanical signal and remove it where the signal is low (Figure 2.4). This mimics osteoblast apposition and osteoclast resorption in real bone (Boyle & Kim (2011)), which is triggered by osteocytes on the trabecular surface.

The algorithm used by Adachi et al. (2001) and Tsubota et al. (2002) regulated the adaptation toward a local uniform von Mises stress state. Convergence was assumed when the difference between the total number of pixel elements between successive iterations fell under 2%. Jang & Kim (2008) and Boyle & Kim (2011) minimised global SED to drive their adaptation simulations and assumed convergence when the average



(a) Bone remodelling. (b) Topology Optimisation.

Figure 2.4: Topology optimisation concept adapted from Boyle & Kim (2011).

density difference between successive iterations fell below 0.5%

In order to capture sufficient trabecular detail required for topology optimisation, high resolution representations of trabecular bone are required, leading to small element sizes in FE models. Tsubota et al. (2002) and Jang & Kim (2008) used 70μ and 50 μm resolution pixel elements respectively in their 2D functional adaptation simulation of the proximal femur. The difference in resolution resulted in the first model containing 0.63 million pixel elements and the second 2.07 million pixel elements. In 3D models the required number of elements becomes even larger. Adachi et al. (2001) carried out a 3D topology adaptation of a 100μm nominal diameter trabecula and of a digital bone cube sample. The model of a single trabecula contained 245,000 10 μm resolution voxel elements while the cube bone sample model contained 8 million 25μ resolution voxel elements. Just over a quarter of these elements represented bone and the remainder represented voids. Boyle & Kim (2011) used 23.2 million 175 μm voxel elements in their 3D simulation of the proximal femur. The exact specification of the cluster wasn't given but a small cluster typically has over 1,000 with large ones approaching 10,000 cores. RAM varies from 512G to 1024GB.

Due to large number of elements in comparison to macro-scale models, these simulations required increased computational power. For example, the simulation by Jang & Kim (2008) ran for 84.5 h and the 3D model used by Boyle & Kim (2011) took 342.9 h to converge, which is over two weeks. Some simulations used initial models which randomly populated the cortical bone envelope with elements simulating trabecular bone (Tsubota et al. (2002), Jang & Kim (2008), Boyle & Kim (2011)) whilst others matched the element resolution to resolution of medical imaging used to create them (Adachi et al. (2001), Hambli (2013)). It has been suggested that the model resolutions need to be at cell size level (20-30 μm) to predict mechanical signals with adequate precision (Boyle & Kim (2011)). This, for a proximal femur model, would require approximately 8 billion elements and could not be solved within a reasonable time frame.

Adachi et al. (2001) applied a single uniformly distributed load case to the top face of the single trabecula model, while the 3D model of a canine bone sample was subjected to the same experimental load which it simulated (Goldstein et al. (1991)). Tsubota et al. (2002) and Jang & Kim (2008) used identical load cases of one-legged stance, maximum abduction and maximum adduction to Beaupré et al. (1990). Boyle & Kim (2011) used a detailed loading simulation of walking and stair climbing (Heller et al. (2005)).

Some studies validated their results by comparison of trabecular architecture parameters, such as trabecular size, against real bone (Adachi et al. (2001)). The computer simulation of animal in vivo adaptation model (Adachi et al. (2001)) found good agreement with observed bone volume fraction changes. It also predicted the size increase in trabeculae aligned with the load direction and resorption of trabeculae at right angles to it, which were observed in the experiment. Boyle & Kim (2011) also found that bone volume fraction agreed well with the data reported by Baum et al. (2010). A study by Hambli (2013) found excellent agreement between predicted and experimentally measured values of apparent ultimate stress (R^2 = 0.98) and compressive strain (R^2 = 0.85). Density predictions of the study by Tsubota et al. (2002) agreed with the results of Carter et al. (1989).

Another approach to validation was to consider trabecular directionality. The single trabecula was found to align with the load direction (Adachi et al. (2001)). Jang & Kim

(2008) calculated the mean trabecular intersection angles in the femur neck (69°) and the lesser trochanter (92°) and found good agreement with data reported by Skedros & Baucom (2007). Boyle & Kim (2011) on the other hand, found that the femur neck trabecula intersected at an angle of between 84°and 90°. The Boyle & Kim (2011) 3D study should have, on the face of it, produced a more precise prediction of trabecular intersection angles than the Jang & Kim (2008) 2D study. Boyle & Kim (2011) hypothesised that the loading environment led to an overestimation of the trabecular volume in a particular direction and skewed the intersection angle prediction.

2.2.5 Structural models

A novel method of representing trabecular anistropy was proposed by van Lenthe et al. (2006). Rather than treating bone tissue as a continuum they suggested micro-scale structural idealisations where individual trabeculae are represented with single beam elements. Their study compared the mechanical properties obtained from compression tests on 42 vertebral bone samples with those predicted by micro-scale continuum and structural models. They found a very good agreement of the structural simulation prediction of Young's Modulus with the test results (R^2=0.85). The continuum and structural model predictions were in excellent agreement (R^2=0.97). The micro-scale continuum models consisted of between 200,000 and 1,000,000 elements of 40 μm nominal size. The number of elements in micro-scale structural models ranged from 3,000 to 15,000. On average, the continuum models took over 50,000s to solve on a Superdome System (Hewlett-Packard, Palo Alto, CA), which is almost 14 hours. The structural models reached a solution in an average of 219s which is over 200 times faster.

Discrete structural elements to model trabecular bone have also been used successfully by the Biomechanics research group at Imperial (Phillips (2012) Phillips et al. (2015), Villette & Phillips (2017), Zaharie & Phillips (2018), Favier et al. (2021), Kaufmann et al. (2021)) who employed meso-scale models. In the initial model the trabecular bone anistropy was modelled by defining random nodes within the volume enclosed by the cortical bone envelope and connecting each node to a number of closest nodes with

strut elements. The number of potential trabecular trajectories was dependent on this initial connectivity. During the adaptation simulation the cross sectional areas of strut elements were adjusted through a series of iterations with the aim of achieving a target strain of 1250 $\mu\epsilon$. The lazy zone was defined as +/- 250 $\mu\epsilon$ so that apposition was triggered at 1500 $\mu\epsilon$ and resorption below 1000 $\mu\epsilon$. During the adaptation simulation potential trajectories were made inactive if the magnitude of strain in a particular strut fell below 250 $\mu\epsilon$. Convergence was assumed when less then 1% of elements required an adjustment in area between successive iteration steps. This approach yielded accurate representation of trabecular bone at meso-scale and correctly predicted behaviour such as fracture (Villette & Phillips (2018)).

2.2.6 Summary

Early bone adaptation simulations focused on the femur and did not explicitly consider trabecular architecture. Simulations often employed phenomenological 2D continuum macro-scale models with simplified loading scenarios and relied on a stress or strain scalar stimuli to drive adaptations. Material properties were assigned in accordance with empirical relationships between density and Young's modulus (Carter & Hayes (1977)). Even though various simplifications were made out of necessity, these studies were able to predict variations in bone mass which correlated well with ex-vivo sections and x-ray findings. However, they provided limited resolution of trabecular bone, identifying main trabecular groupings and directionality only through concentrations of increased density elements. More detailed predictions of trabecular directionality were achieved by 3D model simulations using more representative loading cases, such as the study by Bitsakos et al. (2005) and through consideration of orthotropy by Geraldes & Phillips (2014).

Micro-scale continuum simulations (Tsubota et al. (2002), Boyle & Kim (2011), Jang & Kim (2008)) achieved good agreement between predicted and actual trabecular architectures but at great computational expense. These simulations treat bone as either being present or not; adding material in areas of high mechanical signal modelling apposition and removing it in areas of low mechanical signal modelling resorption. A small

number of simplified load cases representing a range of daily activities were applied in simulations driven by either a stress or strain scalar stimulus. Micro-scale simulations require a high initial resolution and this makes model validation and comparison to real bone difficult.

Verhulp et al. (2006) evaluated differences between macro-scale and micro-scale model predictions. They compared stiffness, strain and stress distributions between three continuum models with different voxel element resolutions. The first one was a micro-scale model with the resolution of 80 μm and the other two were macro scale models with resolutions of 640 μm and 3040 μm respectively. They found reasonable agreement of strain and stress distributions between the three models, with the exception of the strains representative of the trabecula in the femur neck area where there was notable divergence of results. Yield load in low resolution models was overestimated by between 5 and 32 % and stiffness by between 38 and 109 %. Study authors suggested that the better correlation of yield loads was likely due to trabecular alignment with the load direction.

Structural studies have achieved good agreement with ex-vivo tests (van Lenthe et al. (2006)) and have been used to predict femoral fracture with good agreement to in-vitro experimental studies (Villette & Phillips (2018)) and identified activities which could maintain bone health (Zaharie & Phillips (2018), Favier et al. (2021)) whilst offering computational efficiency over continuum models. However, the accuracy of trabecular representation achieved by such models at micro scale is unclear in the context of recent work by authors such as Reznikov et al. (2016, 2020). These studies investigated the trabecular topology using five adult cadaver bone samples. μCT images of the samples were skeletonised to produce lattice networks and analysed for topological patterns. Studies identified two parameters which consistently defined the trabecular architecture. These parameters are: the angle between two trabeculae – the Inter-Trabecular Angle (ITA), and the number of trabeculae connected together at each node - the connectivity. The authors hypothesised that the consequence of these parameters may be that the trabecula are better adapted to multi-directional loading.

In order to improve the micro-scale representation of trabecular bone in structural models and achieve a close correspondence between the adapted model topology and

that observed in micro-CT imaging studies (Reznikov et al. (2016, 2020)) a new adaptation algorithm has been developed in this thesis. Chapter 3 presents this algorithm and the methodology that has been employed in investigating the ability of this algorithm to predict trabecular bone topology which more closely represents that of real bone.

3

Research methodology

3.1 Introduction

The aim of this thesis is to improve the micro-scale representation of trabecular bone in structural models. Its primary goal has been to achieve a close correspondence between the adapted model topology and that observed in CT imaging studies, while maintaining agreement in predicted stiffness and relative density with macro-level continuum studies. As described in Chapter 2, trabecular bone can be treated as a cellular solid using models of lattice structures (Gibson & Ashby (1997), Gibson (2005), Ashby (2006)). Chapters 4, 5 and 6 use structural lattice models to investigate the behaviour of trabecular bone as a cellular solid. This Chapter defines the methodologies of model generation and adaptation simulations which enable this work. The derivation of the iterative adaptation algorithm is presented.

The simulation workflow is summarised in Figure 3.1. Rhinoceros/Grasshopper was utilised to generate lattice geometries by defining node coordinates and their connectivity using scripting components. This information was exported to a number of text files which were manipulated into an Abaqus input file using Matlab. Section properties, boundary conditions and loading were defined at this stage. The process of model generation is described in detail in Section 3.2.

Functional adaptation simulations were carried out iteratively using the adaptation algorithm defined in Section 3.3. The analytical model at the end of the simulation process represents the predicted trabecular bone architecture and the results were processed as described in methodology sections of the relevant chapters.

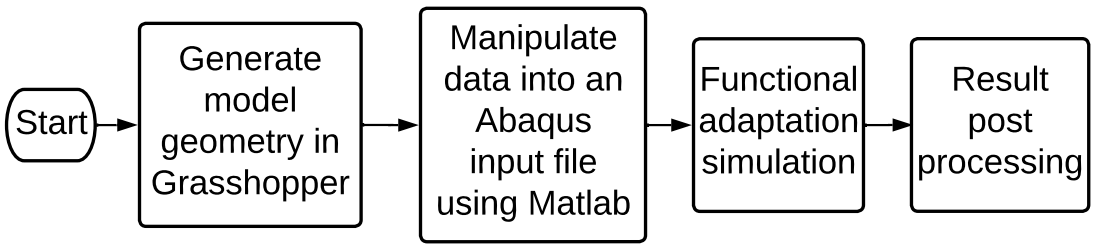


Figure 3.1: Simulation overview.

3.2 Model generation

3.2.1 Near neighbour models

This section provides a short overview of near neighbour (NN) models which have been used in Chapters 4 and 5. A NN lattice is formed of struts connecting each of its nodes to a set of nodes nearest to it. The node connectivity (NC) in a NN model is the number of other nodes an individual node is connected to. The minimum number of nodes an individual node is connected to in the initial models prior to simulations is the nominal NC (NNC). The mean and maximum connectivity are often larger. The NC is changed by adaptation and in converged models it is referred to as the adapted NC (ANC). NN models with NNC of # are referred to as NN# throughout the thesis. Nodes with NC and ANC of # are referred to as NC# and ANC# nodes throughout the thesis.

The NN modelling method creates a range of strut directionalities allowing the adaptation algorithm to favour those on the load path with high strains. The NNC determines the abundance of directionalities and this thesis will investigate the effect of this by considering a range of NNCs. The method adopted by Imperial Structural Biomechanics research group (Phillips (2012), Villette & Phillips (2017), Zaharie & Phillips (2018), Favier et al. (2021), Kaufmann et al. (2021)) uses NN16 models whilst preliminary studies undertaken during the research for this Thesis have established that there is little difference between NN16 and NN14 models. It was thus decided to consider a range of models from NN04 to NN14, incrementing the NNC by 2.

3.2.2 Modelling workflow

A number of studies on a hypothetical cuboid bone sample were undertaken. Three groups of simulations were undertaken to assess the effect of trabecular length, each with a different mean strut length (MSL). The lengths of trabeculae have been reported to vary with age, sex and bone site (Mosekilde (1988), Brickley & Howell (1999), Liu et al. (2008) Mosekilde (1988)) carries out a statistical analysis on 21 samples of ca-

daveric bone and reports the mean trabecular lengths of 577μm, 884μm and 1191μm for ages 20, 50 and 80 respectively. Brickley & Howell (1999) report mean values of 481μm, 898μm and 1016μm for ages 26 to 35, 46 to 55 and above 55 respectively. These two studies are in good agreement. Finally, Kirby et al. (2020) report an overall mean trabecular length of 710μm with a standard deviation 215μm. 700μm is thus considered representative of human bone under the age of 50 and 1000 μm above the age of 50. This informed the decision to consider 0.7mm and 1.0mm MSLs in simulations. A further set of simulations using 1.5mm MSL was considered to evaluate the behaviour in the meso-scale range.

The size of the cube models was governed by the choice of MSL. A minimum of 5 strut lengths was considered appropriate to minimise the effects of boundary conditions. In addition, a large volume of platen tests have been performed on cube samples with 8mm side length (Helgason et al. (2008). This led to a decision to create models measuring 8mm by 8mm by 8mm.

All numerical modelling used the finite element package ABAQUS/Standard, modelling lattice struts with B32 elements. In these elements B signifies beam elements, 3 signifies 3D modelling space and 2 refers to the use of a quadratic shape function in computation of beam deformations. B32 elements use Timoshenko beam theory which is useful for thicker beams, whose shear behaviour may be important. The formulation of these elements makes them efficient for thin beams, where Euler-Bernoulli theory is accurate, as well as for thick beams. Length to thickness ratio in trabeculae can be below 8:1 and the ability of B32 elements to model thicker beams was an important factor in the choice of this element type.

In addition, for efficiency of the adaptation simulations, it is important to establish the variation of the bending moment between the joints, or nodes, where structural members connect to each other. Trabeculae typically thicken at the nodes where they experience a maximum moment. In between the nodes, the bending moment may go from causing tension on one side to causing tension on the other side of trabeculae at least once. It is known as a point of contraflexure where the curvature of the beam reverses and the bending moment is zero. The use of 4 B32 elements (Figure 3.3) to represent each structural member allows points of contraflexure to be captured. Divi-

sion of struts into a greater number of elements would potentially lead to a marginally more efficient distribution of material in adaptation simulations but this would be at the cost of computational efficiency. Chapter 7 provides further discussion on this subject.

The NN model simulations with either stretch or bending dominated lattices are presented in Chapters 4 and 5. Beam elements were used in both bending and stretch dominated models with rotational degrees of freedom released at strut nodes for stretch dominated models (Figure 3.2). This allowed the bending models to be converted into stretch models by inserting a member release command for appropriate elements in the ABAQUS input file. Chapter 6 presents simulations based on a voronoi method of volume partitioning that leads to a low connectivity lattice. Each group of studies examined the effect of variation in trabecular length, loading arrangement and, where possible, NNC using finite element modelling described in this section. This approach allowed for a like for like comparison of bending and stretch models. A preliminary study compared the results of stretch models using Abaqus truss elements and Abaqus beam elements with released rotational degrees of freedom. The difference was found to be negligible.

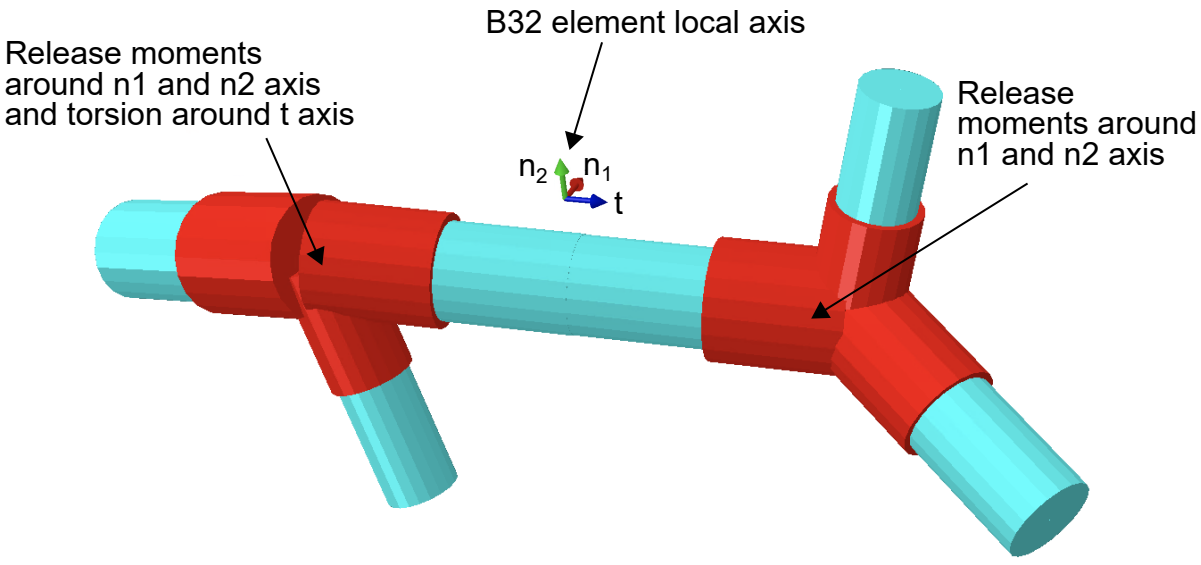


Figure 3.2: Diagram showing releases applied to struts to transform models from rigid to pin jointed lattices. B32 elements at strut ends are shown in red and the ones in the middle in cyan.

Data containing geometry information was written to a series of text files which were manipulated into an Abaqus input file. Young's modulus for the material was set to 18

GPa and the Poison's ratio to 0.3 in accordance with the values published in literature (Turner et al. (1999)). In order to model trabecular thickening at nodes, each strut was divided into four individual finite elements as shown in Figure 3.3.

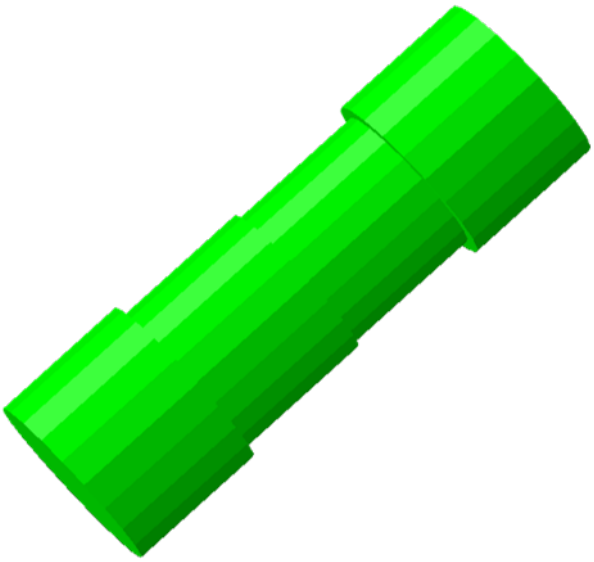


Figure 3.3: Strut division into four finite elements.

The model geometry definition, utilising Grasshopper, followed a workflow as indicated by the flow chart in Figure 3.4. The total number of nodes and the NNC were user defined. The strut length in all models was controlled by the number of joint nodes. These nodes at each end of a strut define its location and orientation, but further nodes in between were introduced to divide struts into more elements and allow the variation of normal strain along the strut length to be taken into consideration. The number of joint nodes combined with NC has a direct impact on the MSL. For a given volume and NC a larger number of joint nodes was required to reduce the MSL.

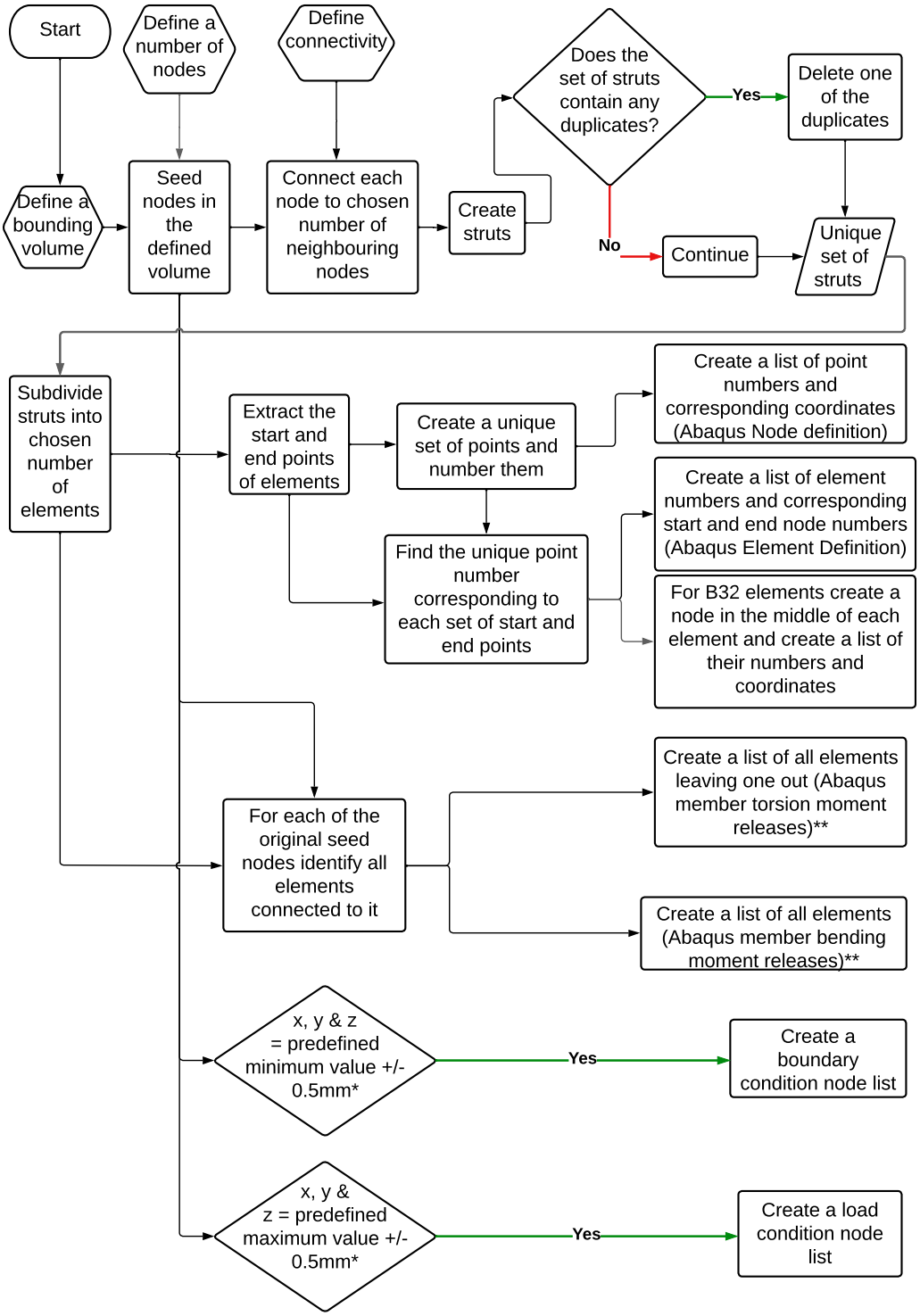


Figure 3.4: Grasshopper Model Generation. * the 0.5mm limit was chosen in order to achieve a uniform load distribution, please refer to the narrative related to Figure 3.5. **Figure 3.2 shows how member releases were applied.

Finally, the loading and boundary conditions were defined. Two loading scenarios were considered for each of the models: uniaxial and triaxial. In Abaqus syntax, boundary conditions and loading are applied in steps. In Step 1, representing the uniaxial load scenario, the model was restrained in three principal directions along the y=0mm plane and a uniform pressure of 1MPa was applied at the opposite face of the cube (Figure 3.5). As an approximation to the uniformly distributed load, point loads were applied to nodes located at the appropriate face of the cube. The total pressure of 1MPa was multiplied by the surface area of 64 mm^2 and divided by the total number of nodes in that face of the cube. For example, if there were 25 nodes in the face y=8mm point loads of 64N/25 =2.56N would have been applied to these nodes in Step 1.

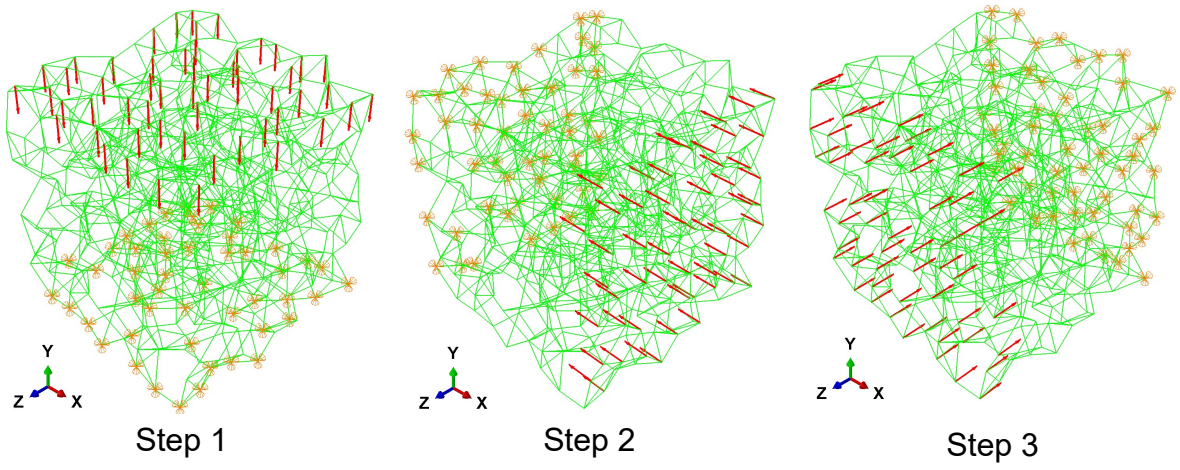


Figure 3.5: Adaptation simulation models boundary conditions.

The boundary conditions and load application nodes were selected with the aim of achieving a uniform load distribution. A node separation equal to the the MSL length was considered adequate to achieve this. For instance, there are 59 support nodes for the NN04 Model with MSL of 1.0mm in Step 1 as shown in Figure 3.5. This number varied from 59 to 68 in the five NN04 models and resulted in support separation of between 0.94mm and 1.08mm, which was considered satisfactory. This number of support nodes was obtained by selection of all nodes along the y axis within 0.5mm of the supported face, the xz plane at y=0mm. This was determined by trial on the NN04 1,0mm MSL models and applied to generation of all models for consistency.

Loads were applied in similar fashion to cube face x=8mm and z=8mm in Steps 2 and 3. The pressure of 1MPa was chosen as it represents the average contact pressure applied to all load bearing joints where trabecular bone is present. Orthopaedic surgeons, in verbal communication, state this as the pressure which acts on these joints and this is confirmed by Harris et al. (2012) who report 1MPa as the average contact pressure on the hip joint.

3.3 Adaptation algorithm

Some of the studies reviewed in Chapter 2 used stress-based while others used strain-based criteria to drive the adaptation simulations. It is reasonable to assume adaptation ensures bone is sufficiently stiff to resist applied loading through a process of optimisation with respect to its ultimate strength. It follows that a remodelling signal would get stronger as the bone yields and approaches failure. Due to strength anisotropy, bone yield criterion is anisotropic in stress but relatively isotropic in strain space and is not dependent upon elastic stiffness or density (Pankaj (2013), Bayraktar et al. (2004), Mercer et al. (2006)). In addition, while there is a range of yield strain values for bone, it is narrower than the corresponding stress value range. This is illustrated in Figure 3.6 where the diagram in a) represents a cellular solid and the diagram in b) provides its homogeneous continuum representation. The solid portion of the cellular solid follows a stress strain relationship given in diagram c). If the material in the cellular solid is organised so that there are more columns in direction 2 than direction 1, the response to uniaxial loading in those directions would be as shown in diagram d). Yield in direction 2 would happen at a higher stress σ_{2y} than in direction 1 σ_{1y}. However, the yield strain in both directions would be identical. Hence strain was chosen to drive adaptation simulations presented in this thesis.

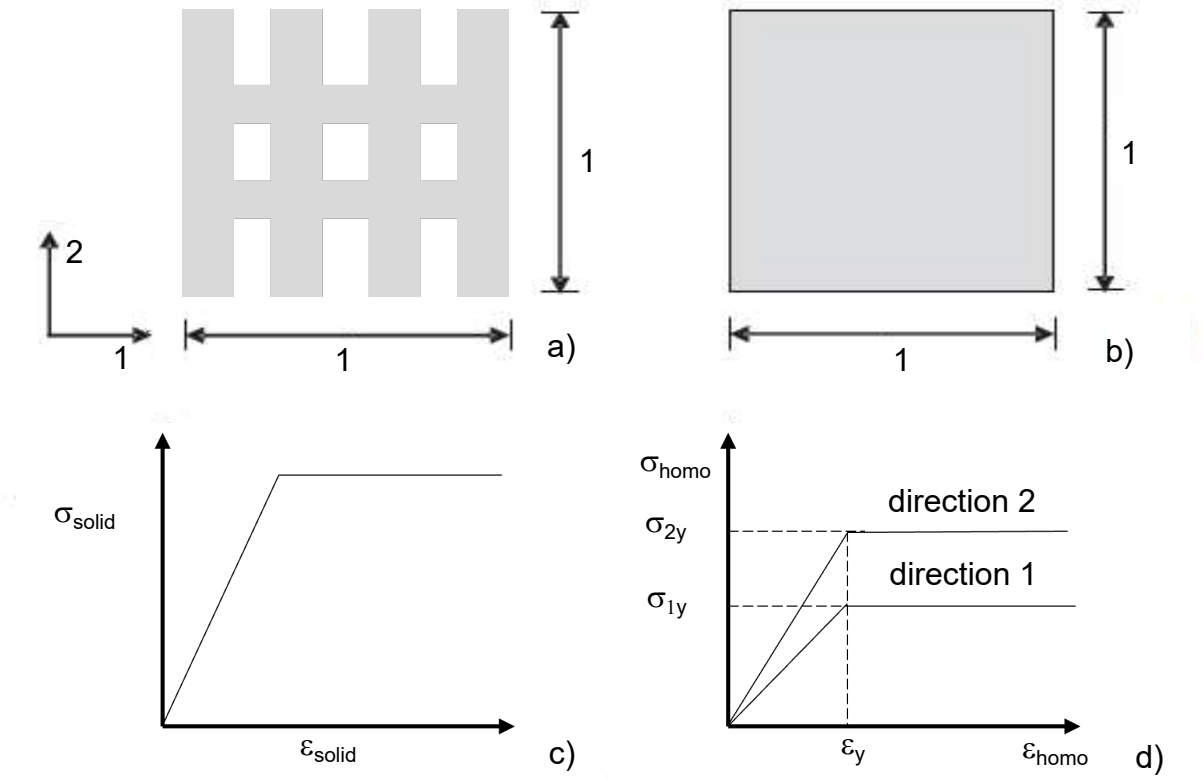


Figure 3.6: Comparison of Stress and Strain Yield Behaviour (extract from Pankaj (2013)).

The adaptation was simulated by an iterative process controlled by a Matlab script. It submitted the input file to Abaqus for analysis, extracted the results using a Python script and adjusted strut radii in accordance with the Mechanostat principle (Frost (1996)). Strut radii were changed in each iteration guiding the strain values in each element towards a target of 1250$\mu\varepsilon$ (Aamodt et al. (1997), Phillips (2012)). The normal activity level which would not trigger bone volume change was simulated with a lazy zone of +/- 250$\mu\varepsilon$ around this target value (Figure 3.7). If the absolute maximum strain fell below 250 $\mu\epsilon$, struts were inactivated, by assigning them a very small radius, simulating bone resorption.

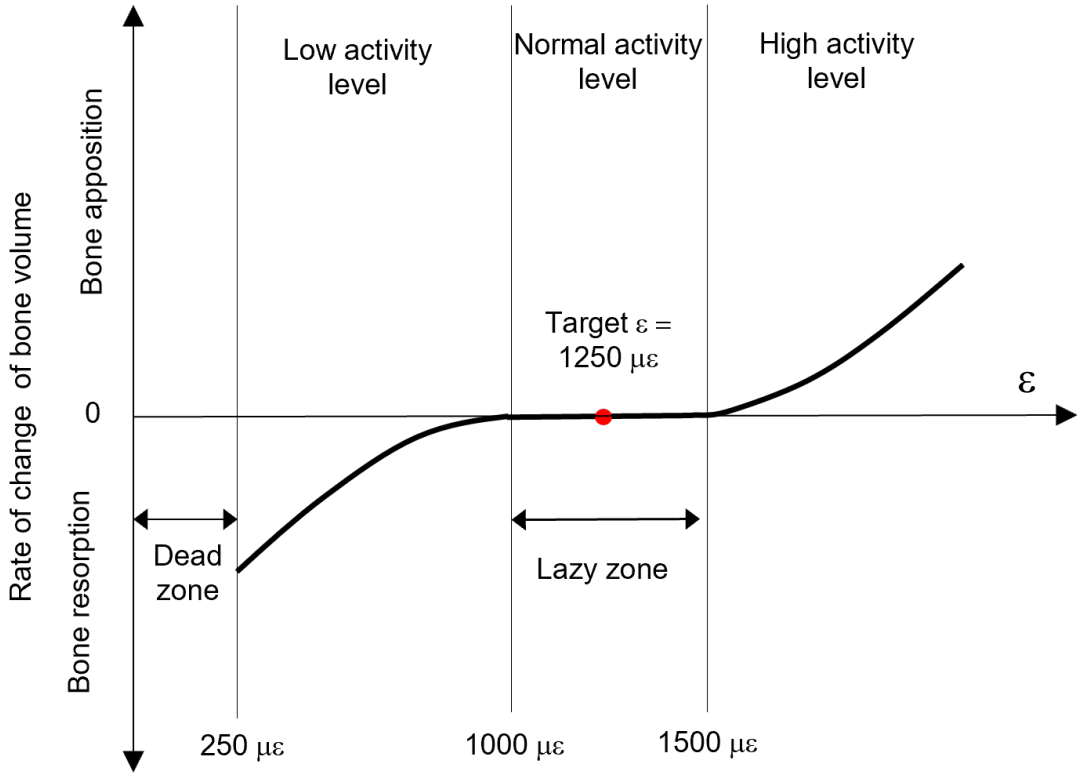


Figure 3.7: Illustration of the mechanostat principle used in the functional adaptation.

Iterations continued until Equation 3.1 was satisfied for 99% of all struts and less than 0.1% of the struts changed radius between successive iterations.

$$1000\mu\varepsilon < |\epsilon_{xx,i,j}|_{\text{max}} < 1500\mu\varepsilon \tag{3.1}$$

where $|\varepsilon_{xx,i,j}|_{\text{max}}$ is the absolute maximum strain for iteration step *i* in element *j*.

The strain $|\varepsilon_{xx}|$ at any point in a given strut for a specific iteration can be calculated in accordance with Equation 3.2 with reference to Figure 3.8.

$$\varepsilon_{xx} = \frac{F_x}{EA} + \frac{M_y z}{EI_{yy}} + \frac{M_z y}{EI_{zz}} \tag{3.2}$$

where $A = \pi r^2$, $I_{yy} = I_{zz} = (\pi r^4)/4$, d is the radial distance form the centre of the strut and E is the Young's modulus. Figure 3.8 defines r as the strut radius, F_x as the axial force, and M_y, M_z as moments about the y and z axis.

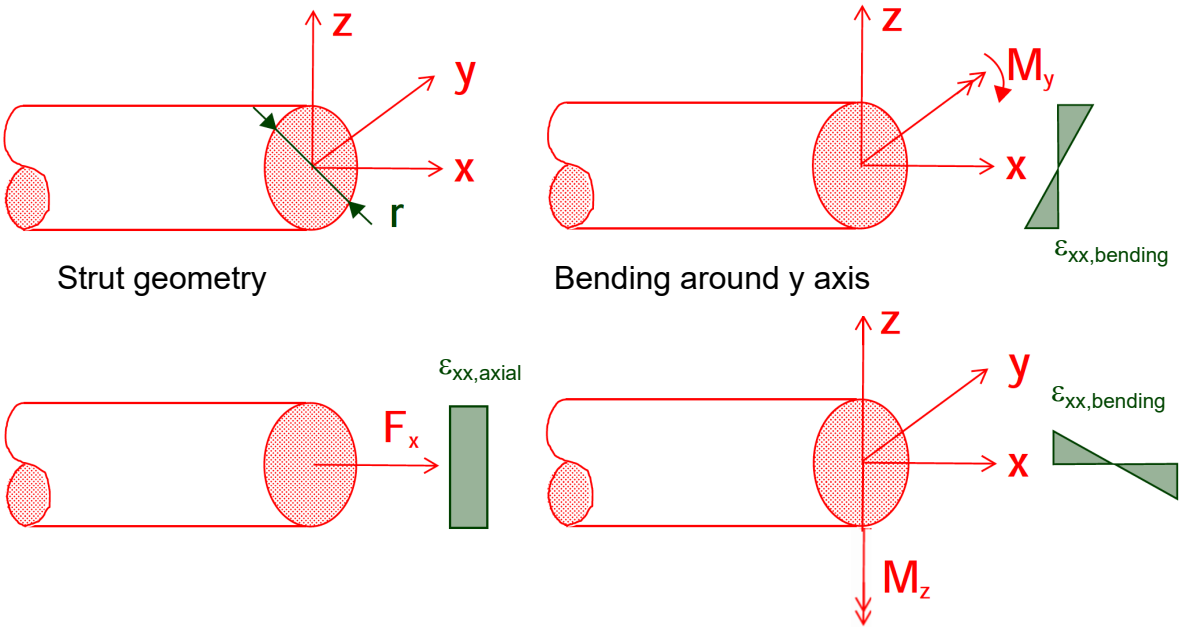


Figure 3.8: Illustration of strain distribution on a typical strut.

Recognising that the maximum strain occurs at the strut perimeter where y = z = r and that moments resolve as forces do leads to Equation 3.3.

$$|\varepsilon_{xx}|_{\max} = \frac{|F_x|}{E\pi r^2} + \frac{4\sqrt{{M_y}^2 + {M_z}^2}}{E\pi r^3} \tag{3.3}$$

Substituting values for iteration i and strut j the absolute maximum strain $|\epsilon_{xx,i,j}|_{\max}$ is defined by the equation 3.4

$$|\varepsilon_{xx,i,j}|_{\max} = \frac{|F_{x,i,j}|}{E\pi r_{i,j}^2} + \frac{4\sqrt{{M_{y,i,j}}^2 + {M_{z,i,j}}^2}}{E\pi r_{i,j}^3} \tag{3.4}$$

The functional adaptation simulation is driven by equation 3.5

$$|\varepsilon_{xx,i+1,j}|_{\max} \rightarrow \varepsilon_{\text{target}} \tag{3.5}$$

where $\varepsilon_{\text{target}}$ is the target strain which transforms Equation 3.4 into Equation 3.6 .

$$|\varepsilon_{\text{target}}| = \frac{|F_{x,i,j}|}{E\pi r_{i+1,j}^2} + \frac{4\sqrt{{M_{y,i,j}}^2 + {M_{z,i,j}}^2}}{E\pi r_{i+1,j}^3} \tag{3.6}$$

During the simulation process the normal strain due to axial force $\varepsilon_{\text{axial},i,j}$ and strut curvatures $\kappa_{y,i,j}$ and $\kappa_{z,i,j}$ due to bending moments are extracted from the Abaqus output. The axial force $F_{x,i,j}$ and moments $M_{y,i,j}$ and $M_{z,i,j}$ can be expressed by equations

$$|F_{x,i,j}| = |\varepsilon_{\text{axial},i,j}| E\pi r_{i,j}^2 \tag{3.7}$$

$$M_{y,i,j} = \kappa_{y,i,j} \frac{E\pi r_{i,j}^4}{4} \tag{3.8}$$

$$M_{z,i,j} = \kappa_{z,i,j} \frac{E\pi r_{i,j}^4}{4} \tag{3.9}$$

Substituting Equations 3.7, 3.8, 3.9 into Equation 3.6 and leads to Equation 3.10

$$\varepsilon_{\text{target}} = \frac{|\varepsilon_{\text{axial},i,j}| r_{i,j}^2}{r_{i+1,j}^2} + \frac{\sqrt{(\kappa_{y,i,j}^2 + \kappa_{z,i,j}^2)} r_{i,j}^4}{r_{i+1,j}^3} \tag{3.10}$$

Multiplying Equation 3.10 through by r_{i+1}^3 and rearranging results in Equation 3.11.

$$\varepsilon_{\text{target}} r_{i+1,j}^3 - |\varepsilon_{\text{axial},i,j}| r_{i,j}^2 r_{i+1,j} - \sqrt{(\kappa_{y,i,j}^2 + \kappa_{z,i,j}^2)} r_{i,j}^4 = 0 \tag{3.11}$$

All variables from iteration i are known as is the target strain which leaves $r_{i+1,j}$ as the only unknown. As Equation 3.11 is a cubic, Matlab roots command was used to calculate the three roots of $r_{i+1,j}$. Application of the Descartes' Rule of Signs (Anderson et al. (1998)) identifies that Equation 3.11 has one positive real root and two negative real or complex roots. The only valid solution for the target radius value is a positive real number, hence the algorithm discards the other two and uses the one positive value as a strut radius in the next iteration step.

For stretch dominated models, the Equation 3.11 reduces to Equation 3.12.

$$\varepsilon_{\text{target}} r_{i+1,j}^3 = |\varepsilon_{\text{axial},i,j}| r_{i,j}^2 r_{i+1,j} \tag{3.12}$$

and further to Equation 3.13 which is the familiar algorithm for NN16 truss element lattice simulations by the Imperial Structural Biomechanics research group (Phillips (2012), Villette & Phillips (2017), Zaharie & Phillips (2018), Favier et al. (2021), Kaufmann et al. (2021)). This demonstrates that this algorithm can be used for both bending and stretch dominated simulations.

$$r_{i+1,j}^2 = \frac{|\varepsilon_{\text{axial},i,j}|}{\varepsilon_{\text{target}}} r_i^2 \tag{3.13}$$

The minimum strut radius was set to 25μm in accordance with published data (Mosekilde (1988), Zhao et al. (2018)) and the radii were varied up to 1000μm mm during adaptation simulations in accordance with Equations 3.11. Struts with strain under 250 μm were inactivated by setting the radius to 0.5 μm. For computational efficiency trabecular elements were classified into 1 of 250 sections, spaced equally between the radii limits. The models were considered to have reached a converged state when 99% of the trabecular elements remained in the same section classification between consecutive iterations, and when the change in the effective number of trabecular elements (non near zero area elements) was below 1% between iterations.

3.4 Summary

This chapter outlines the modelling workflow employed in this thesis, where a novel algorithm for trabecular bone adaptation is applied to a set of virtual trabecular bone samples. The virtual samples consisted of FE beam models measuring 8 x 8 x 8mm which had a uniform 1MPa load applied to one of three faces whilst restrained at the opposite face. The adaptation algorithm uses both bending as well as the axial strain and therefore considers a mechanical stimulus at the surface of a trabecula where osteocytes are known to be active. Chapter 4 presents how this modelling workflow predicts mechanical properties in NN models.

4

Trabecular bone as a cellular solid: predictions of mechanical properties with near neighbour models

4.1 Introduction

Trabecular bone can be represented as a cellular solid and understanding this behaviour is important in predicting its behaviour (Gibson & Ashby (1997), Keaveny et al. (2001), Fenech & Keaveny (1999)). Cellular solids can take an open or closed cell form and are defined by the property of the material they are made from, topology and relative density. Behaviour of an open cell cellular solid can be analysed as a lattice of appropriate nodal connectivity (NC) which exhibits either stretch or bending dominated behaviour. The NC of a lattice is the number of individual struts which join at a single point. NC combined with joint rigidity, which describes whether a joint caries a moment or not, defines lattice topology. In turn, the topology determines whether a lattice is a stretch or a bending dominated structure.

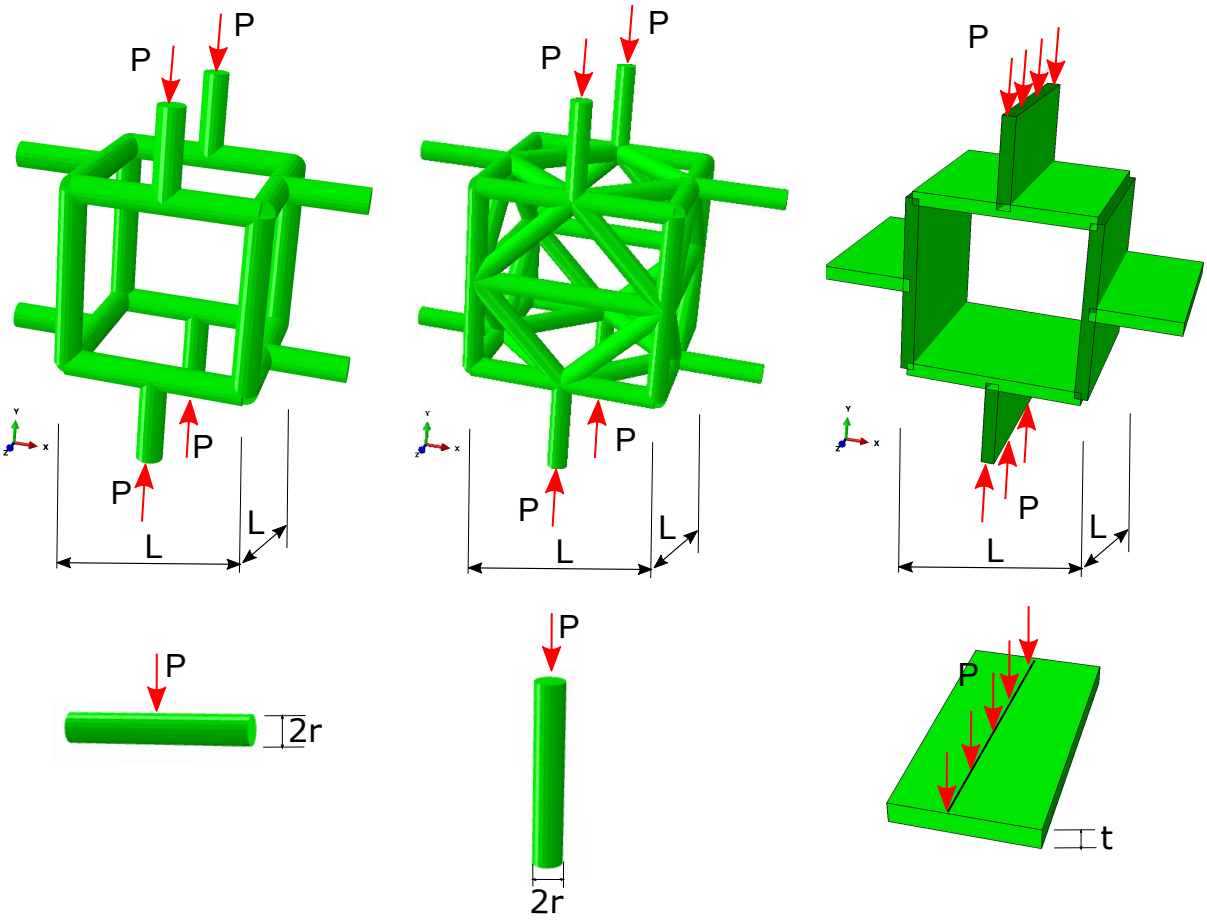
Gibson & Ashby (1997), Gibson (2005) and Ashby (2006) introduce a relationship between the relative density of a cellular solid and its Young's modulus as presented by Equation 4.1.

$$E_i^* = \alpha \, E_s \, \bar{\rho}^{\beta} \tag{4.1}$$

where E_i^* is the Young's modulus of the lattice and E_s is the Young's modulus of the material making up the struts and the subscript i can take a value of 1, 2 or 3 defining the three principal directions. $\bar{\rho}$ is the relative density defined by Equation 4.2 and α and β are constants dependant on the topology of the cellular solid.

$$\bar{\rho} = \frac{\rho^*}{\rho_s} = \frac{v_s}{v_t} \tag{4.2}$$

where ρ^* is the density of the lattice, ρ_s is the density of strut material, v_s is the volume occupied by the struts and v_t is the total volume of the cellular solid including voids. They undertake a theoretical analysis based on simplified structural beam models reproduced in Figure 4.1 and conclude that coefficient β equals 1 for stretch dominated lattices 2 for bending dominated ones and 3 for closed cell foams which they approximate with plates.



a) open cell bending b) open cell stretching c) closed cell

Figure 4.1: Idealised cube models of bending and stretch dominated cellular solids and closed cell foams adopted from Gibson & Ashby (1982).

The relative density ρ of all three idealised foam cells in Figure 4.1 is the ratio of the solid material to the volume of the cell. For cell in Figure 4.1a ρ is defined by:

$$\rho = 12\pi r^2 L/L^3 \tag{4.3}$$

for cell in Figure 4.1b by

$$\rho = (16 + 12\sqrt{2})\pi r^2 L/L^3 \tag{4.4}$$

and for cell in Figure 4.1c by

$$\rho = 4tL^2/L^3 \tag{4.5}$$

For cells in Figure 4.1 a and b this simplifies to :

$$\rho = k_1 r^2 / L^2 \tag{4.6}$$

and for the cell in Figure 4.1c to

$$\rho = k_1 t / L \tag{4.7}$$

It is worth noting that for the two idealised open cells in Figure 4.1 k_1 ranges from 38 to 104 and that as the NC increases in the stretch dominated cell its density tends from that defined by Equation 4.6 towards that defined by Equation 4.7.

The stiffness of each of the three cell types can be assessed by considering the relationship $E = \sigma/\varepsilon$ where E is The Young's modulus, σ is the applied stress and ε is the resulting strain. The applied stress in all three models is $\sigma = P/L^2$ and the strain can be expressed as δ/L. The deformation δ in the low NC open cell is governed by the bending of its edges whilst in a closed cell it is governed by the plate bending of the cell sides. In the high NC model the cell deformation is governed by its edges shortening or elongation. Using elementary mechanics and taking models depicted in Figures 4.1 a, b and c in turn the deflections are $\delta = k_2 P L^3 / E_s r^4$, $\delta = k_2 P L / E_s r^2$ and $\delta = k_2 P L^3 / E_s L t^3$. Combining these equations, Gibson & Ashby (1982) obtain

$$E_i^* = (P/L^2)/((k_2 P L^3 / E_s r^4)/L) = (E_s r^4)/(k_2 L^4) = C_1 \rho^2 E_s \tag{4.8}$$

$$E_i^* = (P/L^2)/((k_2 P L / E_s r^2)/L) = (E_s r^2)/(k_2 L^2) = C_2 \rho E_s \tag{4.9}$$

$$E_i^* = (P/L^2)/((k_2 P L^2 / E_s t^3)/L) = (E_s t^3)/(k_2 L^3) = C_3 \rho^3 E_s \tag{4.10}$$

for open cell bending dominated, open cell stretch dominated and closed cells respectively. These equations are in the same form as Equation 4.1 where α equals C_1, C_2 or C_3 and β is either 2, 1 or 3.

Gibson & Ashby (1997) argue that in reality, the trabecular bone acts as a combination of all these models and that β lies between 1 and 3. Their studies include plots of relative density versus Young's modulus test data from a number of sources which

support these findings. A review of trabecular bone test data by Helgason et al. (2008) presents similar plots and they also conclude that β for trabecular bone lies between 1 and 3, although generally closer to 2.

There are a wealth of studies examining mechanical properties of lattice structures based on models proposed by Gibson & Ashby (1997) and using periodically repeated regular cell patterns (Hutchinson & Fleck (2006), Maskery et al. (2017), Maconachie et al. (2019)). A small number consider trabecular bone as a cellular solid (Jensen et al. (1990), Vajjhala et al. (2000), Guo & Kim (2002), Luxner et al. (2009)) and attempt to model irregular bone topology. However, the irregularities in bone topology considered by these studies are highly idealised and to the author's knowledge, there are no studies which examine how adaptation influenced topology affects the mechanical properties. In particular, the literature does not consider how variations in trabecular strut cross section, length and NC influence relative density, Young's modulus and their relationship.

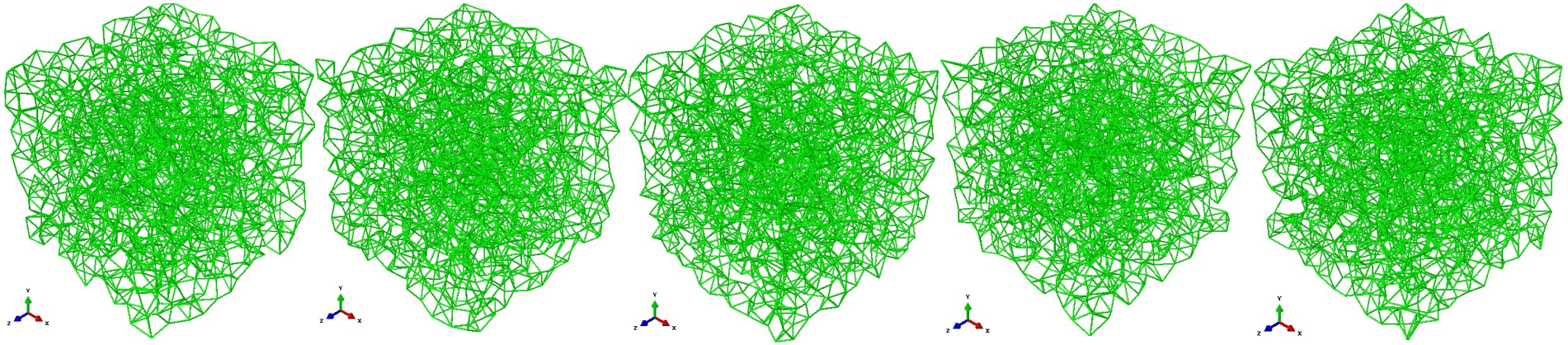
This chapter will examine the relationship between initial and predicted trabecular bone topology and mechanical properties. To this end, a number of abstract trabecular bone samples of varying topology were created and subjected to adaptation simulations. The variation in predicted mechanical properties was examined and compared to values reported in the literature. The Young's modulus and yield strength of a stretch dominated lattice are much greater than those of a bending dominated one of the same relative density. However, because the mechanisms of deformation now involve 'hard' modes (tension, compression) rather than the 'soft' ones (bending), initial yield is followed by plastic buckling or brittle collapse of the struts, leading to post-yield softening. On the other hand, the post yield stress strain curve of a bending dominated lattice has a long plateau where large increases in strain are seen for small rises in stress. Such behaviour means that stretch dominated lattices are more efficient, but bending dominated ones are better for energy absorption (Ashby (2006), Deshpande et al. (2001), Hutchinson & Fleck (2006)). In addition, this behaviour makes stretch dominated lattices prone to sudden and catastrophic failure while bending dominated lattices exhibit stable post yield behaviour (Wu & Yang (2020)). Geometrical imperfections, such as variations in strut size, have been shown to degrade the Elastic Modulus by up to 50%

and the strength by up to 40% in high NC stretch dominated lattices Liu et al. (2017).

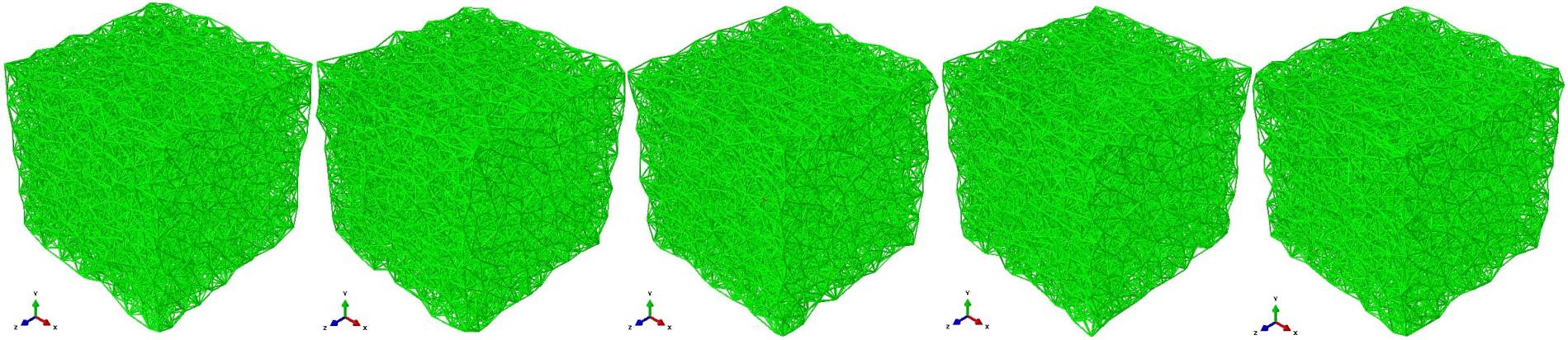
Finally, the efficiency of trabecular structures predicted by various simulations will be evaluated. An efficient structure is able resist a given load with a minimum amount of material. Structural efficiency is commonly evaluated as a strength to weight ratio and this thesis measures it as a ratio of Young's modulus to volume.

4.2 Methodology

A number of trabecular bone studies using models with pinned and fixed joint lattices were undertaken using the modelling methodology outlined in Chapter 2. Nominal NC (NNC) was varied from 4 to 14 and the mean strut length (MSL) of 1.5mm, 1.0mm and 0.7mm were considered. All studies included five models each with a randomly generated geometry. A number of nodes was determined by the user as an input to the Grasshopper component and it governed the MSL. The same Grasshopper component, using a seed input, was then employed to populate a defined cube volume with five unique sets of random nodes. This allowed non-repeating architecture similar to real bone to be simulated and the predictions to be statistically analysed. The examples of five randomly generated geometries for NN04 and NN14 simulations with MSLs of 0.7mm and 1.5mm are presented in Figures 4.2 and 4.3.

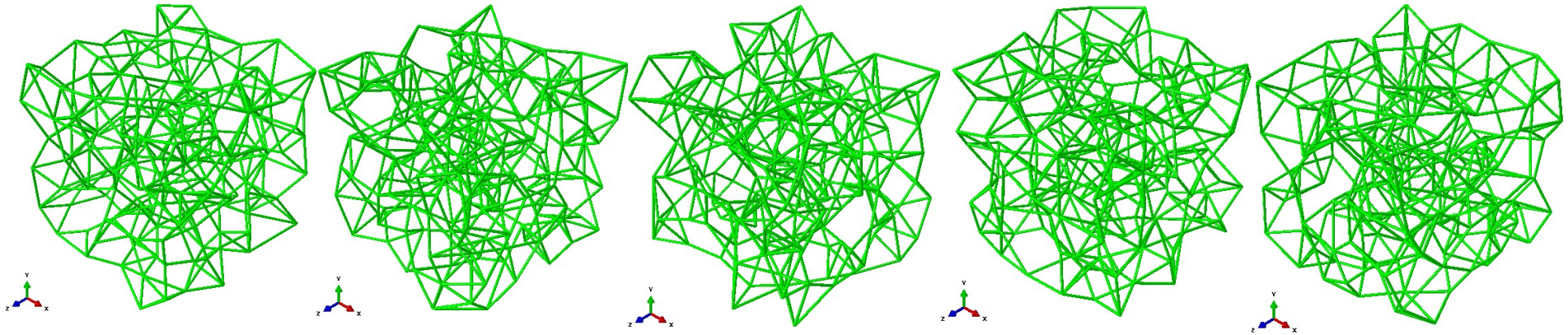


Five initial NN04 models with MSL=0.7mm

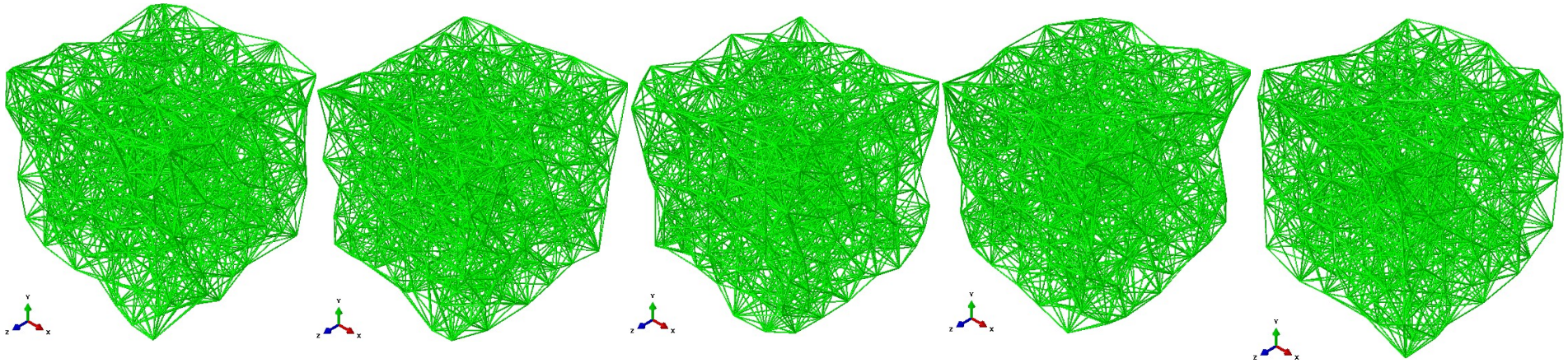


Five initial NN14 models with MSL=0.7mm

Figure 4.2: Five initial NN04 and NN14 models with MSL=0.7mm.



Five initial NN04 models with MSL=1.5mm



Five initial NN14 models with MSL=1.5mm

Figure 4.3: Five initial NN04 and NN14 models with MSL=1.5mm.

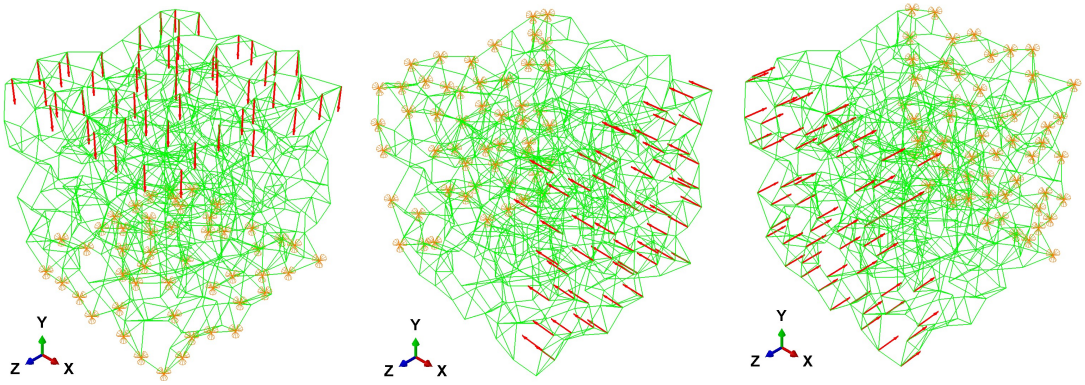
The combination of NNC, loading scenarios and lattice types resulted in a total of 78 simulations which are listed in Table 4.1 using the following naming convention. NN signifies the near neighbour modelling technique and the number which follows defines the NC. The S or B signify a lattice with pinned or fixed joints followed by the MSL and the number defining the the load scenario. For instance, NN14_B_1.5_3 is a study using the near neighbour NNC 14 fixed joint model with MSL of 1.5mm subjected to a triaxial loading scenario. Initially S and B were chosen to signify either a stretch or a bending dominated lattice although this was found to be misleading as a high NC lattice would always behave as a stretch dominated one regardless of the joint fixity.

NC	Lattice type		MSL			Loading	
	Fixed joints	Pinned joints	1.5 mm	1.0 mm	0.7 mm	Triaxial	Uniaxial
16	NN16_B	NN16_S		*_1.0		*_#_3	*_#_1
14	NN14_B	NN14_S	*_1.5	*_1.0	*_0.7	*_#_3	*_#_1
12	NN12_B	NN12_S	*_1.5	*_1.0	*_0.7	*_#_3	*_#_1
10	NN10_B	NN10_S	*_1.5	*_1.0	*_0.7	*_#_3	*_#_1
8	NN08_B	NN08_S	*_1.5	*_1.0	*_0.7	*_#_3	*_#_1
6	NN06_B	NN06_S	*_1.5	*_1.0	*_0.7	*_#_3	*_#_1
4	NN04_B		*_1.5	*_1.0	*_0.7	*_#_3	*_#_1

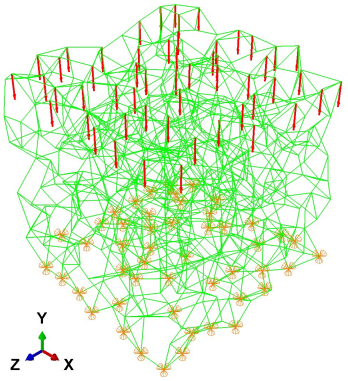
Table 4.1: Simulation models; the symbol * signifies the lattice type portion of the simulation name and the symbol # the strut length portion. The NC4 models with pinned joints were structurally unstable and were thus not considered.

Uniaxial and triaxial loading scenarios were considered. In the uniaxial loading scenario, the absolute strains arising from uniformly distributed loading in the Y direction, as shown in Figure 4.4, were used by the adaptation algorithm. Triaxial loading considered the absolute maximum strain values across three loading steps. Uniformly distributed loading in one of the three principal directions was applied in each of the steps as shown in Figure 4.4.

The uniformly distributed load of 1MPa was used in each of the scenarios. This magnitude was chosen as it represents the average contact pressure applied to all load bearing joints where trabecular bone is present. Orthopaedic surgeons, in verbal communication, state this as the pressure which acts on these joints and this is confirmed by Harris et al. (2012) who report 1MPa as the average contact pressure on the hip joint.



Triaxial loading: uniform load acting in three orthogonal directions



Uniaxial loading: uniform load acting in Y direction only

Denotes zero displacement boundary condition in three orthogonal directions

Denotes point loads simulating contact pressure on a coresponding cube face

Figure 4.4: Triaxial and uniaxial loading scenarios used in the simulations.

A preliminary study evaluating the difference in behaviour between NNC 14 and 16 models with MSL of 1.0mm was undertaken. No significant differences in mechanical property predictions were found and no further simulations with NC 16 were undertaken. The results of 1.0mm MSL for this NC are not presented here but are available in the digital appendix for comparison.

A strut radius range of between 50μm and 500μm was initially applied to simulations. This was based on the reported standard morphological parameters: trabecular bone mean thickness ranges of 116 μm to 223 μm (Hildebrand & Rüegsegger (1997)) and 129 μm to 194 μm (Hildebrand et al. (1999)) and a mean value of 306 μm (Laib et al. (2002). On completion of significant amount of work, and whilst analysing the results for 0.7mm model in particular, it became apparent that the majority of struts were converging on the smallest active radius and distorting the predictions. Many of these elements were oscillating between the dead element radius (1μm) and the smallest active element radius (50μm). The adaptation was driving them towards a size which

was not available in the simulation. Liu et al. (2006), Zhao et al. (2018) and Kirby et al. (2020) use a novel Individual Trabecula Segmentation (ITS) technique for the volumetric spatial decomposition of trabecular bone samples into rods and plates (Stauber & Müller (2006)). ITS allowed them to identify key morphological features amongst the complexity and randomness of trabecular micro structures with much greater accuracy than previous studies. One of such studies by Kirby et al. (2020) reports a rod radius distribution with a minimum value of 25 μm. In light of this finding all of the simulations were repeated using this as a minimum value instead of 50μm. At the other end of the range, the maximum radius was increased to 1000μm as it was found that the strains in some of the low NC bending models exceeded the lazy zone upper limit.

Each simulation evaluates the adapted NC (ANC), trabecular volume, Young's and shear modulii and examines the distribution of strut radii. The behaviour of models as stretch or bending dominated structures was evaluated through consideration of axial and bending components of the total strain, and by examination of factor β in Equation 4.1. In order to calculate β, 5 models of MSL 0.7mm and 5 of MSL 1.5mm were subjected to further simulations with uniform distributed loads ranging from 0.5 to 1.25MPa as shown in Table 4.2. Three low and two high NNC models were subjected to both uniaxial and triaxial loading scenarios. Factor β was also evaluated for models prior to the adaptation simulation. Four data points were obtained by setting strut radii to 50μm, 75μm, 100μm and 150μm. A comparison between initial and adapted behaviour was made.

NC	Simulation		Uniformly Distributed Loading			
	Bending	Stretch	[kN/m^2]			
14	NN14_B_1.5_3	NN14_S_1.5_3	0.50	0.75	1.00	1.25
6	NN06_B_1.5_3	NN06_S_1.5_3	0.50	0.75	1.00	1.25
4	NN04_B_1.5_3		0.50	0.75	1.00	1.25
14	NN14_B_1.5_1	NN14_S_1.5_1	0.50	0.75	1.00	1.25
6	NN06_B_1.5_1	NN06_S_1.5_1	0.50	0.75	1.00	1.25
4	NN04_B_1.5_1		0.50	0.75	1.00	1.25

Table 4.2: List of models subjected to further simulations to obtain the relationship between relative density and Young's modulus.

4.3 Results

This section presents the mechanical property predictions which are closely related to ANC. The ANC is discussed in detail in Chapter 5 but Table 4.3 included here presents the ANC to allow this relationship to be examined. The ANC is generally lower in simulations with lower MSL, lower NNC and for uniaxial as opposed to triaxail simulations. The difference between pinned and rigid jointed model simulation is more apparent for the uniaxial loading predictions.

	NNC	MSL = 0.7mm				MSL = 1.0mm				MSL = 1.5mm			
		Rigid joint simulations		Pinned joint simulations		Rigid joint simulations		Pinned joint simulations		Rigid joint simulations		Pinned joint simulations	
		Mean	SD	Mean	SD	Mean	SD	Mean	SD	Mean	SD	Mean	SD
Uniaxial loading	4	4.0	1.2			4.0	1.2			4.1	1.2		
	6	5.5	1.5	6.0	1.5	5.4	1.6	6.1	1.6	5.5	1.5	6.1	1.5
	8	6.7	1.9	7.2	1.9	6.7	1.9	7.3	1.9	6.8	1.9	7.3	1.9
	10	7.8	2.2	8.3	2.2	7.9	2.1	8.6	2.1	8.0	2.2	8.6	2.2
	12	8.8	2.4	9.3	2.5	9.1	2.4	9.8	2.4	9.1	2.5	9.8	2.5
	14	9.6	2.6	10.2	2.7	10.1	2.5	10.9	2.6	10.4	2.7	11.1	2.7
Triaxial loading	4	4.8	0.9			4.8	0.9			4.8	0.9		
	6	6.9	1.0	6.9	1.0	6.9	1.0	6.9	1.0	7.0	1.1	7.0	1.1
	8	8.9	1.1	8.9	1.1	9.0	1.2	9.0	1.2	9.1	1.3	9.2	1.3
	10	11.0	1.3	11.1	1.3	11.2	1.4	11.2	1.4	11.3	1.5	11.3	1.5
	12	13.1	1.4	13.1	1.4	13.2	1.6	13.3	1.6	13.4	1.8	13.5	1.8
	14	15.1	1.6	15.1	1.6	15.3	1.8	15.3	1.8	15.5	2.0	15.6	2.0

Table 4.3: Mean and standard deviation of ANC values for simulations with different NNC, MSL and loading.

4.3.1 Predicted trabecular architecture and mechanical properties

Figure 4.5 presents a contour plot of element radii in four converged models representing a variety of NNC and loading. By comparing sub-figures a and c to b and d respectively it is evident that the radii in low NNC, NN04, models are higher than in high NNC NN14 models.

Comparison of Figure 4.5 a and b to Figure 4.5 c and d respectively shows higher radii in models subjected to triaxial loading. Uniaxial loading simulations result in trabecular architecture resembling columns aligned with the loading direction. This is more apparent in higher NNC, NN14, models due to smaller element radii.

Figures 4.6 presents contour plots of the bending strain, the axial strain and the radii in one of the five NN04 models for four different simulations. It is evident that the bending strains are higher than the axial strains and that the radii are generally higher in elements with higher bending strains. In some elements with high radii this is the result of the combination of axial and bending strains and was a more common common occurrence in triaxial loading simulation.

Figure 4.7 presents the same data for four higher NNC simulations, three NN14 and one NN06 model. The axial strains in NN14 simulation predictions are higher than the bending ones, the opposite of NN04 simulation predictions. As expected, the difference between the NN14 models with rigid and pinned joints is small, they both behave as stretch dominated lattices. There are some higher strains at joints in the rigid jointed model but that does not effect the global behaviour of the lattice.

The axial strains in NN06 model (Figure 4.7d) are of similar magnitude to the bending ones and higher when compared to equivalent NN04 model results (Figure 4.6b). This suggests that NN06 model, with the ANC of approximately 7, is on the transition between the bending and stretch dominated lattice behaviour.

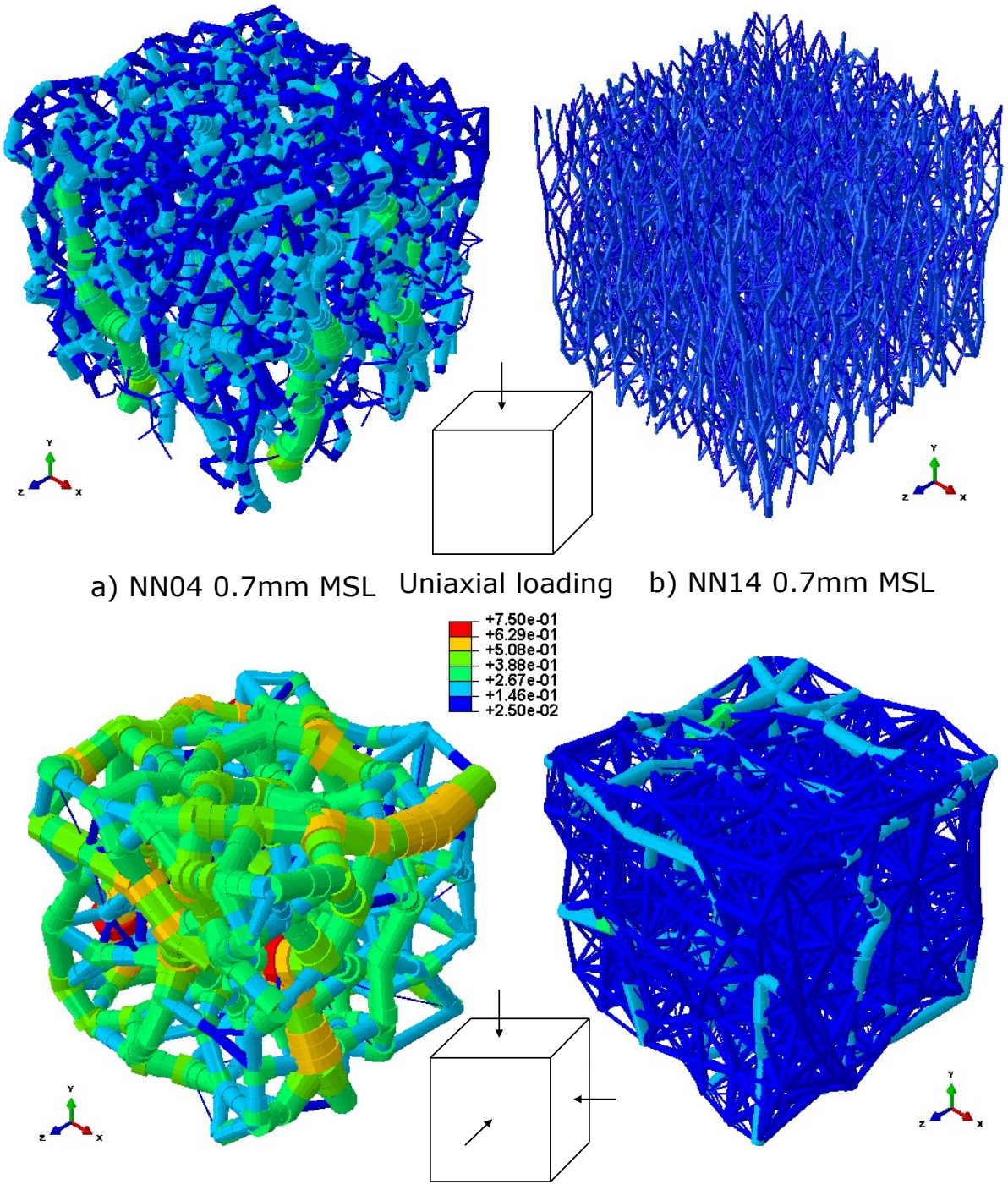


Figure 4.5: Radii contour plots for one of five converged models in four typical simulations. The initial radius prior to adaptation simulations was 25μm. Dead elements with radius of 1μm are not shown.The models were subjected to a uniform pressure of 1MPa either on one or three faces as indicated.

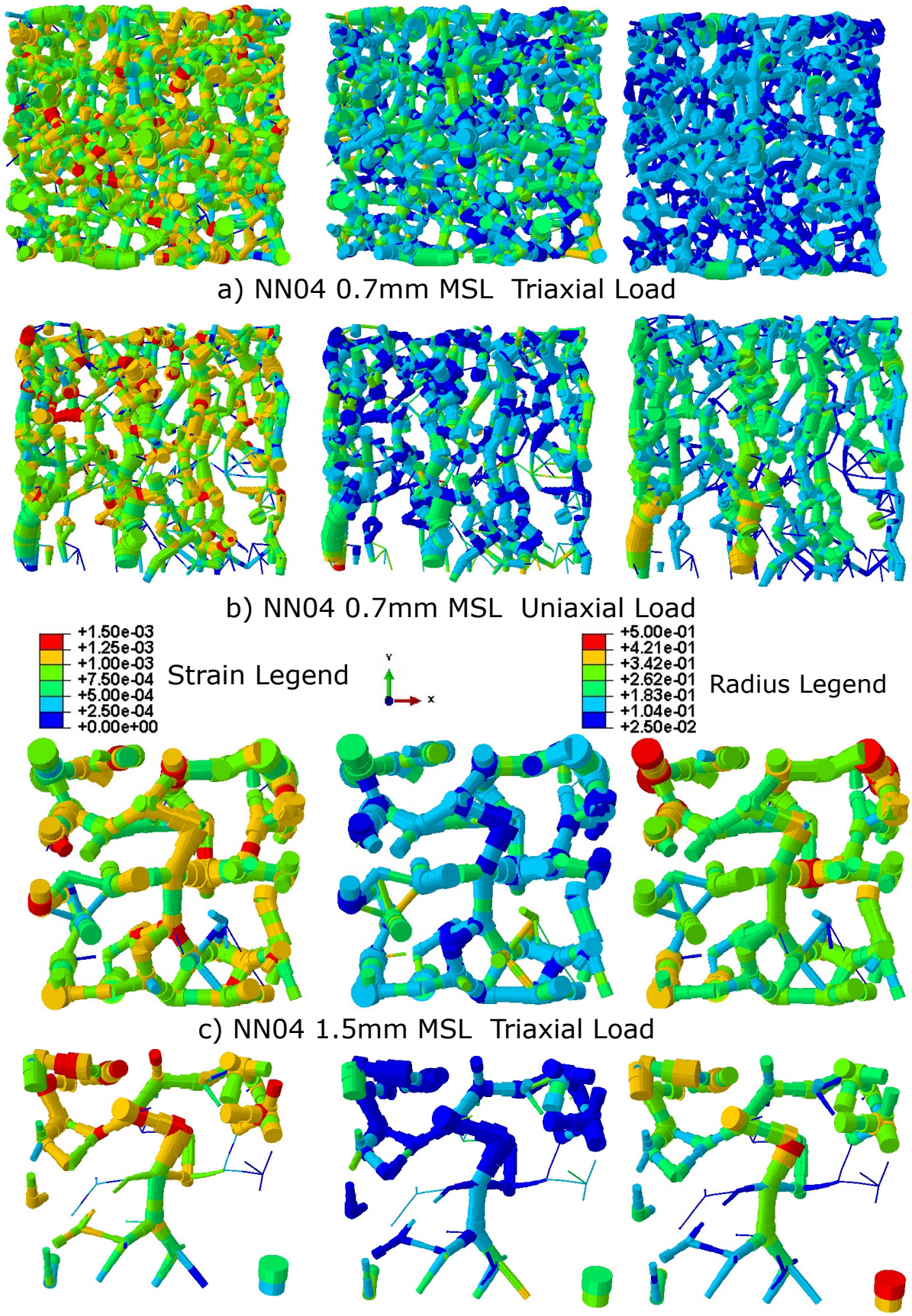


Figure 4.6: Contour plots of the absolute bending strain on LHS, the absolute axial strain in the middle and the radii on the RHS on a 2mm slice through the middle of one of the five NN04 models with MSL and loading as indicated. The initial radius prior to adaptation simulations was 25μm. Dead elements with radius of 1μm are not shown.

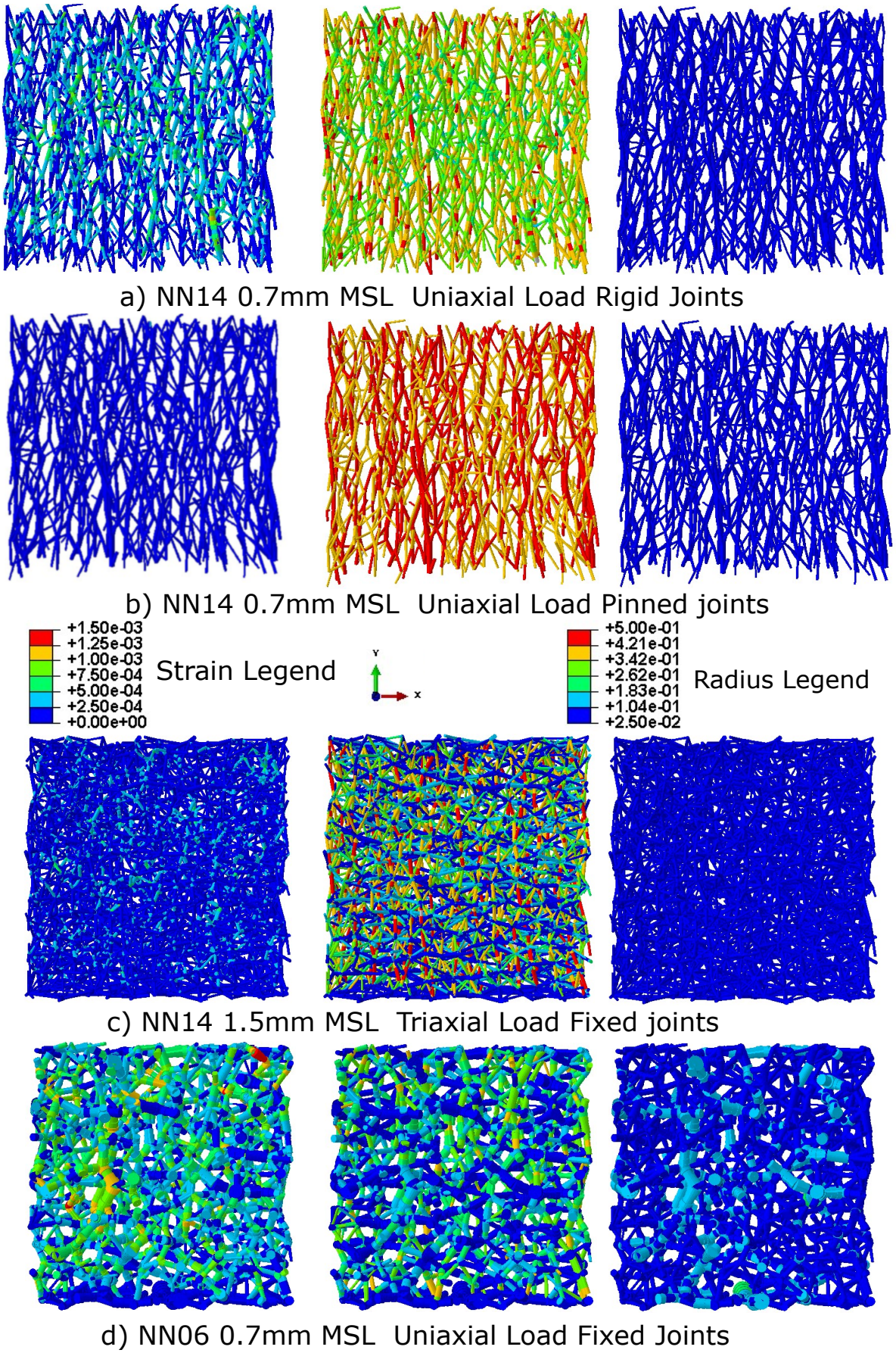
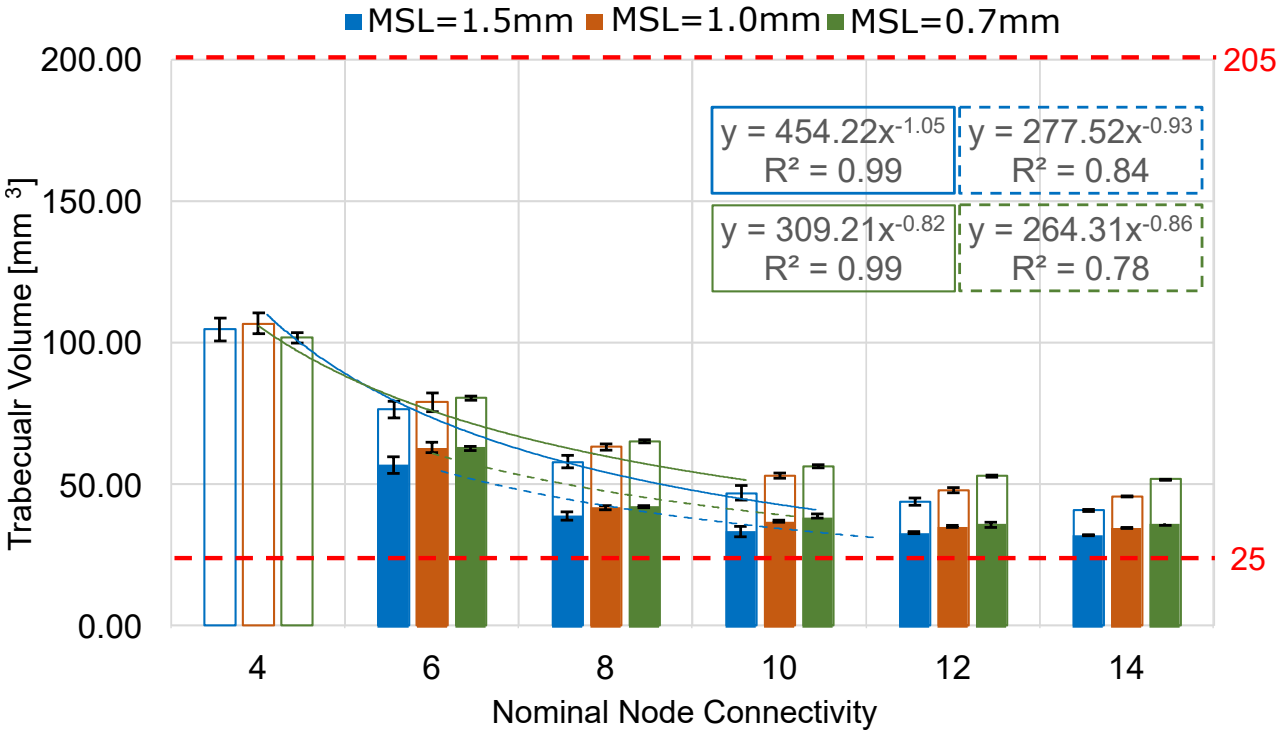


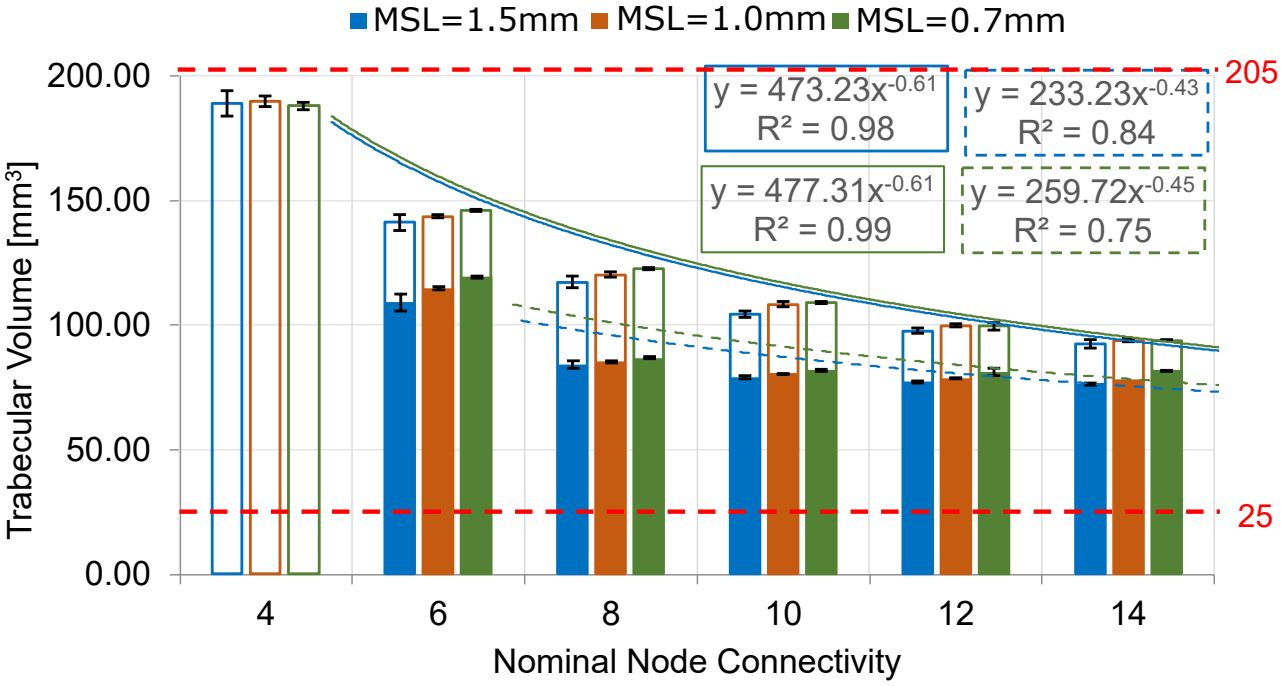
Figure 4.7: Contour plots of the absolute bending strain on LHS, the absolute axial strain in the middle and the radii on the RHS on a 2mm slice through the middle of one of the five NN14 modelswith MSL and loading as indicated. The initial radius prior to adaptation simulations was 25μm. Dead elements with radius of 1μm are not shown.

Figures 4.8a and 4.8b present the predicted trabecular volume for the triaxial and uniaxial loading simulations respectively. The predicted volume increases with the decreasing NNC for both loading scenarios and for all three MSLs. The predicted volume is greater in bending simulations and for the triaxial loading scenario. The relative increase in volume with decreasing NNC is greater in bending simulations as is evident by the fitted trend lines, although this is marginal for the uniaxial loading scenario. The difference in predictions between simulations using different MSLs is only evident under the uniaxial loading scenario, and more apparent in high NNC models.

The predicted volume is between 20% and 40% higher for bending simulations compared to stretch simulations using triaxial loading and between 20% and 50% higher using the uniaxial loading. The predicted difference is consistently highest in simulations using NNC 8 models. The predicted volumes for uniaxial load simulations are approximately half of those predicted by the triaxial load simulations, differences ranging from 180% to 220%. This suggests that trabecular bone subjected to more then a single load case loading is more structurally efficient.



a) Uniaxial loading simulation predictions



b) Triaxial loading simulation predictions

- - - - Volume range calculated from the reported density range for real trabecular bone (Linde et al. (1992), Gibson (2005)).

Figure 4.8: Mean predicted trabecular volume for (a) triaxial and (b) uniaxial load simulations for 5 randomly generated models of each NNC with MSL as shown. The filled bars are for stretch and hollow for bending models. Error bars for the 95% confidence interval are shown. The bars are plotted for NNC whilst the trendlines are plotted for ANC at the end of simulation as presented in table 4.3. A range of trabecular volume calculated from reported density ranges (Linde et al. (1992), Ashby (2006)) is shown for comparison.

Figure 4.10 presents the Young's modulus values for the triaxial loading scenario. In bending simulations, the predicted stiffness in three principal directions remained relatively unchanged at approximately 800 MPa, for all MSLs and for NNC from 14 to 6. The predicted modulus for simulations of NNC of 4 was approximately 750 MPa. In stretch simulations, the stiffness decreased steadily from around 600 MPa to around 500 MPa as the NNC decreased from 14 to 8 with a sharp drop to 400 MPa for NNC of 6.

Under a uniaxial loading scenario the trends were somewhat different (Figure 4.9). In bending simulations the Young's modulus in the loaded direction decreased from approximately 850 MPa to 640 MPa as the NNC changed from 14 to 4. However, following a decrease in stiffness with a change in NNC from 14 to 8 and from 14 to 10 in simulations with MSL of 0.7mm and 1.5mm respectively, there was an appreciable increase in stiffness. This was followed by a decline in stiffness with NNC change towards 4. Similar behaviour was not observed in stretch dominated simulations where the Young's modulus decreased form approximately 650 MPa to 350 MPa. The reasons behind this are discussed in Section 4.4.

The predicted Young's moduli in two unloaded directions were between 5% and 15% of those in the loaded direction. The Young's moduli at the lower end of this range were the predictions of high MSL simulations. Values in high NNC simulations were higher in the stretch models whilst the opposite was true in low NNC ones.

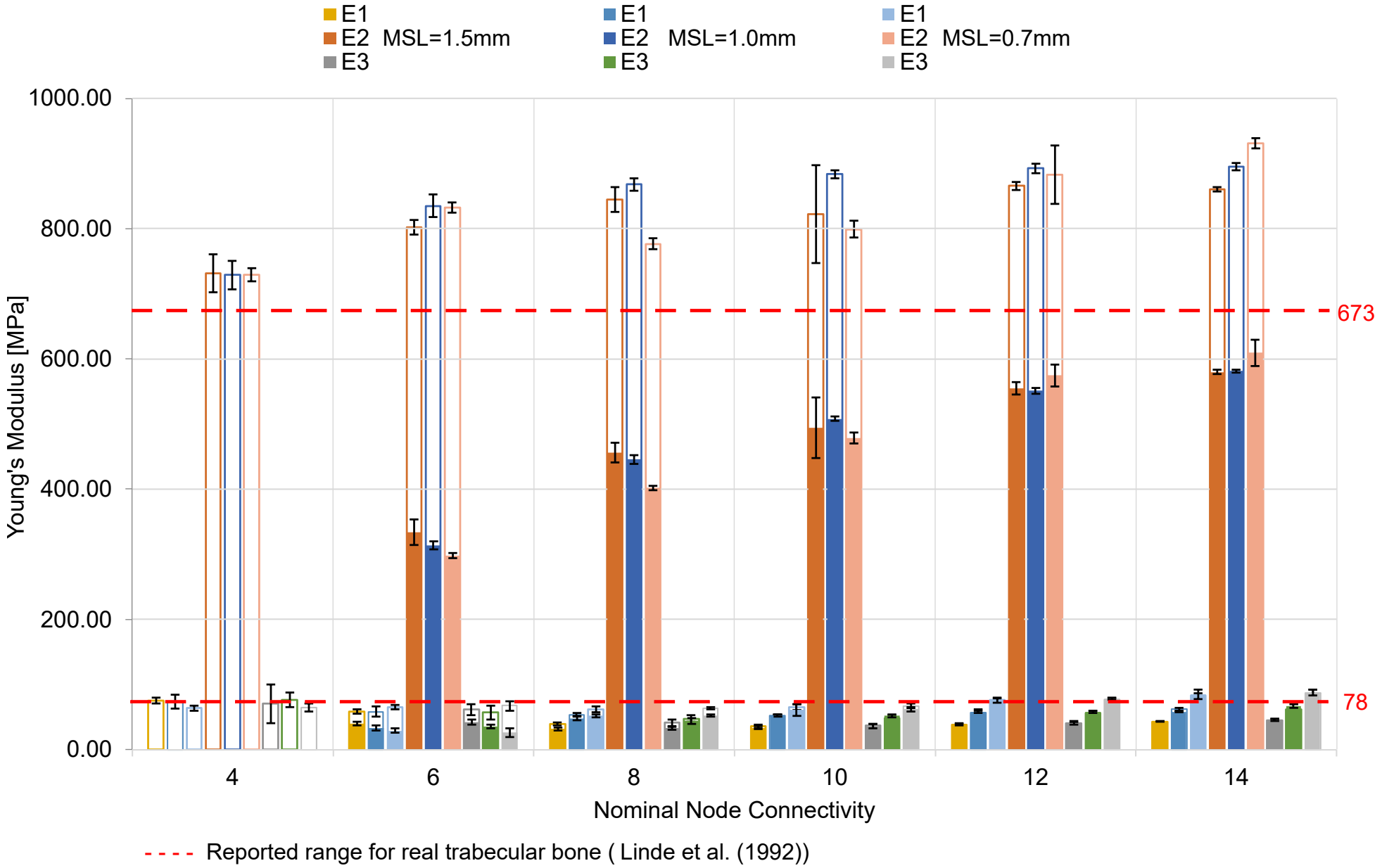


Figure 4.9: Mean Young's modulus values in three principal direction for uniaxial load simulations for 5 randomly generated models of each NNC with MSL as shown. The filled bars are for stretch and hollow for bending models. Error bars for the 95% confidence interval are shown. A range of E values for real bone reported by Linde et al. (1992) is shown for comparison.

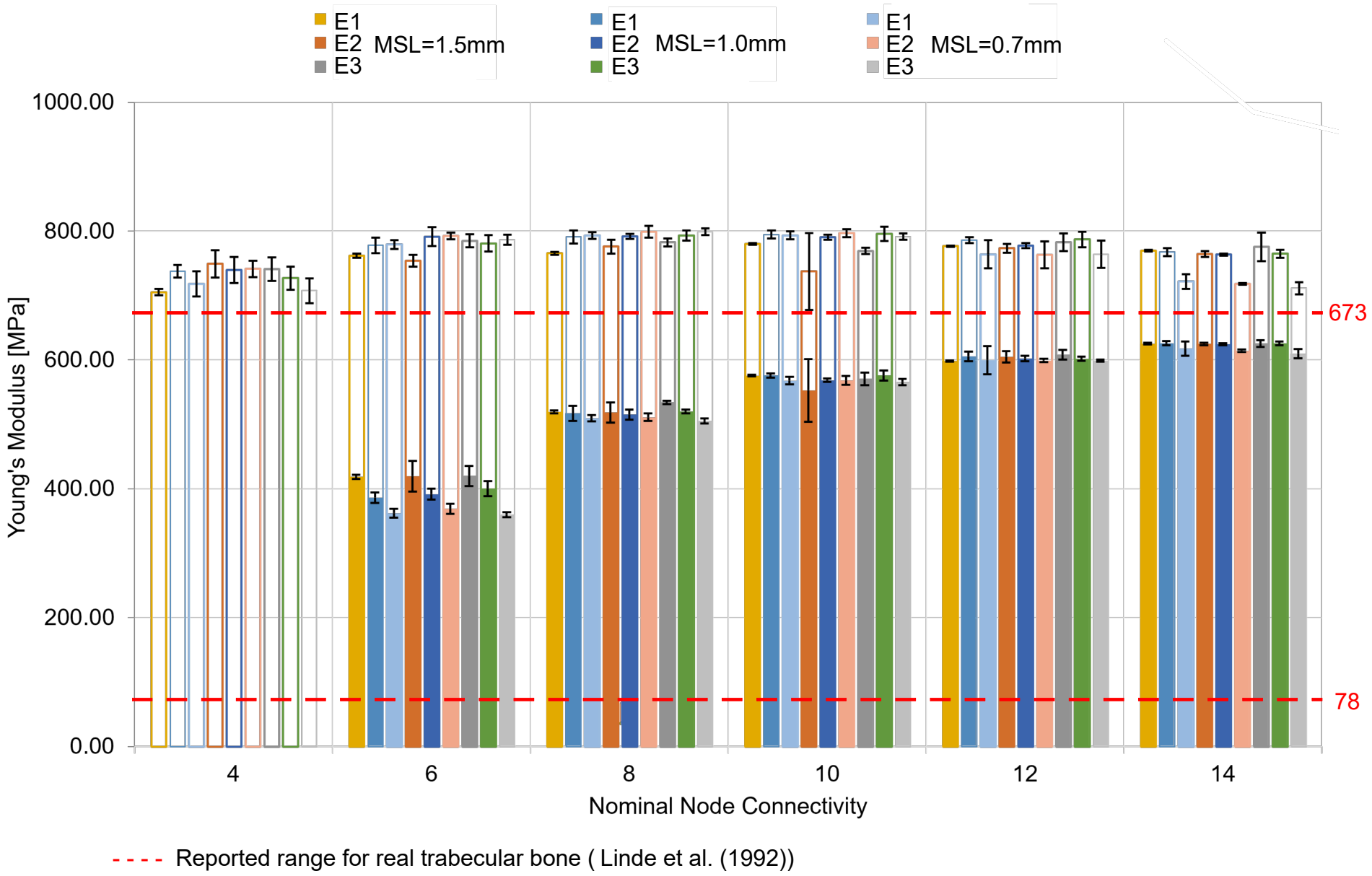


Figure 4.10: Mean Young's modulus values in three principal direction for triaxial load simulations for 5 randomly generated models of each NNC with MSL as shown. The filled bars are for stretch and hollow for bending models. Error bars for the 95% confidence interval are shown. A range of E values for real bone reported by Linde et al. (1992) is shown for comparison.

An efficient structure is able to resist a given load with a minimum amount of material. Structural efficiency is commonly evaluated as a strength to weight ratio and this thesis measures it as a ratio of Young's modulus to volume. Figure 4.11 provides a visual representation of structural efficiency (Ω) correlation with NC, loading and joint rigidity while Table 4.4 presents detailed information. It is evident that models with higher NNC and ones adapted for uniaxial as opposed to triaxial loading are more efficient. The efficiency decreases with decreasing NNC more rapidly in uniaxial then triaxial loading simulations down to very similar values below the NC of about 6. The models with rigid joints were found to be marginally more efficient than the ones with pinned joints. This was expected as the resistance to joint rotation results in the reduction of the cube contraction in the loaded direction and yields higher Young's modulii.

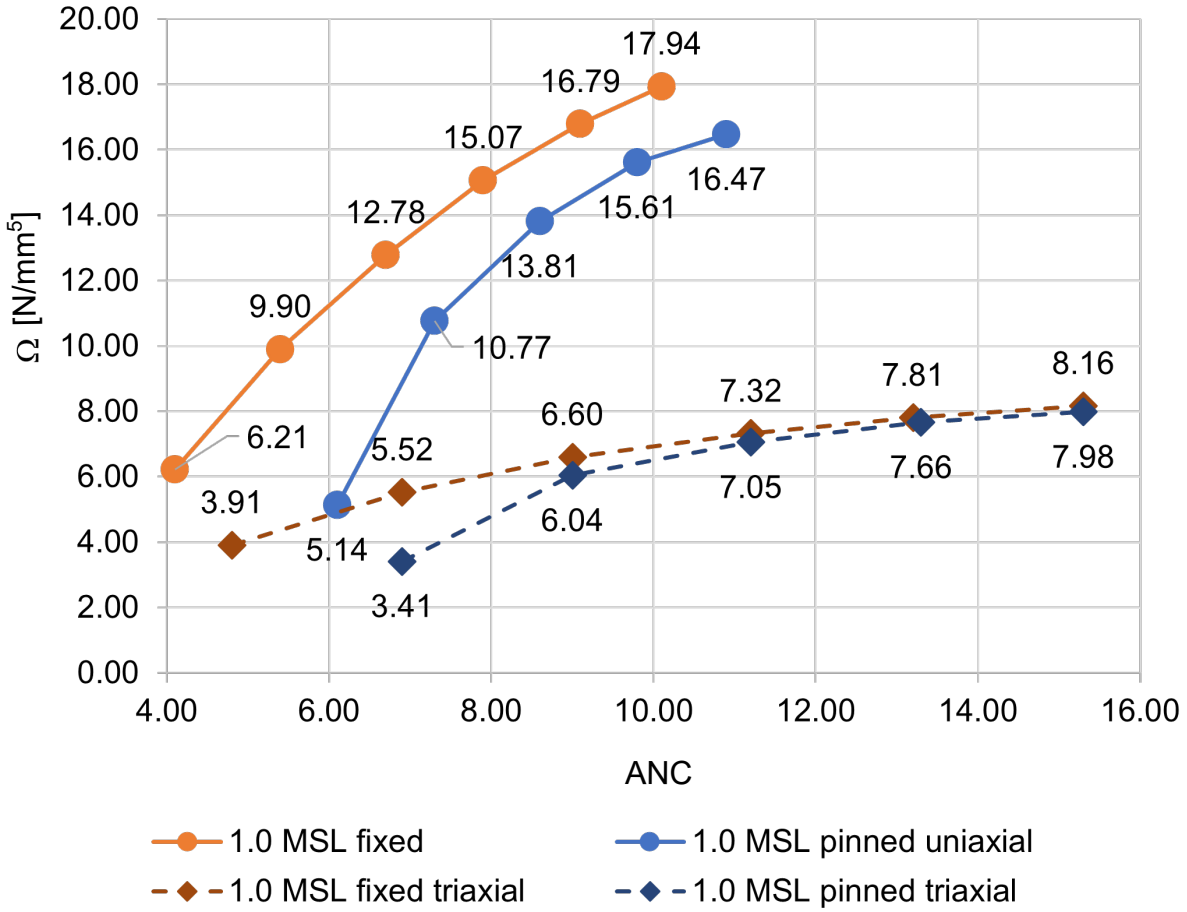


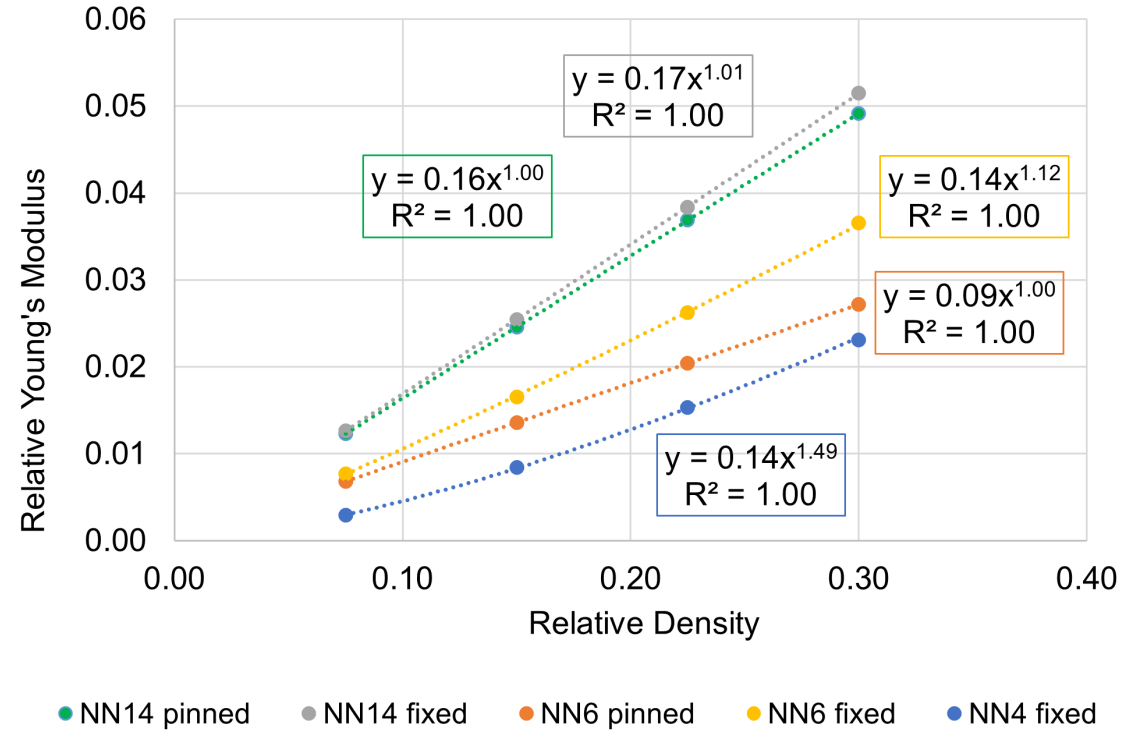
Figure 4.11: Structural efficiency Ω, expressed as Young's modulus divided by trabecular volume, plotted against ANC at the end of adaptation simulation. Only the values for 1.0mm MSL simulations as indicated in the legend are shown to provide a visual effect of the relationship between efficiency, ANC and lattice rigidity. Full results are presented in Table 4.4.

The uniaxial adaptation simulations resulted in more efficient structures. There was a greater decrease in efficiency for predicted NC of between 6 and 9 which was more evident in models with pinned joints. This is explained further in the discussion Section 4.4.

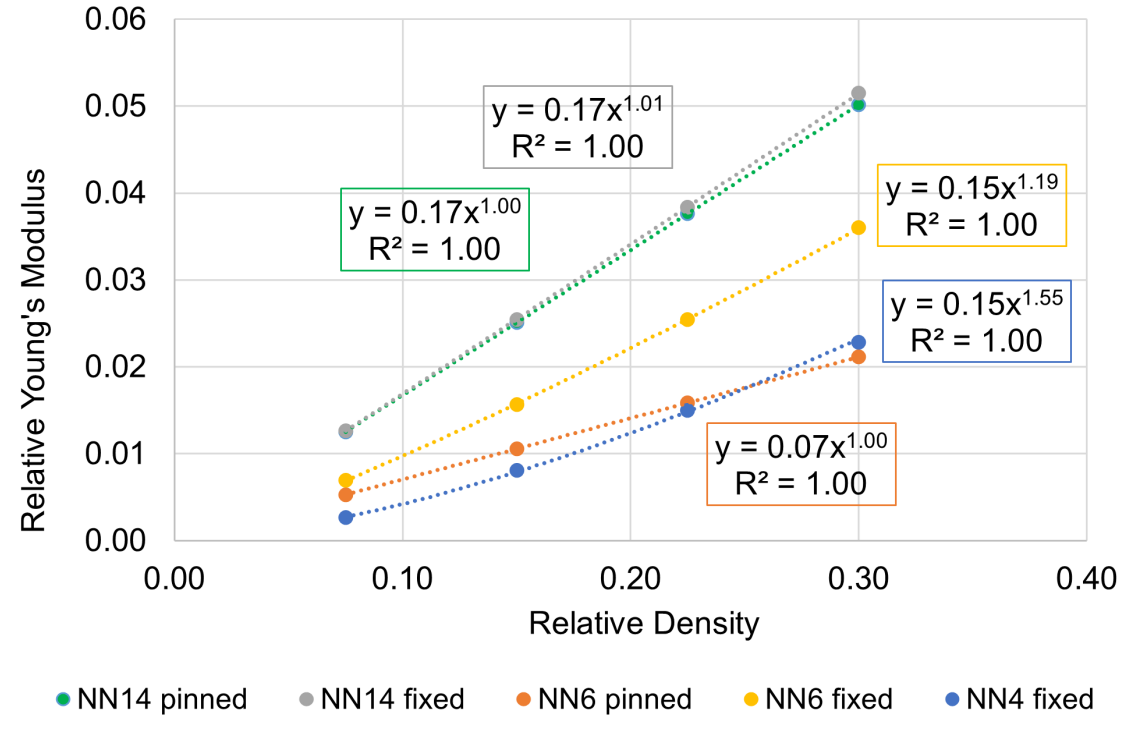
	NNC	MSL = 0.7mm				MSL = 1.0mm				MSL = 1.5mm			
		Rigid joint simulations		Pinned joint simulations		Rigid joint simulations		Pinned joint simulations		Rigid joint simulations		Pinned joint simulations	
		ANC	Ω	ANC	Ω	ANC	Ω	ANC	Ω	ANC	Ω	ANC	Ω
Uniaxial loading	4	4.0	6.62			4.0	6.21			4.1	6.29		
	6	5.5	9.64	6.0	4.68	5.4	9.90	6.1	5.14	5.5	9.42	6.1	5.79
	8	6.7	11.03	7.2	9.27	6.7	12.78	7.3	10.77	6.8	13.09	7.3	11.68
	10	7.8	13.06	8.3	12.05	7.9	15.07	8.6	13.81	8.0	15.65	8.6	14.85
	12	8.8	15.45	9.3	15.06	9.1	16.79	9.8	15.61	9.1	17.61	9.8	16.86
	14	9.6	16.85	10.2	15.09	10.1	17.94	10.9	16.47	10.4	18.97	11.1	18.07
Triaxial loading	4	4.8	3.95			4.8	3.91			4.8	3.98		
	6	6.9	5.45	6.9	3.09	6.9	5.52	6.9	3.41	7.0	5.36	7.0	3.85
	8	8.9	6.54	8.9	5.88	9.0	6.60	9.0	6.04	9.1	6.64	9.2	6.16
	10	11.0	7.32	11.1	6.94	11.2	7.32	11.2	7.05	11.3	7.10	11.3	7.00
	12	13.1	7.69	13.1	7.40	13.2	7.81	13.3	7.66	13.4	7.94	13.5	7.83
	14	15.1	7.67	15.1	7.50	15.3	8.16	15.3	7.98	15.5	8.30	15.6	8.19

Table 4.4: Structural efficiency Ω, expressed as Young's modulus divided by trabecular volume. key results are highlighted in yellow.

Figure 4.12 presents plots of relative density versus the relative Young's modulus for high and low NNC simulations using the MSL of 0.7mm and 1.5mm prior to adaptation simulations. Relative Young's modulus id defined as the apparent Young's modulus of the cellular solid divided by the Yong's modulus of the solid bone. The Young's modulus of 18,000MPa has been assumed for the solid bone. Figures 4.13 and 4.14 present the same data for the models following the adaptation simulation having been subjected to triaxial and uniaxial loading. It is evident that the high NNC simulations predict a linear relationship between them, while the lower NNC simulations predict a power relationship with an exponent between 1 and 2. The gradients of the uniaxial loading simulation curves are steeper then the ones for the triaxial loading simulations.

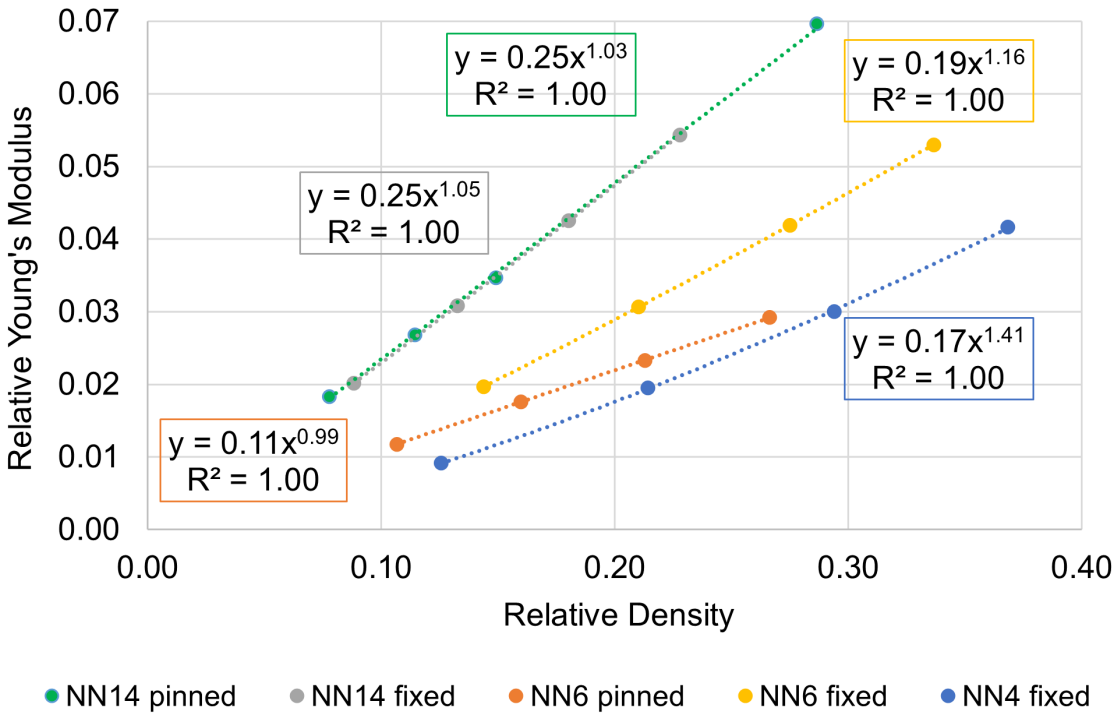


(a) Models with MSL=1.5mm



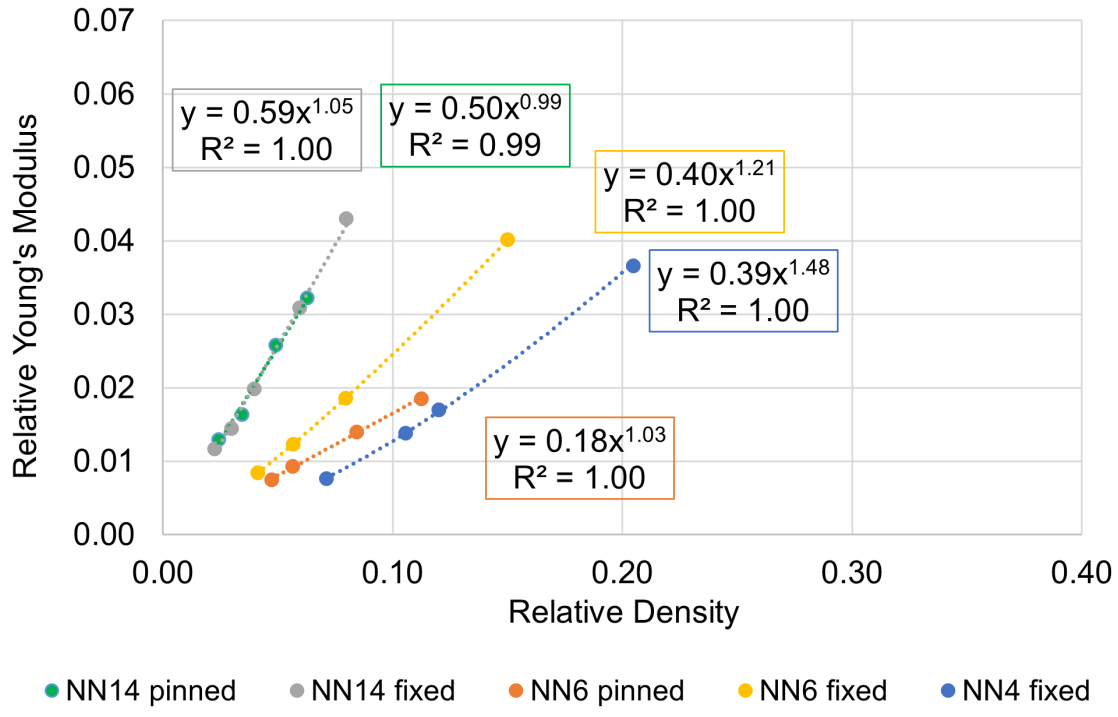
(b) Models with MSL=0.7mm

Figure 4.12: Mean relative Young's modulus plotted against mean relative density using 5 model average values prior to adaptation simulations for (a) MSL=1.5mm and (b) MSL=0.7mm. A curve has been fitted to each data set and the equations of these curves are presented next to them bound by a frame of the same colour. Coefficients of determination (R^2) are also shown.



(a) Triaxial loading simulation predictions

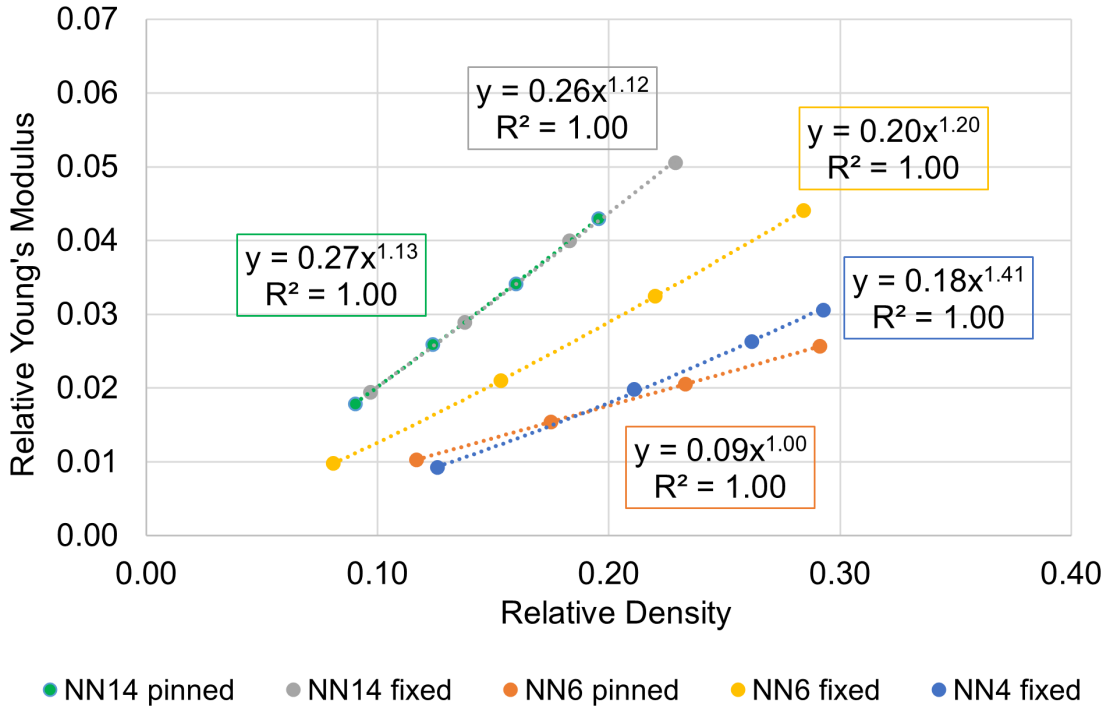
.



(b) Uniaxial loading simulation predictions

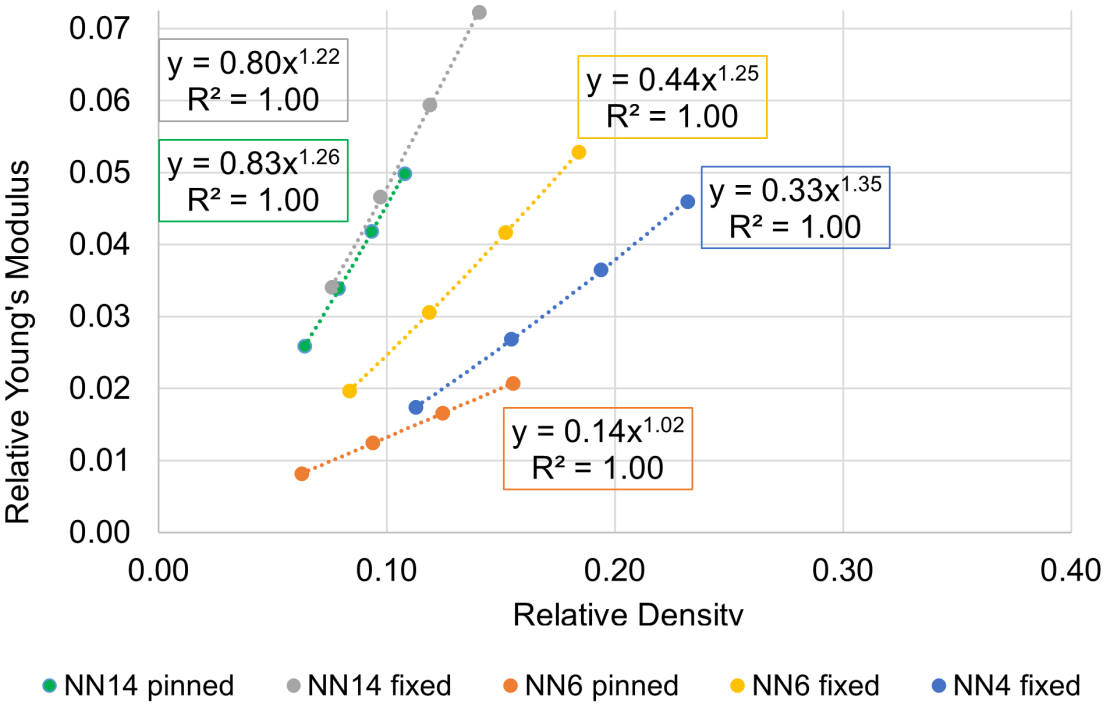
.

Figure 4.13: Mean relative Young's modulus plotted against mean relative density using 5 model average values for MSL=1.5mm at the end of adaptation simulation using (a) triaxial loading scenario and (b) uniaxial loading scenario. A curve has been fitted to each data set and the equations of these curves are presented next to them bound by a frame of the same colour. Coefficients of determination (R^2) are also shown.



(a) Triaxial loading simulation predictions

.



(b) Uniaxial loading simulation predictions

.

Figure 4.14: Mean relative Young's modulus plotted against mean relative density using 5 model average values for MSL=0.7mm at the end of adaptation simulation using (a) triaxial loading scenario and (b) uniaxial loading scenario. A curve has been fitted to each data set and the equations of these curves are presented next to them bound by a frame of the same colour. Coefficients of determination (R^2) are also shown.

4.4 Discussion

Firstly, a comparison will be made between the trabecular bone relative density and stiffness predictions presented in this chapter and those reported in the literature. A significant number of relative density values are reported in the literature, some of which include an average of 0.152 (Linde et al. (1992)) and a range between 0.05 and 0.3 (Gibson (2005)). Ciarelli et al. (1991), Goulet et al. (1994) and Morgan et al. (2003) report ranges of 0.15 to 0.4, 0.06 to 0.36, and 0.046 to 0.42 respectively. The relative density predicted by structural models of varying NC, strut length and nodal fixity reported in this chapter ranged between 0.0627 (95% CI [0.0621, 0.0632]) and 0.368 (95% CI [0.359, 0.378]) to three significant figures. Trabecular bone density is dependant on the loading. The virtual bone samples, used in this thesis, have been subjected to 1.0 MPa loading representative of the joint contact pressure (Harris et al. (2012)) allowing a valid favourable comparison between the study results and the values from literature to be made.

For a given NC and lattice type, the predicted stiffness in three principal directions were approximately the same following the adaptation simulation using the triaxial loading scenario. When subjected to isotropic loading, the adapted structure resembled an isotropic material. However the adaptations simulations using the uniaxial loading scenario predicted significant differences between the stiffness in the direction of the applied load (E_2) and the other two principal directions (E_1 and E_3). E_1 and E_3 predictions are lower across all NC simulations and for both stretch and bending dominated models. At high NNC, the simulations predict a not insignificant stiffness in the E_1 and E_3 which declines with decreasing NC and more rapidly in stretch dominated simulations.

A large number of Young's modulus values reported in the literature are summarised here. Linde et al. (1992) reviewed 25 studies which tested human trabecular bone specimens and recorded Young's modulus range of between 78MPa and 673MPa, whilst (Gibson (2005)) reports a wide range of between 100MPa and 1000MPa. Goulet et al. (1994) and Ciarelli et al. (1991) carried out platen tests on 8mm x 8mm x 8mm bone samples and recorded Young's modulus ranges of 17 MPa to 738 MPa and 494 MPa

to 2379 MPa respectively. The Young's modulus predicted by simulations presented in this Chapter, ranged between 334MPa (95% CI [314MPa, 344MPa]) and 839MPa (95% CI [832MPa, 846MPa]) to three significant figures. These values compare favourably with the values from literature.

Further consideration of relative density, stiffness, their relationship and structural efficiency indicates the importance of NC. The trabecular bone stiffness predicted by all of the simulations decreases with decreasing NC. The rate of decrease is greater in stretch simulations than in bending simulations, in simulations of lower MSL and in simulations subjected to uniaxial as opposed to triaxial loading. However, the predictions of trabecular bone volume increase with decreasing NC. The rate of increase in volume is greater in bending simulations than in stretch simulations, in simulations of higher MSL and in simulations subjected to triaxial as opposed to uniaxial loading. Therefore, it follows that structural efficiency, measured as the ratio of Young's modulus to trabecular volume, varies with NC.

High NNC simulations predict the most efficient trabecular architecture (Table 4.4). There is very little difference in stiffness and relative density predictions between stretch and bending dominated simulations of ANC above 8 which occurs in models with NNC of 10 subjected to uniaxial loading and NNC of 8 for triaxial loading. For instance, bending simulations using 0.7mm MSL models subjected to triaxial loading show a transition between predictions for simulations with NNC of 6 and 8 (Figure 4.10) which have the mean ANC of 6.9 and 8.9 respectively. Such a change is also evident in models with NNC of 8 and 10 subjected to uniaxial loading (Figure 4.9) which have a mean ANC of 6.7 and 7.8 respectively. The cause of this is believed to be the strut radii increase in response to greater bending strains as the models transition away form stretch dominated behaviour.

The strain contour plots for a single model of NN10, NN08 and NN06 simulations in Figure 4.15 show bending strains increasing and axial strains reducing from left to right as the ANC decreases from 7.8 to 6.7 and finally 5.5. The figure shows that the bending and axial strains are approximately equally represented in the NN08 model. This model has an ANC of 6.7 which corresponds well with a NC of 7 reported as a transition point between stretch and bending dominated behaviour in lattice structures

by Buxton & Clarke (2007). At this transition they record a value of 1.4 for the power exponent in the relationship between density and stiffness. This exponent is equivalent to constant β used by Ashby (2006) which was found to be 1.25 for the NN06 model in question.

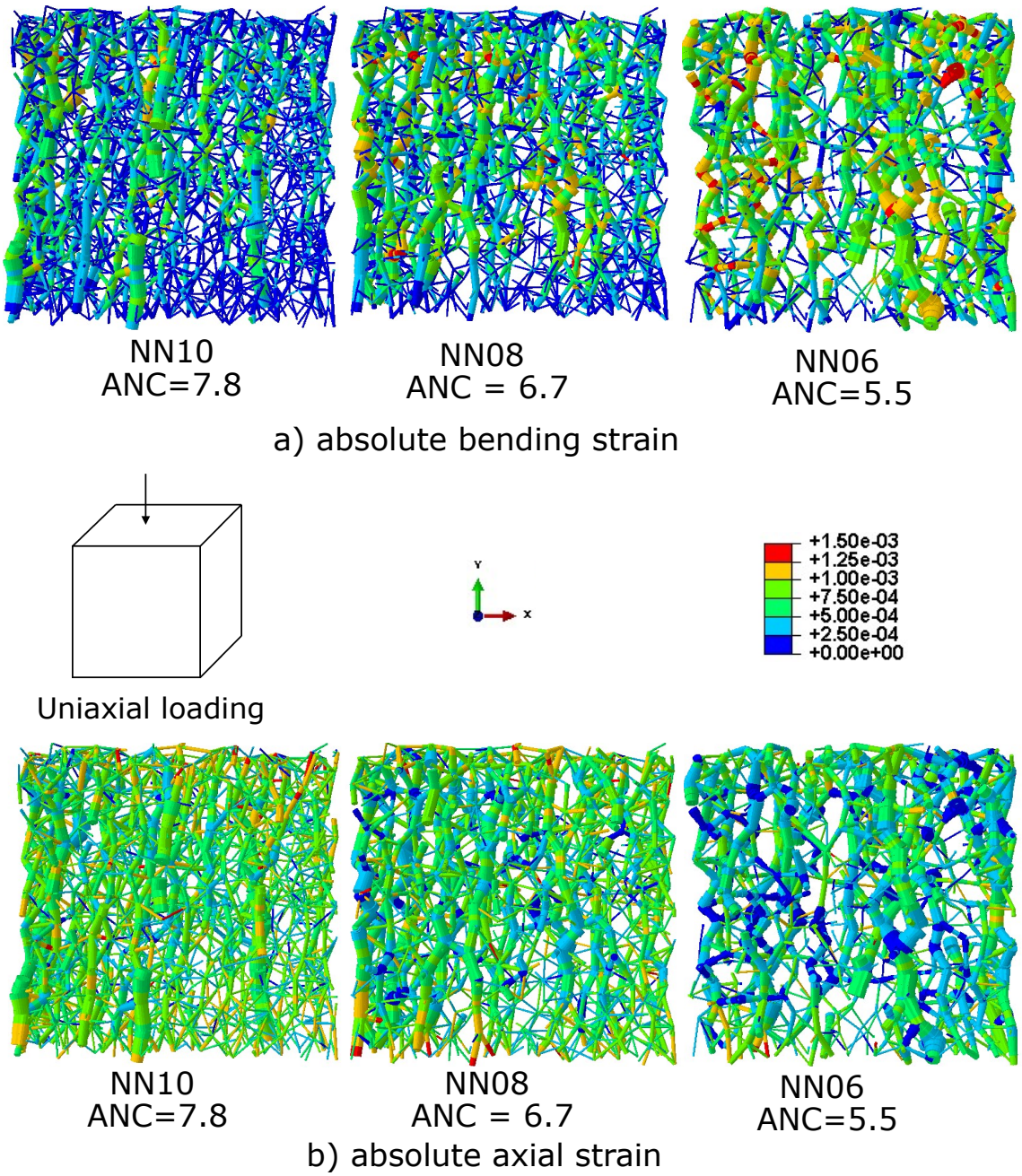


Figure 4.15: Contour plots of the a) absolute bending strain and b) absolute axial strain on a 2mm slice through the middle of one of the five models for NN10, NN08 and NN06 uniaxial loading simulations. The initial radius prior to adaptation simulations was 25μm. Dead elements with radius of 1μm are not shown. The models were subjected to a uniform pressure of 1MPa as indicated.

At high NNC, both bending and stretch models are subjected to predominantly axial

strains. This is shown by Figures 4.7a and b where the bending strain is predominantly below 500 $\mu\varepsilon$ and axial strain is predominately above 750 $\mu\varepsilon$. High NNC lattices provide a large number of possible load paths coinciding with trajectories linking load application points and support nodes. As a result, the adaptation drives such lattices towards column like structures, more evident in high MSL simulations, where there is little out of plane deformation and consequently little bending. Consequently, despite the rotational joint rigidity of such models they demonstrate stretch dominated behaviour. The fixity of joints only serves to marginally reduce overall displacements and slightly increase the predicted stiffness.

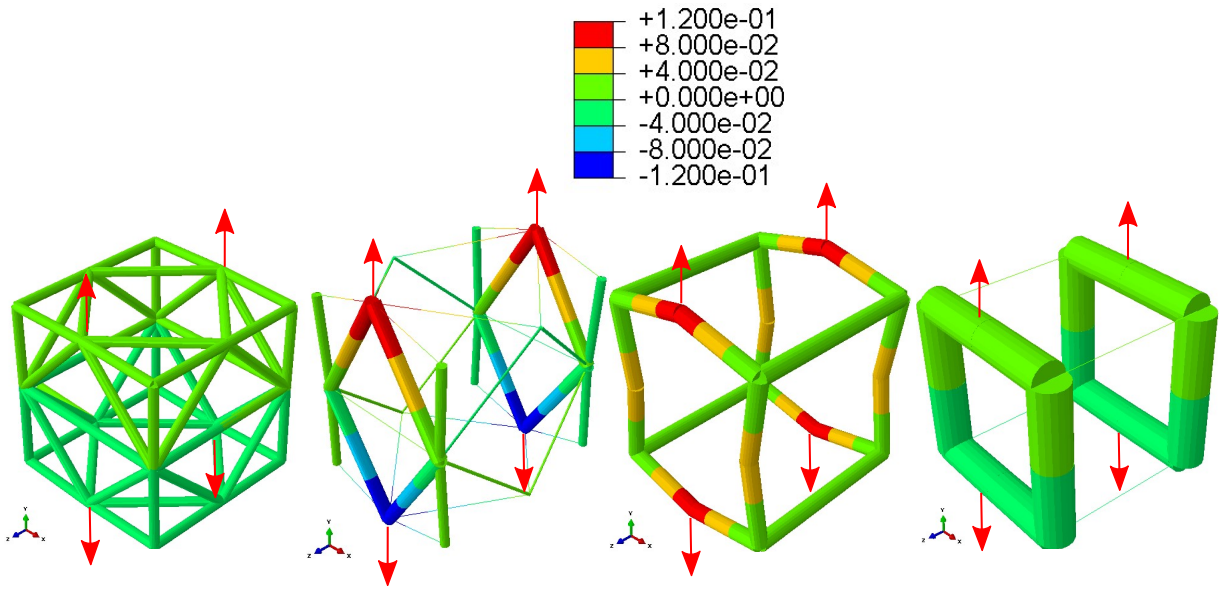
This is further supported by the examination of the relationship between the relative density and stiffness. Prior to adaptation, the relative Young's modulus of both high NNC bending and stretch models varies linearly with the relative density (Figure 4.12). This is what would be expected of a lattice with axially loaded struts (Ashby (2006)). This relationship is maintained post adaptation in both uniaxial and triaxial loading scenarios for high MSL simulations (Figure 4.13). The predicted power exponents in low MSL simulations (Figure 4.14) are approximately 1.1 and 1.2 which is higher then the expected value of 1.0. The most probable reason for this is that the volume predictions are unrealistically high due to presence of large number of struts in the group with the smallest active element radius. If there were smaller active radii available in the algorithm, the adaptation would likely drive most of these elements into a lower radius element set reducing the predicted volume but only marginally effecting the stiffness. This will be further explored in Chapter 4.

At low NNC, the difference emerges between the bending and stretch models. For NN06 pinned joint models, where the initial NC of 6.9 remains unchanged in triaxial and decreases to 6 in the uniaxial simulations, the Young's modulus displays linear dependency on the relative density prior to adaptation (Figure 4.12) and following the adaptation (Figures 4.14 and 4.13). In NN06 fixed joint models, where the initial NC of 6.9 remains unchanged in triaxial and decreases to 5.5 in the uniaxial simulations, the power exponent increases from 1.08 and 1.18 prior to adaptation to between 1.17 and 1.25 following the adaptation depending on the MSL and the loading scenario. In NN04 models, where the initial NC of 4.8 remains unchanged in triaxial and decreases to 4.0

in the uniaxial simulations, a decrease in β from 1.63 and 1.66 to between 1.41 and 1.48 is predicted. Higher exponent for lower NC simulations is in line with the behaviour of lattices becoming more bending dominated as illustrated by higher bending strains and lower axial strains in Figure 4.6. The opposite is true for strains in high NNC lattice models as is evident in Figure 4.7.

The finding that the adaptation decreases the power exponent β from approximately 1.6 to 1.4 for all loading and increases α from approximately 0.15 to approximately 0.33 for uniaxial loading in NN04 models was not anticipated. It suggests that adaptation process drives the lattice towards a more stretch dominated behaviour and greater efficiency. The open cell theory developed by Gibson & Ashby (1997) is based on regular repetitive geometry and adaptation disrupts this in two ways; it creates cells with dissimilar edges which also vary in cross section along their length. Elements which vary in cross sectional size along their length are known as non-prismatic in structural mechanics. In most cases the edges represented by beam elements thicken at nodes which influences whether the cell deformation is governed more by flexure or elastic shortening or elongation and effects the magnitude of exponent β. In addition, the difference between the beams forming specific cell edges and their non prismatic sections have an effect on the relative density and the calculation of the constant k_1 in Equation 4.6 and ultimately on the exponent α.

In order to better understand the charges in lattice behaviour brought about by the adaptation simulations, FE models of idealised foam cells used by Gibson & Ashby (1997) to derive stiffness and relative density relationships were constructed. They were subjected to the adaptation algorithm and relationships between the relative density and Young's modulus before and after adaptation were derived. Figure 4.16 presents the deflected shapes of these models and Figure 4.17 presents the Young's modulus relationships to relative densities. Each curve presented in Figure 4.17 has been fitted to four data points which were obtained by analysing the initial models in Figure 4.16 with four different radii and the adapted models with four different loads. The radii in the initial model were chosen so that the resulting model volume would equate to relative densities of 0.075, 0.15, 0.225 and 0.3. Models were subjected to 1N, 2N, 3N and 4N loads to obtain the adpted relationship.



a) Initial stretch model b) Adapted stretch model c) Initial bending model d) Adapted bending model

Figure 4.16: Contours of displacements in z direction plotted on deflected shapes of idealised open cell foam models inspired by Gibson & Ashby (1997). Each model was subjected to four 1N point loads, two on top and two on bottom face.

It is evident the high NNC stretch model initially has high stiffness and low deflections (Figure 4.16a). The adaptation simulation transforms the lattice into bending dominated lattice which exhibits approximately 10 fold higher deflections under the same load (Figure 4.16b). The reverse is true for the low NNC model shown in Figure 4.16c. The lattice retains bending dominated behaviour but the strut size greatly increases and the model becomes much stiffer with an approximately ten fold reduction in deflections under the same loading.

Initially, both the stretch and bending dominated lattices follow the behaviour predicted by Gibson & Ashby (1997) as can be seen by the plots in Figure 4.17. The initially stretch dominated lattice is shown to have the β coefficient of 1.03 and the bending one of 1.92, a close agreement to theoretical values of 1 and 2. However, after the adaptation these exponents increase to over 3 in both with initially stretch dominated model remaining more efficient through a large increase in the coefficient α. The change in coefficient α has a large influence on cell behaviour and to the authors knowledge there have not been any significant studies examining this.

Figure 4.17, combined with all of the results presented in this chapter, demonstrates

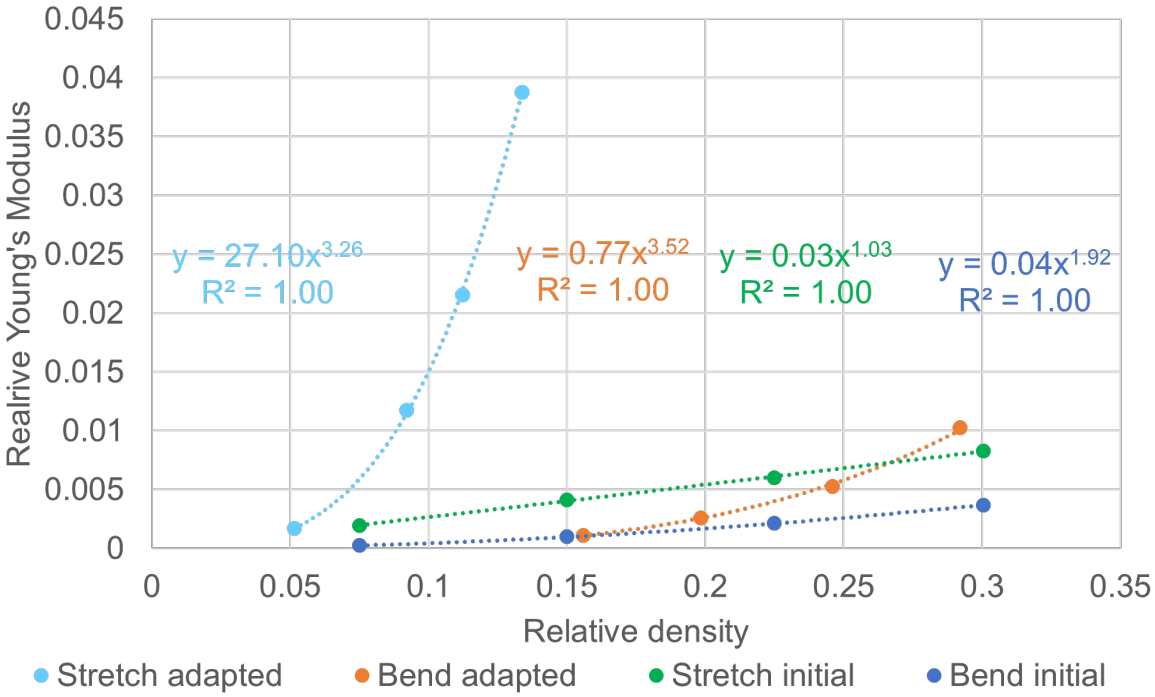


Figure 4.17: Young's modulus versus relative density plots for idealised open foam cells depicted in Figure 4.16.

that the disorder in foam cell organisation brought about by adaptation has an influence on trabecular bone mechanical properties. Liu et al. (2017) examined the effect of manufacturing defects on mechanical properties of regular octet metallic lattices. Three sets of defects were examined: strut waviness, strut thickness variation, and strut over-sizing. An indication of the effect of the strut size variation is illustrated by the reported 50% degradation of the design value of Young's modulus in lattices where the average diagonal struts radius was a half of the average horizontal strut radius. Highly ordered lattices are stronger than more disordered ones, but they are very sensitive to strain localisation and can accumulate damage in locations where this occurs (Luxner et al. (2009). In addition, they are sensitive to the direction of the applied load and if it deviates from the intended direction by only a few degrees, the stiffness and strength drop significantly (Luxner et al. (2007)).

Disordered structures are more robust against changes in applied load orientation and not susceptible to deformation localisation. This may be advantageous for trabecular bone as isolated damaged strut may repair through the process of bone remodelling. The collapse of a whole series of struts is much more difficult to repair by remodelling

and can result in fracture. It follows that some disorder in trabecular arrangement, may be useful in reducing the probability of catastrophic failure and allowing bone to self-heal by repairing accumulated damage through remodelling. However, this higher tolerance to damage generally results in lower stiffness and strength for a given amount of material. The interplay of processes inherent in bone development mean that, somewhat serendipitously, an irregular structure is created. This appears to have an advantage in increasing the bone resistance to catastrophic failure and allowing it to heal.

4.5 Conclusion

The difference between mechanical properties predicted by all of the simulations presented in this chapter are small. The Young's modulus and relative density values correspond favourably with the values reported in the literature (Linde et al. (1992), Ciarelli et al. (1991), Goulet et al. (1994),Gibson (2005)). The use of any of these bone models is therefore likely to predict realistic global behaviour and based on mechanical properties alone, all of the simulations reported in this chapter adequately describe trabecular structural form. This is particularly true of lattices with fixed joints and high NNC lattices with pinned joints.

The validity of comparison with continuum and previous structural models was examined by calculation of macro scale strains in cube samples used in this thesis (Table 4.5). The individual struts in models presented in this thesis have been adapted to a target strain of $1250\mu\varepsilon$. This governs their stifness and determines deformation under load. However, the cube samples, as a whole, while influenced by behaviour of individual struts, may experience a higher or a lower apparent strain. The value of this apparent strain is an indication of how the cube samples would have responded had they been modelled as a homogeneous continuum. This apparent strain was calculated by applying a uniform load to cube samples and measuring resulting deformations.

All the bending simulations considered predict strain in the range of the lazy zone of $1000\mu\varepsilon < \varepsilon < 1500\mu\varepsilon$, used in the adaptation algorithm. These strains are exceeded in the stretch model predictions particularly for low NNC and for uniaxial loading. This

demonstrates that high NNC models and low NNC models with fixed joints globally behave as continuum models and corresponds with the finding that predictions of these simulations more closely match those in the literature.

One significant difference in predictions arises out of consideration of uniaxial loading. The two Young's moduli in unloaded directions E_1 and E_3 are approximately 10% of the modulus E_2. They decrease with decreasing NC and more so in stretch simulations. If the trabecular bone takes the form of a stretch dominated lattice and is optimised, predominantly to a load in a single direction, then it would have very low stiffness in other directions. This fact, combined with the findings presented in Table 4.5, suggest that the trabecular bone can adopt either a stretch or bending dominated structure at high NC but can only reasonably be a bending dominated structure at low NC.

Consideration of the Young's modulus dependence on relative density identified a further interesting finding. The adaptation of low NNC bending models leads to a more efficient trabecular structure than predicted by standard theory of cellular solids (Ashby (2006)). In addition, there is evidence in the literature that a disorganised lattice such as predicted by the adaptation simulations is better able to resist damage and self heal. However, it would likely have lower stiffness and strength than a more organised lattice (Luxner 2007, 2009).

Finally, this Chapter has examined mechanical property predictions of structural models using trabecular micro-architecture more representative of real bone than previous studies (Phillips et al. (2015), Zaharie & Phillips (2018), Favier (2020)) . Chapter 5 considers the ability of these simulations to predict trabecular topology which closely matches that of real bone by investigating the adapted trabecular size, NC and corresponding inter-trabecular angle (Reznikov et al. (2016)).

Triaxial loading						
Nominal connectivity	Stretch models mean strut length [mm]			Bending models mean strut length [mm]		
	0.7	1	1.5	0.7	1	1.5
14	1628	1602	1600	1392	1309	1307
12	1669	1660	1653	1309	1286	1292
10	1760	1760	1809	1254	1264	1355
8	1957	1941	1929	1251	1262	1288
6	2710	2554	2384	1261	1263	1325
4				1348	1351	1334

Uniaxial loading						
Nominal connectivity	Stretch models mean strut length [mm]			Bending models mean strut length [mm]		
	0.7	1	1.5	0.7	1	1.5
14	1641	1719	1724	1192	1240	1290
12	1740	1815	1804	1257	1244	1283
10	2091	1968	2023	1389	1256	1349
8	2488	2243	2191	1429	1279	1314
6	3352	3187	2996	1333	1329	1383
4				1523	1522	1517

Table 4.5: Abstract bone cube samples strains [$\mu\varepsilon$] at macro-scale resulting from the 1 MPa uniformly distributed loading at the end of adaptation simulation.

5

Trabecular bone at micro-scale: morphological features predictions

5.1 Introduction

5.1.1 Overview of morphological characteristics

Trabecular bone is defined by its mechanical properties, as discussed in Chapter 4, and its morphological features, which will be examined in this Chapter. The structural models developed by the Imperial College Structural Biomechanics research group (Phillips (2012) Phillips et al. (2015), Villette & Phillips (2017), Zaharie & Phillips (2018), Favier et al. (2021), Kaufmann et al. (2021)) predicted trabecular trajectories which compared favourably with those observed in medical imaging studies (Singh et al. (1970) Gallois & Japoit (1925), Macchiarelli et al. (1999)) and correctly predicted behaviour such as fracture loads and patterns (Villette & Phillips (2018)). However, the the ability of such models to predict trabecular properties at micro-scale is unclear in the context of recent work by authors such as Reznikov et al. (2016, 2020). Therefore, this Chapter will compare the predictions of nodal connectivity (NC), Inter Trabecular Angle (ITA) and trabecular thickness with the values derived from imagining studies and reported in literature (Reznikov et al. (2016, 2020), Hildebrand & Rüegsegger (1997), Liu et al. (2008), Kirby et al. (2020), Doube et al. (2011))

Chapter 2 defines NC as the number of trabeculae meeting at a node. NC has been found to be fundamental to trabecular bone behaviour and therefore the interplay between the nominal NC (NNC) and adapted NC (ANC) is studied first. This allows the subsequent examination of how both of these parameters affect the ITA and trabecular thickness predictions.

Reznikov et al. (2015, 2016, 2017, 2020) identify a new trabecular bone parameter, the ITA which is further discussed in subsection 5.1.2. The ITAs are angles between an individual trabecula and all the others meeting at a specific node. By definition, the ITA and nodal connectivity are interdependent and the number of ITAs at each node depends on the connectivity. For instance, for NC4 nodes there are six such angles. Reznikov et al. (2016) report the proportion of nodes with NC of 3, 4, 5 and 6 and above and these values give an approximate mean NC of 3.4.

The trabecular size has been considered next. In the context of the simulations used in this thesis the trabecular size is represented by strut radii which, as described in Chapter 4, range from 25μm to 1000 μm. The mean radii predicted by these simulations were compared with the reported mean thickness ranges of 116 μm to 223 μm (Hildebrand & Rüegsegger (1997)) and 129 μm to 194 μm (Hildebrand et al. (1999)) and a mean value of 306 μm (Laib et al. (2002)). Studies by Liu et al. (2006), Zhao et al. (2018) and Kirby et al. (2020) which use a novel ITS technique for the volumetric spatial decomposition of trabecular bone samples into rods and plates (Stauber & Müller (2006)) were also considered in the comparison. Using the data reported by Zhao et al. (2018) it is possible to calculate an approximate mean trabecular rod diameter of 98 μm and an approximate mean trabecular plate thickness of 123 μm. This thesis does not consider plates, so in order to achieve density and stiffness equivalent to real bone the struts used in the simulations presented in it, need to be representative of both types of trabeculae. It is thus considered that an 116μm average of mean values for plates and rods is an appropriate value for comparison.

Finally, the effect of the dead zone on adaptation predictions will be investigated. Favier (2020) and Favier et al. (2021) report a tendency of the structural models to overpredict the abundance of the trabeculae with the smallest radius. They note that in some of the models these elements make up 80% of the total number of trabecular elements. The authors suggest that these elements provide a base stiffness to the bone whilst the larger elements adapt in accordance to the loading environment. These elements are referred to as the ground matrix. The study suggests that a better match between the predicted trajectories and in vivo observations may be achieved by refining the trabecular radius range in the adaptation algorithm. This thesis implements this suggestion. In addition this Chapter will consider the effect of the dead zone. Preliminary work included in Appendix A has identified that an increase in the dead zone threshold reduces the number of elements in the smallest category.

5.1.2 Review of morphological characteristics imaging studies

The accuracy of trabecular representation at micro scale achieved by computer simulations models is unclear in the context of recent work by authors such as Reznikov et al. (2014*a*,*b*, 2015, 2016, 2017, 2020). These studies used cadaver proximal femur bone samples to investigate 3D trabecular bone collagen fibril structure, trabecular bone topology and how it differs between normal and pathological bone.

The lamellae, found in trabecular bone (Figure 2.1c), situated on the outer surface of the trabecula, are oriented along its axis (Reznikov et al. (2015)). This is consistent with osteocytes, positioned at the bone surface, as they organise collagen fibres in the direction of loading, thus aligning the trabeculae in that direction. μCT images of 14 samples obtained from the proximal femur of two cadaveric donors were used in this study. A comparison was drawn with a similar study (Reznikov et al. (2014*b*)) examining cortical bone in the femoral shaft, which included 12 samples from three individuals of varying ages. That study found that lamellae on the outer surface of the femoral shaft aligned with its axis, which broadly corresponds to the direction of loading.

A subsequent study (Reznikov et al. (2016)) further investigated trabecular directionality. It examined bone samples from different regions of the proximal femora obtained from cadaver donors of different age and sex, as outlined in Table 5.1. μCT scans, with the pixel size of between 43μm and 47μm, of the samples were obtained. Scans were then processed with a graphic editor to remove cortical bone and artefacts and create 3D digital samples of trabecular bone.

Sex	Age	Anatomic site
Male	63	Femoral head; metaphysis; neck
Male	20	Femoral head
Female	20	Metaphysis; neck
Female	79	Metaphysis
Female	54	Metaphysis

Table 5.1: Samples used in the Reznikov et al. (2016) study.

A thinning algorithm, known as skeletonization, was then applied to each sample.

Each trabecula was represented as an edge with exactly one voxel thickness, roughly corresponding to the longitudinal axis of each trabecula. As the axes of the trabeculae are not absolutely straight, Euclidean distance defining struts by their branching points, was used instead. The resulting network of edges was represented by a list of vectors which were topologically equivalent to trabecular struts in the original 3D image.

The resulting edge matrix which contained a list of coordinates representing nodes and a list of vectors representing the struts was analysed in MATLAB. Nodal connectivity (NC) for each node was established by calculating how many struts (vectors) connected it too other nodes. Additionally, the angles between each pair of struts emanating from the same node, known as inter-trabecular angles (ITA), were computed. Struts were defined by vectors so ITAs could be calculated using conventional mathematics. The reported proportion of nodes with NC of 3, 4, 5 and 6 and above and the corresponding mean ITAs are given in Table 5.2.

NC	Proportion	ITA
3	65% - 75%	116.3^{o}
4	19%-27%	107.6^{o}
5	4% - 7%	103.1^{o}
> 5	< 1.5%	100^{o}

Table 5.2: Proportion of nodes of specified nodal connectivity (NC) in typical trabecular bone and the associated ITA values (Reznikov et al. (2016)).

The difference in the these novel trabecular bone characteristics between the normal and pathological bone was investigated next. Reznikov et al. (2017) compared the heel bone trabecular architecture in the normal foot with that which has been subjected to historical foot binding. In a normal foot the heel bone, tarsals and metatarsals form an arch with the plantar fascia acting as a tie. This arrangement leads to multi directional load trajectories and the trabecular architecture adapts to them by increased anisotropy. However, in the bound foot, where body weight is primarily supported through near-unidirectional load transfer, the anisotropic pattern fails to develop. Skeletonization and subsequent NC and ITA analysis revealed very little difference between the normal and bound foot samples and good correspondence with the previous Reznikov et al. (2016) study. These findings suggest that the anisotropic trabecular bone archi-

tecture is an acquired characteristic that reflects recurrent loading conditions. In other words it emerges from a biological blue print trough growth of trabecula more closely aligned with load trajectories.

Finally, the difference in NC and ITA between species was considered. Ben-Zvi et al. (2017) investigated these bone parameters in porcine proximal femora and mandibles. The reported abundance of NC3 NC4 and NC5 nodes were 71% 21% and 7% respectively. The reported mean ITAs for porcine proximal femora were 115° in NC3 nodes, 106° in NC4 nodes and 102° in NC5 nodes. These values are very similar to those reported for the human femora given in Table 5.2. This suggests that the original findings of the Reznikov et al. (2016) study apply to species other than humans.

In summary these studies (Reznikov et al. (2014*b*, 2015, 2016, 2017, 2020)) collectively suggest that the topological characteristics of NC of around 4, with a predominant value of 3, and ITA values which correspond to efficient space filling are features present in all trabecular bone and that a biological trabecular bone blueprint adapts to the applied loading through increased anisotropy.

5.2 Methodology

This Chapter examines the morphological data predicted by the same simulations presented in Chapter 4 and listed in Table 4.1. Morphological data was extracted from the relevant Abaqus output files. Matlab scripts were used to call up a Python script and extract strut radius, nodal coordinates and the graph connectivity between the coordinates which defines the strut direction and length. This information was temporarily stored in the Matlab workspace, processed as required and the output was saved to either a figure, Microsoft Excel or a text file. The coordinate and strut definition information was processed in Matlab to calculate the NC and the ITAs and strut radii were extracted. A detailed description of how the NC, ITA and radii data was collected and analysed statistically is now presented.

Radius values were extracted for five models of each simulation in turn, discarding

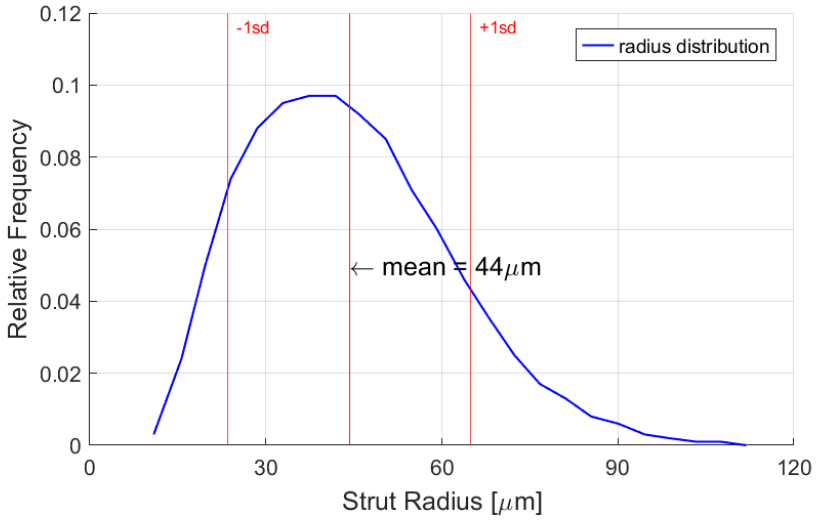


Figure 5.1: Mean strut radius distribution data reproduced from Kirby et al. (2020).

the data for dead elements with radius of 0.5μm. The radius of a strut was calculated as the average of the four element radii forming it. These values are then compared to mean radii reported by Zhao et al. (2018) and Kirby et al. (2020) and reproduced in Figure 5.1. Radius data for each set of adaptation parameters run with five different geometries were thus obtained and statistical calculations could be implemented without the need for further processing. Possible limitations of studies by Zhao et al. (2018) and Kirby et al. (2020) and the supporting data in other literature (Liu et al. (2006), Stauber & Müller (2006)) is discussed in the introduction. However, it was decided that the radii distribution reported in their studies allows useful comparison with the simulation predictions included in this thesis.

Connectivity and ITA data were extracted at the same time due to their interdependence. Abaqus model files contain connectivity data for each node in the form of beam element definitions. NC is determined by the number of active elements at a specific node. Only joint nodes were considered and not the nodes which divide struts into four elements. Connectivity information was extracted from Abaqus files, selecting only joint nodes and excluding the dead elements with radius of 0.5μm. The connectivity of each joint was then stored in a matrix with a joint number and the connectivity. For example, a NC of 4 would have been stored for joint J_n in Figure 5.2. Statistics are presented for five sets of NC and radius data from each adaptation scenario.

Once NC was determined, ITA values could be calculated as this defined the num-

ber of angles that existed at each node, in the case of the example in Figure 5.2 this is 6. Abaqus element definition and node coordinates were used to define the vectors of all elements joined at a specific node, V_1 to V_4 in the example. The algorithm then evaluated the angles between vectors, using the Matlab subspace function. The calculation started with V_1 and evaluated all the angles between it and all other vectors up to V_n where n was equal to NC. The process was then repeated, incrementing the starting vector by 1 until V_{n-1} was reached.

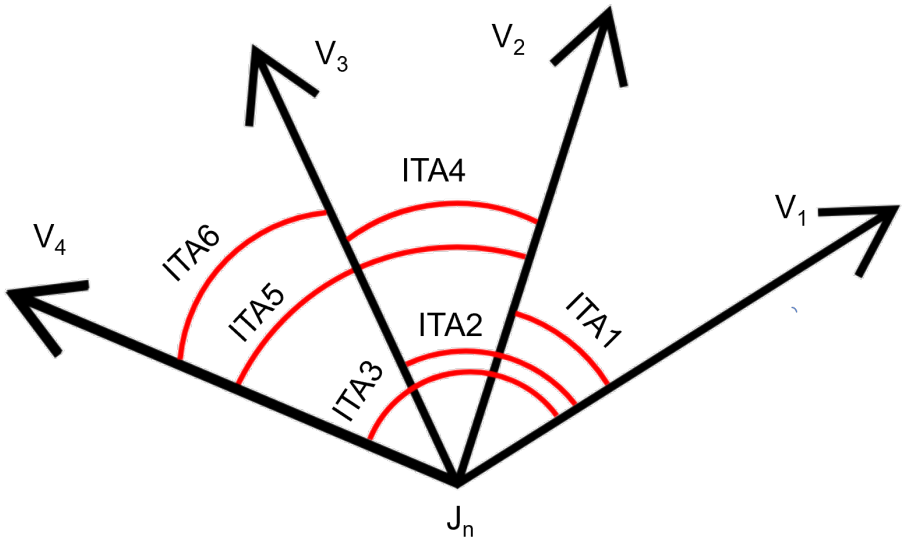


Figure 5.2: Illustration of ITA angle measurement.

The mean, mode, standard deviation and minimum and maximum NC values were calculated from the extracted data and downloaded into a table presented in the results section. The mean, median, standard deviation and the 95 % confidence intervals were calculated from the extracted radius and ITA data and downloaded into a table. Radius data histograms overlaid with probability distribution curves were plotted and a selection included in the results section. The abundance of nodes with all present ANC values was calculated and the ITA statistical data was only presented for the three most abundant ones. ITA distributions for nodes with ANC of 3, 4, 5 and 6 and above were plotted, but only for simulations where such nodes more than 5% of total nodes. These NCs were chosen to enable comparison with data in the study by Reznikov et al. (2016).

Finally, the adaptation simulations were repeated for sixteen selected simulations listed in Table 5.3 using an amended algorithm with the dead zone threshold coinciding with the lower limit of the lazy zone, 1000 $\mu\varepsilon$ where these have been carried out. The

simulations were chosen so as to cover the range of high and low mean strut length, high and low nominal connectivity and both uniaxial and triaxial loading. The predicted trabecular volume, Young's modulus connectivity, trabecular radius data and ITA data from these simulations were compared with the ones using the original dead zone. These results are presented along with the others and identified as such.

NN04_B_0.7_1_NDZ	NN04_S_0.7_1_NDZ
NN14_B_0.7_1_NDZ	NN14_S_0.7_1_NDZ
NN04_B_0.7_3_NDZ	NN04_S_0.7_3_NDZ
NN14_B_0.7_3_NDZ	NN14_S_0.7_3_NDZ
NN04_B_1.5_1_NDZ	NN04_S_1.5_1_NDZ
NN14_B_1.5_1_NDZ	NN14_S_1.5_1_NDZ
NN04_B_1.5_3_NDZ	NN04_S_1.5_3_NDZ
NN14_B_1.5_3_NDZ	NN14_S_1.5_3_NDZ

Table 5.3: List of additional simulations with no dead zone.

The algorithm was amended to inactivate the elements experiencing strains below 1000 μm, the lazy zone lower limit. Dead elements were reactivated, by assigning them the lowest active radius, if in the subsequent iteration cycles the strain in such elements increased sufficiently. The strain at which this occurred was assumed to be of the magnitude which would equate to a 1000 μm strain in an element with 25μm radius. For pure axial strain this would be a strain of 1000 μm scaled by the ratio of the radii to the power of two, $25^2/0.5^2 = 2,500$, and for pure bending by the radii to the power of three $25^3/0.5^3 = 125,000$. Each element would have experienced a different combination of axial and bending strains during the simulation iterations. This would also change for a particular element in different iterations. As the ratio would not be constant it was decided to use the lower limit throughout. The drawback of this approach is the possibility of activating some elements with lower strains than warranted although they would be inactivated in subsequent iterations.

5.3 Results

5.3.1 Nodal connectivity

Table 5.4 presents the mean, mode, standard deviation minimum and maximum NC values before and after adaptation. Results for simulations with dead zone thresholds of 250$\mu\varepsilon$ and 1000$\mu\varepsilon$ are presented. NC for pinned joint models remains unchanged by triaxial adaptation simulations unless a higher threshold for dead zone is applied. The largest change is observed in bending models subjected to uniaxial loading. The mode of all triaxial simulations is equal to NNC. In uniaxial simulations, whilst the mode is close to NNC, it tends to be slightly lower and further reduced when the higher dead zone threshold is applied. Conversely, the mean values tend to be higher than the nominal values in triaxial simulations and lower in the uniaxial simulations. This is more pronounced in higher NNC and in bending simulations. The NC range remains the same in all triaxial loading simulations except for the ones with NNC of 4. The minimum NC reduces to 1 in all but high initial NC MSL=1.5mm simulations. The maximum NC in these simulations reduces more markedly for ones with high initial NC.

Table 5.5 presents the prevalence of the nodes with four most common ANC in those simulations. For instance for the NN04 simulations subjected to uniaxial loading present the prevalence of nodes with ANC of 3, 4, 5 and 6 are presented while for the same models subjected to triaxial loading nodes with ANC of 4, 5, 6 and 7 are presented. The ANC values are further reduced by 1 in the equivalent simulations with an increased dead zone threshold. In general, the adaptation simulations reduce the NC and this reduction is greater in higher NNC models. Not unexpectedly the models with higher NNC converge to higher ANC values.

		MSL = 0.7 mm					MSL = 1.0 mm					MSL = 1.5 mm				
		Bending simulations														
Load	NNC	Mean	Mode	SD	Min	Max	Mean	Mode	SD	Min	Max	Mean	Mode	SD	Min	Max
Initial	4	4.8	4	0.9	4	9	4.8	4	0.9	3	8	4.8	4	0.9	4	8
	6	6.9	6	1	5	12	6.9	6	1	5	11	7	6	1.1	5	11
	8	9	8	1.1	6	16	9.1	8	1.2	6	15	9.2	8	1.3	7	15
	10	11.1	10	1.3	7	19	11.2	10	1.4	8	19	11.4	10	1.5	8	18
	12	13.1	12	1.4	8	23	13.3	12	1.6	9	21	13.5	12	1.8	9	21
	14	15.1	14	1.6	9	27	15.3	14	1.8	9	26	15.6	14	2	10	25
Uniaxial	4	4	4	1.2	1	9	4	4	1.2	1	8	4.1	4	1.2	1	7
	4*	3.4	4	1.1	1	8						3.6	4	1.1	1	7
	6	5.5	6	1.5	1	11	5.4	6	1.6	1	11	5.5	6	1.5	1	10
	8	6.7	7	1.9	1	14	6.7	7	1.9	1	14	6.8	7	1.9	1	13
	10	7.8	8	2.2	1	16	7.9	8	2.1	1	17	8	8	2.2	1	14
	12	8.8	9	2.4	1	17	9.1	9	2.4	1	17	9.1	9	2.5	2	17
	14	9.6	10	2.6	1	20	10.1	10	2.5	1	19	10.4	11	2.7	2	20
	14*	3.8	4	1.4	1	12						6.2	5	3	1	18
Triaxial	4	4.8	4	0.9	1	9	4.8	4	0.9	1	8	4.8	4	0.9	2	8
	4*	4.4	4	1	1	9						4.5	4	1	1	8
	6	6.9	6	1	4	11	6.9	6	1	4	11	7	6	1.1	5	11
	8	8.9	8	1.1	6	16	9	8	1.2	6	15	9.1	8	1.3	7	15
	10	11	10	1.3	7	19	11.2	10	1.4	8	19	11.3	10	1.5	8	17
	12	13.1	12	1.4	8	23	13.2	12	1.6	9	21	13.4	12	1.8	9	21
	14	15.1	14	1.6	9	27	15.3	14	1.8	9	26	15.5	14	2	10	25
	14*	7	7	2.2	1	16						9.4	10	2.1	2	17
		Stretch simulations														
Uniaxial	6	6	6	1.5	1	11	6.1	6	1.6	1	11	6.1	6	1.5	1	11
	6*	5.2	5	1.5	1	10						5.6	6	1.5	1	10
	8	7.2	8	1.9	1	14	7.3	8	1.9	1	13	7.3	8	1.9	1	14
	10	8.3	9	2.2	1	16	8.6	9	2.1	1	18	8.6	9	2.2	2	16
	12	9.3	10	2.5	1	17	9.8	10	2.4	1	17	9.8	10	2.5	2	17
	14	10.2	11	2.7	1	20	10.9	12	2.6	1	20	11.1	11	2.7	4	20
	14*	5.7	6	1.9	1	15						7.6	4	3.7	1	18
Triaxial	6	6.9	6	1	5	12	6.9	6	1	5	11	7	6	1.1	5	11
	6*	6.7	6	1	1	12						6.9	6	1.1	4	11
	8	8.9	8	1.1	6	16	9	8	1.2	6	15	9.2	8	1.3	7	15
	10	11.1	10	1.3	7	19	11.2	10	1.4	8	19	11.3	10	1.5	8	17
	12	13.1	12	1.4	8	23	13.3	12	1.6	9	21	13.5	12	1.8	9	21
	14	15.1	14	1.6	9	27	15.3	14	1.8	9	26	15.6	14	2	10	25
	14*	7.7	8	2.5	1	17						11.1	11	2.2	3	19

Table 5.4: The mean, mode, standard deviation, minimum and maximum NC before and after adaptation tabulated by MSL, loading scenario, lattice type and initial NC. Dead zone of 250$\mu\varepsilon$ has been used except for simulations with * next to the NNC value which indicate that the dead zone of 1000$\mu\varepsilon$ has been used. Key results are highlighted in yellow.

Load	NNC	MSL = 0.7 mm				MSL = 1.0 mm				MSL = 1.5 mm			
		Bending simulations											
		Mean	Mode	SD	Max	Mean	Mode	SD	Max	Mean	Mode	SD	Max
Uniaxial	4	4	5	6	7	4	5	6	9	4	5	6	9
		46.5%	33.8%	14.3%	4.5%	46.5%	33.8%	14.3%	4.5%	46.5%	33.8%	14.3%	4.5%
	4*	3	4	5	6					3	4	5	6
		31.3%	24.5%	16.6%	9.7%					31.3%	24.5%	16.6%	9.7%
	10	10	11	12	13	10	11	12	13	10	11	12	13
		38.3%	28.9%	17.2%	8.5%	38.3%	28.9%	17.2%	8.5%	38.3%	28.9%	17.2%	8.5%
	14	14.0	15.0	16.0	17.0	14.0	15.0	16.0	17.0	14.0	15.0	16.0	17.0
		31.3%	24.5%	16.6%	9.7%	31.3%	24.5%	16.6%	9.7%	31.3%	24.5%	16.6%	9.7%
	14*	3	4	5	6					3	4	5	6
		31.3%	24.5%	16.6%	9.7%					31.3%	24.5%	16.6%	9.7%
Triaxial	4	4	5	6	7	4	5	6	9	4	5	6	9
		46.1%	33.6%	14.0%	4.3%	46.5%	33.8%	14.3%	4.5%	46.5%	33.8%	14.3%	4.5%
	4*	6	7	8	9					6	7	8	9
		43.4%	32.8%	16.2%	5.2%					43.6%	33.1%	16.4%	5.3%
	10	10	11	12	13	10	11	12	13	10	11	12	13
		37.7%	28.4%	17.0%	8.4%	38.3%	28.9%	17.2%	8.5%	38.3%	28.9%	17.2%	8.5%
	14	14	15	16	17	13	14	15	16	6	7	8	9
		31.2%	24.6%	16.6%	9.6%	26.7%	17.2%	9.3%	4.0%	43.6%	33.1%	16.4%	5.3%
	14*	14	15	16	17					14	15	16	17
		31.2%	24.6%	16.6%	9.6%					31.3%	24.5%	16.6%	9.7%
Uniaxial		Stretch simulations											
	6	6	7	8	9	6	7	8	9	6	7	8	9
		43.6%	33.1%	16.4%	5.3%	43.6%	33.1%	16.4%	5.3%	43.6%	33.1%	16.4%	5.3%
	6*	6	7	8	9					6	7	8	9
		43.4%	32.8%	16.2%	5.2%					43.6%	33.1%	16.4%	5.3%
	10	10	11	12	13	10	11	12	13	10	11	12	13
		38.3%	28.9%	17.2%	8.5%	38.3%	28.9%	17.2%	8.5%	38.3%	28.9%	17.2%	8.5%
	14	13	14	15	16	13	14	15	16	13	14	15	16
		26.7%	17.2%	9.3%	4.0%	26.7%	17.2%	9.3%	4.0%	26.7%	17.2%	9.3%	4.0%
	14*	14	15	16	17					14	15	16	17
		31.3%	24.5%	16.6%	9.7%					31.3%	24.5%	16.6%	9.7%
Triaxial	6	6	7	8	9	6	7	8	9	6	7	8	9
		43.6%	33.1%	16.4%	5.3%	43.6%	33.1%	16.4%	5.3%	43.6%	33.1%	16.4%	5.3%
	6*	6	7	8	9					6	7	8	9
		43.4%	32.8%	16.2%	5.2%					43.6%	33.1%	16.4%	5.3%
	10	10	11	12	13	10	11	12	13	10	11	12	13
		38.3%	28.9%	17.2%	8.5%	38.3%	28.9%	17.2%	8.5%	38.3%	28.9%	17.2%	8.5%
	14	13	14	15	16	13	14	15	16	13	14	15	16
		26.7%	17.2%	9.3%	4.0%	26.7%	17.2%	9.3%	4.0%	26.7%	17.2%	9.3%	4.0%
	14*	14	15	16	17					14	15	16	17
		31.3%	24.5%	16.6%	9.7%					31.3%	24.5%	16.6%	9.7%

Table 5.5: Proportions of nodes with four most prevalent NC following adaptation simulations. Results are tabulated by the loading, initial NC and MSL. Each simulation entry gives NC on top and its proportion below. Dead zone of 250$\mu\varepsilon$ has been used except for simulations with * next to the NNC value which indicate that the dead zone of 1000$\mu\varepsilon$ has been used. Representative results are presented here with full results available in the appendix Table A.1.Key results are highlighted in yellow.

Figure 5.3 presents the node geometry of four example nodes with the most common ANC in NN04 simulations with MSL of 0.7mm: 3, 4, 5 and 6. The variation in predicted geometry of these 4 nodes in response to the change in dead zone threshold is presented in Figure 5.4. Figures 5.5 and 5.6 present the predicted geometry of these same nodes when models are subjected to triaxail loading with dead zone at 250$\mu\varepsilon$ and 1000$\mu\varepsilon$ respectively.

NC4, NC5 and NC6 nodes in Figure 5.3 transform into NC3, NC4 and NC5 nodes whilst NC3 node remains unchanged when the dead zone threshold is increased (Figure 5.4). When subjected to triaxial loading the NC4, NC5 and NC6 nodes remain with same connectivity but element radius increases. The NC3 node transforms to NC5 (Figure 5.5). There is no apparent change in the node architecture when the dead zone threshold is increased in the simulations subjected to triaxial loading (Figure 5.6).

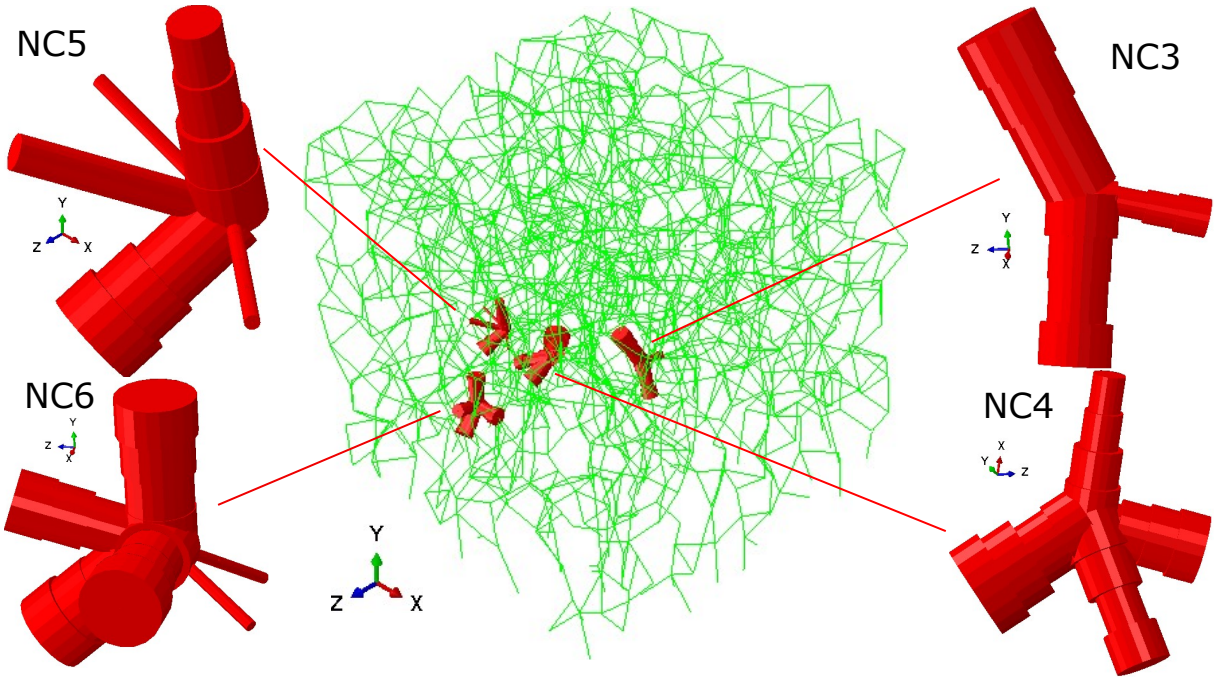


Figure 5.3: Examples of node geometry for NC3, NC4, NC5 and NC6 in NN04 model with MSL=0.7mm and fixed joints following a uniaxial adaptation simulation with dead zone at 250$\mu\varepsilon$. The mean connectivity following the adaptation of this simulation is 4.0

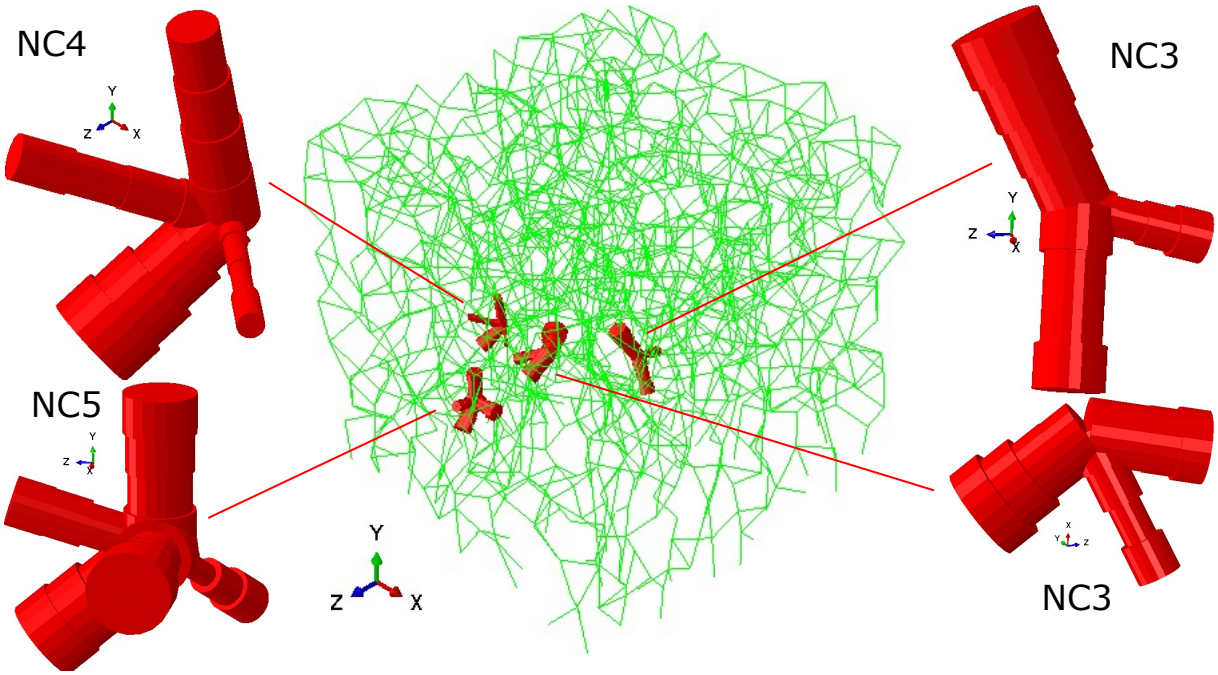


Figure 5.4: Geometry of the same nodes presented in Figure 5.3 for a model with the same parameters as in Figure 5.3 except that the dead zone is set at 1000$\mu\varepsilon$. NC4, NC5 and NC6 nodes in Figure 5.3 transform into NC3, NC4 and NC5 nodes whilst NC3 node remains unchanged. The mean connectivity following this simulation is 3.4

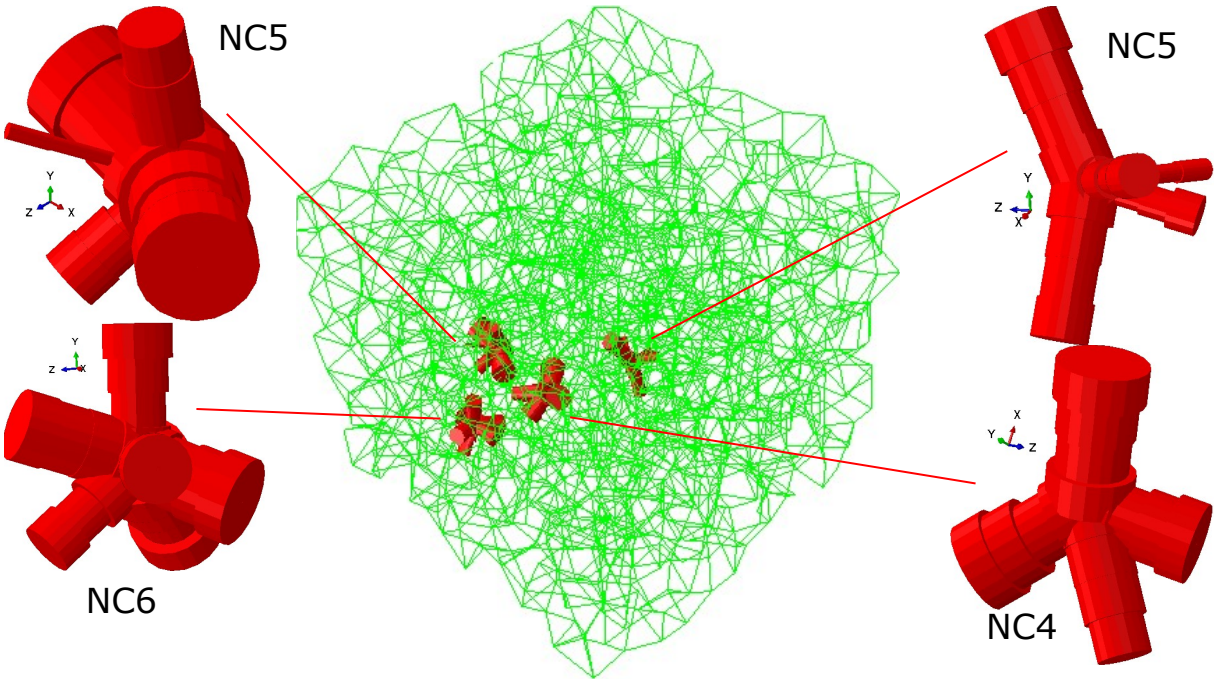


Figure 5.5: Geometry of the same nodes presented in Figure 5.3 for a model with the same parameters as in Figure 5.3 except that it was subjected to a triaxial loading. The NC4, NC5 and NC6 nodes remain with same connectivity but element radius increases. The NC3 node transforms to NC5. The mean connectivity following this simulation is 4.8

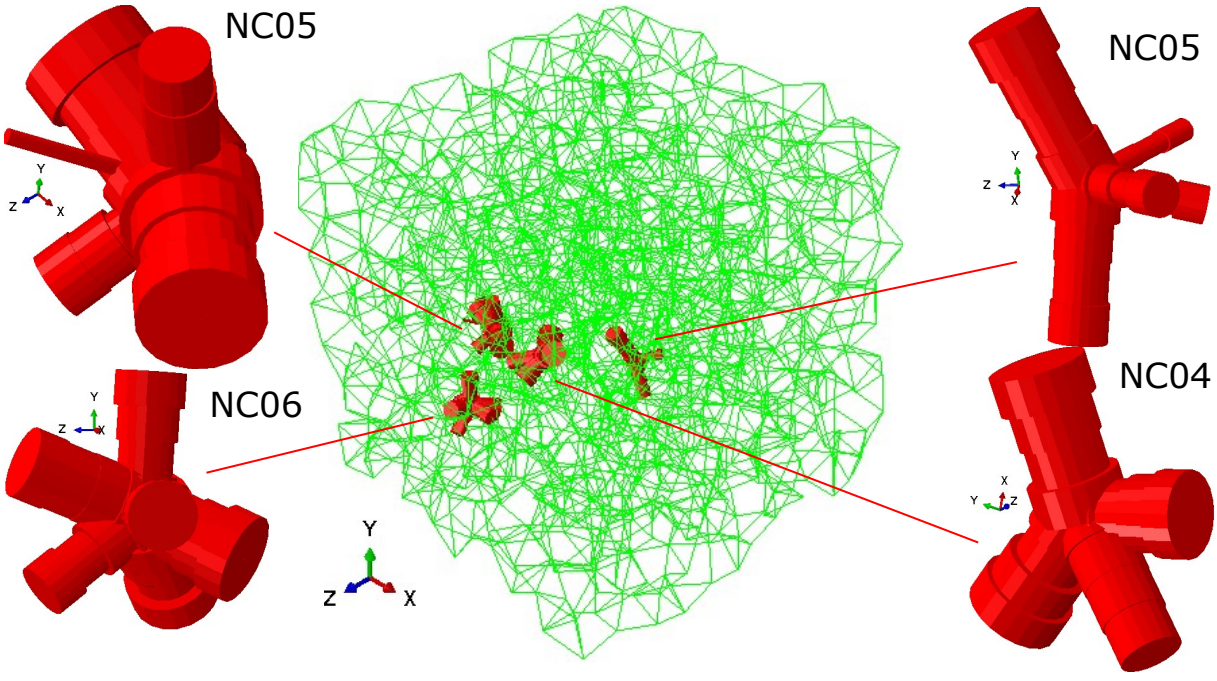


Figure 5.6: Geometry of the same nodes presented in Figure 5.3 for a model with the same parameters as in Figure 5.3 except that it was subjected to a triaxial loading and the dead zone was set at 1000$\mu\varepsilon$. There is no apparent change for example nodes from predictions in Figure 5.5 but the mean NC decreases to 4.4.

Figure 5.7 presents the node geometry of four example nodes with the most common ANC in NN14 simulations with fixed nodes and MSL of 0.7 mm: 9, 10, 11 and 12. The variation in predicted geometry of these 4 nodes in response to the change in dead zone threshold is presented in Figure 5.8. Figures 5.9 and 5.10 present the predicted geometry of these same nodes when models are subjected to triaxail loading with dead zone at 250$\mu\varepsilon$ and 1000$\mu\varepsilon$ respectively.

NC09, NC11 and NC12 nodes in Figure 5.7 transform into NC06, NC03 and NC04 nodes whilst elements in NC10 all became inactive when the dead zone threshold is increased (Figure 5.8). The NC9, NC10, NC11 and NC12 nodes transform into NC14, NC16, NC13 and NC14 nodes respectively in simulations with triaxial loading (Figure 5.9). NC09, NC10, NC11 and NC12 nodes in Figure 5.7 transform into NC10, NC09, NC05 and and NC06 nodes when the dead zone threshold is increased. (Figure 5.10).

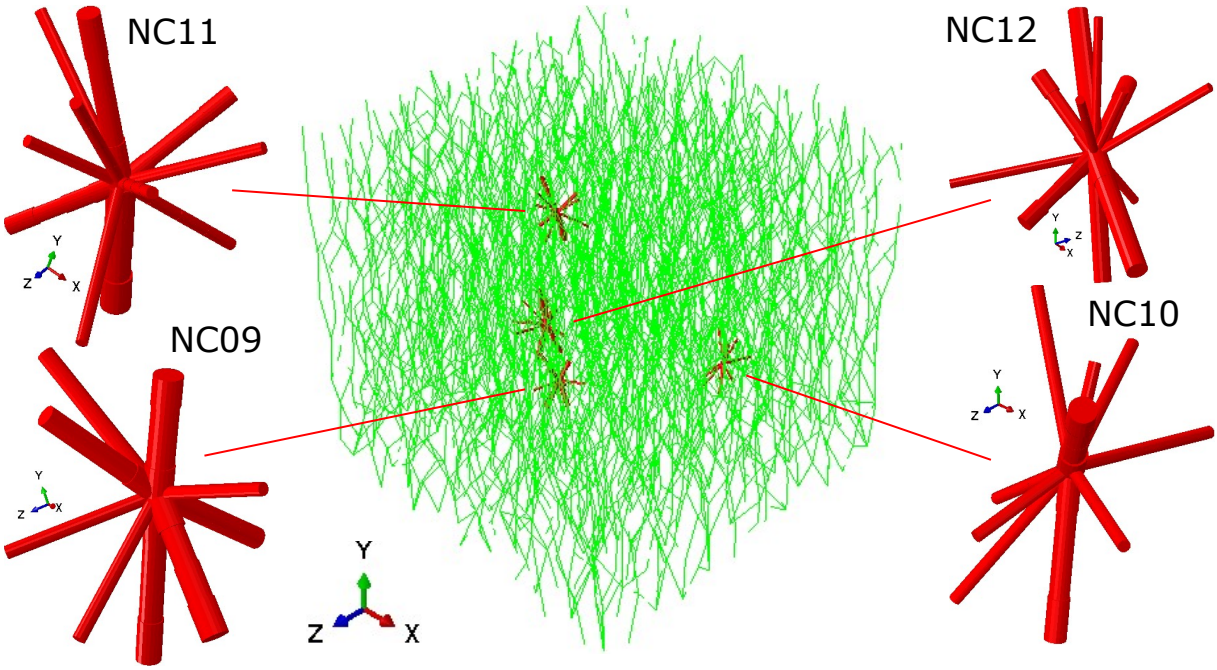


Figure 5.7: Examples of node geometry for NC09 NC10, NC11 and NC12 in NN14 model with MSL of 0.7mm and fixed joints following a uniaxial adaptation simulation with dead zone at 250$\mu\varepsilon$. The mean connectivity following this simulation is 9.6

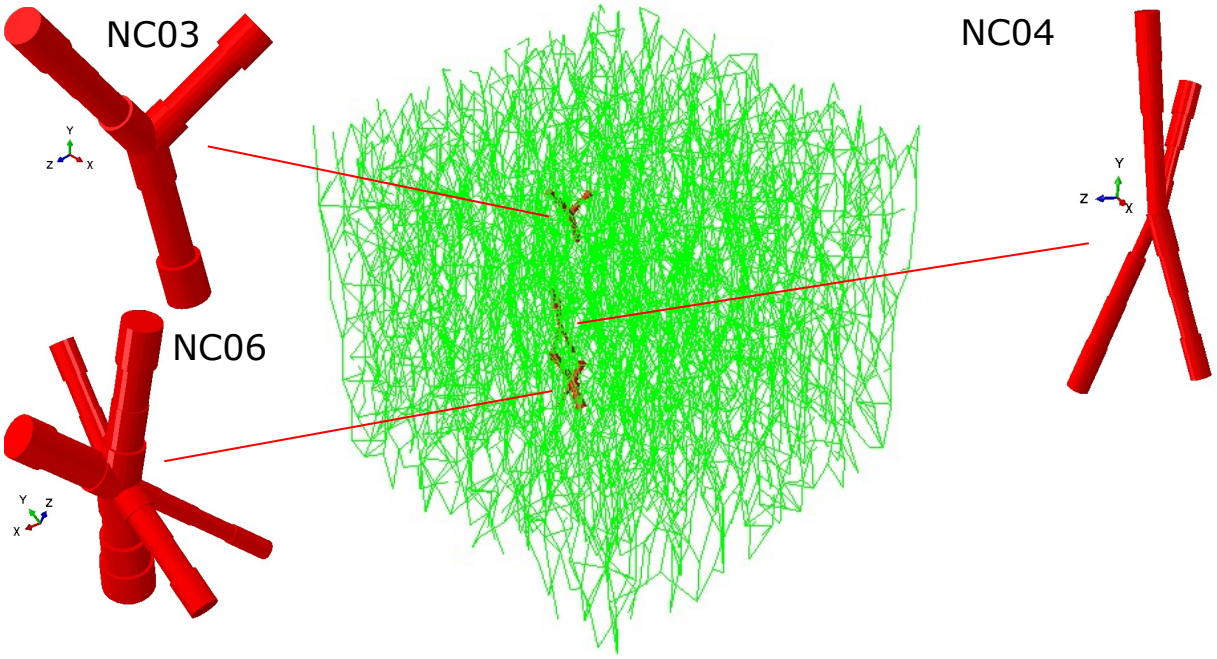


Figure 5.8: Geometry of the same nodes presented in Figure 5.7 for a model with the same parameters as in Figure 5.7 except that the dead zone is set at 1000$\mu\varepsilon$. NC09, NC11 and NC12 nodes in Figure 5.7 transform into NC06, NC03 and NC04 nodes whilst elements in NC10 all became inactive. The mean connectivity following the adaptation of this simulation is 3.8.

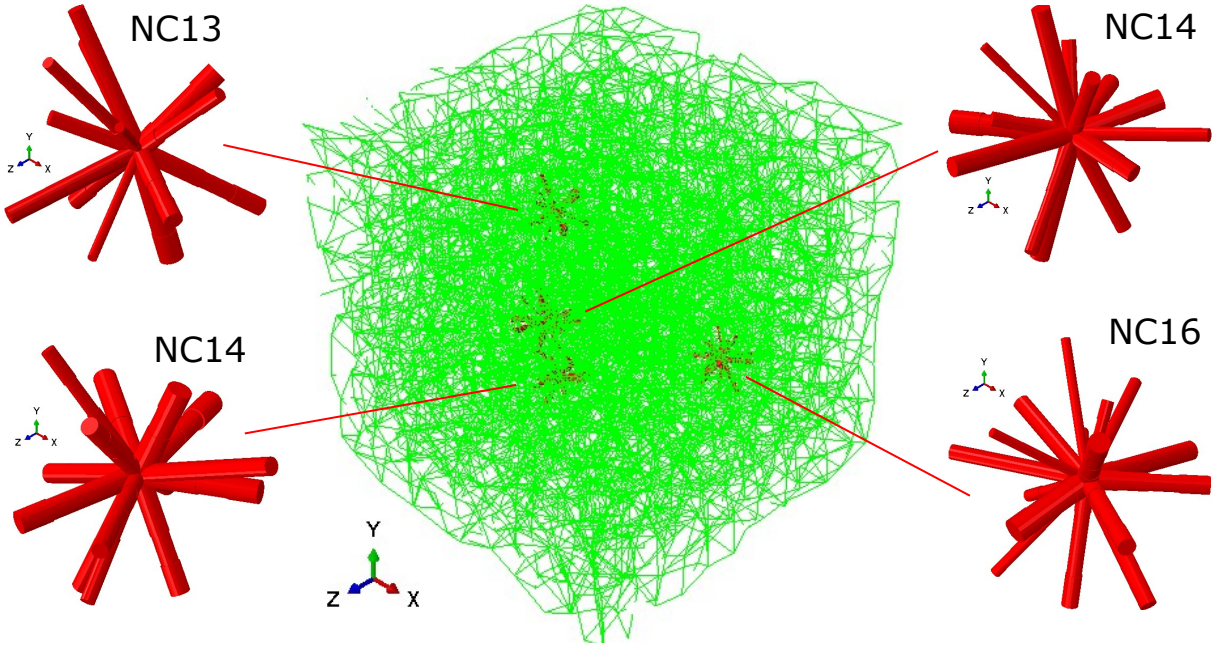


Figure 5.9: Geometry of the same nodes presented in Figure 5.7 for a model with the same parameters as in Figure 5.7 except that it was subjected to a triaxial loading. The NC9, NC10, NC11 and NC12 nodes transform into NV14, NC16, NC13 and NC14 nodes respectively. The mean connectivity following this simulation is 15.1

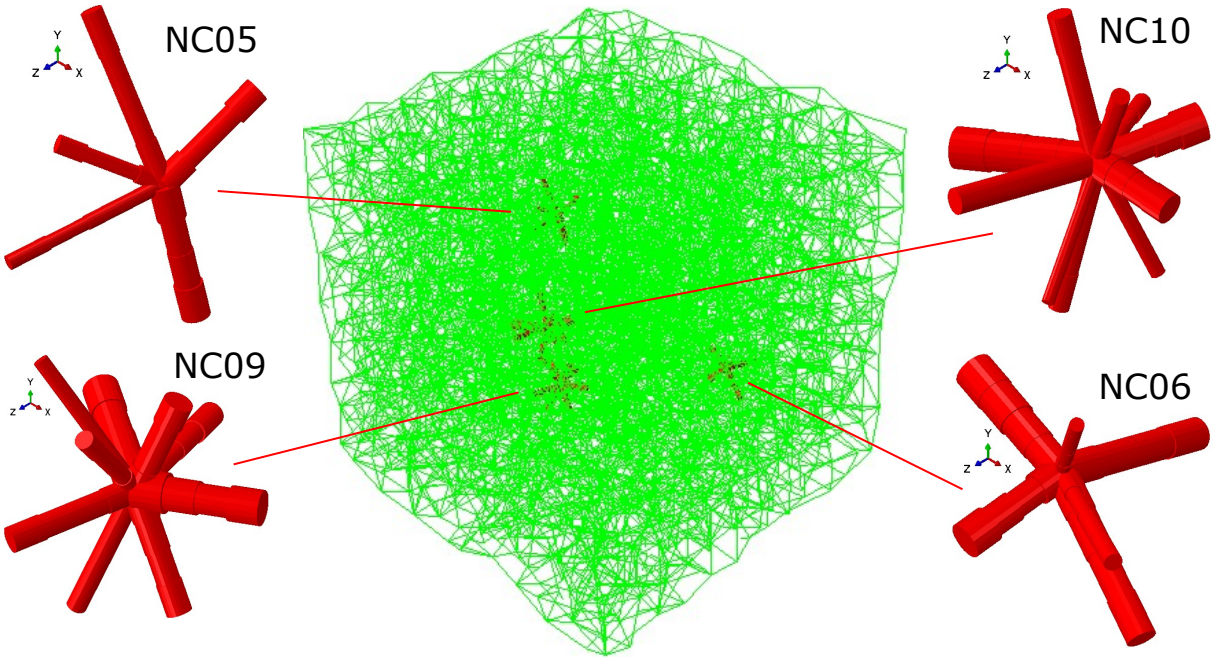


Figure 5.10: Geometry of the same nodes presented in Figure 5.7 for a model with the same parameters as in Figure 5.7 except that it was subjected to triaxial loading and the dead zone was set at 1000$\mu\varepsilon$. NC09, NC10, NC11 and NC12 nodes in Figure 5.7 transform into NC10, NC09, NC05 and and NC06 nodes. The mean connectivity following the adaptation of this simulation is 7.0.

5.3.2 ITA

Tables 5.6 and 5.7 present the mean, median, standard deviation, minimum and maximum ITA values for a selection of representative simulations presented in this thesis. The complete set of values are included in the Appendix Tables A.3, A.2, A.5 and A.5. ITA values for the nodes with the four most prevalent ANC for each simulation are presented.

The highest ITAs of 103.4° and 105.6° are predicted for the ANC of 3 by the fixed joints simulation with NNC of 4, MSL of 0.7mm subjected to uniaxial loading with the dead zone threshold of 250 $\mu\varepsilon$ and 1000 $\mu\varepsilon$ respectively. This angle reduces to 101.4° for equivalent simulations using MSL of 1.0mm and 98.3°and 99.9° for equivalent simulations using the MSL of 1.5mm. The prevalence of nodes with ANC of 3 in triaxial loading simulations and all simulations with pinned joints is negligible and thus no conclusions on ITAs can be drawn.

The predicted mean ITA for all simulations using fixed joints which predict ANC of 4 and 5 are close to a 100° although as low as 90° in NNC 14 simulations using a dead zone threshold of 1000 $\mu\varepsilon$. The significant prevalence of nodes with ANC of 4 and 5 nodes in simulations with pinned joints occurs only in the ones subjected to uniaxial loading and with NNC of 6. These node have a mean ITA of approximately 95°. The ITA of all nodes with ANC of 6 and above tend towards 90°. This is further explained in the discussion section.

The predicted ITAs are lower in simulations with the higher MSL. In order to obtain a specific NNC, which is the smallest NC, the mean NC in these models is larger. For instance the models with NNC of 4 have an initial mean NC of 4.794 and 4.816 to three significant figures for simulations with MSL of 0.7mm and 1.5mm respectively. This results in mean NC of 4.015 and 4.071 after uniaxial and 4.766 and 4.798 after triaxial loading simulations. These differences increase in higher NNC simulations. As the NC increases a larger number of struts occupy the same volume and the angle between them reduces. This is disused further in Section 5.4.

	NNC	ANC	MSL = 0.7 mm					MSL = 1.0 mm					MSL = 1.5 mm				
			Mean	Median	SD	Min	Max	Mean	Median	SD	Min	Max	Mean	Median	SD	Min	Max
Uniaxial loading	4	3	103.6	99.6	34.3	36.1	178.4	101.4	97.4	34.7	31.2	177.8	98.3	94.4	33.9	34.1	177.5
		4	99.0	95.4	33.0	24.6	179.6	97.5	93.8	32.9	29.3	178.8	96.7	92.9	33.1	16.7	179.2
		5	99.8	96.3	32.6	27.9	179.1	99.4	95.8	33.0	34.4	177.8	98.2	94.5	33.3	32.2	178.8
		6	99.4	95.9	32.8	34.2	179.2	99.6	96.0	33.2	30.6	177.6	98.4	94.7	33.5	31.6	179.1
	4*	2	123.0	119.6	35.6	36.2	178.7						99.9	95.1	38.2	32.4	174.8
		3	105.6	102.1	33.5	29.6	179.6						101.0	97.3	33.8	34.1	179.0
		4	100.8	97.3	32.6	31.5	179.1						98.7	95.0	33.4	16.7	179.2
		5	100.6	97.2	32.2	32.8	179.1						100.1	96.6	32.7	32.5	179.1
	10	7	93.9	89.1	36.9	0.3	179.4	92.3	87.4	37.2	6.6	179.1	89.6	84.3	38.1	2.0	179.2
		8	93.6	88.8	36.9	2.4	179.4	92.5	87.6	37.2	1.0	179.5	89.5	84.4	37.6	7.0	179.4
		9	93.8	89.0	36.9	2.3	179.5	92.7	87.8	37.2	1.0	179.1	89.8	84.6	37.6	1.2	179.1
		10	94.1	89.3	37.0	2.0	179.5	93.0	88.1	37.2	5.5	178.9	92.5	87.4	37.9	2.4	178.8
	14	9	92.3	86.9	39.2	1.8	179.8	90.5	84.8	39.5	0.9	179.2	87.3	81.2	40.0	2.6	179.1
		10	92.0	86.6	39.0	0.2	179.6	90.3	84.6	39.4	0.1	179.5	88.2	82.3	39.8	1.5	179.1
		11	92.3	86.8	38.9	0.3	179.9	91.1	85.5	39.2	0.2	179.8	88.3	82.5	39.7	1.3	179.0
		12	92.5	87.1	38.9	0.2	179.8	91.3	85.8	39.1	0.3	179.3	90.3	84.6	39.6	2.6	179.4
	14*	2	123.8	112.6	65.3	3.3	178.7										
		3	103.5	95.3	50.7	3.2	179.8						92.8	84.8	47.5	7.4	177.2
		4	101.4	94.1	47.6	2.3	179.9						90.4	83.0	45.2	2.9	178.8
		5	98.9	91.9	45.9	2.3	179.8						90.6	83.3	44.9	2.1	179.1
		6											89.9	83.1	43.2	3.2	178.8
Triaxial loading	4	4	97.1	93.4	33.0	24.6	179.6	95.4	91.6	32.9	26.3	178.4	92.4	88.6	32.6	16.8	179.2
		5	99.3	95.8	32.6	27.9	179.1	98.4	94.8	32.9	31.0	179.9	96.9	93.1	33.2	16.7	178.8
		6	99.1	95.5	32.8	27.9	179.0	99.3	95.7	33.1	20.4	177.6	98.7	95.0	33.3	31.6	177.5
		7	98.9	95.3	32.7	34.5	179.1	98.6	94.9	33.1	36.5	176.7	98.7	94.9	33.6	38.3	179.1
	4*	3	104.0	100.3	34.1	35.7	177.8						98.4	94.6	33.7	42.0	174.8
		4	99.7	96.1	32.8	24.6	179.6						94.5	90.8	32.6	16.8	179.2
		5	100.5	97.1	32.4	29.6	179.1						98.6	94.9	33.0	16.7	179.1
		6	99.9	96.5	32.3	33.4	178.8						98.9	95.2	33.1	31.6	177.1
	10	10	91.4	86.6	36.6	0.9	179.7	88.7	83.6	36.9	0.1	179.9	84.5	79.2	36.8	0.9	179.1
		11	93.9	89.1	36.8	1.7	179.7	92.9	88.0	37.1	2.2	179.8	90.7	85.5	37.6	1.2	179.0
		12	94.4	89.6	37.0	2.0	179.9	93.9	89.0	37.4	1.2	179.3	92.7	87.6	37.8	2.4	179.4
		13	94.6	89.7	37.3	3.0	179.6	94.2	89.3	37.5	1.0	179.3					
	14	14	90.2	84.9	38.3	0.1	179.9	87.9	82.3	38.6	0.1	179.8	82.8	76.9	38.5	1.5	179.2
		15	92.2	86.9	38.5	0.2	179.8	91.2	85.8	38.8	0.1	179.9	88.8	83.1	39.2	1.4	179.4
		16	93.2	87.9	38.6	0.2	179.6	92.5	87.1	38.9	0.3	179.8	91.1	85.5	39.4	1.2	179.2
		17	93.3	88.0	38.8	0.3	179.9	92.9	87.5	39.0	2.1	179.8	92.4	86.9	39.5	1.3	179.4
	14*	6	98.4	93.2	39.2	1.9	179.8										
		7	96.9	91.9	38.3	1.6	179.8										
		8	96.2	91.2	38.0	0.3	179.6						90.9	85.2	39.6	2.8	179.1
		9	95.9	91.0	37.9	1.8	179.9						90.8	85.3	39.1	1.5	179.2
		10											91.2	85.6	39.2	1.3	179.0
		11											92.5	87.0	39.2	1.4	178.9

Table 5.6: The ITA mean, median, standard deviation (SD), minimum (min) and maximum (max) values for representative fixed joints simulations. ITAs for four most prevalent ANCs are presented. Dead zone of 250$\mu\varepsilon$ has been used except for simulations with * next to the NNC value which indicate that the dead zone of 1000$\mu\varepsilon$ has been used. Full results are available in the Appendix Figures A.2 and A.3.Key results are highlighted in yellow.

			MSL = 0.7 mm					MSL = 1.0 mm					MSL = 1.5 mm				
	NNC	ANC	Mean	Median	SD	Min	Max	Mean	Median	SD	Min	Max	Mean	Median	SD	Min	Max
Uniaxial loading	6	5	95.9	91.9	34.3	11.2	179.6	93.3	89.2	34.2	19.1	178.0	90.1	85.8	34.2	16.8	177.4
		6	95.8	91.8	34.2	10.8	179.7	94.6	90.5	34.4	8.1	179.9	92.4	88.1	34.7	14.8	179.2
		7	97.0	93.0	34.3	9.1	179.5	96.6	92.5	34.8	16.7	179.1	95.4	91.1	35.2	13.6	177.5
		8	97.0	92.9	34.6	20.4	179.5	96.7	92.5	35.0	21.6	179.2	96.4	92.1	35.3	19.0	178.3
	6*	4	96.1	92.0	34.5	21.2	178.5						88.5	84.0	34.6	17.7	177.5
		5	96.7	92.7	34.4	9.1	178.8						92.3	87.9	35.2	23.3	178.8
		6	96.9	92.9	34.2	17.9	179.6						93.5	89.3	34.5	14.8	179.0
		7	97.4	93.4	34.4	23.7	179.5						96.7	92.4	35.2	15.8	179.1
	10	7	93.4	88.6	37.0	2.2	179.3	91.0	86.0	37.2	11.8	179.1	87.3	82.0	37.6	5.4	178.3
		8	93.3	88.5	36.9	1.7	179.5	91.6	86.7	37.1	1.0	179.8	88.3	83.2	37.2	1.2	179.1
		9	93.6	88.8	36.8	2.0	179.7	92.5	87.6	37.0	2.2	179.3	90.3	85.2	37.5	2.0	179.4
		10	94.1	89.3	36.9	3.5	179.9	93.1	88.2	37.1	1.0	179.2	91.9	86.7	37.9	1.3	179.1
	14	9	91.9	86.4	39.0	1.6	179.7										
		10	92.0	86.6	38.7	0.4	179.6	90.4	84.9	39.2	0.1	179.3	87.4	81.5	39.4	2.5	178.8
		11	92.2	86.8	38.7	0.2	179.9	90.3	84.7	39.1	0.5	179.5	88.1	82.3	39.4	1.6	179.1
		12	92.5	87.1	38.8	0.2	179.8	91.3	85.8	39.0	0.3	179.4	89.7	84.0	39.4	2.1	179.4
		13						91.9	86.4	39.0	0.5	179.7	90.5	84.9	39.5	1.3	179.0
	14*	4	93.9	87.6	42.5	4.0	179.6						91.3	84.1	44.7	2.9	178.8
		5	95.6	89.5	42.1	0.2	179.9						90.9	84.3	42.9	3.1	179.0
		6	95.1	89.2	41.2	2.1	179.5						90.1	83.5	42.7	6.2	178.8
		7	94.8	88.9	40.9	2.7	179.8						87.0	80.6	41.2	2.0	178.1
Triaxial loading	6	6	94.3	90.2	34.2	7.2	179.2	92.2	88.0	34.3	5.0	179.9	88.5	84.1	34.3	12.3	179.0
		7	96.7	92.6	34.3	9.7	179.7	95.9	91.8	34.7	4.2	179.1	94.6	90.3	35.1	13.6	179.2
		8	97.0	92.9	34.6	9.1	179.5	96.6	92.4	35.0	8.1	179.2	95.8	91.5	35.5	9.9	178.8
		9	96.7	92.6	35.0	23.6	179.2	96.7	92.4	35.3	21.6	178.2	96.4	92.1	35.4	13.3	179.1
	6*	5	92.6	88.3	34.9	11.2	178.9										
		6	94.9	90.9	34.1	10.8	179.6						89.8	85.4	34.3	16.3	179.0
		7	97.0	93.0	34.3	14.5	179.7						95.0	90.7	35.0	14.8	179.2
		8	97.1	93.1	34.6	9.1	179.5						96.1	91.8	35.4	13.2	178.8
		9											96.6	92.3	35.2	16.9	179.1
	10	10	91.3	86.4	36.6	0.7	179.7	88.7	83.7	36.8	0.1	179.9	84.6	79.4	36.9	0.9	179.1
		11	93.8	89.1	36.8	0.9	179.7	92.9	88.0	37.1	2.2	179.8	90.5	85.3	37.6	1.2	179.0
		12	94.4	89.6	37.0	2.0	179.9	93.9	89.0	37.4	1.2	179.7	92.7	87.6	37.9	1.3	179.4
		13	94.5	89.7	37.3	3.0	179.6	94.2	89.3	37.5	1.0	179.3	93.7	88.6	38.2	5.0	179.1
	14	14	90.3	84.9	38.3	0.1	179.9	87.9	82.3	38.6	0.1	179.8	82.7	76.8	38.4	1.5	179.2
		15	92.2	86.9	38.5	0.2	179.8	91.2	85.7	38.8	0.1	179.9	88.7	83.0	39.1	1.4	179.4
		16	93.2	87.9	38.6	0.2	179.6	92.5	87.1	38.9	0.3	179.8	91.3	85.7	39.4	1.2	179.2
		17	93.3	88.0	38.8	0.3	179.9	92.9	87.5	39.0	2.1	179.8	92.4	86.8	39.5	1.3	179.4
	14*	6	96.5	91.2	39.3	1.7	179.8										
		7	96.1	91.0	38.7	0.3	179.8										
		8	95.8	90.7	38.4	1.7	179.9										
		9	95.7	90.7	38.0	2.3	179.4										
		10											87.9	82.0	39.7	1.5	179.2
		11											90.3	84.6	39.3	1.4	179.0
		12											90.9	85.3	39.3	1.3	179.1
		13											92.2	86.7	39.3	1.6	178.8

Table 5.7: The ITA mean, median, standard deviation (SD), minimum (min) and maximum (max) values for representative pinned joint simulations. ITAs for four most prevalent ANCs are presented. Dead zone of 250$\mu\varepsilon$ has been used except for simulations with * next to the NNC value which indicate that the dead zone of 1000$\mu\varepsilon$ has been used. Full results are available in the Appendix Figures A.4 and A.5. Key results are highlighted in yellow.

Table 5.8 presents the prevalence of nodes with ANC of 3, 4, 5 and 6; the nodal connectives reported by the Reznikov et al. (2016) study. Figures 5.11 and 5.12 present the ITA distributions for nodes with a greater than 5% prevalence of such nodes. Therefore, distributions for nodes with ANC 3, 4, and 5 are presented for the following fixed joint simulations with 0.7mm MSL: uniaxially loaded NN04 with 250$\mu\varepsilon$ and 1000$\mu\varepsilon$ dead zone thresholds, triaxially loaded NN04 with 1000$\mu\varepsilon$ dead zone threshold and the uniaxially loaded NN14 with a 1000$\mu\varepsilon$ dead zone threshold. Among pinned joint models, only uniaxially loaded NN14 simulation with 1000$\mu\varepsilon$ dead zone threshold had a significant abundance of nodes with ANC under consideration.

Load	NNC	MSL = 0.7 mm				MSL = 1.0 mm				MSL = 1.5 mm			
		Fixed joint simulations											
		3	4	5	6	3	4	5	6	3	4	5	6
Uniaxial	4	17.8%	42.2%	22.2%	7.0%	18.8%	39.7%	21.7%	8.0%	15.3%	43.1%	21.9%	8.5%
	4*	32.6%	34.2%	11.4%	2.4%					29.2%	36.4%	14.6%	3.7%
	6	4.0%	11.0%	24.8%	32.5%	5.1%	12.1%	24.8%	30.2%	6.3%	10.9%	25.6%	29.5%
	8	3.5%	4.6%	9.5%	18.0%	4.1%	5.7%	9.9%	18.1%	2.3%	4.3%	6.8%	9.6%
	10	2.8%	3.3%	4.7%	9.5%	2.4%	3.8%	5.4%	9.0%	16.3%	19.0%	17.3%	12.0%
	12	2.2%	2.8%	3.3%	5.4%	1.1%	2.9%	3.7%	4.9%	1.0%	2.5%	4.6%	7.0%
	14	1.5%	2.2%	3.0%	4.2%	0.6%	1.3%	2.9%	4.4%	0.3%	0.9%	3.1%	3.8%
	14*	24.9%	26.4%	17.5%	8.3%					10.2%	16.6%	17.6%	15.1%
Triaxial	4	1.0%	46.1%	33.6%	14.0%	0.7%	46.2%	32.7%	15.4%	0.5%	46.7%	30.6%	16.9%
	4*	11.0%	44.8%	29.5%	10.2%					9.3%	45.4%	27.6%	13.2%
	6	0.0%	0.0%	0.9%	43.4%	0.0%	0.0%	1.0%	42.5%	0.0%	0.0%	1.1%	41.0%
	8-12	0.0%				0.0%				0.0%			
	14	0.0%				0.0%				0.0%			
	14*	3.8%	7.0%	11.6%	15.8%					0.1%	1.0%	1.8%	4.4%
		Pinned joint simulations											
Uniaxial	6	2.0%	4.4%	16.6%	37.3%	3.1%	4.5%	14.3%	36.1%	15.3%	34.6%	21.4%	12.2%
	6*	3.5%	15.7%	29.4%	28.3%					4.4%	10.9%	23.9%	31.5%
	8	2.6%	2.7%	5.2%	13.8%	3.3%	3.6%	4.7%	11.5%	2.9%	4.1%	8.9%	14.5%
	10	2.4%	2.5%	3.1%	5.6%	1.7%	3.0%	3.1%	5.5%	0.9%	3.3%	3.9%	8.0%
	12	1.8%	2.2%	2.1%	3.0%	0.8%	2.1%	3.0%	3.5%	0.4%	1.5%	3.4%	4.4%
	14	1.4%	1.9%	2.3%	2.7%	0.3%	0.9%	2.1%	3.0%	0.0%	0.6%	1.9%	3.4%
	14*	5.9%	14.7%	20.3%	21.1%					6.9%	14.8%	14.5%	10.0%
Triaxial	6	<1%			43.6%	<1%			42.2%	<1%			40.8%
	6*	0.2%	0.5%	5.1%	42.8%					0.0%	0.3%	3.7%	41.6%
	8-12	0.0%				0.0%				0.0%			
	14	0.0%				0.0%				0.0%			
	14*	2.5%	4.7%	9.0%	12.1%					0.0%	0.2%	0.5%	0.9%

Table 5.8: The prevalence of Nodes with ANC 3, 4, 5 and 6 for simulations with different NNC, MSL and loading. Dead zone of 250$\mu\varepsilon$ has been used except for simulations with * next to the NNC value which indicate that the dead zone of 1000$\mu\varepsilon$ has been used. Key results have been highlighted in yellow.

Values predicted by simulations using models with MSL of 0.7mm are closer to those

reported by Reznikov et al. (2016). The predicted ITA distributions for ANC3 nodes in both MSL 0.7mm and 1.5mm simulations is disjointed with notable fluctuations in relative frequency between adjacent bins. This is most likely caused by the smaller number of ANC3 nodes compared to ANC4 and ANC5 nodes. The mean predicted ITA of 105.6° for this ANC in the uniaxially loaded NN04 simulation with dead zone threshold of 1000$\mu\varepsilon$ using fixed joint models is the closest to 116.3° reported by Reznikov et al. (2016) . This is followed by values of 103.6° and 104.0° in uniaxially loaded NN04 simulation with dead zone threshold of 250$\mu\varepsilon$ and triaxially loaded NN04 simulation with dead zone threshold of 1000$\mu\varepsilon$. The only pinned jointed simulation presented in Figure 5.11 predicts the ITA of 82° for ANC3 nodes and is the furthest from the imaging study reported (Reznikov et al. (2016) and the ideal ITA values. This is further explained in the discussion section.

Both high NNC simulations exhibit double peak distributions for all ANCs below 6; at approximately 60° and 150°. The dip between peeks occurs at just above 90.0°. Both of these simulations have a dead zone threshold set at 1000$\mu\varepsilon$ and are loaded uniaxially. Therefore, it is not surprising that struts at right angles to the loaded direction experience a strain below the threshold, become inactive and that there are a small number of 90.0° ITAs.

The predicted ITAs for three NN04 simulations presented are between 99.0° and 101° for both ANC4 and ANC5 nodes. These values are close to the values of 107.6° and 103.1° reported by Reznikov et al. (2016). For nodes with ANC of 6 and above the ITA distributions for all simulations with substantial presence of such nodes become very similar and the mean ITA tends to 90°.

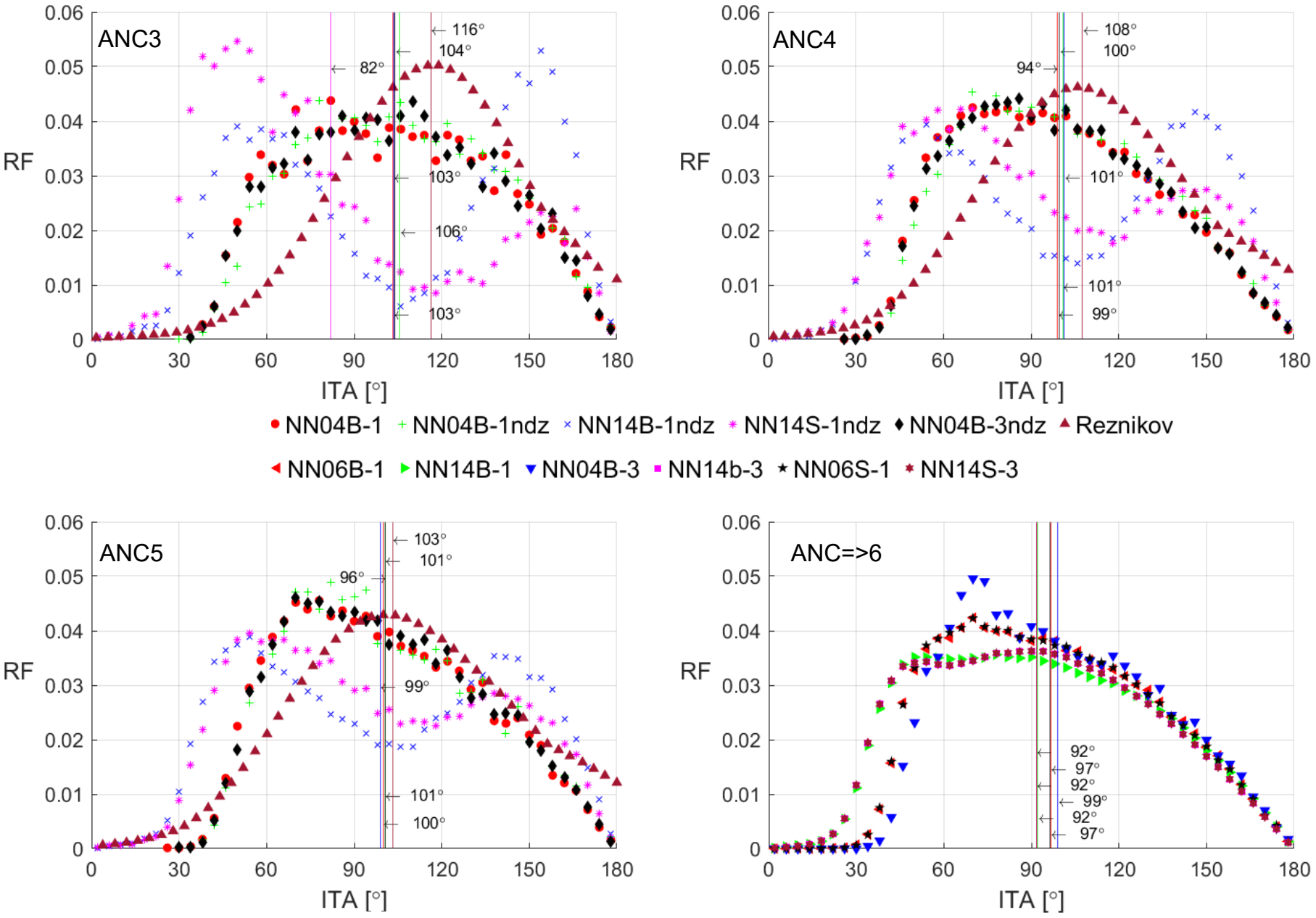


Figure 5.11: Relative frequency (RF) of ITA grouped in 4° bins for nodes with ANC of 3, 4, 5 and 6 and over. Combined results from five different models with MSL of 0.7 mm, different NC as shown in the legend and where B signifies fixed joint and S pinned joint simulations. The number following the fixity description defines uniaxial (1) or triaxial (3) loading scenarios. Simulations with dead zone set at the lower limit of the lazy zone are followed by letters NDZ.

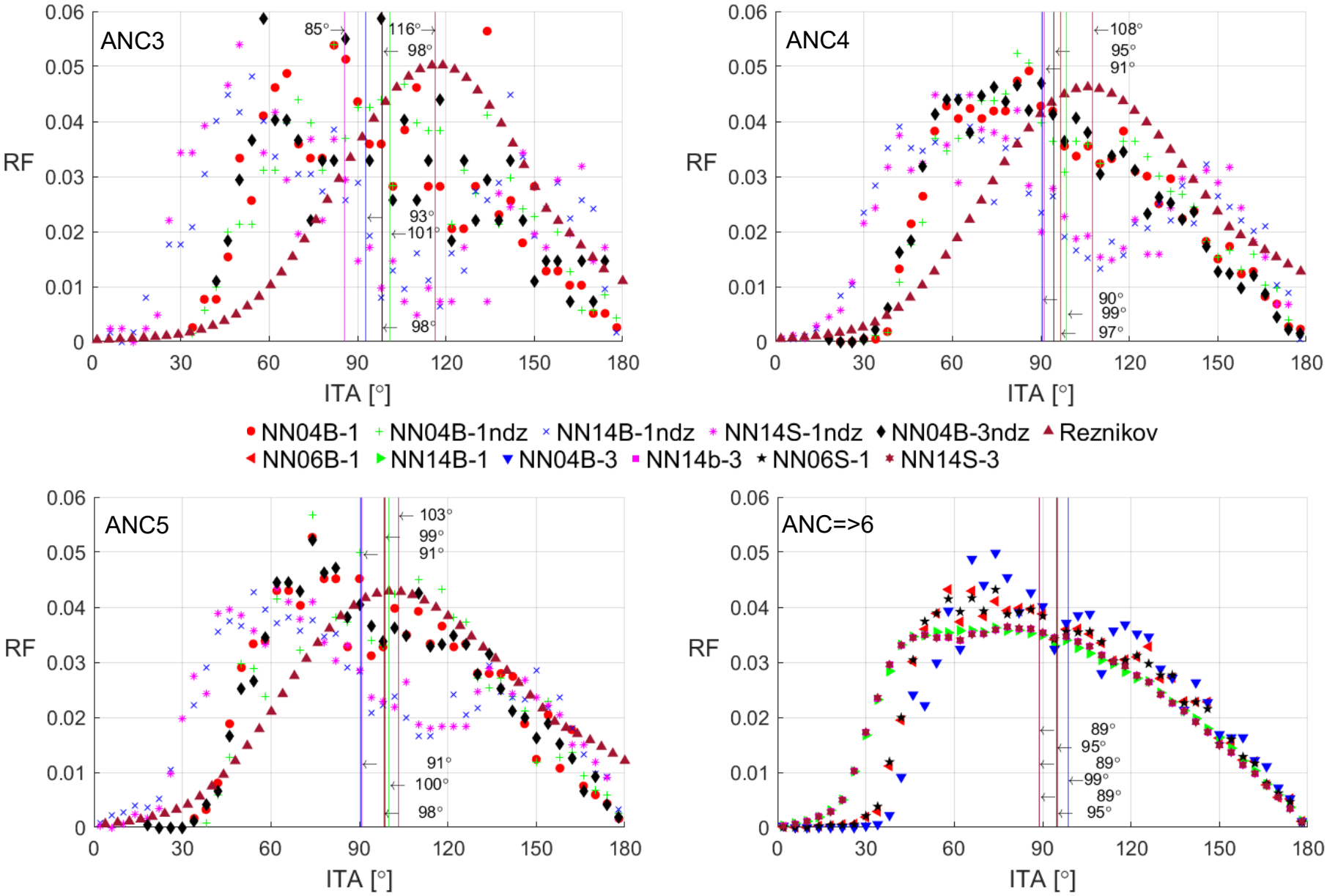


Figure 5.12: Relative frequency (RF) of ITA grouped in 4° bins for nodes with ANC of 3, 4, 5 and 6 and over. Combined results from five different models with MSL of 1.5 mm, different NC as shown in the legend and where B signifies fixed joint and S pinned joint simulations. The number following the fixity description defines uniaxial (1) or triaxial (3) loading scenarios. Simulations with dead zone set at the lower limit of the lazy zone are followed by letters ndz.

5.3.3 Trabecular thickness

In the context of the simulations used in the thesis the trabecular thickness is represented by the beam element diameter. In the introduction section it is reasoned that the mean element diameter value of 116μm (radius of 58μm) is the appropriate value for comparison of simulation trabecular thickness predictions to real bone.

Table 5.9 presents the mean, median, standard deviation and the 95 % confidence intervals for active strut radii for NN simulations presented in this thesis. The minimum and maximum values are also included. This enables comparisons of strut radii between different simulations to be made. For instance, mean radius for fixed joint NN4 simulations with 0.7mm MSL subjected to uniaxial loading is 107.7μm (95% CI [102.8, 112.9]). The median value is 90.9 μm and the range is from 25 μm to 470.3 μm. This indicates that this distribution is right skewed as are radii distributions for all NN simulations. Right skewed distributions are evident on the diagrams in Figures 5.13, 5.14 and 5.15 which present histograms and the distribution curves for NN04, NN06 and NN14 simulations respectively. Figure 5.13 also includes the simulation predictions with the dead zone threshold of 1000 $\mu\varepsilon$ whilst these diagrams for other simulations are presented in the Appendix Figures A.6, A.7 and A.7.

In general, the predicted mean strut radii are smaller in the higher NNC simulations and increase with the increasing MSL and number of load cases. Pinned jointed models predict smaller mean radii than the fixed jointed simulations. In fixed joint models uniaxially loaded NN08 and triaxially loaded NN10 simulations with 0.7 MSL predicted trabecular thickness closest to that of real bone. The predicted mean radius in all of the pinned joint simulations is comparable to the thickness of real bone. However, in high NNC simulations, as can be seen on diagrams for NN14 simulations in Figure 5.15 the radii distributions are heavily skewed and the frequency of the smallest elements is very high. Such distributions do not compare well with real bone as can be established by comparing to Figure 5.1.

	NNC	MSL = 0.7 mm							MSL = 1.0 mm							MSL = 1.5 mm						
		Mean	95\% CI		Median	SD	Min	Max	Mean	95\% CI		Median	SD	Min	Max	Mean	95\% CI		Median	SD	Min	Max
			Min	Max						Min	Max						Min	Max				
	Fixed joint simulations																					
Uniaxial Loading	4	107.7	102.8	112.9	90.8	75.3	25.0	470.3	152.6	141.2	165.0	125.0	114.8	25.0	639.2	212.1	185.8	242.2	170.1	167.4	25.0	850.3
	4*	131.4	124.5	138.6	121.2	63.8	28.8	469.3								248.9	215.3	287.7	223.9	137.9	28.8	854.1
	6	67.4	65.1	69.7	57.3	45.8	25.0	397.3	89.3	84.3	94.6	72.2	69.1	25.0	558.6	126.7	114.9	139.7	99.0	105.2	25.0	739.0
	8	50.3	48.9	51.7	44.1	31.0	25.0	393.5	65.5	62.5	68.6	54.9	46.3	25.0	443.4	87.9	81.2	95.2	70.4	69.6	25.0	520.2
	10	41.2	40.3	42.3	37.3	22.3	25.0	351.3	52.6	50.5	54.7	45.4	34.0	25.0	378.1	67.7	63.3	72.4	55.8	50.0	25.0	474.1
	12	36.3	35.5	37.0	33.6	17.1	25.0	343.6	44.6	43.1	46.2	39.6	26.3	25.0	359.0	57.1	53.9	60.6	48.3	39.5	25.0	481.8
	14	33.1	32.5	33.7	31.3	13.5	25.0	335.9	39.8	38.6	41.0	36.1	21.1	25.0	359.0	49.4	46.9	52.0	42.8	31.8	25.0	366.6
	14*	64.4	62.4	66.5	61.6	23.3	25.0	229.4								72.9	68.1	78.1	64.4	43.5	25.0	362.8
Triaxial Loading	4	138.8	136.1	141.6	127.4	69.5	25.0	428.1	192.3	186.1	198.8	174.8	101.6	25.0	554.7	267.1	252.4	282.6	236.9	157.3	25.0	742.8
	4*	148.2	145.1	151.3	141.5	54.7	28.8	454.9								284.2	268.0	301.4	267.6	119.6	28.8	742.8
	6	91.1	89.7	92.5	82.8	48.0	25.0	385.8	122.4	119.4	125.5	108.5	72.3	25.0	454.9	169.2	162.2	176.5	147.3	106.8	25.0	604.6
	8	66.9	66.1	67.7	61.2	34.2	25.0	389.7	88.3	86.5	90.0	78.0	52.9	25.0	458.8	119.2	115.2	123.3	101.6	80.6	25.0	550.9
	10	53.2	52.6	53.7	49.3	25.0	25.0	332.1	69.5	68.4	70.7	61.9	40.2	25.0	355.1	93.0	90.4	95.6	79.8	61.6	25.0	481.8
	12	45.0	44.7	45.4	42.7	17.8	25.0	232.3	58.1	57.2	58.9	52.6	31.3	25.0	339.8	75.8	74.0	77.7	65.2	49.9	25.0	497.1
	14	39.6	39.3	39.9	38.4	11.7	25.0	97.9	50.5	49.9	51.2	46.7	24.4	25.0	286.0	65.0	63.7	66.4	56.7	40.7	25.0	443.4
	14*	59.9	59.2	60.6	56.6	24.4	25.0	374.3								91.2	88.8	93.7	85.0	41.5	28.8	504.8
	Pinned joint simulations																					
Uniaxial Loading	6	64.9	63.9	66.0	60.1	30.9	25.0	232.3	84.9	82.7	87.2	76.7	46.1	25.0	324.4	114.9	109.8	120.2	102.2	66.8	25.0	428.1
	6*	74.9	72.2	77.6	70.9	29.9	25.0	220.8								125.4	119.5	131.6	115.7	61.1	25.0	428.1
	8	44.6	44.0	45.2	41.6	20.1	25.0	220.8	57.5	56.2	58.8	52.2	30.6	25.0	251.5	76.3	73.5	79.3	66.6	47.9	25.0	274.5
	10	37.2	36.8	37.7	35.3	14.8	25.0	213.1	46.5	45.6	47.4	42.6	23.4	25.0	201.6	59.3	57.4	61.2	52.1	36.1	25.0	255.3
	12	33.3	32.9	33.6	32.0	11.5	25.0	151.7	40.2	39.6	40.9	37.4	18.7	25.0	201.6	51.1	49.7	52.6	45.4	29.9	25.0	247.6
	14	31.0	30.7	31.3	30.1	9.3	25.0	147.8	36.5	35.9	37.0	34.3	15.4	25.0	197.7	45.1	44.0	46.3	40.7	24.8	25.0	243.8
	14*	36.0	35.1	36.9	33.8	15.5	10.0	142.5								57.2	55.4	59.0	51.2	32.4	25.0	232.3
Triaxial Loading	6	86.2	84.9	87.5	82.7	30.5	25.0	243.8	115.8	112.9	118.7	110.3	43.7	25.0	324.4	157.0	150.5	163.8	149.1	61.5	25.0	416.5
	6*	87.6	86.2	88.9	84.5	28.6	25.0	243.8								159.1	152.4	166.0	152.4	56.7	28.8	416.5
	8	59.0	58.3	59.7	56.3	22.0	25.0	167.0	79.1	77.6	80.7	74.5	33.4	25.0	224.6	107.8	104.2	111.5	99.7	51.5	25.0	309.1
	10	48.1	47.6	48.6	46.1	16.8	25.0	170.9	63.7	62.7	64.8	59.8	27.7	25.0	193.9	85.2	82.8	87.6	77.5	44.8	25.0	270.7
	12	41.5	41.1	41.9	40.1	13.2	25.0	109.4	53.9	53.2	54.7	50.7	23.2	25.0	186.2	71.4	69.7	73.2	64.8	38.1	25.0	240.0
	14	37.0	36.8	37.3	36.2	10.0	25.0	82.6	47.4	46.8	48.0	44.8	19.4	25.0	163.2	61.9	60.6	63.2	56.2	32.8	25.0	228.4
	14*	53.2	52.6	53.8	50.9	19.1	25.0	305.2								76.1	74.2	78.0	72.6	28.4	28.8	243.8

Table 5.9: The mean, 95 % Confidence intervals (CI), median, standard deviation(SD), the minimum (min) and the maximum (max) of active strut radii [mm] for the NN simulations presented in this chapter. Statistical distributions are calculated from 5 randomly generated models of each nominal connectivity with mean strut length (MSL), lattice type and loading as shown. Dead zone of 250$\mu\varepsilon$ has been used except for simulations with * next to the NNC value which indicate that the dead zone of 1000$\mu\varepsilon$ has been used. Key results are highlighted in yellow.

The radii distribution on the left hand side diagrams in Figure 5.13 are skewed and the frequency of elements with the lowest radii is high. This is more prominent in the uniaxially loaded simulations. The radii distribution curves which exclude the elements with the smallest radius of 25μm more closely resemble distribution observed in real bone (Figure 5.1). The differences between the two curves is absent on the RHS diagrams and a cross check with Table 5.9 confirms that the minimum radius in these simulations with the dead zone threshold of 1000μm is 28.8μm. However, the NN04 simulations presented in Figure 5.13 predict the mean radii of between 108μm and 284μm and thus overestimate the real bone value of 58μm.

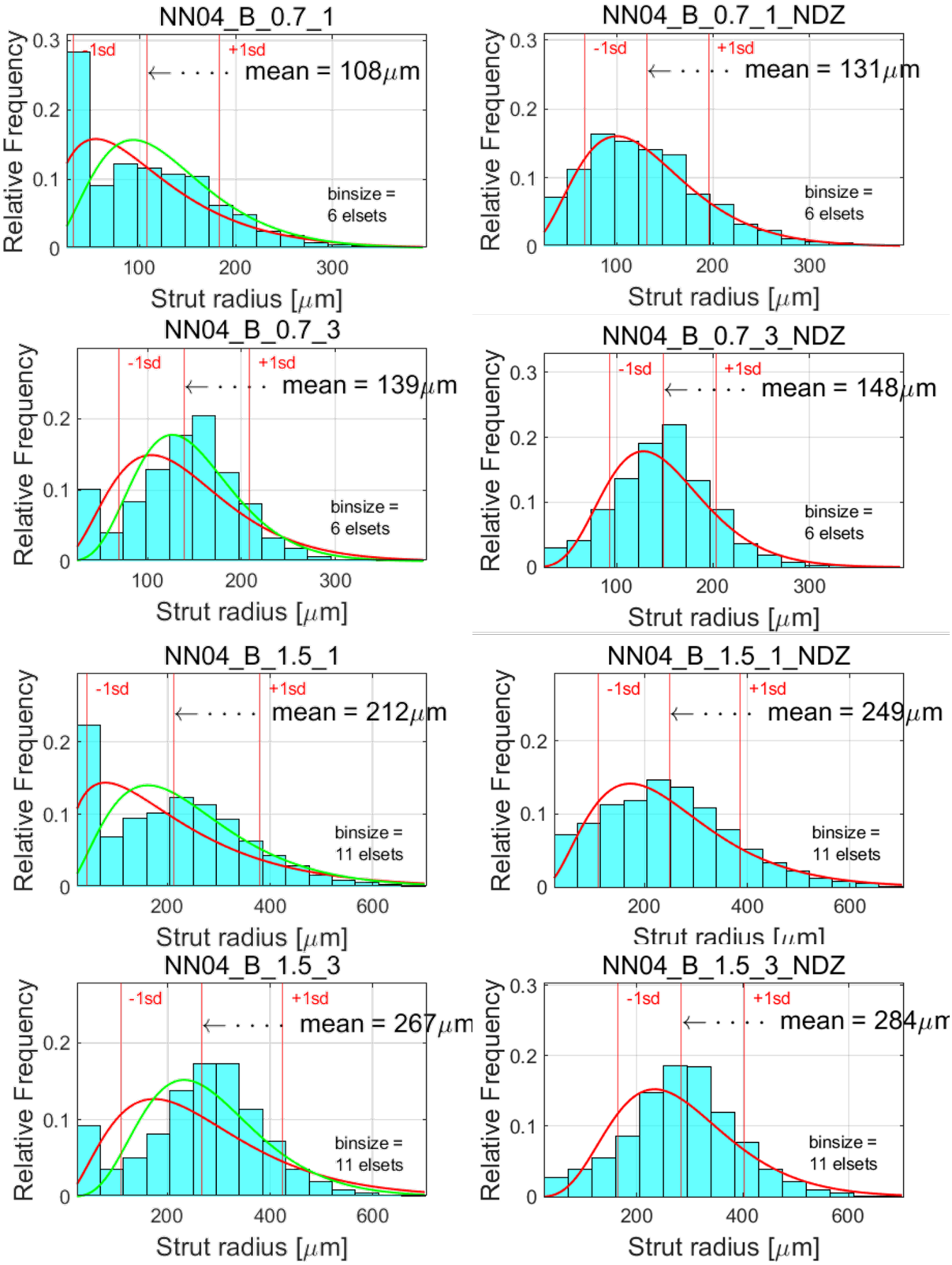


Figure 5.13: Comparison of strut radii distributions for NN04 adaptation simulations. Each diagram presents simulation data combined from 5 randomly generated models and the headings identify the MSL and the loading. Letters NDZ signify that a dead zone threshold pf 1000$\mu\varepsilon$ has been used. Each bar represents a number of strut radii element sets and the number of sets is annotated on diagrams. The histogram in light blue and the red distribution curve represent the full set of data. The distribution curve in green excludes the elements with the smallest radius of 25 μm.

It is evident from Figure 5.14 that for low NNC models with fixed and pinned joints predict significantly different radii distributions. Distributions for fixed joint simulations are more skewed and there is a greater abundance of elements with the smallest radius as is evident in difference between the red and green distributions curves. These are almost identical in pinned joint simulations, particularly for triaxialy loaded ones. They more closely resemble the distribution observed in real bone (Figure 5.1).

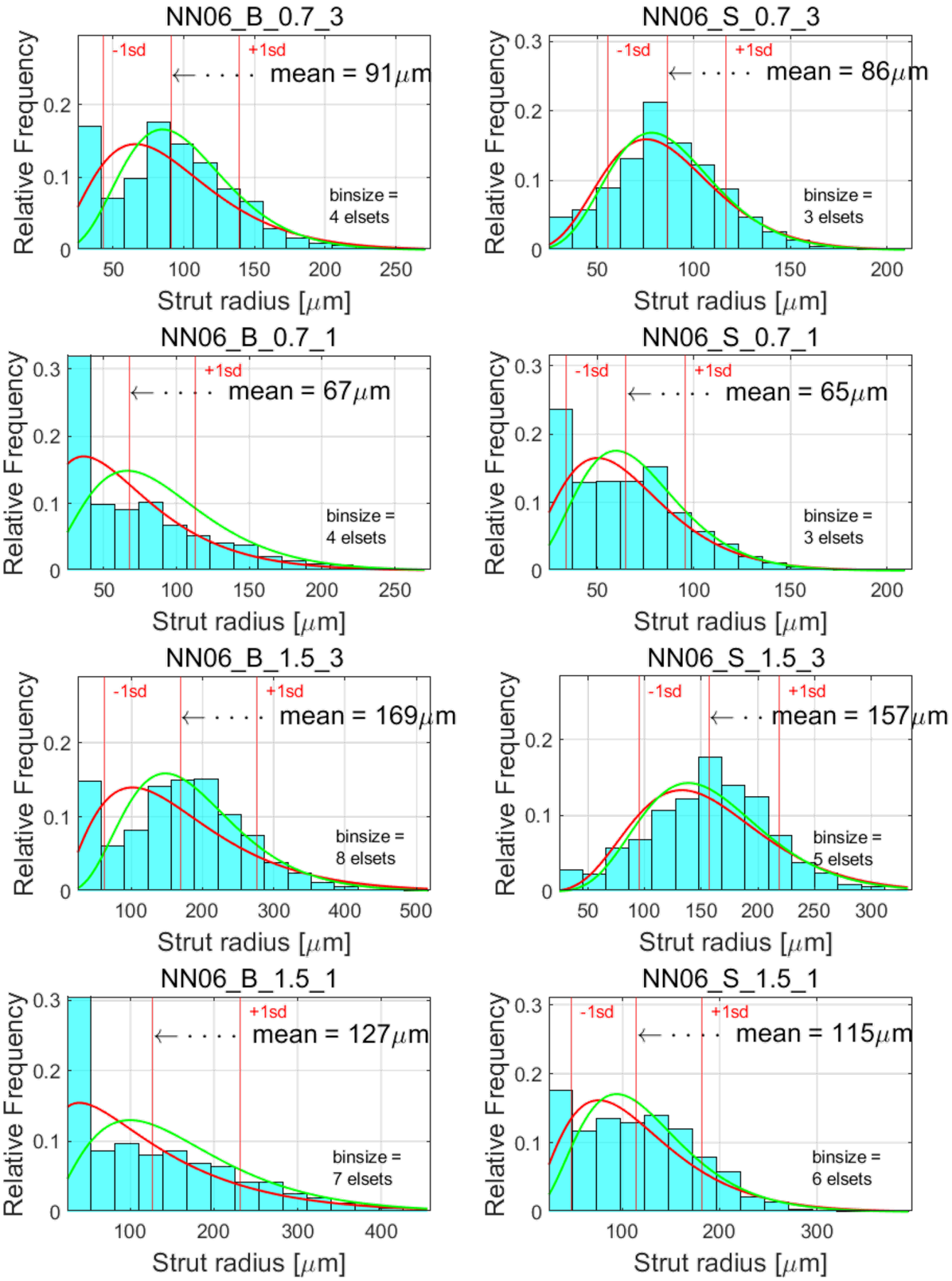


Figure 5.14: Comparison of strut radii distributions for NN06 adaptation simulations. Each diagram presents simulation data combined from 5 randomly generated models and the headings identify the MSL and the loading. Each bar represents a number of strut radii element sets and the number of sets is annotated on diagrams. The histogram in light blue and the red distribution curve represent the full set of data. The distribution curve in green excludes the elements with the smallest radius of 25 μm.

It is evident from Figure 5.15 that the predicted radii distributions for high NNC models with fixed and pinned joints do not differ very much. This further supports the conclusions drawn in Chapter 4, that the high NNC models behave as stretch dominated structures regardless of the joint fixity.

The NN14 simulations presented in Figure 5.15 predict the mean radii of between 31μm and 49μm and compare well with the real bone value of 58μm. The mean radius predictions further increase to a maximum of 64μm and 91μm in simulations with MSL of 0.7mm and 1.5mm with dead zone threshold of 1000 $\mu\varepsilon$.

All radii distributions are skewed and the frequency of elements with the lowest radii is high. There is a significant difference between curves which either include or exclude the smallest radii elements. The curves which exclude the 25μm radii elements more closely resemble distribution observed in real bone (Figure 5.1). In general, the increase in dead zone threshold reduces the radii distribution curves right skew and increases the mean radii. This is more pronounced in simulations with high NNC, uniaxial loading and stretch models.

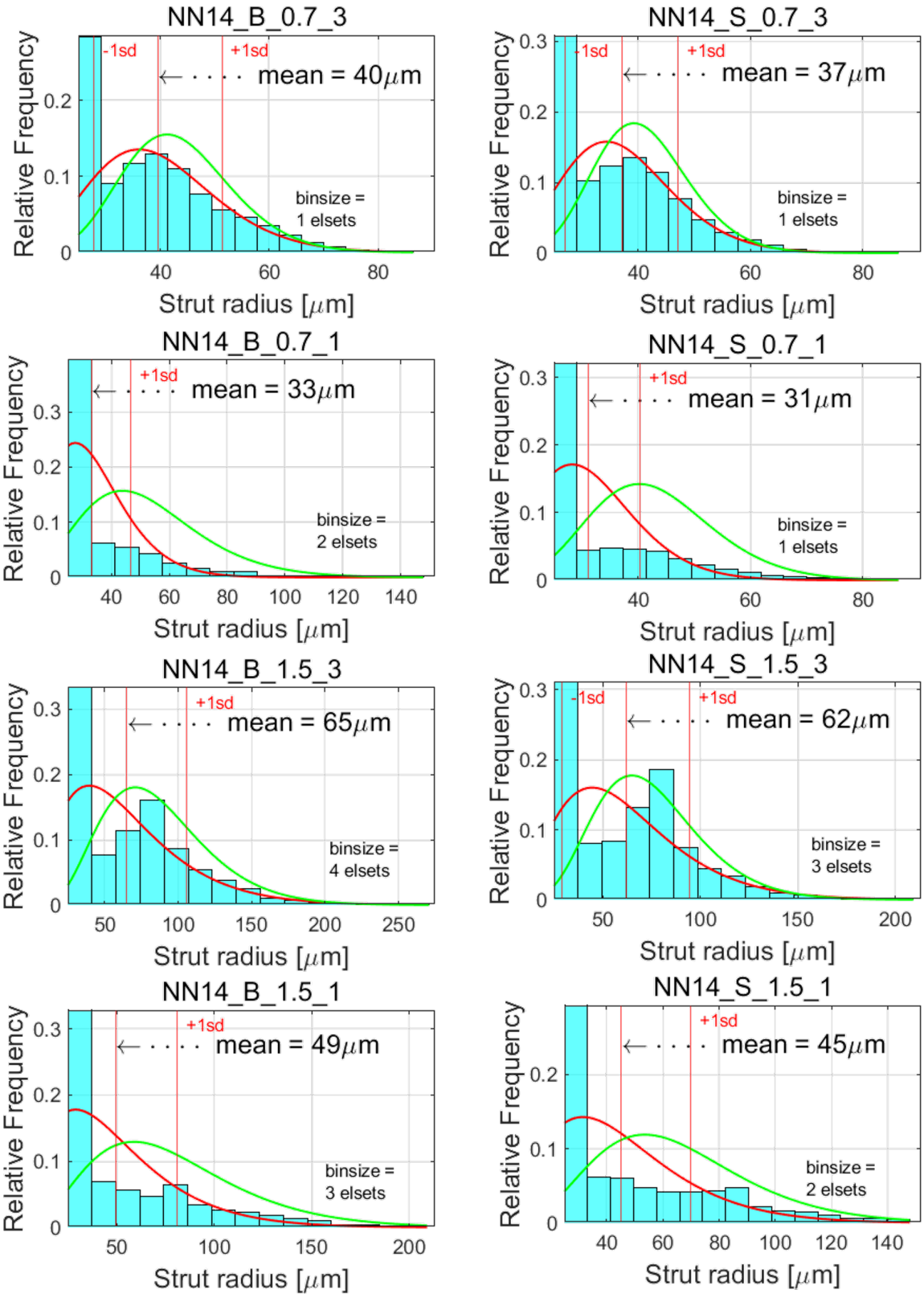


Figure 5.15: Comparison of strut radii distributions for NN14 adaptation simulations. Each diagram presents simulation data combined from 5 randomly generated models and the headings identify the MSL and the loading. Each bar represents a number of strut radii element sets and the number of sets is annotated on diagrams. The histogram in light blue and the red distribution curve represent the full set of data. The distribution curve in green excludes the elements with the smallest radius of 25 μm.

Tables 5.10 and 5.11 present the comparison of predicted trabecular volumes and Young's modulii between the simulations which use a dead zone threshold of 250 $\mu\epsilon$ and 1000 $\mu\epsilon$t. A difference of above 10% has been considered significant and such values have been shaded in Tables 5.10 and 5.11. The majority of them occur for high connectivity simulations and for models with MSL of 0.7mm.

			MSL=0.7mm						MSL=1.5mm					
			Dead Zone						Dead Zone					
			250με			1000με			250με			1000με		
			NNC 4	NNC 6	NNC1 4	NNC4	NNC6	NNC1 4	NNC 4	NNC 6	NNC1 4	NNC4	NNC6	NNC1 4
Triaxial Loading	Pinned	Mean		119.4	81.9		119.1	74.1		109.1	76.3		109	73.9
		% change					-0.3%	-9.5%					-0.1%	-3.1%
		95\% CI		118.6	81.9		118.2	73.9		105.6	75.9		105.5	73.4
				120.2	81.9		120	74.3		112.5	76.8		112.4	74.4
	Fixed	Mean	187.6		93.7	187.4		107	188.6		92.3	188.4		93.7
		% change				-0.1%		14.2%				-0.1%		1.5%
		95\% CI	186.1		93.6	185.8		106.4	183.7		90.7	183.6		92.1
			189.1		93.8	188.9		107.5	193.5		93.8	193.3		95.2
Uniaxial Loading	Pinned	Mean		63.7	40.4		66.7	30.5		57.6	32.1		58	30.5
		% change					4.7%	-24.5%					0.7%	-5.0%
		95\% CI		62.6	40.3		65.5	30.3		54.6	31.8		55.3	30.2
				64.8	40.5		67.9	30.7		60.6	32.4		60.8	30.8
	Fixed	Mean	99.3		49.8	98.8		56.8	104.8		40.9	104.6		42.1
		% change				-0.5%		14.1%				-0.2%		2.9%
		95\% CI	97.8		49.5	97.4		56.4	100.7		40.5	100.5		41.4
			100.7		50	100.2		57.3	108.8		41.2	108.6		42.8

Table 5.10: Comparison of the predicted five model mean trabecular volumes [mm^2] for simulations with dead zone thresholds of 250 $\mu\varepsilon$ and 1000$\mu\varepsilon$. Values are presented for high and low NNC simulations using MSL of 0.7 and 1.5mm subjected to either a triaxial or uniaxial loading scenario.

			MSL=0.7mm						MSL=1.5mm					
			Dead Zone						Dead Zone					
			250με			1000με			250με			1000με		
			NNC4	NNC6	NNC14	NNC4	NNC6	NNC14	NNC4	NNC6	NNC14	NNC 4	NNC 6	NNC14
Triaxial Loading	Stretch	Mean		369	614.1		367.4	600.8		419.4	624.9		418.1	622.5
		% change					-0.4%	-2.2%					-0.3%	-0.4%
		95\% CI		361.2	612		360.1	594.4		395.4	623		393.9	619.8
				376.7	616.2		374.6	607.1		443.4	626.8		442.2	625.2
	Bend	Mean	742		718.6	742.1		878.4	736.4		765.3	735.4		788
		% change				0.0%		22.2%				-0.1%		3.0%
		95\% CI	729.1		717.4	729.1		876.4	713.2		760.8	712.3		785.6
			754.9		719.8	755		880.4	759.5		769.9	758.6		790.4
Uniaxial Loading	Stretch	Mean		298.3	609.3		151.5	573.3		333.7	580		314.5	408
		% change					-49.2%	-5.9%					-5.8%	-29.7%
		95\% CI		294.5	589		140.9	553.3		313.8	576.8		301.1	397
				302.1	629.7		162.1	593.3		353.6	583.2		327.8	418.9
	Bend	Mean	656.7		838.7	655.5		933.4	650.2		775.1	651		809.3
		% change				-0.2%		11.3%				0.1%		4.4%
		95\% CI	647.6		831.6	647.1		931.2	631.4		772.1	632.6		793.3
			665.8		845.8	663.9		935.7	669.1		778.1	669.3		825.2

5.4 Discussion

All simulations with NNC of 8 and above result in the minimum ANC of 6 (Table 5.4) whereas only 1.5% of nodes in trabecular bone possess connectivity above 5 as reported by Reznikov et al. (2016) and summarised in Table 5.2. Prior to adaptation, all models apart from those of NNC 4 do not possess any nodes of connectivity under 5. The adaptation drives down NC, but in models of high NNC and particularly in those subjected to triaxial loading, this is marginal. In fact, no difference in mean NC before and after adaptation can be observed for simulations of NNC 6 and above subjected to triaxial loading. In the uniaxial simulations differences in NC prior and post adaptation can be observed in all NNC models, but are more evident in lower NNC models. Adaptation drives down the connectivity in bending models more than stretch models and in those with lower MSL. All simulations with NNC of 6 and above do not match the findings presented by Reznikov et al. (2016) and thus based on connectivity criteria alone cannot be considered good candidates for trabecular structural form.

NNC 4 models are the only ones that approach the NC reported by Reznikov et al. (2016). These adaptations result in mean ANCs of between 3.4 and 4.8 for simulations with 0.7mm MSL models. This compares well with approximate mean NC of 3.4 for real bone reported by their study. Simulations with 1.5mm MSL models result in higher ANCs of between 3.6 and 4.8.

Reznikov et al. (2016) (Table 5.2) report the proportion of nodes with NC of 3, 4 and 5 as 65%-75%, 19%-27% and 4%-7%. The prevalence of these nodes in NN04 models with MSL of 0.7mm subjected to uniaxial loading are 17.8%, 42.2% and 22.2% (Table 5.8) and thus compare favourably with values reported by this study. However, the simulation under-predicts the ANC3 node and over-predicts the ANC5 node prevalence. The equivalent triaxialy loaded simulation predicts 1.0%, 46.1% and 33.6% proportion of these nodes which compares less favourably with the study findings. A closer match is achieved by increasing the dead zone threshold to 1000 $\mu\varepsilon$. The prevalence of nodes with ANC of 3, 4 and 5 then becomes 32.6%, 34.2% and 11.4% in simulations subjected to uniaxial loading and 11%, 44.8% and 29.5% in simulations

subjected to triaxial loading.

The simulations presented in this thesis use two idealised loading environments whilst real bone is likely subjected to a loading between these two, with addition of shear loading. Subjecting the models to such loading would probably results in node proportions in between the uniaxial and triaxail values reported in this thesis. Nevertheless, it is hard to envisage the proportion of ANC3 nodes increasing to values reported by Reznikov et al. (2016). A possible reason for this discrepancy is that the trabecular bone consists of both rod and plate like structures (Gibson & Ashby (1997), Liu et al. (2008), Zhao et al. (2018)) but the analytical models used in this thesis only consider circular struts to represent rods. In addition, it is not clear how the imaging studies used for connectivity comparisons to real bone (Reznikov et al. (2014*b*),Reznikov et al. (2016)) treat plate like trabeculae. This lack of clarity makes the like for like comparison of nodes with NC 3, 4 and 5 proportions difficult. However, both the study and this thesis support the hypothesis that the proportion of such nodes is high in real bone and that the mean NC is approximately 4.

In addition, to being a metric in it's own right, connectivity has an influence on the ITA. The ITA results will be discussed in context of the values reported by the Reznikov et al. (2016) imaging study but the reasons why trabecular bone and indeed any lattice may be optimised towards a particular ITA will be considered. An optimal ITA value allows the struts meeting at a particular node to efficiently span the space on the way to connecting to the node at their opposite end. In order to aid the understanding of optimal ITAs it is useful to consider the valence-shell electron-pair repulsion (VSEPR) theory which explains the chemical bond angles between electrons and the nucleus (Gillespie (1963)). This is also often referred to as Thompson problem which seeks to find the positions of n particles which are constrained to lie on the surface of the unit sphere with unit electric charge such that the energy is minimal. The resulting points are then in equilibrium under the action of their mutual Coulomb repulsions and the only net forces acting on each particle being normal to the sphere on which they lie (Atiyah & Sutcliffe (2003)).

The solution to the Thompson problem can be found by a sphere packing task where the equilibrium position of electrons is established by considering a nucleus as one

sphere and the electron as spheres placed on the circumference of the sphere representing the nucleus. It transpires that the electron equilibrium locations are the vertices of a polyhedron, which is generically a deltahedron (Atiyah & Sutcliffe (2003). Bonds for atoms with different number of pairs of electrons and the corresponding polyhedron are illustrated in Figure 5.16. Intuitively bond angle for an atom with two electron pairs is 180° and for three pairs it is 120°. For three electron pairs the equilibrium locations are defined by vertices of a tetrahedron and the bond angle is 109.5°. For 5 and 6 electron pairs the vertices of a triagonal bipyramid and octahedron with angles of 120° and 90° as shown in the Figure 5.16 define the equilibrium locations.

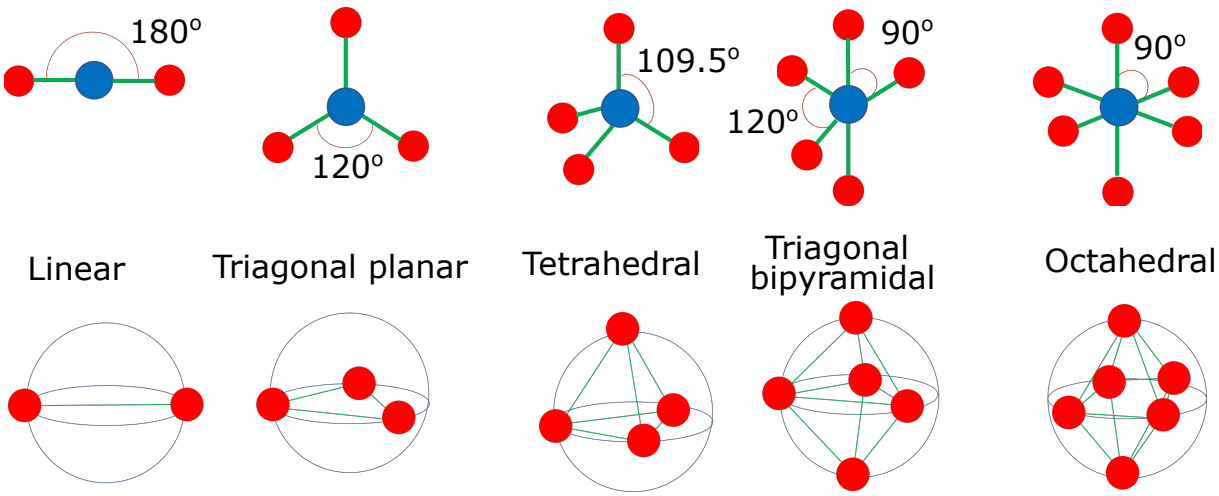


Figure 5.16: Ideal ITAs. The diagrams illustrate the bond angles between the nucleus in blue an electrons in red.

The bonds defined by electron equilibrium locations are equivalent to structural elements efficiently spanning a predetermined distance between a number of nodes. Therefore, it follows that for NC4 the mean optimum ITA is 109.5°. Following this through and calculating the angles between all possible pairs of bonds the optimum mean ITAs for NC5 and NC6 are both 108°. As the NC increases the mean ITA decreases but it becomes difficult to calculate analytically by hand. Matlab script was used to calculate vertex coordinates of an Icosahedron (12 vertices) and a Dodecahedron (20 vertices). Angles between vectors from centres of these polyhedra to each of their vertices were calculated enabling the optimum mean ITAs to be established as 98.2° and 94.7°. This suggests that as the NC increases the optimum mean ITA tends towards 90° which would not be unexpected for a continuum. As the NC increases a lattice begins to resemble a continuum and at some very high NC it would not be pos-

sible to distinguish its mechanical behaviour from that of a continuum. Therefore, it is not unexpected that an optimum mean ITA tends to 90° as the NC increases.

The imaging study by Reznikov et al. (2016) reported the mean ITAs of 116.3°, 107.6° and 103.1° for nodes with NC 3, 4 and 5 respectively. These are in good agreement with the optimal mean ITAs of 120°, 109.5° and 108°. The closest predictions to these values are derived form NN04 simulations with fixed joints. In particular the uniaxially loaded 0.7mm MSL models predict the mean ITAs of 103.6°, 99.0° and 98.8°for the nodes with the same NC. A closer agreement with ITAs of 105.6°, 100.8° and 100.6° is achieved for an equivalent simulation with the dead zone threshold increased to 1000$\mu\varepsilon$. In addition, the triaxially loaded NN04 models with dead zone threshold at 1000$\mu\varepsilon$ predict ITAs of 104.0°, 99.7° and 100.5° which are as close to theoretical optimum values and imaging study findings as any. The NN14 uniaxial simulation with dead zone threshold at 1000$\mu\varepsilon$ compares well with imaging studies in terms of the mean NC and the ITA predictions but the ITA distribution with a double peak (Figures 5.11 and 5.12) makes them unrealistic. Therefore based on the ITA criteria alone NN04 simulations with fixed joints are considered good candidates for trabecular structural form.

The NN04 simulations with MSL of 1.0mm and 1.5mm predict marginally lower ITA values. The predicted ITAs are lower in simulations with the higher MSL. A possible reason for this is that in order to achieve the same NNC models with higher MSL will have more nodes with NC above the NNC and thus have a higher initial mean NC. For instance, the models with MSL of 0.7mm and 1.5mm have an initial mean NC, to three significant figures, of 4.794 and 4.816 respectively. This results in mean NC of 4.015 and 4.071 after uniaxial and 4.766 and 4.798 after triaxial loading simulations. As the optimal ITA reduces with increasing connectivity it stands to reason that higher MSL simulations with marginally higher mean ANC would predict lower ITAs. This occurs due to a lower number of joint nodes required to define models with higher MSL. The reduction in joint nodes is not proportional to the change in MSL.

Simulations with NNC of 6 and above have a low prevalence of nodes with ANC of 3, 4 and 5 which is not unexpected. The optimal ITA for high connectivity lattice structures tends to 90° and this is evident in the simulation results reported in this Chapter,

particularly in Figures 5.11 and 5.12. Therefore, models used in these simulations are not considered to be good candidates for trabecular bone structural form.

Despite close alignment between the optimum ITA values, imaging study reported values (Reznikov et al. (2016)) and the NNC4 simulations presented in this thesis, differences remain. It is unlikely that trabecular bone experiences such idealised environment which would have an effect on its trajectories and thus the ITA. The uncertainty of how the imaging study treats plate like trabeculae and the fact that the simulations used in this thesis do not model plates could account for the differences between the ITAs reported by the two.

The NC and ITA predictions suggest that low NNC models yield closer predictions to real bone whilst high NNC simulation's radii predictions more closely match the real trabecular bone thickness. The NNC14 simulations predict a mean radius of between 31μm and 40μm which closely compare to real bone mean trabecular thickness of approximately 100μm to 120 μm (Stauber & Müller (2006), Liu et al. (2008), Zhao et al. (2018)). However, the distribution curves of all four of these simulations have a high right skew and a very large number of elements with the smallest radius. The radii distribution curves which exclude the elements with the smallest radius of 25 μm more closely resemble distribution observed in real bone (Figure 5.1). The mean radius predictions further increase to a maximum of 64μm and 91μm in simulations with MSL of 0.7mm and 1.5mm with a dead zone threshold of 1000$\mu\varepsilon$. These mean radii remain closely matched to the real bone thickness and the radii distributions provide a better match then those obtained when the dead zone is set at 250$\mu\varepsilon$.

The NN04 simulations with 0.7mm MSL predict mean radii of 108μm and 139μm for uniaxial and triaxial loading when the dead zone threshold of 250$\mu\varepsilon$ is used. The predominance of elements with the smallest radii is large. These predictions change to 131μm and 148μm when dead the zone threshold is increased to 1000$\mu\varepsilon$. For MSL of 1.5mm these values are 212μm, 267μm, 249μm and 284μm. Even though the values for 0.7mm MSL are lower they appear to match poorly with real bone.

Some of this discrepancy may be caused by the lack of plate like trabeculae in the simulation models. Figure 5.17 presents a simplified example of how the bending

stiffness of 5 circular elements may be replicated by a singe plate element. The circular struts were assumed to be spaced at 0.7mm which is the MSL. The largest mean strut radius of 148$\mu\varepsilon$ is predicted by the NNC3 07mm MSL simulation is that for a triaxialy loaded models with the high dead zone threshold. Using this strut radius it has been determined that the 3mm wide plate would need a thickness t=75μm and t=196μm to replicate the bending stiffness of 5 struts around the Y and X axis respectively. This is a very simplified localised calculation which omits the effect of axial deformation but it demonstrates how an introductions of a relatively small number of plates in a large bone model may lead to the reduction of mean overall trabecular thickness.

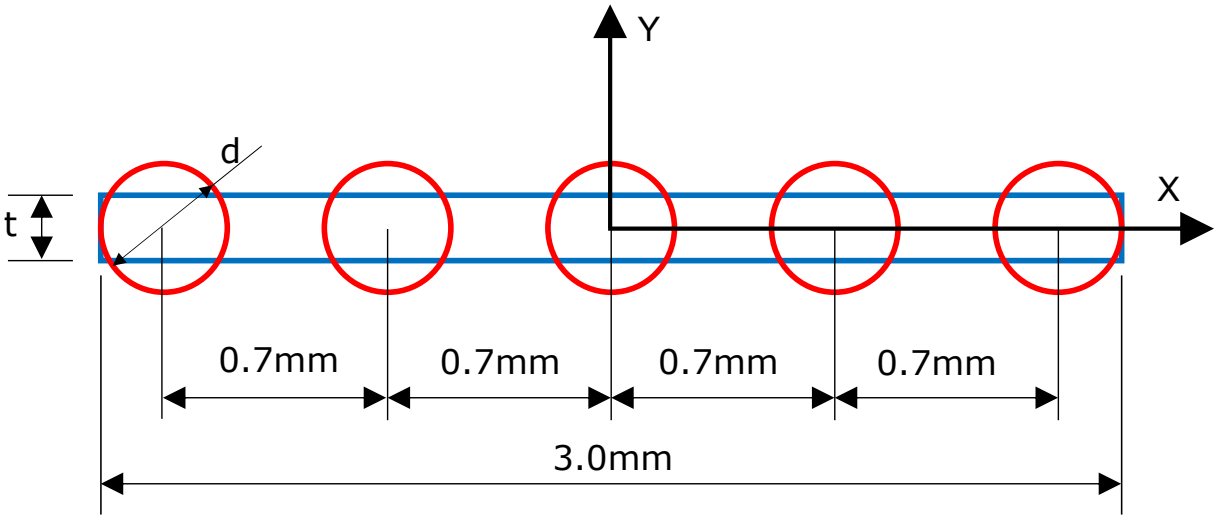


Figure 5.17: An illustration of how a single plate may replicate the bending stiffness of five circular struts.

5.5 Summary

Consideration of the morphological features presented in this Chapter leads to a conclusion that NN04 bending models present the most suitable candidate for trabecular structural form when employing NN simulations. The increase of dead zone threshold to 1000$\mu\varepsilon$ has been examined in response to findings that structural models tend to overpredict the abundance of the trabeculae with the smallest radius. This was observed in this thesis and reported in studies by Favier (2020) and Favier et al. (2021). Radii distributions which more closely resemble that of real bone have been obtained as a result but only for low NNC models. The NC and ITA values which more closely

match those reported in imaging studies (Reznikov et al. (2016) have been observed in models with dead zone threshold of 1000$\mu\varepsilon$. The E value and density predictions for theses simulations were found not to differ greatly from the ones predicted by simulations using the dead zone threshold to 250$\mu\varepsilon$ (Tables 5.11 and 5.10).

As discussed, trabecular bone can be considered as an open cell foam (Gibson & Ashby (1997)). Such foams often form, both naturally and artificially, from an expanding gas or liquid whose bubbles form cells in the material into which they are introduced. This process often leads to formation of Voronoi structures and Chapter 6 will investigate whether Voronoi cells provide a structural form which provides a further improved comparison with trabecular bone.

6

Trabecular bone as a Voronoi structure

6.1 Introduction

Previous chapters discussed near neighbour (NN) simulation predictions of trabecular bone macro-scale properties (Chapter 4) and its topological properties (Chapter 5). The predicted macro-scale properties of Young's modulus and relative density were found to compare well with those of real bone. The morphological predictions of connectivity, trabecular radius and inter trabecular angle (ITA) did not compare as well with actual bone. This chapter will examine whether an alternative to NN model simulations yields predictions closer to those reported in the literature for real bone.

As discussed in Chapter 4, the trabecular bone structure can be described as a combination of a closed and an open cell foam (Gibson & Ashby (1997)). A closed cell foam consists of interconnecting plates and shells while an open cell foam consists of a network of interconnected struts, which form a three-dimensional lattice-like structure. This thesis will focus on open cell foam representation of trabecular bone. There are a variety of foaming process, both natural and artificial, but in many a supersaturated gas is induced to separate from a liquid. Gas bubbles nucleate throughout the liquid and grow. If the bubbles all nucleate randomly in space but at the same time, and grow with the same linear growth rate, then the initial structure is a random Voronoi honeycomb (two dimensions) or a Voronoi foam (three dimensions).

A Voronoi diagram created from a random set of points appears much more irregular than, for instance, a bee honeycomb, and Voronoi foam cells are much more angular than trabecular bone. (Gibson & Ashby (1997)). There are several reasons for this. In biological processes cells and organisms have a finite size, meaning that a cell cannot form closer than a certain distance to another. Weaire & Rivier (1984) took account of such a minimum separation in their modelling work and created Voronoi networks which more closely resembled those observed in nature. Discrepancies that remain are due to shaping of foams by processes other than competitive growth (Gibson & Ashby (1997)). Surface tension and pressure differentials play important roles in determining the morphology and characteristics of foams formed by gas or liquid diffusion. In the context of cellular materials like bone and wood, the shapes of cells are further

influenced by the loads they resist (Currey (2012)).

In addition, topology considerations present a further justification that an adapted Voronoi lattice may predict trabecular morphology and macro-scale properties which compare well with real bone. Voronoi foam cells are formed by faces bound by edges meeting at nodes. Using Euler's law, Gibson & Ashby (1997) conclude that in a Voronoi foam the most common number of edges meeting at a node is 4 and that the most common number of faces meeting at an edge is 3. Reznikov et al. (2016) report that the proportion of nodes with nodal connectivity (NC) of 3 in real bone is between 65% and 75%. A lattice model with an initial NC of 4 is more likely to favourably compare with this finding by predicting a predominance of nodes with NC of 3 following the adaptation simulation. As was discussed in Chapter 5 lower NC leads to higher ITAs, so this reduction in NC predictions is also likely to more closely match the mean ITAs observed in the imaging studies (Reznikov et al. (2014*b*), Reznikov et al. (2016)).

6.2 Methodology

Similar methodology as employed in NN simulations, and discussed in Chapters 3, 4 and 5 was used. The only difference was in the initial geometry generation. In the NN models the 8mm cube was populated with random points which were each connected to the specified number of nearest points. The Voronoi models were based on diagrams of that name which, in 2D, partition a plane into regions around a given set of points usually referred to as seeds. For each seed there is a corresponding region, called a Voronoi cell, consisting of all points of the plane closer to that seed than to any other (Figure 6.1).

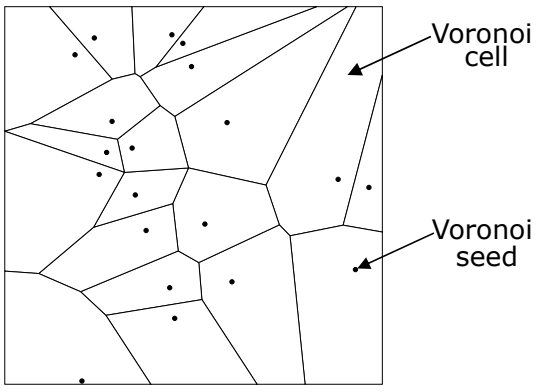
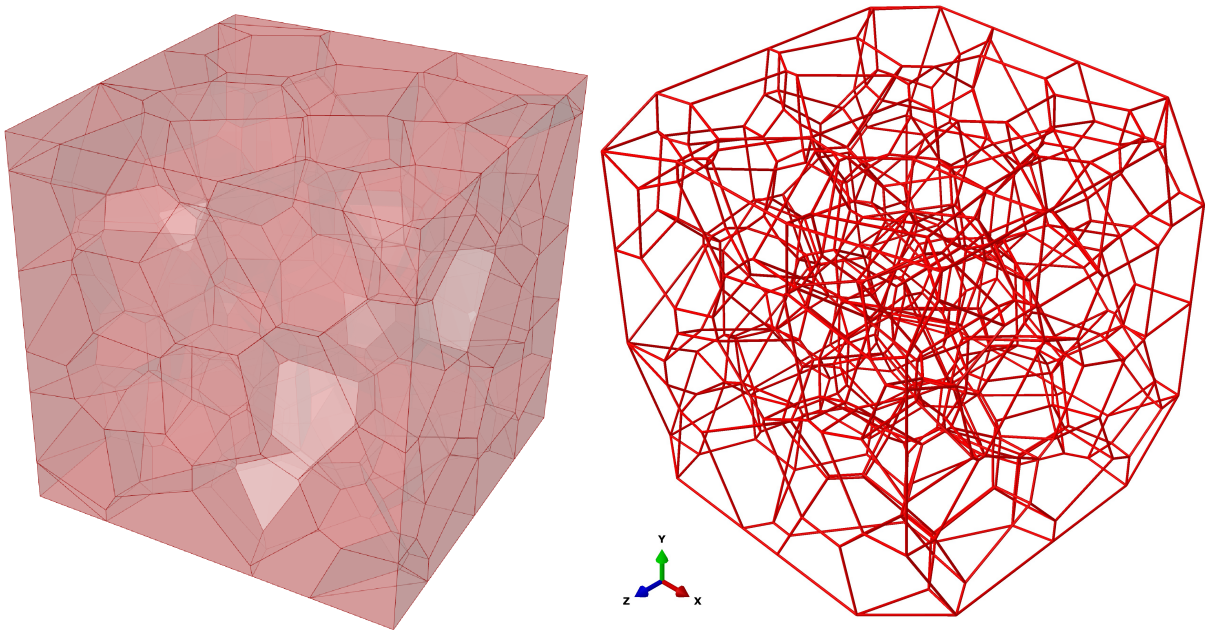


Figure 6.1: Illustration of a Voronoi diagram in 2D.

Figure 6.2 illustrates Voronoi cells In 3D where volumes as opposed to areas are created around cells and faces form boundaries as opposed to edges in 2D. Edges where faces of these volumes meet were extracted to form a lattice. Rhinoceros/Grasshopper was used to randomly populate a cubic volume with a number points which were used as Voronoi cell seeds. The geometry of the cell edges was extracted to create a network of lines. Very short lines, under 0.1mm, were merged into single points. The lines were divided into four and the coordinates of resulting nodes and the graph connectivity information exported into Abaqus input file. Once the Abaqus input file was created the workflow described in Chapter 3 was followed which is now summarised.



Rhinoceros/Grasshopper model of a 8mm x 8mm x 8mm cube populated with 101 Voronoi seeds to form cells with an average edge length of 1mm.

Voronoi cell edge geometry extracted into Abaqus to form a lattice model.

Figure 6.2: Illustration of a Voronoi diagram in 3D.

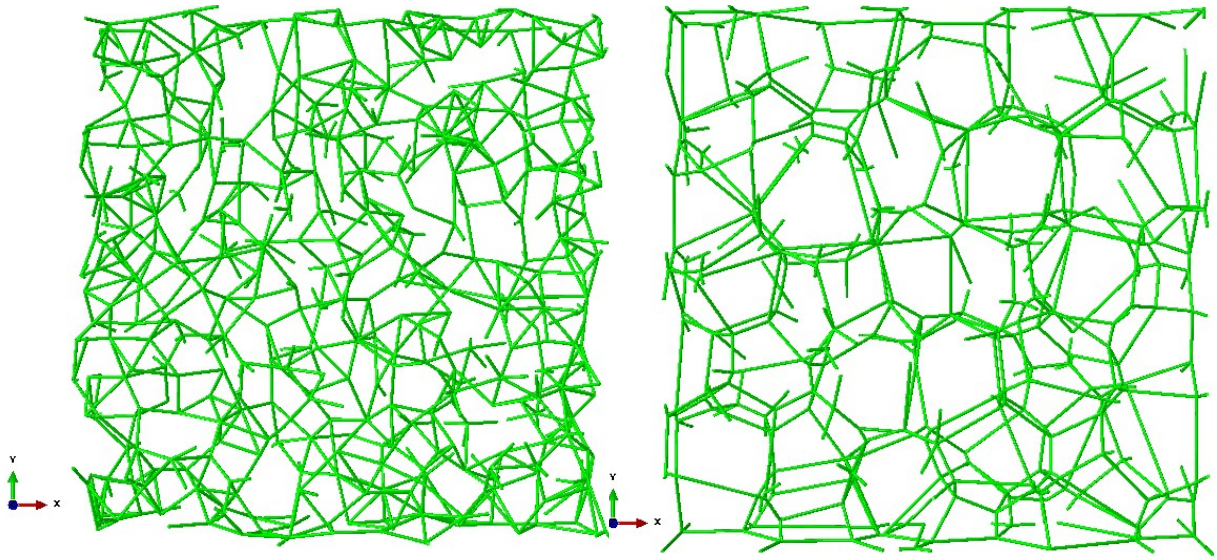
A number of studies using models MSL of 0.7mm, 1.0mm and 1.5mm were considered. All studies included five models with a randomly generated geometry. Rhinoceros/Grasshopper seed function was used to randomly populate the defined cube volume with the chosen number of Voronoi seeds. This allowed non-repeating architecture similar to real bone to be simulated and the predictions to be statistically analysed.

Two loading scenarios were evaluated; simultaneous uniformly distributed loading in three orthogonal directions and a uniformly distributed loading in Y direction. The uniformly distributed load of 1MPa was used in each of the scenarios. This magnitude

was chosen as it represents the average contact pressure applied to all load bearing joints where trabecular bone is present.

The macro scale behaviour of models as cellular solids was examined by evaluation of factor β in Equation 4.1. In order to calculate β, 5 models of mean strut length 0.7mm and 5 of mean strut length 1.5mm were subjected to four further simulations with uniform distributed loads of 0.5MPa, 0.75MPa, 1.0MPa and 1.25MPa. Factor β was also evaluated for models prior to the adaptation simulation. Four data points were obtained by setting strut radii to 50μm, 75μm, 100μm and 150μm. A comparison between initial and adapted behaviour was made.

On competition of simulations the architecture, mechanical and topological properties predicted by the Voronoi models were examined and compared with NN04 simulations. Out of all of the NN simulations considered in Chapters 3 and 4 the NN04 was chosen for comparison with Voronoi simulations as their topological properties are closely matched as is illustrated in Figure 6.3.



2mm slice through a NN04 model with MSL=0.7mm

2mm slice through a Voronoi model with MSL=0.7mm

Figure 6.3: 2mm slice through initial NN04 and Voronoi models with MSL=0.7mm showing similar topology.

6.3 Results

This section presents the predicted trabecular architecture and mechanical properties (Subsection 6.3.1), predicted trabecular topology (Subsection 6.3.2) and the impact increasing the dead zone threshold has on mechanical properties and trabecular topology (Subsection 6.3.3).

6.3.1 Predicted trabecular architecture and mechanical properties

Figure 6.4 presents the adapted architecture following uniaxial and triaxial loading simulations for one of the Voronoi models with MSL of 0.7mm. For comparison, Figure 6.5 presents the adapted architecture following uniaxial and triaxial loading simulations for one NN04 model with MSL of 0.7mm. The axial and bending strain contours are shown. Figure 6.6 present the frequency plots of axial and bending strains for same models.

The adapted architecture presented in Figure 6.4 for the uniaxial simulation resembles a collection of columns zig-zagging along the Y direction. This pattern is created by an increase in cross section of beam elements aligned with load direction and simulates bone apposition. The axial strains in most elements are below the lazy zone threshold of 1000$\mu\varepsilon$ which is evident form Figure 6.6 with mean axial strain of 384$\mu\varepsilon$ and 445$\mu\varepsilon$. Bending strains are higher with mean values of 682$\mu\varepsilon$ and 766$\mu\varepsilon$. Generally, the bending strains are higher than axial strains at nodes and axial strains are higher than bending strains in the two elements forming the middle of the strut. The exception to this is in elements forming pillar like motifs which have low NC. The axis of these elements are closely aligned with the load , resulting in significant axial but low bending strains.

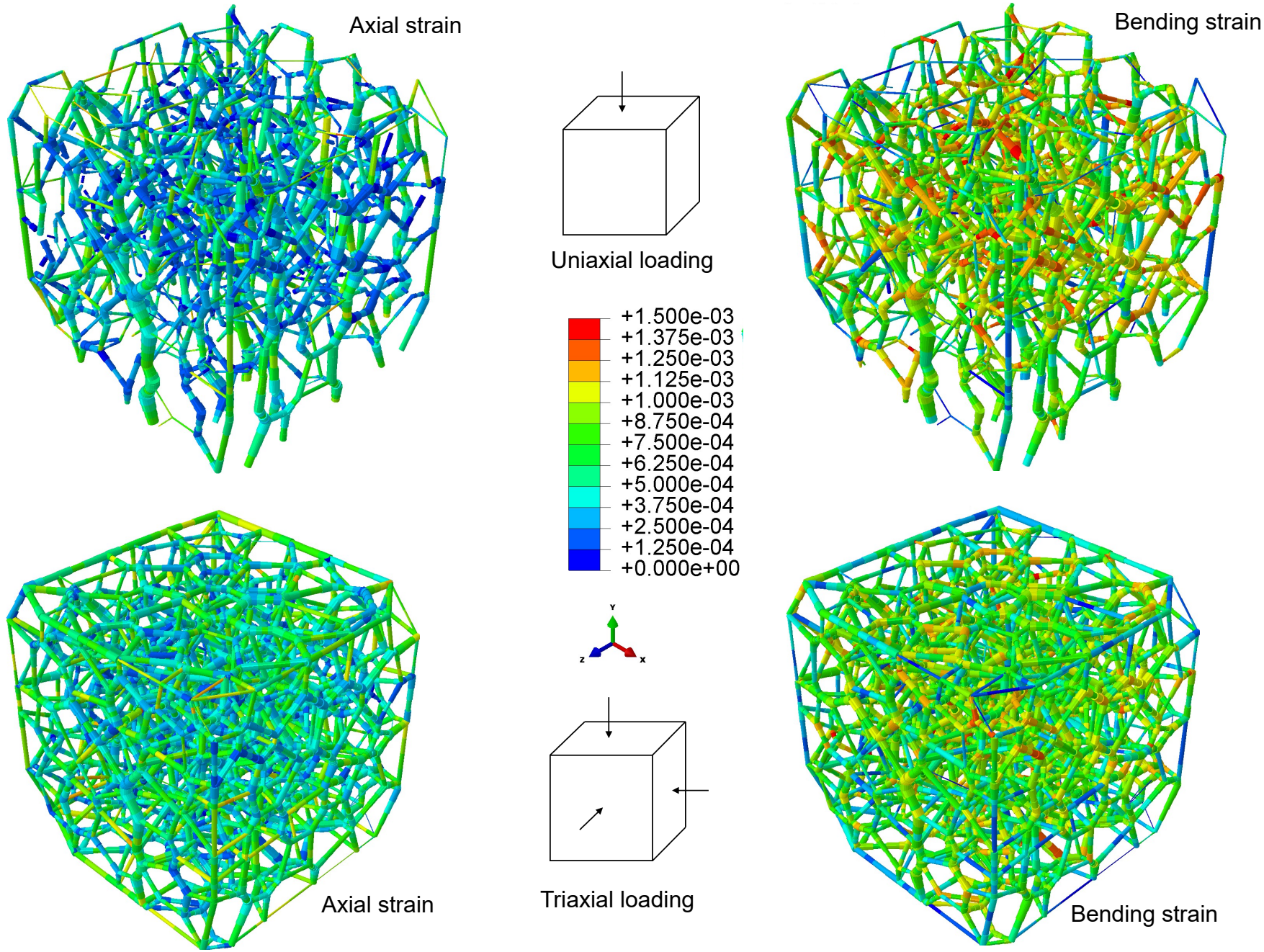


Figure 6.4: Absolute maximum axial and bending strains in one of the five Voronoi models with MSL=0.7mm. The initial radius prior to adaptation simulations was 25μm. Dead elements with radius of 1μm are not shown. The models were subjected to a uniform pressure of 1MPa either on one or three faces as indicated.

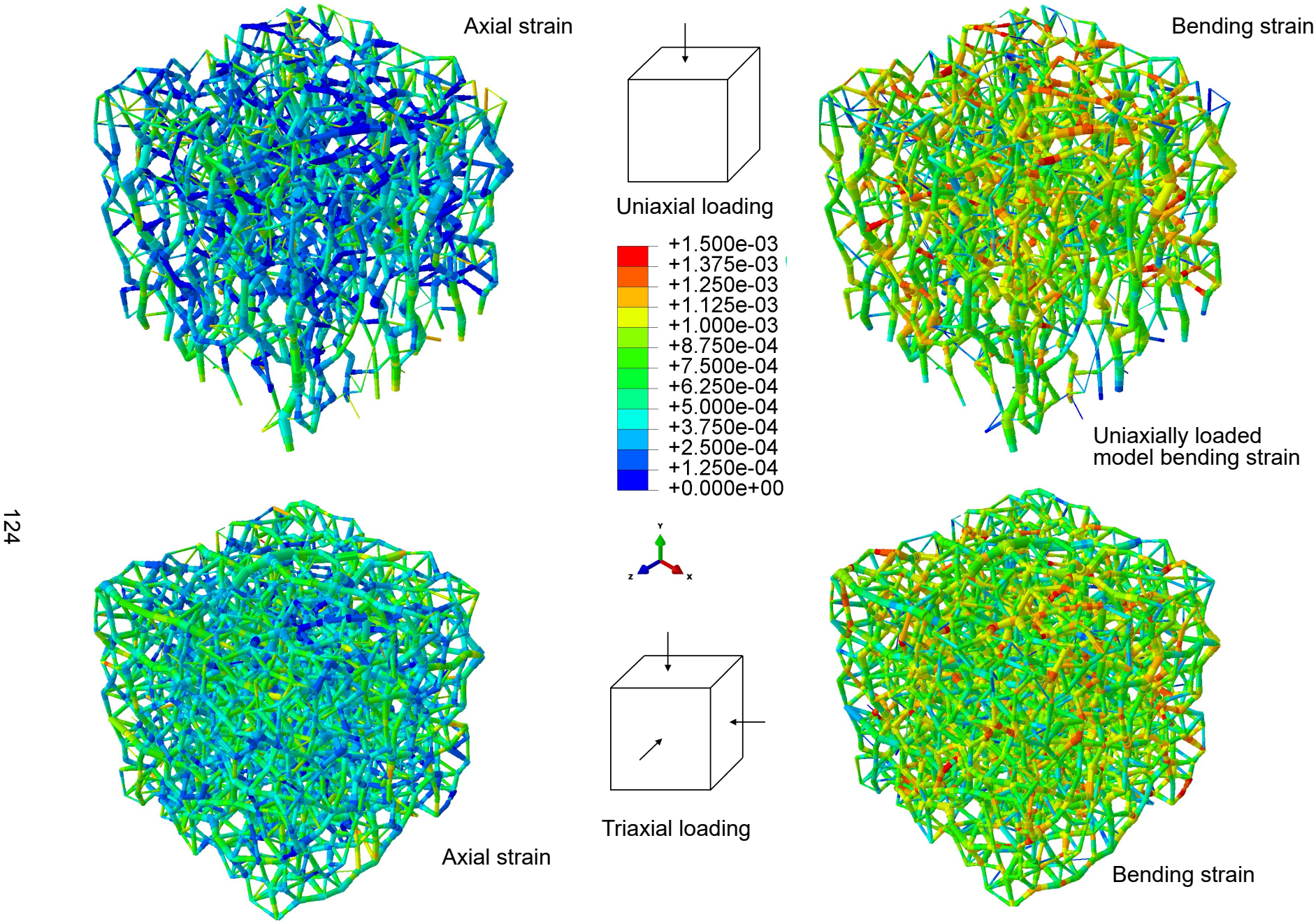
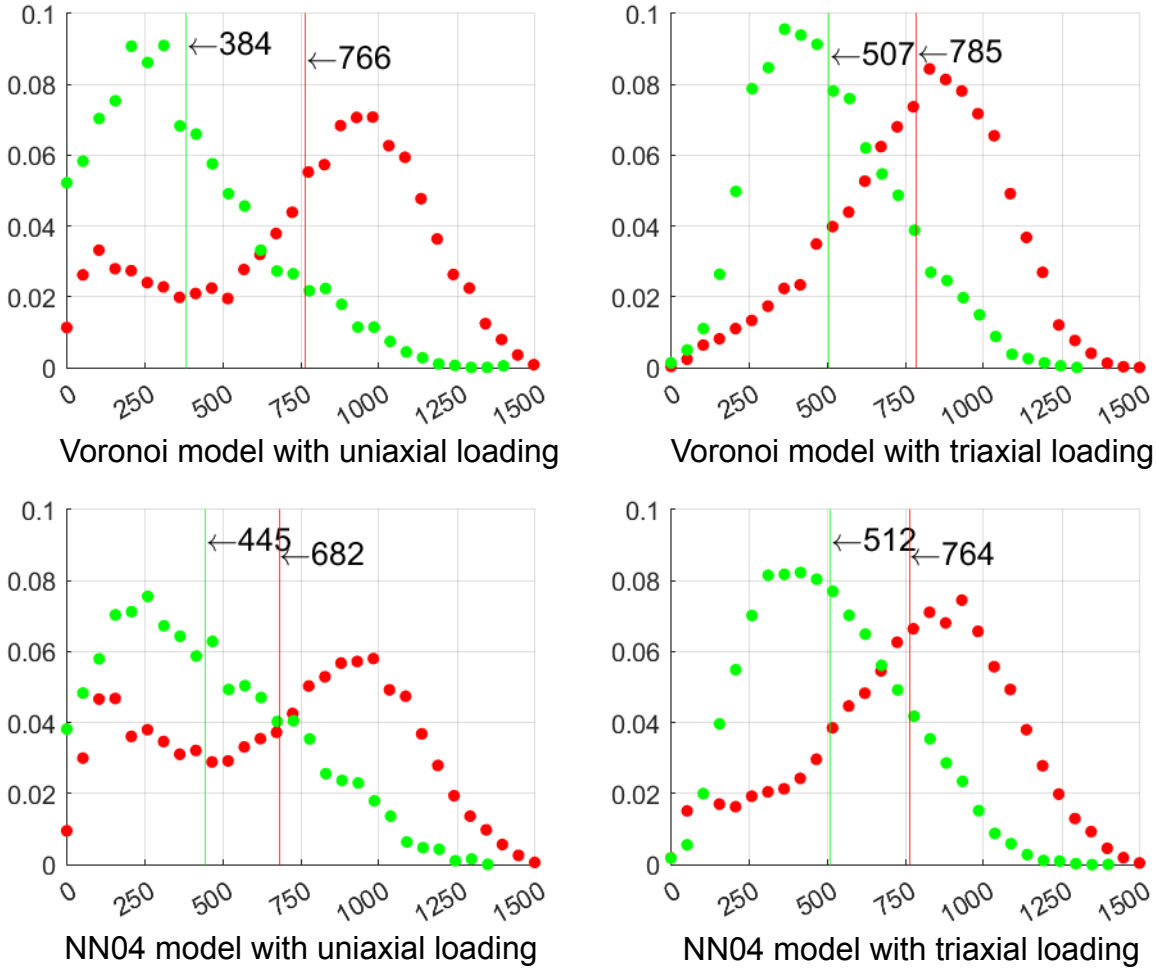


Figure 6.5: Absolute maximum axial and bending strains in one of the five NN04 models with MSL=0.7mm. The initial radius prior to adaptation simulations was 25μm. Dead elements with radius of 1μm are not shown.The models were subjected to a uniform pressure of 1MPa either on one or three faces as indicated.

The triaxial loading simulation predicts a more uniform architecture. The variations in element radii are smaller. The majority of elements experience axial strains below the lower lazy zone threshold of 1000$\mu\varepsilon$ but higher than those for the uniaxial loading simulation with mean value of 507$\mu\varepsilon$ as opposed to 384$\mu\varepsilon$. The bending strains, on the other hand, remain approximately the same with mean values of 766$\mu\varepsilon$ and 785$\mu\varepsilon$. It is worth noting that the mean axial strain is greater in triaxial as opposed to uniaxial loading simulations while the mean bending strain remains approximately equal.



Voronoi model with uniaxial loading | Voronoi model with triaxial loading

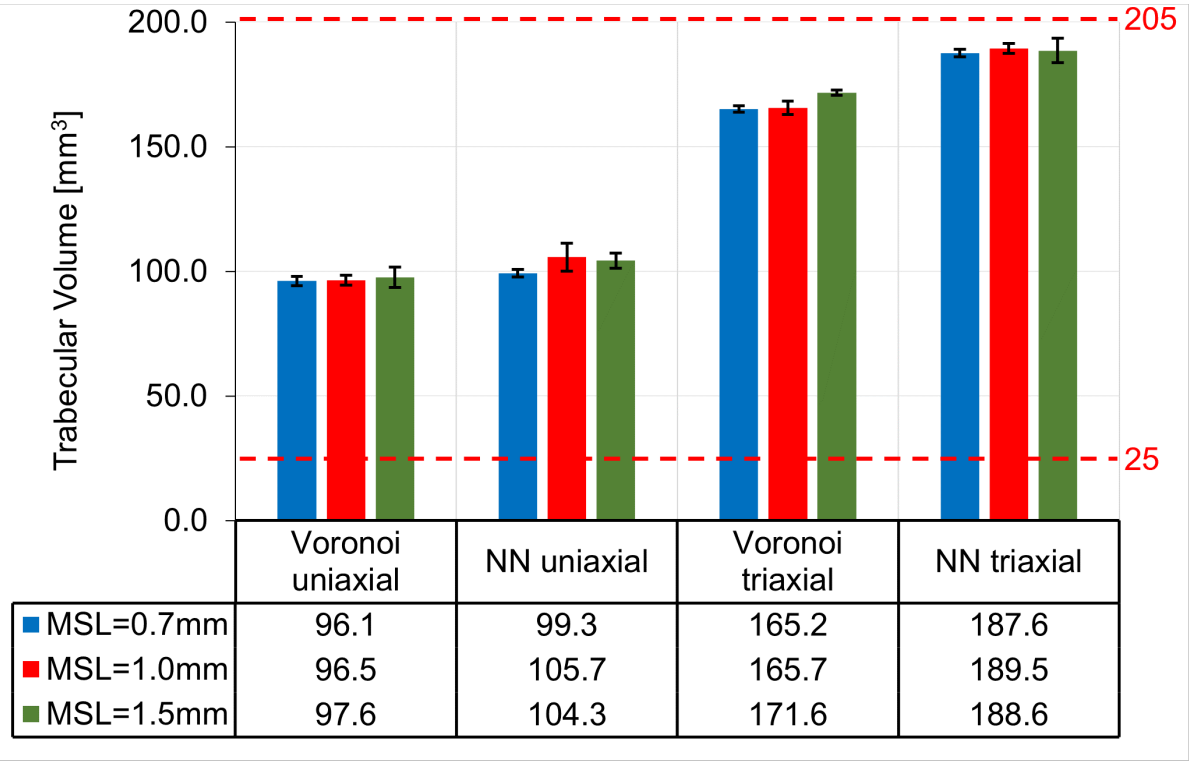
NN04 model with uniaxial loading | NN04 model with triaxial loading

Figure 6.6: Frequency distributions of axial strain in green and bending strain in red for one of the five models in Voronoi and NN04 simulations with MSL of 0.7mm. Mean values for each distribution are represented by a vertical line and annotated accordingly. 50$\mu\varepsilon$ bin size has been used.

For comparison, Figure 6.5 presents the adapted architecture following uniaxial and triaxial loading simulations for one NN04 model with MSL of 0.7mm. The architecture predicted by NN simulations under triaxial loading is less uniform than that predicted by Voronoi models but otherwise similar (Figure 6.4). The strain distributions are similar

with mean axial strains (512$\mu\varepsilon$ and 507$\mu\varepsilon$) and mean bending strains (764$\mu\varepsilon$ and 785$\mu\varepsilon$) being approximately the same. In the uniaxial loading simulations Voronoi simulations predict higher bending strains; the mean is 766$\mu\varepsilon$ as opposed to 682$\mu\varepsilon$. The predicted axial strains are lower; the mean is 384$\mu\varepsilon$ as opposed to 445$\mu\varepsilon$

The NN04 models appear denser suggesting a higher volume and this is evident in Figure 6.7 which presents the comparison of predicted trabecular volume between the Voronoi and NN04 models. Voronoi models predict a lower trabecular volume, whilst both simulations predict lower volumes for uniaxial loading scenario as opposed to the triaxial loading scenario.

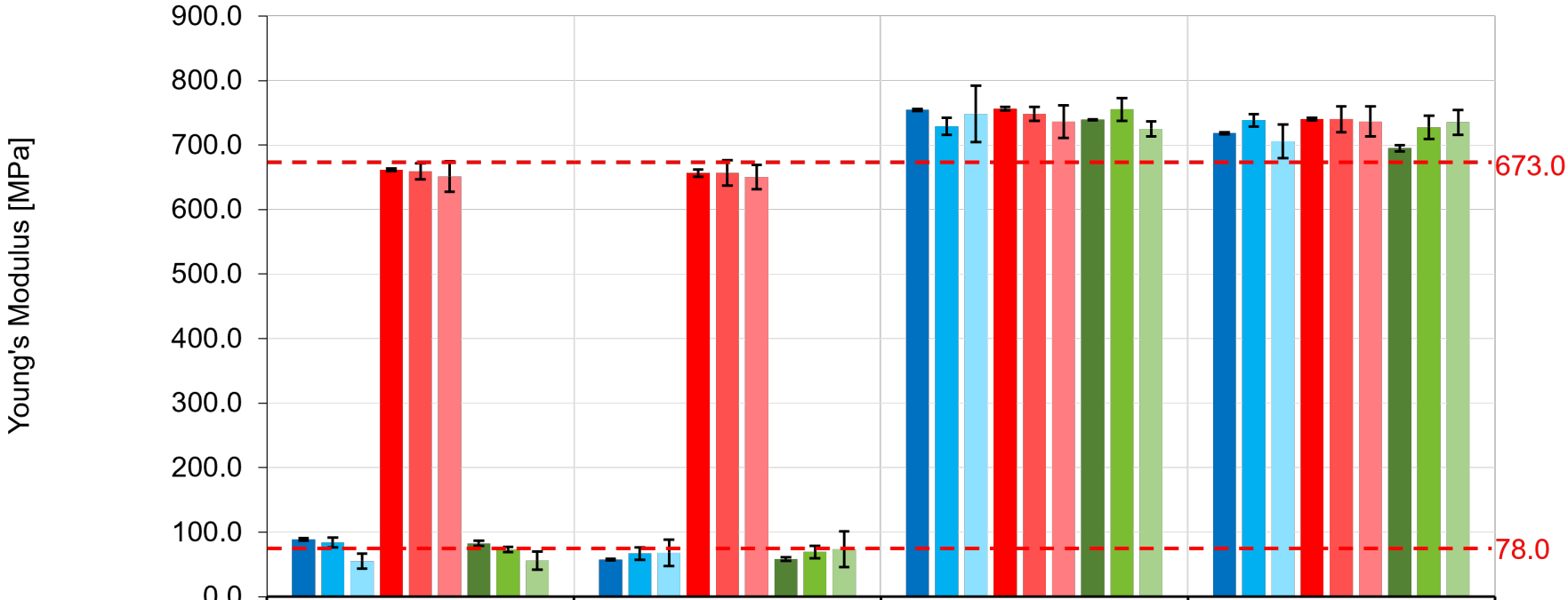


	Voronoi uniaxial	NN uniaxial	Voronoi triaxial	NN triaxial
MSL=0.7mm	96.1	99.3	165.2	187.6
MSL=1.0mm	96.5	105.7	165.7	189.5
MSL=1.5mm	97.6	104.3	171.6	188.6

- - - - Volume range calculated from the reported density range for real trabecular bone (Linde et al. (1992), Gibson (2005)).

Figure 6.7: Mean predicted trabecular volume of 5 randomly generated models with MSL as shown for Voronoi and NN04 simulations. 95% confidence interval error bars are shown. A range of trabecular volume calculated from reported density ranges (Linde et al. (1992), Ashby (2006)) is shown for comparison.

Figure 6.8 compares Young's modulus predictions for the Voronoi and NN04 simulations. The predicted Young's modulus for triaxial loading simulations was approximately 750MPa. Values were marginally lower for NN simulations but were consistent across the three directions for both Voronoi and NN04 models.



	Voronoi uniaxial	NN uniaxial	Voronoi triaxial	NN triaxial
E1 MSL=0.7mm	88.8	57.4	754.4	718.5
E1 MSL=1.0mm	83.8	66.8	729.0	738.3
E1 MSL=1.5mm	55.1	68.2	748.4	705.7
E2 MSL=0.7mm	661.7	656.7	756.4	740.5
E2 MSL=1.0mm	659.2	656.9	748.3	740.1
E2 MSL=1.5mm	651.2	650.2	736.2	736.4
E3 MSL=0.7mm	82.6	58.1	739.1	695.1
E3 MSL=1.0mm	73.0	69.0	755.4	727.6
E3 MSL=1.5mm	55.5	73.6	725.1	735.4

- - - - Reported range for real trabecular bone (Linde et al. (1992))

Figure 6.8: Mean predicted Young's Modulus Values of 5 randomly generated models with MSL as shown for Voronoi and NN04 simulations. 95% confidence interval error bars are shown. A range of E values for real bone reported by Linde et al. (1992) is shown for comparison.

The uniaxial loading simulations predicted the Young's modulus of 650MPa in the loaded direction. This was 87% of the Young's modulus predicted in each direction by the triaxial loading simulations. The values in the two unloaded directions were between 6% and 14% of Young's modulus in the loaded direction. The difference between the Voronoi and NN04 predictions in the loaded direction were less evident than in those predicted by triaxial loading simulations. In the other two principal directions the Voronoi models predicted a higher modulus for 0.7mm MSL simulations but a smaller one for 1.5mm MSL simulations.

The predicted trabecular volume was lower and the predicted Young's modulus slightly higher for Voronoi simulations than for NN04 simulations. This implies greater material efficiency of the predicted Voronoi architecture as shown in Table 6.1. For example, the structural efficiency for Voronoi simulations with MSL of 0.7mm subjected to uniaxial loading is 6.88N/mm^5 (95% CI [6.63, 7.14]) compared to NN value of 6.62N/mm^5 (95% CI [6.43, 6.81]) for MSL of 0.7mm.

Loading	Simulation	Mean Strut Length [mm]								
		0.7			1			1.5		
		Efficiency [E/V]			Efficiency [E/V]			Efficiency [E/V]		
		mean	95% CI		mean	95% CI		mean	95% CI	
			min	max		min	max		min	max
Uniaxial	Voronoi	6.88	6.63	7.14	6.83	6.56	7.12	6.67	6.17	7.22
	NN04	6.62	6.43	6.81	6.21	5.73	6.75	6.24	5.88	6.61
Triaxial	Voronoi	4.58	4.42	4.74	4.52	4.38	4.66	4.29	4.12	4.46
	NN04	3.95	3.81	4.08	3.91	3.76	4.06	3.90	3.69	4.14

Table 6.1: Structural efficiency, expressed as Young's modulus divided by trabecular volume, for Voronoi and NN nominal connectivity 4 simulations. The 95% maximum confidence intervals of structural efficiency are calculated from the maximum values of E and minimum values of V using the 95% confidence intervals for those values. The opposite was done for the minimum confidence intervals.

Figure 6.9 presents plots of relative density versus the relative Young's modulus for Voronoi and NN simulations with MSLof 0.7mm and 1.5mm prior to adaptation simulations, whilst Figure 6.10 presents the same information following the adaptation simulations. The predicted power exponent for Voronoi simulations is higher than it is for

NN04 simulations both before and following the adaptation indicating that the Voronoi models exhibit more bending dominated behaviour.

All individual curves within three families, pre-adaptation, post-adaptation subjected to uniaxial loading and post-adaptation subjected to triaxial loading, demonstrate a similar relationship between the Young's modulus and relative density. The constants α and β, as defined by Equation 1.2, have a similar magnitude. Curves for uniaxial loading adaptation demonstrate an increase of constant α from the un-adapted value whilst the constant β marginally decreases. With the triaxial adaptation there is a larger decrease in constant β whilst the constant α stays approximately the same. There does not appear to be a significant difference between the behaviour of Voronoi and NN04 simulations.

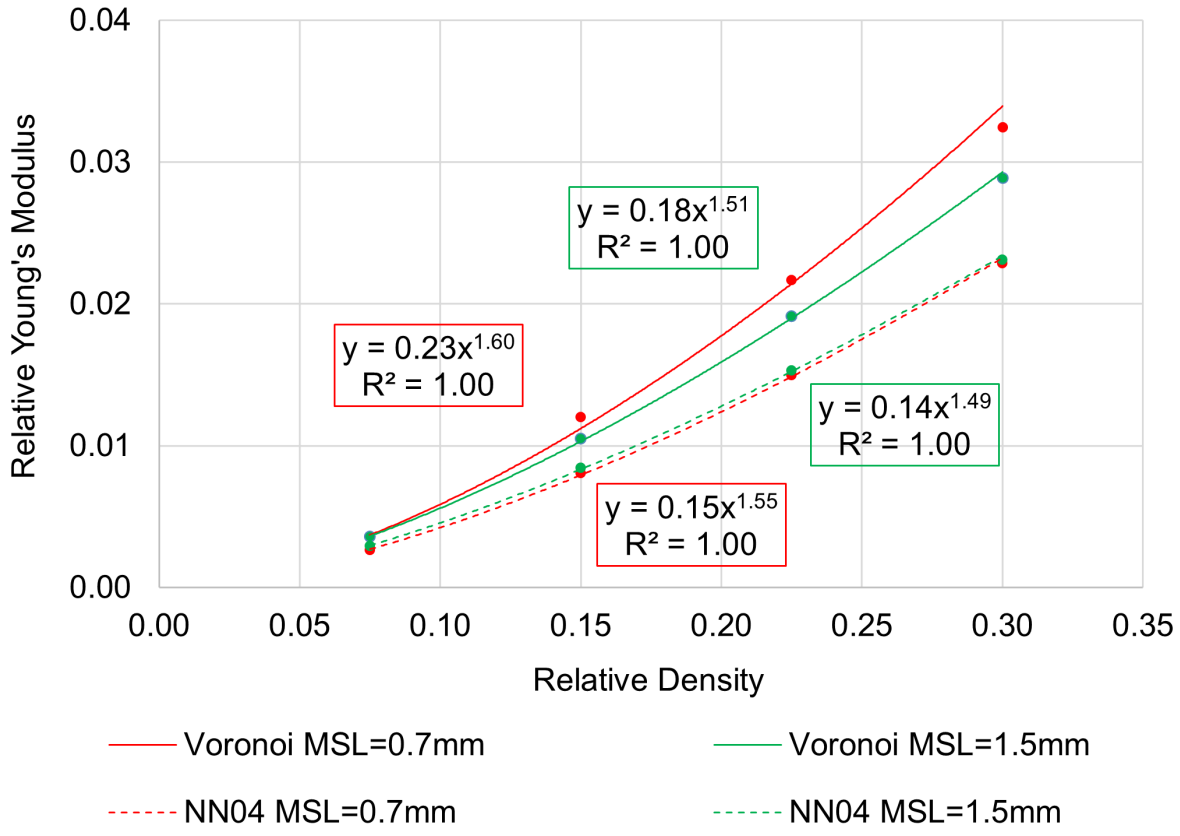


Figure 6.9: Mean Relative Young's Modulus plotted against mean relative density for 5 models prior to adaptation for Voronoi model and NN04 model simulations. A curve has been fitted to each data set and the equations of these curves are presented next to them bound by a frame of the same colour. Coefficients of determination (R^2) are shown. The curves do not fit to data points exactly due to variability of 5 models. The upper and lower bound curves are shown for the worst fit Voronoi 0.7mm MSL results.

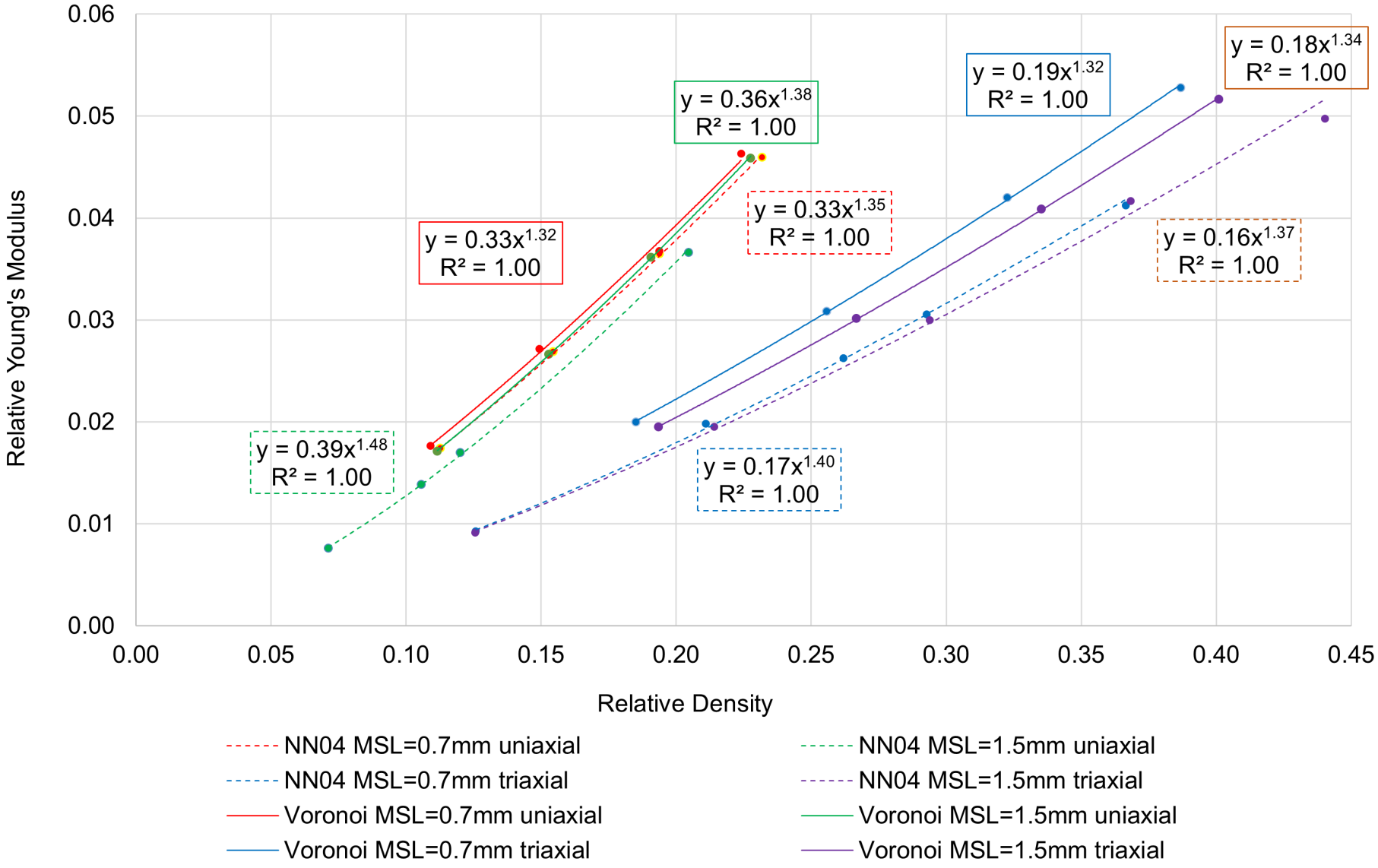


Figure 6.10: Mean Relative Young's Modulus plotted against mean relative density for 5 models at the end of adaptation for Voronoi model and NN04 model simulations. A curve has been fitted to each data set and the equations of these curves are presented next to them bound by a frame of the same colour. Coefficients of determination (R^2) are shown.

6.3.2 Predicted trabecular topology

Table 6.2 presents the nodal connectivity for Voronoi and NN04 simulations before and after adaptation. NN04 simulation results are presented as they match the Voronoi simulation predictions most closely. The Voronoi simulations NC is lower for all scenarios and is less influenced by adaptation than the NN04 NC. Connectivity is well preserved under triaxial loading with negligible change in NN04 models. In Voronoi simulations the only noticeable change is in a minor standard deviation difference in models with MSL of 0.7mm. The minimum ANC of 1 implies a connection to an element that has been inactivated. This occurs at load application nodes where elements connected to these nodes in the unloaded directions experience low strains.

	MSL [mm]	Voronoi					NN04				
		Mean	Mode	SD	Min	Max	Mean	Mode	SD	Min	Max
Initial	0.7	**4.1**	**4**	**0.4**	**2**	**10**	**4.8**	**4**	**0.9**	**4**	**9**
	1	**4.1**	**4**	**0.4**	**2**	**8**	**4.8**	**4**	**0.9**	**3**	**8**
	1.5	**4.1**	**4**	**0.4**	**2**	**7**	**4.8**	**4**	**0.9**	**4**	**8**
Uniaxial loading	0.7	3.7	4	0.8	1	8	4.0	4	1.2	1	9
	1	3.6	4	0.9	1	7	4.0	4	1.2	1	8
	1.5	3.4	4	0.9	1	6	4.1	4	1.2	1	7
Triaxial loading	0.7	4.1	4	0.5	2	10	4.8	4	0.9	1	9
	1	4.1	4	0.4	2	8	4.8	4	0.9	1	8
	1.5	4.1	4	0.4	2	7	4.8	4	0.9	2	8

Table 6.2: Initial connectivity and ANC for Voronoi and NN04 simulations with 0.7mm, 1.0mm and 1.5mm MSL. The table presents mean, mode, standard deviation (SD), minimum and maximum values for uniaxial and triaxial loading simulations.

Table 6.3 presents the abundance of nodes with ANC3, ANC4 and ANC5 in Voronoi and NN04 simulations as well as the values reported in the study by Reznikov et al. (2016). ANC4 nodes are the most common in all simulations with the highest proportion of approximately 60% and 40% in uniaxial Voronoi and NN04 simulations respectively. The approximate proportions dramatically increase for triaxial Voronoi simulations to over 90% and only slightly in NN04 simulations to just below 50%. These predictions do not match the imaging study results as Reznikov et al. (2016) report that ANC4 nodes form approximately a quarter of all nodes. This study also reports ANC3 nodes as most predominant presenting approximately two thirds of all nodes whilst the Uni-

MSL [mm]	Model type	Loading	Connectivity			
			ANC3	ANC4	ANC5	ANC>5
0.7	Voronoi	Uniaxial	23.05%	65.32%	2.21%	9.42%
		Triaxial	0.67%	93.47%	1.82%	4.04%
	NN04	Uniaxial	17.85%	42.19%	22.24%	17.72%
		Triaxial	1.04%	46.08%	33.60%	19.28%
1	Voronoi	Uniaxial	24.78%	62.47%	2.26%	10.49%
		Triaxial	1.11%	93.22%	2.95%	2.72%
	NN04	Uniaxial	18.78%	39.73%	21.71%	19.78%
		Triaxial	0.69%	46.20%	32.70%	20.41%
1.5	Voronoi	Uniaxial	29.61%	53.70%	1.44%	15.25%
		Triaxial	1.52%	92.70%	3.85%	1.93%
	NN04	Uniaxial	15.29%	43.06%	21.88%	19.77%
		Triaxial	0.51%	46.75%	30.59%	22.15%
Topological study values			65% - 75%	19%-27%	4% - 7%	<1.5%

Table 6.3: Abundance of ANC 3, 4, 5 and >5in Voronoi and NN04 models at the end of adaptation simulations. The topological study values reported by Reznikov et al. (2016) are also included.

axial simulations predict the proportion of ANC3 nodes of approximately 20%. Their presence in triaxial simulations is negligible. The Voronoi predictions for ANC5 nodes match closely with imaging study values whilst the NN04 simulations predict a much greater prevalence of these nodes.

Table 6.4 presents the comparison of predicted ITA values between the Voronoi and NN04 simulations for ANC3, ANC4, ANC5 and above ANC5. The Voronoi simulations predict higher ITAs for ANC3 and ANC4 than the NN04 simulation. For ANC5 nodes and higher the predicted ITAs become very similar which is not unexpected as the lattice begins to resemble a continuum. Finally it is worth noting that the predicted ITAs of 109.3° and 109.1° for ANC4 in Voronoi uniaxial and triaxial simulations closely match the tetrahedral angle of 109.5° and the imaging study reported value of 107.6°. This will be explained in more detail in the discussion section.

	MSL [mm]	ANC	Voronoi Simulations ITA [°]						NN04 Simulations ITA [°]					
			Mean	95\% CI +/-	Median	SD	Min	Max	Mean	95\% CI +/-	Median	SD	Min	Max
Uniaxial loading	0.7	3	112.5	29.9	109.1	34.2	2.8	180.0	103.4	30.1	99.6	34.3	36.1	178.4
		4	109.3	27.5	106.3	31.3	6.4	180.0	99.0	29.0	95.4	33.0	24.6	179.6
		5	99.7	34.7	94.5	39.6	3.3	179.4	99.8	28.6	96.3	32.6	27.9	179.1
		>5	100.2	34.5	95.1	39.4	6.5	179.4	99.2	28.8	95.6	32.9	34.2	179.2
	1.0	3	111.7	32.7	107.6	37.3	6.0	180.0	101.4	30.4	97.4	34.7	31.2	177.8
		4	108.7	28.1	105.6	32.1	5.1	180.0	97.5	28.8	93.8	32.9	29.3	178.8
		5	99.2	34.8	93.9	39.7	2.8	179.3	99.4	28.9	95.8	33.0	34.4	177.8
		>5	99.7	35.5	94.3	40.5	3.4	180.0	99.2	29.2	95.5	33.3	30.6	177.6
	1.5	3	111.0	29.7	107.5	33.9	9.4	180.0	98.3	29.7	94.4	33.9	34.1	177.5
		4	107.6	28.3	104.4	32.3	8.3	180.0	96.7	29.0	92.9	33.1	16.7	179.2
		5	97.3	34.0	92.2	38.8	14.1	155.8	98.2	29.2	94.5	33.3	32.2	178.8
		>5	100.7	40.6	93.7	46.3	6.1	151.9	98.5	29.4	94.7	33.5	31.6	179.1
Triaxial loading	0.7	3	118.4	80.7	95.5	92.1	5.7	179.3	94.3	30.5	90.0	34.8	36.6	165.8
		4	109.1	27.7	106.1	31.6	7.9	180.0	97.1	29.0	93.4	33.0	24.6	179.6
		5	95.4	30.9	91.1	35.2	2.8	180.0	99.3	28.6	95.8	32.6	27.9	179.1
		>5	97.8	34.1	92.7	38.9	13.3	170.2	99.0	28.8	95.4	32.9	27.9	179.2
	1.0	3	115.2	77.3	93.7	88.2	6.0	180.0	85.3	24.9	82.2	28.4	37.0	152.3
		4	108.4	28.4	105.2	32.4	5.1	180.0	95.4	28.9	91.6	32.9	26.3	178.4
		5	93.4	31.3	88.8	35.8	2.8	179.2	98.4	28.9	94.8	32.9	31.0	179.9
		>5	98.9	36.5	93.2	41.6	3.0	180.0	99.1	29.1	95.4	33.2	20.4	177.6
	1.5	3	111.7	49.9	102.2	56.9	9.4	175.7	91.1	27.6	87.5	31.5	47.1	156.7
		4	107.4	27.9	104.2	31.9	8.3	180.0	92.4	28.6	88.6	32.6	16.8	179.2
		5	84.6	31.4	79.6	35.8	2.4	165.1	96.9	29.1	93.1	33.2	16.7	178.8
		>5	98.5	40.4	91.4	46.1	6.1	177.6	98.7	29.3	94.9	33.4	31.6	179.1

Table 6.4: Comparison of ITA values for Voronoi and NN04 simulations for various values of MSL and two loading scenarios. The mean, 95% Confidence interval (CI), median, standard deviation (SD), minimum (Min) and maximum (Max) values are presented. ITAs are grouped by nodes with the same ANC. Statistical distributions are calculated from 5 randomly generated models of each simulation. Key results have been highlited in yellow.

Figure 6.11 presents the graphs of ITA relative frequency for ANC3, ANC4 and ANC5 nodes. Each graph presents raw results grouped in bands of 4° and a statistically fitted distribution. Results of simulations using the three different MSL subjected to uniaxial loading are presented on the top row and the ones using the triaxial loading on the bottom row. Results of Reznikov et al. (2016) study are superimposed on each sub-figure to enable visual comparison.

The predicted ITA distributions at the end of the uniaxial loading simulations will be considered first. The graphs of each ANC reported demonstrate similar distributions

for each of the three different MSL simulations. In turn, each of these compares well with the distributions reported by Reznikov et al. (2016) with the closest visual match for ANC3. Referring to Table 6.4 the predicted ITA for Voronoi simulation with MSL of 0.7mm is 112.5° (95% CI [103.6°, 122.3°]) which compares more favourably with the value of 116.3° reported by Reznikov et al. (2016) than the closest NN04 result of 103.4° (95% CI [94.4°, 113.3°]). The fitted distributions match well with the simulation result data for ANC3 and ANC4 but less well for ANC5. The large scatter of data points in the ANC5 distribution is due to their small number as these nodes make up less than 2.5% of all nodes in the model (Table 6.3).

In triaxial loading simulations the ANC4 nodes make up over 92% of the nodes in adapted models and for that reason these are the only distributions which fit the previously reported data well. Referring to Table 6.4, the predicted ITA for Voronoi simulation with MSL of 0.7mm is 109.1° (95% CI [106.1°, 112.3 °]) which compares favourably with the value of 107.6°reported by Reznikov et al. (2016) and the tetrahedral bond angle of 109.5°.

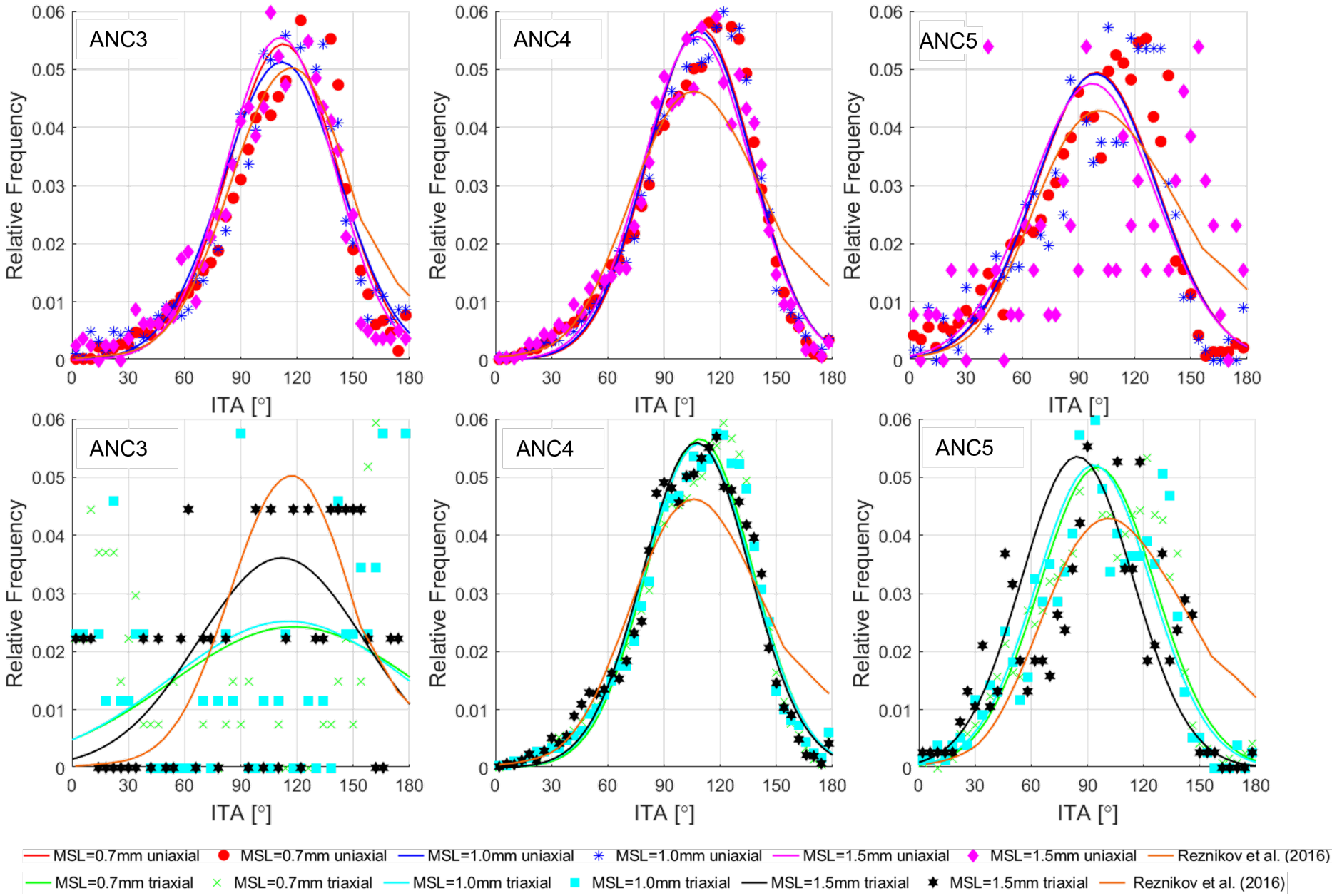


Figure 6.11: Comparison of ITA distribution simulation predictions for ANC3, ANC4 and ANC5 with those reported by Reznikov et al. (2016). Top row presents results of uniaxial and bottom row of triaxial loading simulations.

Figure 6.12 presents the predicted strut radii distributions for the three MSL and two loading scenario simulations. The mean predicted radius increases with increasing MSL and is greater for triaxial as opposed to uniaxial loading simulations. There is a tendency to overpredict the frequency of the elements with the smallest radius, which is more evident in uniaxial and simulations with the shortest MSL. The distribution skew is eliminated by excluding those elements.

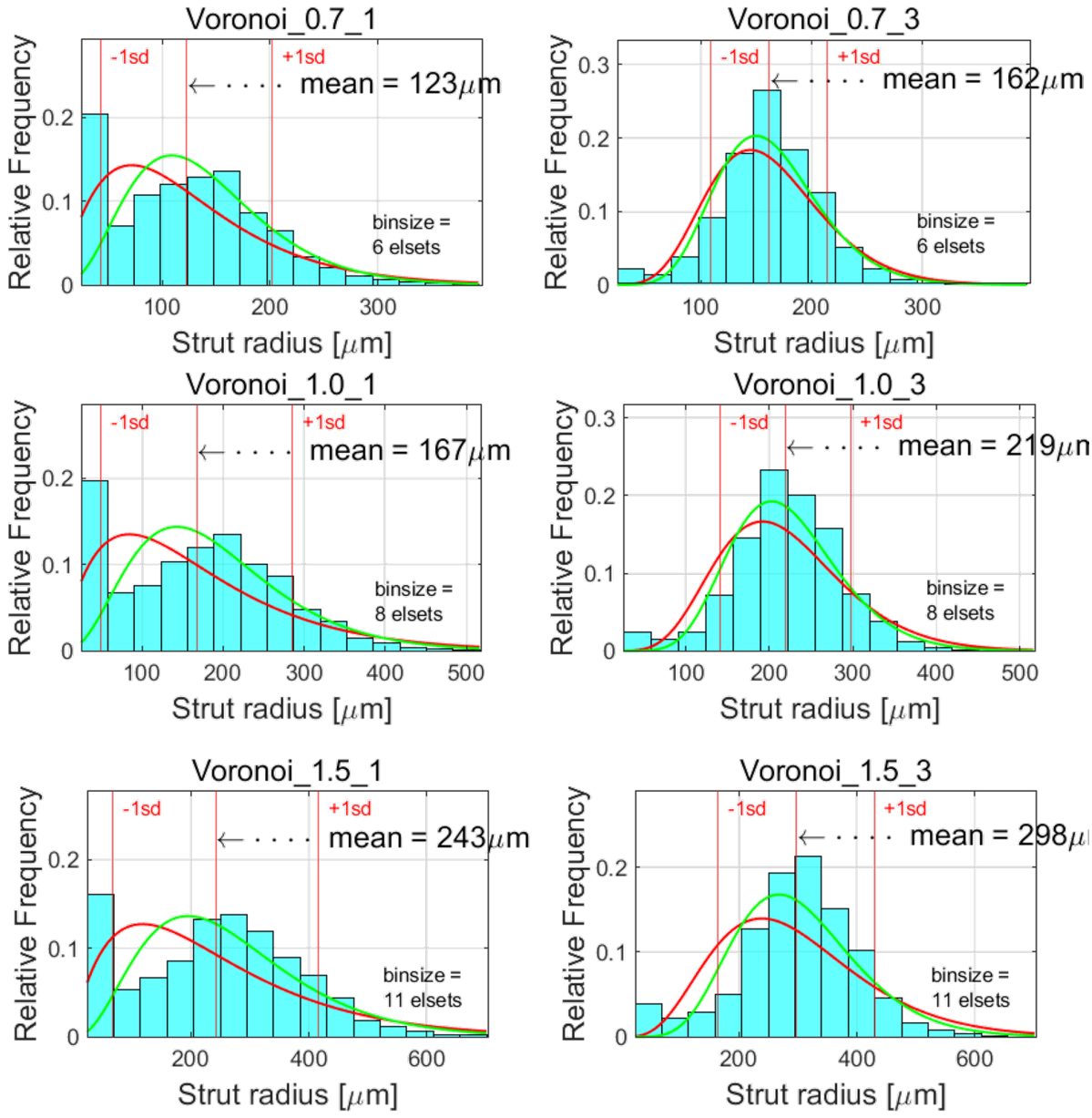


Figure 6.12: Mean strut radii distribution for bending simulations for 5 randomly generated Voronoi models. The distribution curve in green excludes the elements with the smallest radius of 25μm.

6.3.3 Impact of dead zone threshold

Table 6.5 presents the predicted mean NC values at the end of Voronoi and NN04 simulations. Values for adaptation simulations using a dead zone threshold of 250$\mu\varepsilon$ and 1000$\mu\varepsilon$ are compared. The mean NC reduces in all simulations with lowest observed value of 3.2 in Voronoi simulation with MSL of 0.7mm with the increased dead zone threshold. The mode in Voronoi simulations reduces form 4 to 3 while it remains 4 in NN04 simulations. This compares well with Reznikov et al. (2014*b*) study which reports a mean connectivity of around 3.2 to 3.4.

		msl=0.7mm				msl=1.5mm			
		Dead Zone < 250με		Dead Zone < 1000με		Dead Zone < 250με		Dead Zone < 1000με	
		NN04	V	NN04	V	NN04	V	NN04	V
Uniaxial	Mean	4	3.7	3.4	3.2	4.1	3.4	3.6	3.1
	SD	1	0.8	1.1	0.9	1.2	0.9	1.1	0.9
	Mode	4	4	4	3	4	4	4	3
	Min	1	1	1	1	1	1	1	1
	Max	9	8	8	7	7	6	7	6
Triaxial	Mean	4.8	4.1	4.4	4	4.8	4.1	4.5	3.9
	SD	0.9	0.5	1	0.5	0.9	0.4	1	0.4
	Mode	4	4	4	4	4	4	4	4
	Min	1	2	1	2	2	2	1	2
	Max	9	10	9	9	8	7	8	6

Table 6.5: Comparison of Mean NC at the end of the adaptation between simulations using dead zone threshold of 250$\mu\varepsilon$ and 1000$\mu\varepsilon$. NN04 and Voronoi(V) simulations each with MSL of 0.7mm or 1.5mm are compared.

Table 6.6 shows the ANC3 predominance of approximately 40% in Voronoi simulations with the increased threshold, which is the most common observed connectivity reported by Reznikov et al. (2014*b*). However that study reports 65-75% predominance of these nodes. The fact that this thesis finds five times as many ANC5 nodes as the Reznikov et al. (2014*b*) study is the reason why the mean NCs are in good agreement.

		MSL=0.7mm					
		Dead Zone		Dead Zone			
		< 250με		< 1000με			
		NN04	V	NN04	Δ	V	Δ
		MSL=0.7mm					
Uniaxial	ANC3	17.8%	23.1%	32.6%	83.1%	40.9%	77.1%
	ANC4	42.2%	65.3%	34.2%	-19.0%	37.4%	-42.7%
	ANC5	22.2%	2.2%	11.4%	-48.6%	1.2%	-45.5%
Triaxial	ANC3	1.0%	0.7%	11.0%	1000.0%	5.2%	642.9%
	ANC4	46.1%	93.5%	44.8%	-2.8%	88.9%	-4.9%
	ANC5	33.6%	1.8%	29.5%	-12.2%	2.3%	27.8%
		MSL=1.5mm					
Uniaxial	ANC3	15.3%	29.6%	29.2%	90.8%	41.1%	38.9%
	ANC4	43.1%	53.7%	36.4%	-15.5%	35.9%	-33.1%
	ANC5	21.9%	1.4%	14.6%	-33.3%	1.0%	-28.6%
Triaxial	ANC3	0.5%	1.5%	9.3%	1760.0%	8.9%	493.3%
	ANC4	46.7%	92.7%	45.4%	-2.8%	86.7%	-6.5%
	ANC5	30.6%	3.9%	27.6%	-9.8%	2.4%	-38.5%

Table 6.6: Comparison ANC3, ANC4 and ANC5 abundance between simulations using dead zone threshold of 250$\mu\varepsilon$ and 1000$\mu\varepsilon$. NN04 and Voronoi(V) simulations each with MSL of 0.7mm or 1.5mm are compared. In addition to absolute connectivity values the results for dead zone threshold of 1000$\mu\varepsilon$ include the difference (Δ) from the results for dead zone threshold of 250$\mu\varepsilon$.

Table 6.7 presents the predicted trabecular volume and Table 6.8 the predicted Young's modulus at the end of Voronoi and NN04 simulations. Values for adaptation simulations using a dead zone threshold of 250$\mu\varepsilon$ and 1000$\mu\varepsilon$ are compared. The differences are negligible.

	MSL=0.7mm						MSL=1.5mm					
	Dead Zone < 250με		Dead Zone < 1000με				Dead Zone < 250με		Dead Zone < 1000με			
	NN04	V	NN04	Δ	V	Δ	NN04	V	NN04	Δ	V	Δ
Uniaxial	99.3	96.1	98.8	-0.48%	95.6	-0.56%	104.3	97.6	104.6	0.30%	97.7	0.07%
Triaxial	187.6	165.2	187.4	-0.14%	165.1	-0.06%	188.6	171.6	188.4	-0.10%	171.6	-0.01%

Table 6.7: Comparison of trabecular volume [mm^3] at the end of the adaptation between simulations using dead zone threshold of 250$\mu\varepsilon$ and 1000$\mu\varepsilon$. NN04 and Voronoi(V) simulations each with MSL of 0.7mm or 1.5mm are compared. In addition to absolute trabecular volume values the results for dead zone threshold of 1000$\mu\varepsilon$ include the percentage difference (Δ) from the results for dead zone threshold of 250$\mu\varepsilon$.

.

	MSL=0.7mm						MSL=1.5mm					
	Dead Zone < 250με		Dead Zone < 1000με				Dead Zone < 250με		Dead Zone < 1000με			
	NN04	V	NN04	Δ	V	Δ	NN04	V	NN04	Δ	V	Δ
Uniaxial	656.7	661.7	655.5	-0.18%	661.6	-0.01%	650.2	651.2	651	0.10%	652.6	0.20%
Triaxial	742	756.4	742.1	0.01%	756.2	-0.03%	736.4	736.2	735.4	-0.10%	735.9	-0.03%

Table 6.8: Comparison of Young's modulus [MPa] at the end of the adaptation between simulations using dead zone threshold of 250$\mu\varepsilon$ and 1000$\mu\varepsilon$. NN04 and Voronoi(V) simulations each with MSL of 0.7mm or 1.5mm are compared. In addition to absolute trabecular volume values the results for dead zone threshold of 1000$\mu\varepsilon$ include the percentage difference (Δ) from the results for dead zone threshold of 250$\mu\varepsilon$.

.

Table 6.9 presents the predicted ITAs at the end of Voronoi and NN04 adaptation simulations. Values for adaptation simulations using a dead zone threshold of 250$\mu\varepsilon$ and 1000$\mu\varepsilon$ are compared. Differences are small with the only appreciable changes in ANC3 nodes for triaxial NN04 simulations with both MSLs and a Voronoi simulation with MSL of 1.5mm. The abundance of ANC3 nodes markedly increases in all three of these simulation affecting the ITA predictions.

Loading	ANC	Statistical measure	MSL=0.7mm				MSL=1.5mm			
			Dead Zone < 250με		Dead Zone < 1000με		Dead Zone < 250με		Dead Zone < 1000με	
			NN04	V	NN04	V	NN04	V	NN04	V
Uniaxial	3	Mean	103.4	112.5	105.6	112.5	98.3	111	101	111.7
		SD	34	34.2	33.5	32.3	33.9	33.9	33.8	31.2
		Median	99.6	109.1	102	109.4	94.4	107.5	97	108.8
	4	Mean	99	109.3	100.8	109.1	96.7	107.6	98.7	107.7
		SD	33	31.3	32.6	30	33.1	32.3	33.4	33.4
		Median	95.4	106.3	97	106.4	92.9	104.4	95	104.3
	5	Mean	99.8	-	100.6	-	98.2	-	100.1	-
		SD	33	-	32.2	-	33.3	-	32.7	-
		Median	96	-	97	-	94.5	-	97	-
Triaxial	3	Mean	-	-	104	-	91.1	111.7	98.4	105.2
		SD	-	-	34.1	-	31.5	56.9	33.7	100.9
		Median	-	-	100	-	87.5	102.2	95	36.9
	4	Mean	97.1	109.1	99.7	109.1	92.4	107.4	94.5	107.4
		SD	33	31.6	32.8	30.8	32.6	31.9	32.6	104.4
		Median	93.4	106.1	96	106.2	88.6	104.2	91	31.2
	5	Mean	99.3	-	100.5	-	96.9	84.6	98.6	-
		SD	33	-	32.4	-	33.2	35.8	33	-
		Median	96	-	97	-	93.1	79.6	95	-

Table 6.9: Comparison of ITAs for ANC3, ANC4 and ANC5 between simulations using dead zone threshold of 250$\mu\varepsilon$ and 1000$\mu\varepsilon$. NN04 and Voronoi(V) simulations each with MSL of 0.7mm or 1.5mm are compared. ITAs were not shown for ANCs with 5% predominance or less as given in the Table 6.6

NN14 simulations predict a greater degree of directionality when the dead zone threshold is increased to 1000$\mu\varepsilon$ than any other simulation. The NN14 simulations initially have a minimum of 14 struts with different directions at each node which would suggest that this simulation would achieve greater directionality regardless of the dead zone threshold magnitude. However, as illustrated by Figure 6.13, a significant number of elements in one NN14 model experience a strain above 250$\mu\varepsilon$ at the end of the first iteration. As a consequence, and despite a large number of load paths available in the model, a significant number of elements not aligned with the load directions, shown in light blue in Figure 6.13, are retained through to convergence. When the dead zone threshold is increased to 1000$\mu\varepsilon$ these elements are deactivated during adaptation and a more directionally aligned architecture, shown in green, emerges.

In the Voronoi model presented in Figure 6.13 all elements at the end of first iteration experience a high strain of between 530,000$\mu\varepsilon$ and 800,000 $\mu\varepsilon$. This is approximately four to five times higher than the lazy zone upper limit. In the second iteration the elements increase in size and a larger differentiation in the strain magnitude is evident. Very few if any elements are deactivated. Between the second iteration and the convergence elements undergo a further size adjustment which could be described as 'fine tuning'. A small number of elements are deactivated and this is more evident in the simulation with the dead zone of 1000$\mu\varepsilon$. The NN04 model which has a similar topology behaves in a similar way. Trabecular directionality in this model develops by the growth of elements aligned with the load direction. This supports the hypothesis posed by Reznikov et al. (2017) that trabecular bone anistropy emerges form a biological blueprint.

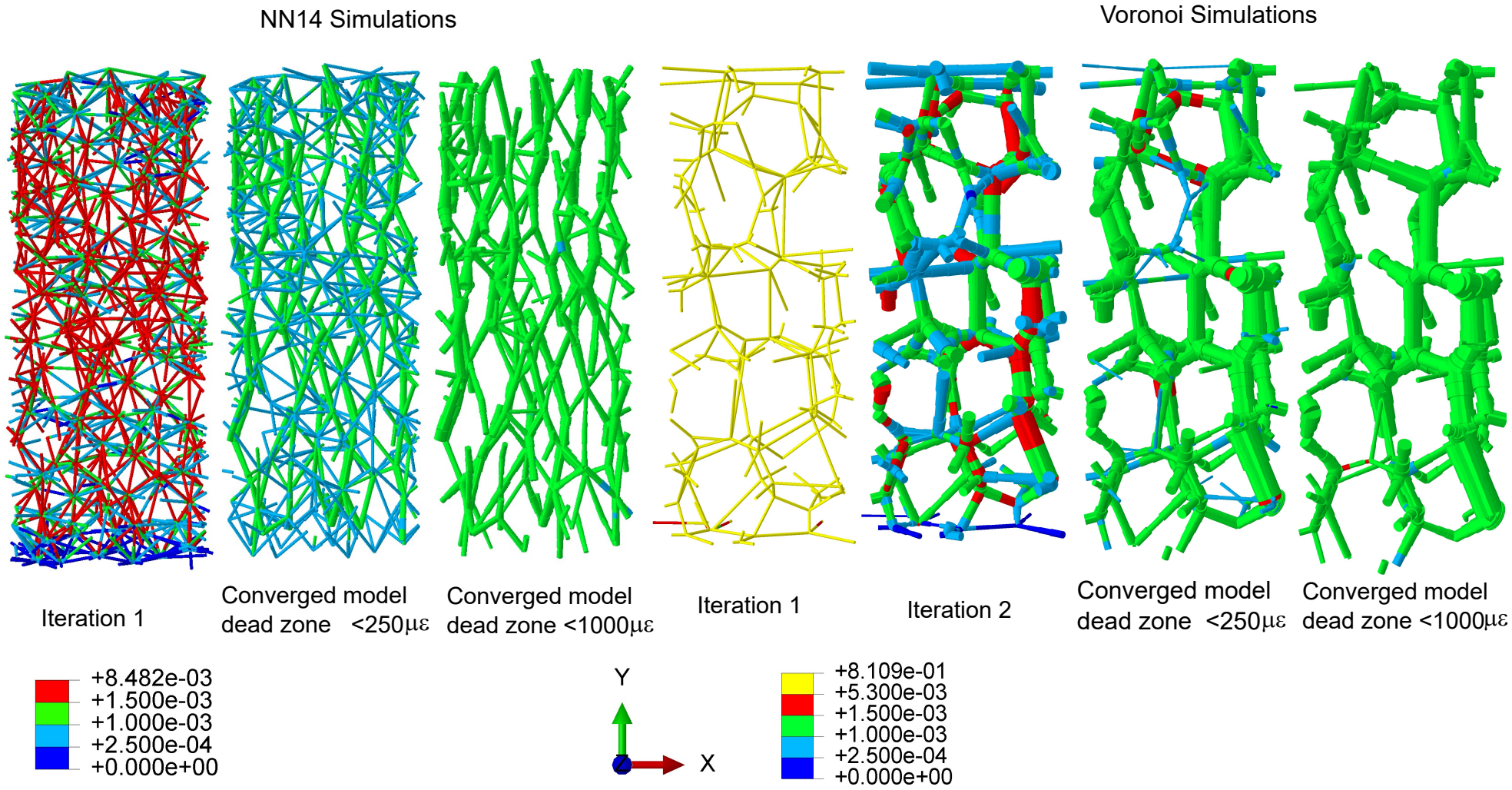


Figure 6.13: A 3mm wide by 2mm thick slices through the full 8mm height of one of Voronoi and NN models with initial connectivity 14 at he start and the end of simulations showing the absolute maximum total strain. The Voronoi model additionally shows the strains at the end of the second iteration as the large strain magnitude at the end of the first iteration prevents meaningful differentiation and comparison.

Figure 6.14 presents the element radii distributions comparing the results between the simulations using a dead zone threshold of 250$\mu\varepsilon$ and 1000$\mu\varepsilon$. The most notable observation is that there is no difference in distributions with and without the elements of the smallest radius for simulations with the dead zone threshold of 1000$\mu\varepsilon$. This is confirmed by Table 6.10 which supplements this Figure and identifies the smallest element radius of 28.8$\mu\varepsilon$ in these simulations.

The mean and median radii are larger in all simulations with dead zone threshold of 1000$\mu\varepsilon$ than corresponding ones with dead zone threshold of 250$\mu\varepsilon$. Standard deviations are smaller in simulations with MSL of 0.7mm but larger in ones with MSL of 1.5mm.

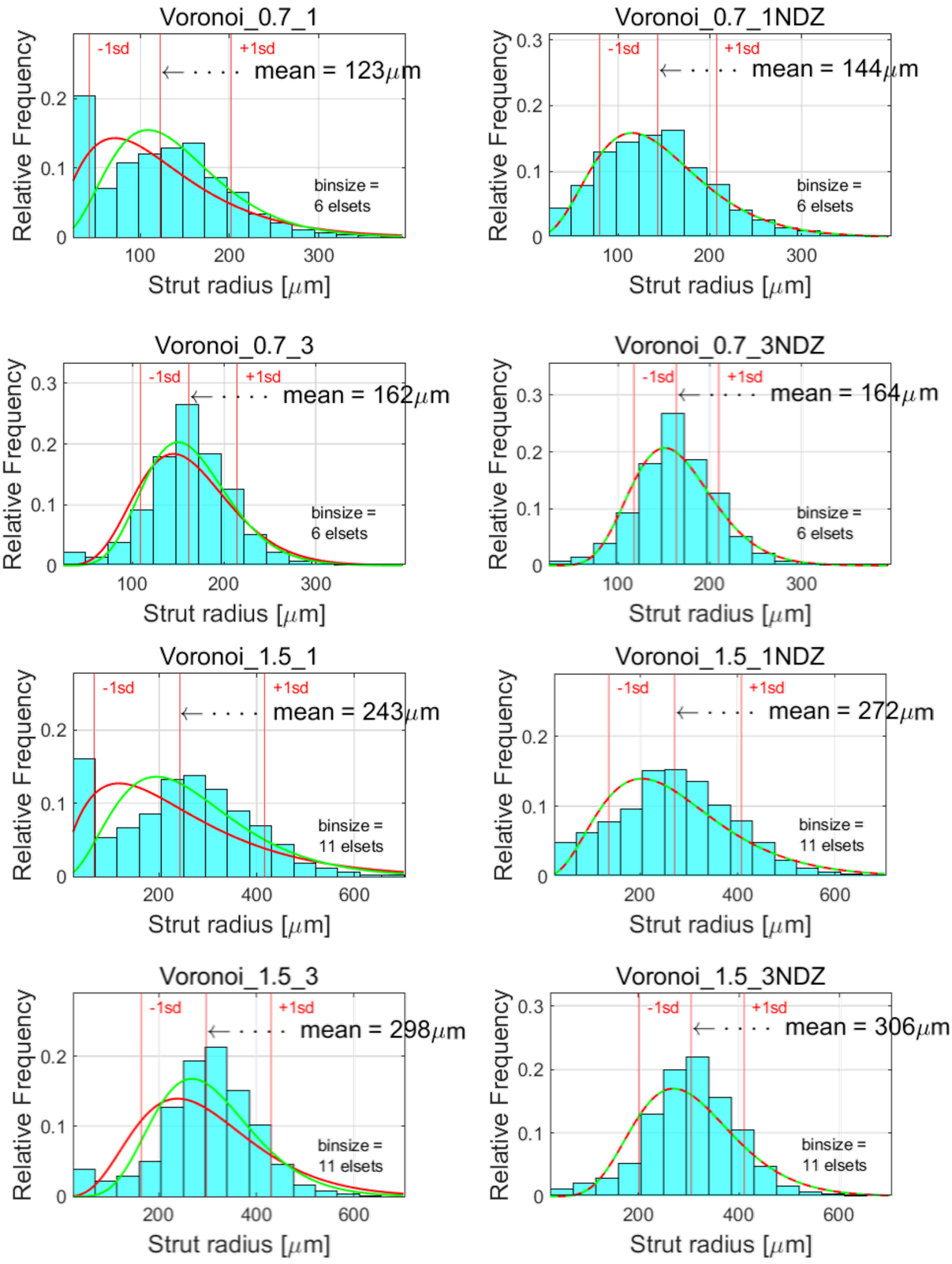


Figure 6.14: Comparison of strut radii distributions for Voronoi adaptation simulations. Each diagram presents simulation data combined from 5 randomly generated models and the headings identify the MSL and the loading. Letters NDZ signify that a dead zone threshold of 1000$\mu\varepsilon$ has been used. Each bar represents a number of strut radii element sets and the number of sets is annotated on diagrams. The histogram in light blue and the red distribution curve represent the full set of data. The distribution curve in green excludes the elements with the smallest radius of 25μm.

MSL [mm]	Simulation	Dead zone	Loading	Strut radius [μm]					
				Mean	95\% CI +/-	Median	SD	Min	Max
0.7	Voronoi	< 250με	Uniaxial	122.9	69.4	106.3	79.2	25	474.1
			Triaxial	161.8	45.9	156.1	52.4	25	401.2
		< 1000με	Uniaxial	143.5	55.6	134.3	63.4	28.8	455.9
			Triaxial	163.9	40.2	159.6	45.9	28.8	389.7
	NN04	< 250με	Uniaxial	107.7	66.0	90.8	75.3	25	470.3
			Triaxial	138.8	60.9	127.4	69.5	25	428.1
		< 1000με	Uniaxial	131.4	55.9	121.2	63.8	28.8	469.3
			Triaxial	148.2	47.9	141.5	54.7	28.8	454.9
1.5	Voronoi	< 250με	Uniaxial	167.4	103.4	140.6	118	25	524
			Triaxial	219.2	68.1	210.1	77.7	25	466.4
		< 1000με	Uniaxial	270.8	118.6	248.6	135.3	28.8	661.2
			Triaxial	305.1	91.7	293.2	104.6	28.8	637.3
	NN04	< 250με	Uniaxial	152.6	100.6	125	114.8	25	639.2
			Triaxial	192.3	89.1	174.8	101.6	25	554.7
		< 1000με	Uniaxial	248.9	120.9	223.9	137.9	28.8	854.1
			Triaxial	284.2	104.8	267.6	119.6	28.8	742.8

Table 6.10: The mean, 95% Confidence intervals (CI), median, standard deviation(SD), the minimum (Min) and the maximum (Max) of active strut radii for Voronoi and NN04 simulations. Statistical distributions are calculated from 5 randomly generated models with either 0.7mm or 1.5mm MSL, simulation type and loading as shown. The strut radius has been calculated as the average of 4 element radii making up each strut, in line with methodology of other topological studies (Liu et al. (2008), Kirby et al. (2020)).

6.4 Discussion

Functional adaptation simulations using Voronoi models presented in this chapter and NN04 simulations presented in Chapters 4 and 5 predict trabecular architectures which compare favourably with in-vivo and imaging observations. Predictions from simulations using MSL of 0.7mm compare more favourably than the others. These adaptations result in mean ANCs of between 3.4 and 4.8 which compare well with approximate mean NC of 3.4 for real bone reported by Reznikov et al. (2016). The predicted mean ITA values for ANC3 nodes were 112.5° and 103.4°for Voronoi and NN04 simulations respectively. These values compare favourably with the value of 107.6°reported by Reznikov et al. (2016) and the tetrahedral bond angle of 109.5°. However, a dead zone threshold limit increase to 1000$\mu\varepsilon$ resulted in an even closer resemblance to real bone. Some topological predictions also became closer to those observed in the literature.

The relative density and Young's modulus predictions are derided from simulations using a 1.0MPa loading. Whilst this loading is representative of joint contact pressure it is by no mean universal to the skeletal system. The impact of this is considered in the trabecular thickness discussion towards the end of this section. Notwithstanding this limitation, the relative density and Young's modulus values predicted by Voronoi model simulations at macro-scale compared favourably with those reported in the literature. The predicted relative density varied from 0.188 (95% CI [0.184, 0.191]) for simulations subjected to uniaxial loading to 0.335 (95% CI [0.333, 0.337]) for simulations subjected to triaxial loading. A significant number of relative density values are reported in the literature, some of which include an average of 0.152 (Linde et al. (1992)) and a range between 0.05 and 0.3 (Gibson (2005)). Ciarelli et al. (1991), Goulet et al. (1994) and Morgan et al. (2003) report ranges of 0.15-0.4, 0.06-0.36, and 0.046-0.42 respectively. There was a small variation of 3.9% in predicted relative density between Voronoi simulations using the MSL of 1.5mm and 0.7mm. The predicted relative density was lower in Voronoi simulations than in NN04 models. The difference for simulations of corresponding MSL and loading varied from 3.9% to 14.4%.

In consideration of the model, and by extension real bone, stifness in orthogonal dir-

ections it is useful to consider the concept of robustness. Structural design codes define robustness as the ability of a structure to withstand events like fire, explosions, impact or the consequences of human error, without being damaged to an extent disproportionate to the original cause (BSE (2014)). Applying this principle to bone, robustness would be considered as its ability to withstand the loading, from an event such as a fall or an impact, that it is not commonly applied and the bone hasn't adapted to without a significant fracture.

The predicted stiffness values in three principal directions were approximately the same following the adaptation simulation using the triaxial loading scenario, as was noted for NN simulations in Chapter 4 . When subjected to isotropic loading, the adapted structure resembled an isotropic material. The difference between the E_2 predictions for Voronoi and NN simulations was under 2% for both uniaxial and triaxial simulations (Figure 6.8). In terms of absolute values, the predicted value of E_2 to three significant figures varied from 651MPa (95% CI [628MPa, 675MPa] for uniaxial loading simulations to 756MPa (95% CI [736MPa, 777MPa]) for triaxial loading simulations. This compares favourably with a large number of Young's modulus values reported in the literature and summarised here. Linde et al. (1992) reviewed 25 studies which tested human trabecular bone specimens and recorded Young's modulus range of between 78MPa and 673MPa, whilst (Gibson (2005)) reports a wide range of between 100MPa and 1000MPa. Goulet et al. (1994) and Ciarelli et al. (1991) carried out platen tests on 8mm x 8mm x 8mm bone samples and recorded Young's modulus ranges of 17MPa to 738MPa and 494MPa to 2379MPa respectively.

However, the adaptation simulations using the uniaxial loading scenario predict significant differences between the stiffness in the direction of the applied load (E_2) and the other two principal directions (E_1 and E_3). Voronoi simulations predict 40-50% higher values of E_1 and E_3 for this loading in 0.7mm MSL simulations than the NN04 simulations. This makes them more robust against an accidental loading applied in a direction not aligned with the principal axis. The robustness changes in favour of NN04 models for simulations using the MSL of 1.5mm. The E_1 and E_3 values were 20-25% higher in these simulations than the equivalent Voronoi ones. The higher resistance to off axis loading of 0.7mm MSL Voronoi and 1.5mm MSL NN04 simulations is confirmed by the

shear moduli predictions presented in Table 6.11. G_{12} and G_{23} values are approximately 10% higher in 0.7mm MSL Voronoi simulations than equivalent NN04 ones. In 1.5mm MSL NN04 simulations values of these modulii are approximately 30% higher. The reduction in resistance of Voronoi simulations to out of plane loading with increase in MSL is caused by a higher degree of directional alignment evident in Table 6.12. The struts aligned with the load direction in the Voronoi simulations with 1.5mm MSL increase in size at the expense of the orthogonal ones, resulting in the reduced stiffness in directions perpendicular to the load.

		NN04			Voronoi		
		G_{12}	G_{13}	G_{23}	G_{12}	G_{13}	G_{23}
MSL=0.7mm	Mean	11.5	37.0	11.6	13.0	42.9	12.7
	SD	2.2	3.0	1.6	1.2	3.4	1.0
	95% CI +/-	1.4	1.8	1.0	0.7	2.1	0.6
MSL=1.5mm	Mean	10.2	36.8	10.1	7.9	31.9	7.3
	SD	3.5	8.4	2.5	3.5	6.3	2.2
	95% CI +/-	2.2	5.2	1.5	2.2	3.9	1.4

Table 6.11: Shear modulus [MPa] value predictions for NN04 and Voronoi simulations subjected to uniaxial loading. Mean, standard deviation and confidence intervals are calculated from 5 model results for each simulation.

With such similar predictions of Young's modulus and relative density, it follows that Voronoi and NN04 simulations demonstrate a similar relationship between the Young's modulus and relative density and behave as bending dominated lattices. The constants α and β, as defined by Equation 1.2, have a similar magnitude in both. β values vary between 1.32 and 1.48, with value of 1 indicting a stretch dominated and 2 a bending dominated lattice (Gibson & Ashby (1997)). However, the trabecular architecture predicted by Voronoi simulations is marginally less dense but stiffer than that predicted by NN04 simulations. This results in slightly greater structural efficiency. Evaluated as a ratio of Young's modulus to trabecular volume (Table 6.1), predictions are from 4% to 7% and from 10% to 14% higher for Voronoi simulations subjected to uniaxial and triaxial loading simulations respectively. Nevertheless, based on mechanical property predictions and structural efficiency the only thing that distinguishes the Voronoi and

NN simulations is the greater robustness at 0.7mm MSL.

Voronoi simulations appear to predict topology which more closely resembles real trabecular bone than the NN04 simulations. The mean NC at the end of the adaptation varies between 3.4 and 4.1 depending on the MSL and the loading scenario. These values range from 4.0 to 4.8 in NN04 simulations where the predictions are closest to Voronoi simulations. With the increase in dead zone threshold the NC at the end of adaptation decreases in all simulations but more so in ones with high NC. For instance, in the NN14 simulations subjected to uniaxial loading, the connectivity decreases from 9.6 to 3.2. However, the Voronoi simulations predict mean connectivity of 3.2 for uniaxial and 4.0 for triaxial loading simulations which most closely match those reported in imaging studies.

Under triaxial loading, connectivity undergoes little change through the adaptation simulations particularly for low NNC simulations. For instance, in Voronoi models with MSL of 0.7mm the mean connectivity at the beginning and the end of the adaptation is 4.1. With the increase in dead zone threshold the mean NC only reduces by 0.1 to 4.0 Real bone does not experience either uniaxial or triaxial loading and it is likely that subjected to more realistic loading the final connectivity would be somewhere between the two. This would closely agree with topological studies of trabecular bone CT images which report a mean connectivity of about 3.4 (Reznikov et al. (2016). With the increase in dead zone threshold, the NN04 and NN14 simulations subjected to uniaxial loading predict the mean connectivity of 3.4 and 3.8 respectively which approach the value reported by Reznikov et al. (2016). However, triaxial loading simulations for these simulations predict a higher NC of 4.4 and 7 at the end of adaptation. Simulations using models with higher MSL in Voronoi simulations predict the mean NC which is comparable to that of models with lower MSL. However NN models with higher MSL predict higher NC at the end of the adaptation than their equivalents with lower MSL.

In addition to being a metric in it's own right, connectivity has an influence on the ITA. The mean predicted ITA for ANC3 nodes in uniaxial loading simulations is approximately 112° compared to approximately 100° for ANC5 nodes. Struts connected to nodes with fewer other struts occupy a larger volume and need to achieve a larger separation to do so efficiently. As they all terminate at a single point, the separation is

achieved by a greater angle between them. The ideal ITAs were discussed in Chapter 5 and illustrated in Figure 5.16. It is well recognised in organic chemistry that carbon molecules which contain 5 atoms have bonds with angles of 109.5 between them (Marks et al. (1996)). This bond is referred to as a tetrahedral bond where the arrangement consist of 4 atoms at vertices of a tetrahedron and one in its centre. As tetrahedrons efficiently fill space (Goldberg (1974)) it can be inferred that molecules with this bond do the same. The predicted ITA for ANC4 nodes in Voronoi simulations vary from 107.4° to 109.3° depending on the MSL and the loading which is close to the theoretical tetrahedral bond and the mean ITA of 107.4° for NC4 nodes reported by Reznikov et al. (2016). The predicted ITA for ANC3 nodes in uniaxial Voronoi simulations vary from 111.0° to 112.5° and do not correspond as well with the ideal ITA of 120° and that reported by Reznikov et al. (2016) of 116.3°. The predicted ITA of between 111.7° to 118.4° for triaxial Voronoi simulations are a better match. Finally, the predicted ITA for ANC5 nodes of 99.7°in Voronoi uniaxial simulation with MSL 0.7mm is the closest match to the ideal ITA of 108°and that reported by Reznikov et al. (2016) of 103.1°.

In simulations subjected to triaxial loading, the mean ITA in ANC3 nodes increases, stays relatively unchanged in ANC4 nodes and decreases for ANC5 nodes. This is caused by the decrease in prevalence of ANC3 nodes and increase of ANC4 and ANC5 nodes (Table 6.3). In the triaxial loading simulation more struts are simulated with strains above the dead zone threshold, resulting in a higher predicted NC and reducing the number of ANC3 nodes to about 1%. On the other hand, the prevalence of ANC4 nodes increases from about 60% to over 92%. With such a high prevalence of ANC4 nodes, a further increase is not likely to introduce much variability and influence the mean and this is borne out by standard deviation values which remain unaffected. However, the mean ITA does decrease in ANC5 nodes despite the prevalence remaining similar in both uniaxial and triaxial simulations.

In NN04 simulations, the greater ANC in simulations subjected to triaxial loading influences the ITA in a different way. The increase in prevalence of ANC4 and ANC5 nodes causes a decrease in the mean ITA. With the NN04 simulations the relatively small increase in prevalence of ANC4 nodes from approximately 42% to 46% (Table 6.3) has a significant effect on reducing the mean ITA, whereas a much larger increase

in prevalence in the Voronoi simulations does not. The prevalence of ANC5 nodes increases and the mean ITA decreases in both the Voronoi and NN04 simulations. In NN04 models, the prevalence of ANC3 nodes decreases and the mean ITA decreases which is opposite to what happens with Voronoi models. Voronoi models are generated using Delaunay triangulations which are know to maximise the minimum angles (Chen & Xu (2004)). This is not the case in the NN04 model generation resulting with more struts with smaller angles between them,thus reducing the mean ITA.

The increase in dead zone threshold has a negligible effect on Voronoi mean ITA, it marginally increases the mean ITA in NN04 simulations subjected to uniaxial loading, significantly increases them for those subjected to triaxial loading and in all NN14 simulations. In NN14 simulations using the dead zone threshold of 250$\mu\varepsilon$ predicted an absence of ANC3 ANC4 and ANC4 nodes but predict mean ITAs comparable with those predicted by Voronoi simulations for these ANCs when the dead zone threshold is increased to 1000$\mu\varepsilon$.

The NC and ITA predictions suggest that Voronoi simulations yield closer predictions to real bone whilst NN14 simulation's radii predictions more closely match the real trabecular bone thickness. The NN14 simulations predict a mean radius of between 31μm and 40μm which closely compare to real bone mean trabecular thickness of approximately 100μm to 120μm (Stauber & Müller (2006), Liu et al. (2008), Zhao et al. (2018)). However, the distribution curves of all four of these simulations have a high right skew and a very large number of elements with the smallest radius. The radii distribution curves which exclude the elements with the smallest radius of 25μm more closely resemble distribution observed in real bone (Figure 5.1). The mean radius predictions further increase to a maximum of 64μm and 91μm in simulations with MSL of 0.7mm and 1.5mm with dead zone threshold of 1000$\mu\varepsilon$. These mean radii remain closely matched to the real bone thickness and the radii distributions provide a better match then those obtained when the dead zone is set at 250$\mu\varepsilon$.

Both the NN04 and Voronoi predictions compare less well with real bone mean trabecular thickness of approximately 100μm to 120μm (Stauber & Müller (2006), Liu et al. (2008), Zhao et al. (2018)). The NN04 simulations with 0.7mm MSL predict the mean radii of 108μm and 139μm for uniaxial and triaxial loading when the dead zone

threshold of 250$\mu\varepsilon$ is used. The predominance of elements with the smallest radii is large. These predictions change to 131μm and 148μm when dead the zone threshold is increased to 1000$\mu\varepsilon$. For MSL of 1.5mm these values are 212μm, 267μm, 249μm and 284μm. The Voronoi simulations with 0.7mm MSL predict a mean trabecular radius of 123μm and 162μm for uniaxial loading and triaxial loading simulations when the dead zone threshold of 250$\mu\varepsilon$ is used. The predominance of elements with the smallest radii is large. For MSL of 1.5mm these values are 144μm, 164μm, 272μm and 306μm. NN04 simulations overpredict the prevalence of elements with the smallest radii values in models and skew trabecular radii distributions towards them. In Voronoi models the smallest radii skew is only evident in uniaxial loading simulations. The triaxial loading stimulates a sufficient number of elements to a higher magnitude so that the adaptation algorithm assigns larger radii to a greater number of elements.

Some of this discrepancy between real bone and the NN04 and Voronoi predictions may be caused by the lack of plate like trabeculae in the simulation models. This is discussed in Chapter 5 and Figure 5.17 presents a simplified example of how the bending stiffness of 5 circular elements may be replicated by a singe plate element. It demonstrates that the bending stiffness of 148μm can be replaced by a single plate 3mm long by 75μm thick. This very simplified localised calculation demonstrates how introduction of a relatively small number of plates in a large bone model may lead to the reduction of mean overall trabecular thickness.

In addition trabecular thickness as well as the relative density and Young's modulus predicted by the simulations in this thesis are dependant on the applied loading of 1.0MPa. Trabecular bone elastic properties and size vary with different anatomic sites, and change with ageing and disease (Morgan & Keaveny (2001)). Morgan et al. (2003) have shown that modulus density relationships are also influenced by the anatomic site. It is likely that this variability is at least partly influenced by the loading and whilst 1.0MPa is considered representative of the loading on trabecular bone in joint contact sites (Harris et al. (2012)) it doesn't act everywhere. Consequently different predictions would be obtained for sites with different loading environments.

The ability of simulations to predict trabecular trajectories is now discussed. The strain plots presented in Figures 6.4 and 6.5 demonstrate very similar architecture in

Voronoi and NN04 simulations subjected to uniaxial loading. A significant number of elements are shown aligning with the load direction. In order to quantify this directionality absolute values of vector components of each element were multiplied by their respective areas creating three values for each element. All area weighted components were added together and normalised. The resulting three values are refereed to as direction index and are given in Table 6.12 for six different simulations. A value of the direction index closer to 1 in a particular direction signifies a higher degree of alignment in that direction. NN14 simulation is included as Chapter 5 identified this simulation's ability to closely match trabecular trajectories with the applied loading direction. In addition the ability of high NC models to do this was identified in previous work by Phillips et al. (2015), Zaharie & Phillips (2018) and Favier et al. (2021).

		Voronoi			NN04			NN14		
		Direction indices								
		X	Y	Z	X	Y	Z	X	Y	Z
MSL=0.7mm	Dead Zone < 250με	0.47	0.74	0.48	0.49	0.72	0.49	0.46	0.75	0.47
	Dead Zone <1000με	0.46	0.76	0.47	0.49	0.72	0.49	0.34	0.87	0.35
MSL=1.5mm	Dead Zone < 250με	0.38	0.83	0.41	0.49	0.74	0.46	0.31	0.90	0.31
	Dead Zone <1000με	0.38	0.83	0.41	0.49	0.74	0.46	0.29	0.91	0.29

Table 6.12: Direction index for a single model of Voronoi, NN04 and NN14 simulations with 0.7mm and 1.5mm MSL and dead zone thresholds of 250$\mu\varepsilon$ and 1000$\mu\varepsilon$. The values given are element area weighted absolute values of vector components.

Table 6.12 shows that all simulations with 0.7mm MSL predict similar directionality following the adaptations with dead zone threshold of 250$\mu\varepsilon$ with the Y direction index of between 0.72 and 0.75. However, NN14 simulations predict a greater degree of directionality when the dead zone threshold is increased to 1000$\mu\varepsilon$. At first, this appears counter-intuitive. The NN14 simulations initially have a minimum of 14 struts with different directions at each node which would suggest that this simulation would achieve greater directionality regardless of the dead zone threshold magnitude. However, as illustrated by Figure 6.13, a significant number of elements in one NN14 model experience a strain above 250$\mu\varepsilon$ at the end of the first iteration. As a consequence, and

despite a large number of load paths available in the model, a significant number of elements not aligned with the load directions, shown in light blue in Figure 6.13, are retained through to convergence. When the dead zone threshold is increased to 1000$\mu\varepsilon$ these elements are deactivated during adaptation and a more directionally aligned architecture, shown in green, emerges. In the Voronoi model presented in Figure 6.13 trabecular directionality develops by the growth of elements aligned with the load direction. This supports the hypothesis posed by Reznikov et al. (2017) that trabecular bone anistropy emerges form a biological blueprint. The NN04 model which has a similar topology behaves in a similar way.

Directional alignment of the NN04 model is not influenced by the increase in dead zone threshold and is similar to that of NN14 model when the dead zone threshold is set at 250$\mu\varepsilon$. The effect of 250$\mu\varepsilon$ dead zone threshold on NN14 model is to retain struts which loosely follow the load direction. At macro-scale these individual struts present as their vector summation to a larger single strut. Hence, directionality is similar.Voronoi simulations have a comparable mean connectivity of 4 but do not offer as many load paths as NN04 simulations and derive their directional alignment from their space filling efficiency. In order to generate simulations with a MSL of 0.7mm, NN04 simulations required an average of 1600 joint nodes, whilst in Voronoi simulations this number was 1349; 15.7% smaller. In addition, shortest path analysis from a node nearest to the centre of the bottom face (x=4, y=0 z=4) to a node nearest to the centre of top face (x=4, y=8 z=4) was undertaken using Matlab. The average distance for 5 NN04 models was 10.3mm, whilst it was 10.1mm for the 5 Voronoi models. Both of these measures indicate that the Voronoi and NN04 simulations have similar capability for strut alignment with the loading direction.

Whilst both NN04 and Voronoi simulations with 0.7mm MSL exhibit similar directionality, Voronoi simulations with 1.5mm MSL show a higher degree of alignment with the loading direction than the equivalent NN04 simulations (Table 6.12). The hypothesis that this is caused by a fewer struts aligned with the loading direction in Voronoi simulations was explored by the consideration of the total number of struts and the shortest path analysis from the loaded to the supported faces. The mean number of struts in Voronoi simulations is 401 as opposed to 474 in NN04 simulations, 15% fewer. The

average of 10 shortest paths was 11mm and 10.8mm for Voronoi and NN04 simulations respectively. This indicates that, as hypothesised, the Voronoi models have fewer direct paths from the loaded to the supported face. The elements along these paths experience high strains in early iterations and, guided by the adaptation, their area increases. Model stiffness in this direction increases which attracts load and increases strains. Eventually an equilibrium is reached but as a consequence the Voronoi simulations display a higher degree of alignment with load direction.

6.5 Summary

Voronoi, NN simulations with either high NNC or with bending dominated behaviour predict continuum level mechanical properties consistent with the ranges for anatomical sites reported in experimental studies. Voronoi simulations predict a trabecular architecture which is more structurally efficient and display greatest robustness at MSL of 0.7mm.

Regrading the topology predictions, Voronoi simulations predict NC which compares most favourably with values reported in the imaging study by Reznikov et al. (2016). The predicted ITAs in these simulations are closest to the ideal values and correspond well with those reported in the imaging study. None of the simulations presented in this thesis predict trabecular thickness which compares well with real bone. One of the reasons for this discrepancy may be the lack of plate like trabeculae in the simulation models. The representative loading environment would also have a bearing on these predictions.

Unexpectedly a dependence of the modulus density relationships on the MSL has been identified. The simulations with shorter MSL have been found to be more efficient. This is not well understood but may be caused by shear deformations which are not considered in the simplified modulus density relationship developed by Gibson & Ashby (1997). Their work explores this and concludes that the simplified relationships yields good approximations but that shear deformations can be significant. The simulations with MSL of 0.7mm have higher shear modulii than the ones with 1.5mm (Table 6.11).

Consequently shear deflections make a larger contribution to overall displacements in 1.5mm MSL simulations leading to somewhat lower modulii for the same relative density.

Voronoi simulations emerge as the most favourable candidate for representation of trabecular bone. As discussed in Chapter 2 Imperial Structural Biomechanics research group successfully used NN simulations with high NNC to obtain accurate representation of trabecular bone at meso-scale and predicted behaviour such as fracture (Villette & Phillips (2018)). Chapter 7 will now examine two femur models using 0.7mm MSL to compare the behaviour of the Voronoi and NN14 simulations to compare the predictions of trabecular trajectories, connectivity, strut radius and mechanical properties. As stated earlier the high NC models used in previous studies (Phillips et al. (2015), Zaharie & Phillips (2018),Villette & Phillips (2018) Favier et al. (2021)) predictions compare well with real bone. Implementing a NN14 and a Voronoi simulation on a proximal femur would allow a comparison with this previous work.

7

Proximal femur adaptation simulations

7.1 Introduction

Early femur adaptation simulations used phenomenological 2D continuum macro-scale models with simplified loading scenarios and relied on a stress, strain or strain energy density scalar stimuli to drive adaptations. Material properties were assigned in accordance with empirical relationships between density and Young's modulus (Carter & Hayes (1977)). These studies were able to predict variations in bone mass which correlated well with ex-vivo sections and x-ray findings. However, they provided limited resolution of trabecular bone, identifying main trabecular groupings and directionality only through concentrations of increased density finite elements. More detailed predictions of trabecular directionality were achieved by 3D model simulations using more representative loading cases, such as the study by Bitsakos et al. (2005) and through consideration of orthotropy by Geraldes & Phillips (2014).

Micro-scale model simulations (Tsubota et al. (2002), Boyle & Kim (2011), Jang & Kim (2008)) achieved good agreement between predicted and actual trabecular architectures, but at great computational expense. These simulations treat bone as either being present or not; adding material in regions of high mechanical signal modelling apposition and removing it in regions of low mechanical signal modelling resorption. A small number of simplified load cases representing a range of daily activities were applied in simulations driven by either a stress or strain scalar stimulus. Micro-scale simulations require a high initial resolution and this makes model validation and comparison to real bone difficult.

Structural models have achieved good agreement with ex-vivo tests (van Lenthe et al. (2006) and have achieved a qualitatively favourable comparison with bone architecture in several anatomic sites including the femur, pelvis and spine (Phillips et al. (2015), Villette & Phillips (2017), Zaharie & Phillips (2018), Favier et al. (2021)) whilst offering computational efficiency over continuum models. The resulting structural models of the femur provide good predictions of fracture loads and fracture patterns (Villette & Phillips (2018)). However, the ability of such models to predict trabecular properties at micro-scale is unclear in the context of recent work by authors such as Reznikov

et al. (2016, 2020).

The work reported in Chapters 4, 5 and 6 demonstrates that both Voronoi and near neighbour (NN) simulations predict continuum level mechanical properties consistent with those reported in experimental studies, regardless of the initial connectivity. The simulations using a shorter mean strut length (MSL) of 0.7 mm predict marginally more efficient structures. A hypothesis proposed in Section 6.5 is that this is due to smaller shear displacements in these simulations which have a higher shear modulus. However, low nominal node connectivity (NNC) bending simulation predictions of connectivity, inter trabecular angle (ITA) and trabecular radii are closest to those recorded in topological studies of trabecular bone CT images (Reznikov et al. (2016)). Voronoi simulation predictions compare marginally better to real bone than low NNC NN simulations, whilst NN with NNC of 14 (NN14) simulations, which aggressively deactivate elements with a low stimulus, also perform well.

The aim of this chapter was to compare the bone adaptation predictions of a Voronoi low connectivity bending lattice model and a high connectivity NN lattice model at the macro scale of the proximal femur. This has allowed a comparison of the novel trabecular bone model presented in this thesis with the established modelling methodology used by the Structural Biomechanics Group at Imperial (Phillips (2012), Phillips et al. (2015), Villette & Phillips (2017)).

7.2 Methodology

7.2.1 Finite element model

The finite element (FE) model was created from an existing anonymised external geometry of the proximal femur for which subject information was unavailable. An IGS format graphics file of the proximal femur external envelope was imported into Rhinoceros/Grasshopper and used to create a mesh of 10,079 triangular shell elements with 2mm nominal edge length representing the cortical bone.

A lattice of struts representing trabecular bone was then generated within this cortical bone envelope in one of two ways. For the Voronoi model the femur envelope was bounded by a closely fitted box, the edges of which are shown in green in Figure 7.1. This box was populated by random points, the number of which was controlled by the user. The points outside the femur envelope shown in red in Figure 7.1 were deleted and the remaining ones depicted in blue crosses were used as Voronoi seeds. Some of the voronoi cells generated were internal to the femur envelope and some had edges crossing the envelope. The edges which crossed the femur envelope were divided at the intersection and the external parts shown in green were deleted. The blue portions inside the femur and the whole cells shown in blue were retained. The cell edges were extracted, merging the edges separated by less than 0.1 mm into a single line to create a network of trabecular struts. The ends of the edges which were cut at the femur envelope boundary were connected to the nearest node of the shell mesh.

In order to achieve a required MSL the number of the initial random points was varied. The number of points were chosen randomly and the resulting MSL evaluated. If the MSL was too high the number of points were increased and if it was too low the number of points were decreased. 128,000 points resulting in 24,737 Voronoi seeds were used to obtain a 0.7mm MSL in the model used. This resulted in 315,426 edges and 138,202 nodes. The complete model with 4 divisions of each strut included 1,951,737 nodes and 1,024,700 Abaqus B32 beam elements. For clarity, Figure 7.1 was generated with 600 random points and shows 116 Voronoi seeds.

For the NN14 model the Voronoi cell seeds and generated vertices were used as trabecular lattice nodes. Each of the nodes was connected to the 14 other nearest nodes thus creating a high connectivity lattice. The struts crossing the femur envelope were trimmed and connected to the shell element mesh as before. Due to a high number of struts in this model and a resulting computational inefficiency they were not subdivided. Abaqus B32 beam elements with fixed nodes were used as opposed to truss elements used in previous work (Phillips (2012), Phillips et al. (2015), Villette & Phillips (2017)). The adaptation algorithm used both bending as well as the axial strain and therefore considered a mechanical stimulus at the surface of a trabecula where osteocytes are known to be active. The previous structural model (Phillips (2012)) considered only the

axial stain which is constant across a particular element cross-section.

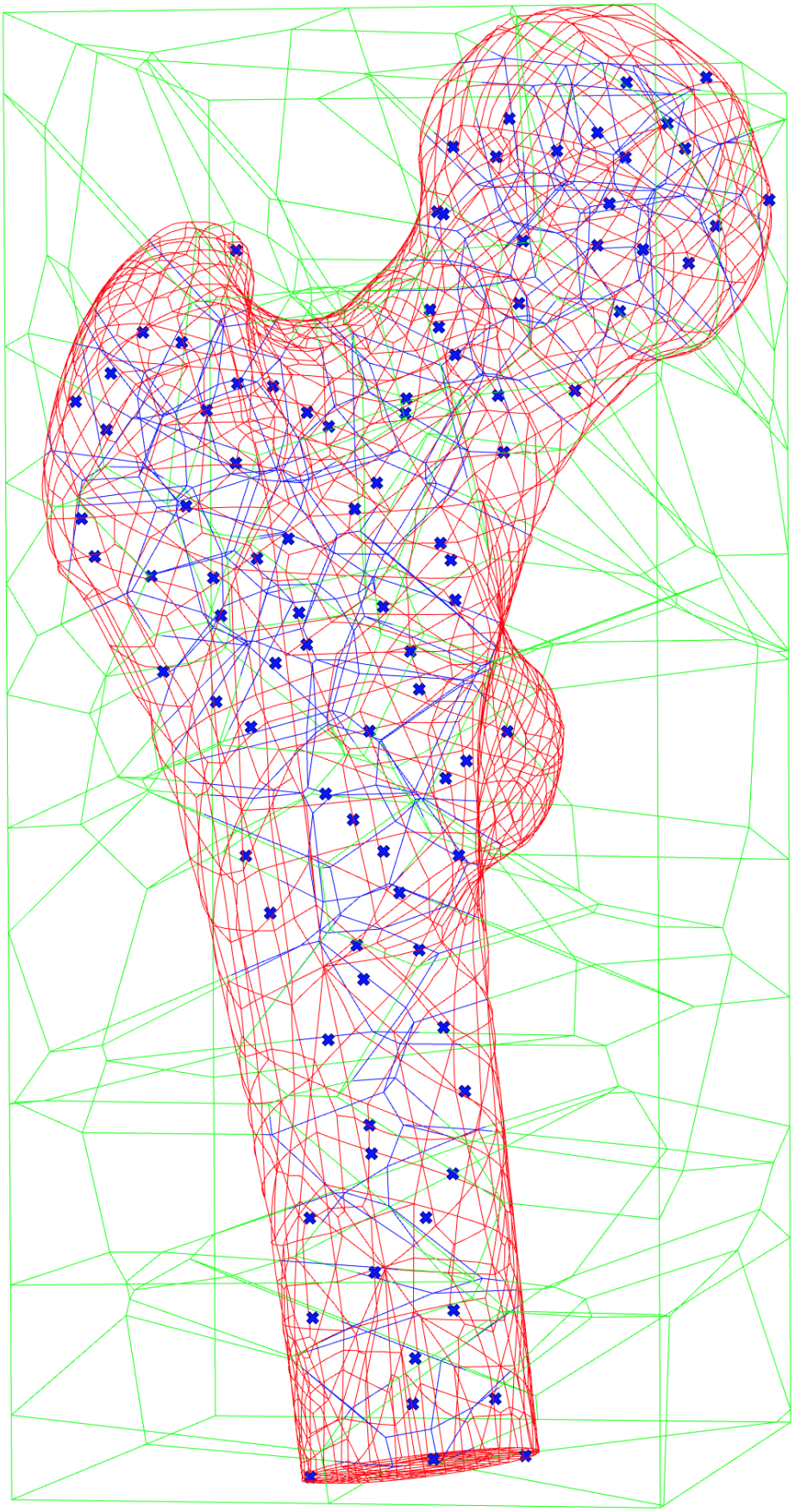


Figure 7.1: Illustration of the Voronoi femur model Grasshopper definition. For clarity 116 Voronoi seeds generated with 600 random points are shown. The model used in the adaptation simulation used 24,737 Voronoi seeds generated from 128,000 random points which achieved a 0.7mm MSL.

The same bone material properties were assigned to all elements, with a Young's modulus of 18,000 MPa, and a Poisson's ratio of 0.3, based on literature values for bone at the tissue level (Turner (1998)). The loads applied to the model were a combination of hip joint contact force, the action of the abductor muscles and the iliotibial band associated with normal walking (Bergmann et al. (2001), Phillips (2012)). These loads were chosen as they arise from the most frequent daily activity (Morlock et al. (2001)). Loads were applied as point loads as shown in Figure 7.2, with the exception of the joint contact force which was distributed over twenty four nodes. This was considered reasonable as the insertion areas of the abductor muscles and iliotibial band on the femur are relatively small, in comparison to the large surface area of the femoral head, through which loads are transferred at the hip joint.

Figure 7.2 also indicates the boundary conditions. Displacements in the vertical z direction were restrained for all shell element nodes at the distal edge of the model. This provided translational stability in z direction and rotational stability in the transverse plane. Displacements in x and y directions were also restrained at one other node to prevent translation in these directions whilst a further node was restrained in y direction to prevent rotation around the z axis.

7.2.2 Adaptation simulations

The model was subjected to an iterative process, controlled by Matlab, in which the cortical shell element thicknesses and trabecular beam radii were varied in response to the resulting strains based on the Mechanostat hypothesis (Frost (1996)). The absolute target strain value of 1250$\mu\varepsilon$ was used and the lazy zone limits were set at 1000$\mu\varepsilon$ and 1500$\mu\varepsilon$. The dead zone limit, below which beam elements were inactivated simulating resorption, was set at 250 $\mu\varepsilon$. Shell elements were only subjected to thickness adjustments and all remained active throughout the iterative process.

The beam radii were varied from 25μm to 4000μm in accordance with Equations 3.11 as explained in Chapter 3. The dead zone radius was set at 0.5μm. The external femur surface was obtained from a CT scan and the external dimensions were assumed to be fixed. Therefore, only the shell element strains on the internal face of the cortex

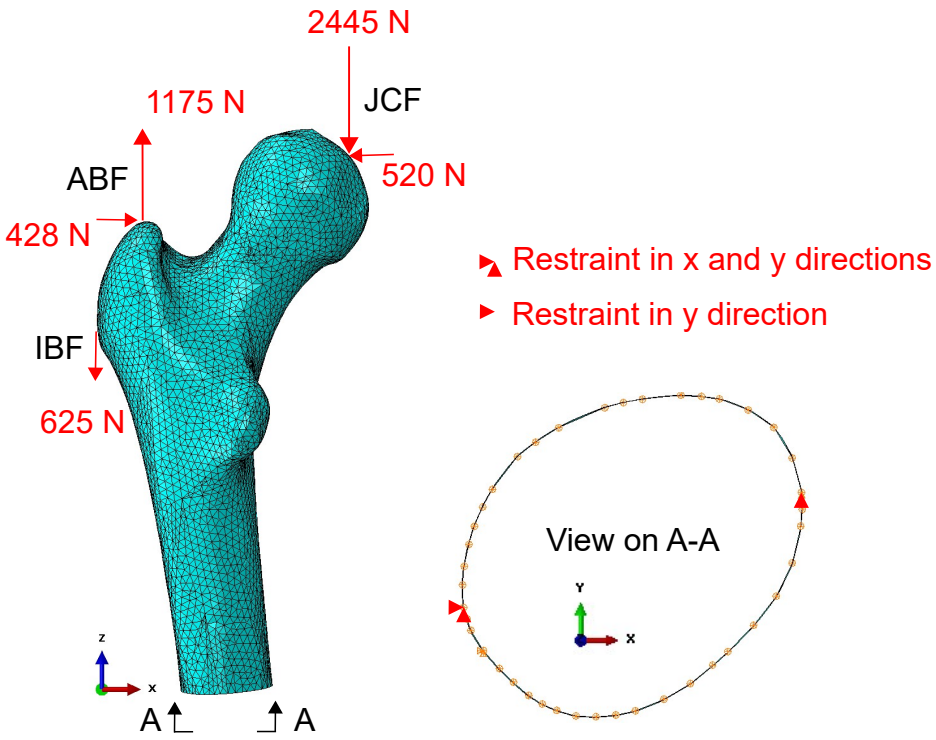


Figure 7.2: Finite element model of the proximal femur showing the loading and the boundary conditions. JCF is the joint contact force, ABF is the abductor muscle force, and IBF is the iliotibial band force. View A-A on the distal end of the femur shows the boundary conditions. The model is restrained in the z direction at all nodes at the distal end, two nodes are restrained in the y direction and one in the x direction.

were considered and the shells were only allowed to grow in thickness on that face. The shell thicknesses were varied from 0.1mm to 10mm in accordance with the Equation 7.1.

$$T_{i+1,j} = T_{i,j}\frac{|\varepsilon_{i,j}|}{\varepsilon_t} \tag{7.1}$$

where $|\varepsilon_{i,j}|$ and $T_{i+1,j}$ are the maximum absolute principal strain and shell thickness for the ith iteration in the jth shell element. The thickness change was limited to $0.5T_{i,j} < T_{i+1,j} < 1.5T_{i,j}$. The importance of controlling this rate is twofold. Firstly, it is recognised that cortical bone responds more slowly to an adaptation stimulus than trabecular bone. Secondly, the strain used in adaptation consists of axial and bending strain components which are not considered separately in the shell elements and a change in shell thickness has a different impact on each.

For computational efficiency, trabecular and cortical elements were classified into 1

of 500 sections, spaced equally between the radius and thickness limits respectively, as appropriate. The models were considered to have reached a converged state when 99% of the trabecular and cortical elements remained in the same section classification between consecutive iterations, and when the change in the effective number of trabecular elements (non near zero area elements) was below 1% between iterations. The developed iterative adaptation was found to be robust and numerically stable for both femur models.

7.2.3 Data analysis

Once convergence was reached in both the Voronoi and the NN14 models connectivity, the ITA and element radius distributions were extracted as for the cube models in Chapters 4, 5 and 6. Relative density and Young's modulus calculations were performed on a 8mm x 8mm x 8mm cubes of beam elements extracted from the centre of the femoral head and the greater trochanter. All nodes and beams, other then those within this volume, were deleted. A new Abaqus input file containing these elements together with their section properties was created. Finally, the boundary conditions were defined at the three pairs of parallel faces of the newly created model in a similar manner as was the case for the cube models (Figure 3.5). One of the face pair had a unit displacement case applied to it and the other had the movement in that direction restrained, which allowed the Young's modulus of the cube to be evaluated.

7.3 Results

Convergence was achieved after 35 iterations for the Voronoi model and 32 for the NN14 model. The active number of struts in the converged models were 181,400 (4 elements per strut) in the Voronoi model and 510,555 (single element per strut) in the NN14 model. The total volumes of trabecular and cortical bone were found to be 47,537mm^3 and 19,736mm^3 respectively in the Voronoi model and 66,274mm^3 and 6,814mm^3 in the NN14 model. The NN14 model predicts a larger volume of trabecular bone and a smaller volume of cortical bone and an overall lower total bone volume. The differences are explained in the discussion section.

7.3.1 Predicted trabecular architecture and mechanical properties

Figure 7.3 present 2mm thick slices through the Voronoi femur model at the end of the adaptation and Figure 7.4 presents the femoral head and the greater trochanter close up of the same slice. Figures 7.5 and 7.11 presents a 2mm thick slice through the NN14 femur model at the end of the adaptation with and without the beam elements within the shell thickness on the medial side. Figure 7.7 presents the femoral head and the greater trochanter close up of the same slice. Figure 7.8 presents the comparison of the trabecular architecture predicted by both models with that of real bone. Trabecular trajectories can be observed clearly with the five trabecular groups identified by Singh et al. (1970) present in both models. In addition, Ward's triangle and the femoral canal are clearly visible, although these are populated by the a number of small ($r = 25\mu$m) elements in the NN14 model. Trajectories are marginally better defined in the NN14 model, which is particularly evident in the secondary compressive group where the majority of elements align in the mediolateral direction with very few in the proximal to distal direction.

The thin layer of cortex at the femoral head and the greater trochanter, as well as the thickening in the femoral shaft and the inferior femoral neck, matches clinical observations (Stephenson & Seedhom (1999), Treece et al. (2010)). A number of large trabecular elements running parallel to the femoral shaft are observed within the thickness of the cortex on the medial and lateral aspects, while a number of smaller trabecular elements are observed running perpendicular to the femoral shaft in the anterior and posterior aspects. This is particularly evident in the medial aspect of the NN14 model. These results are consistent with the femur bending about the anterior-posterior axis during walking and are more pronounced in these models than previous work by Phillips (2012) and Phillips et al. (2015), thought to be due to boundary condition effects. There is also a large thickening of the shell elements which is not representative of real bone at the point of application of the iliotibial band force and at the distal edge due to to boundary conditions. This cortex thickening is present in both models but more apparent in the Voronoi model.

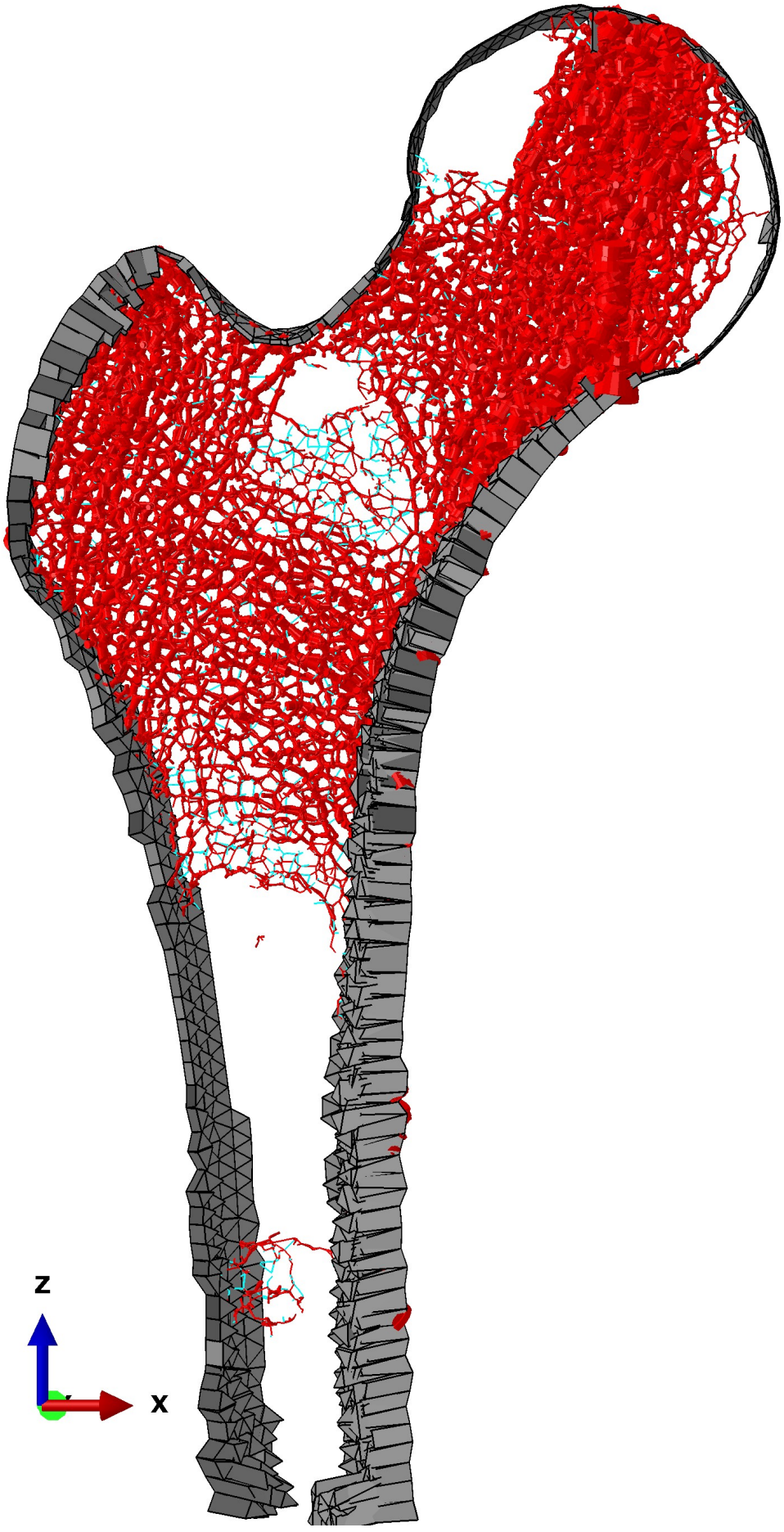


Figure 7.3: A 2mm thick slice through the converged Voronoi model of the proximal femur showing trabecular and cortical architecture. Inactive elements with a radius of 0.5μm are omitted and the elements with the smallest active element radius of 25μm are shown in cyan.

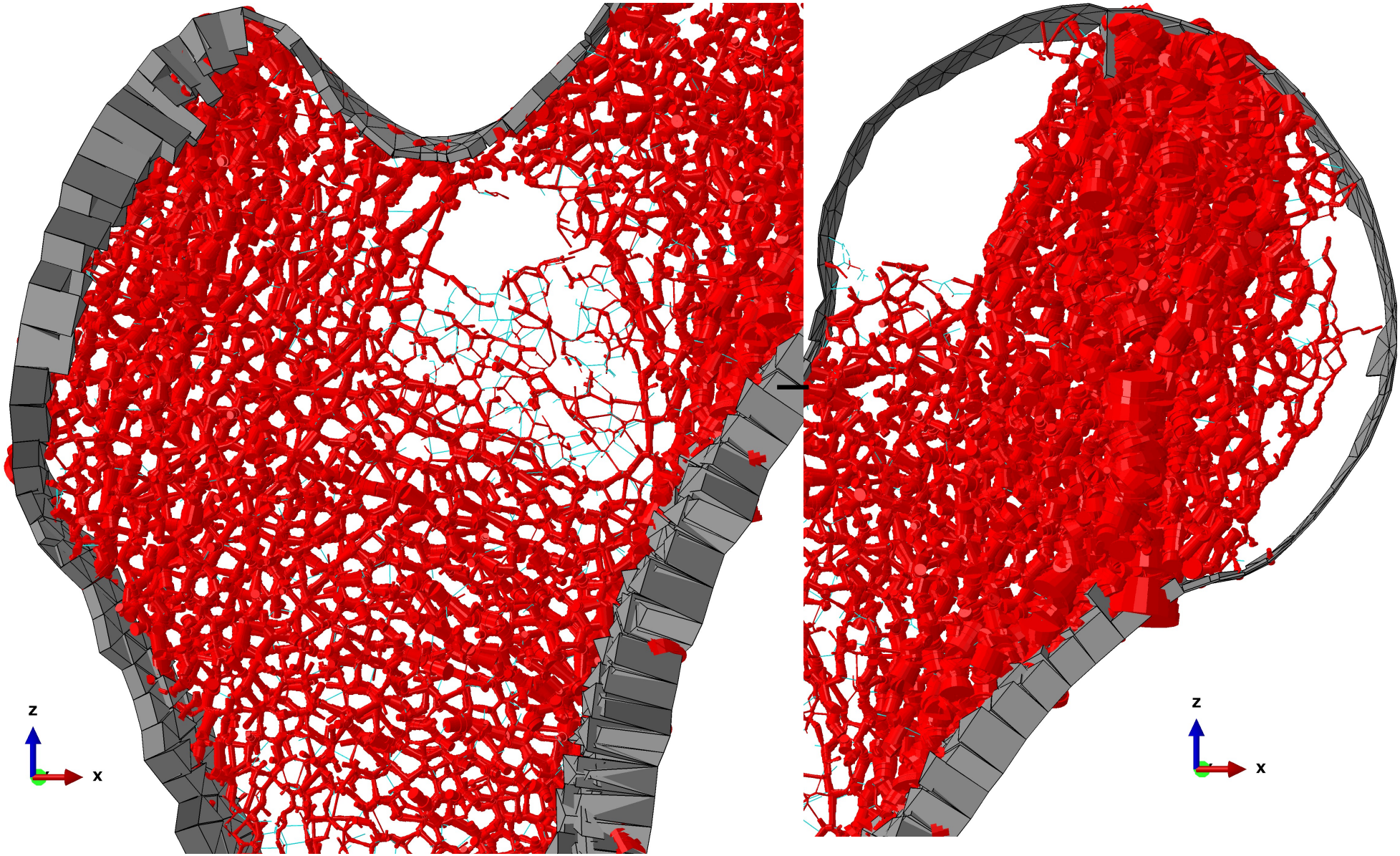


Figure 7.4: A close up of the converged Voronoi model in Figure 7.3. Trabecular trajectories in the greater trochanter and the femoral head are shown with greater resolution. Ward's triangle is clearly defined. Inactive elements with a radius of 0.5μm are omitted and elements with the smallest active element radius of 25μm are shown in cyan.

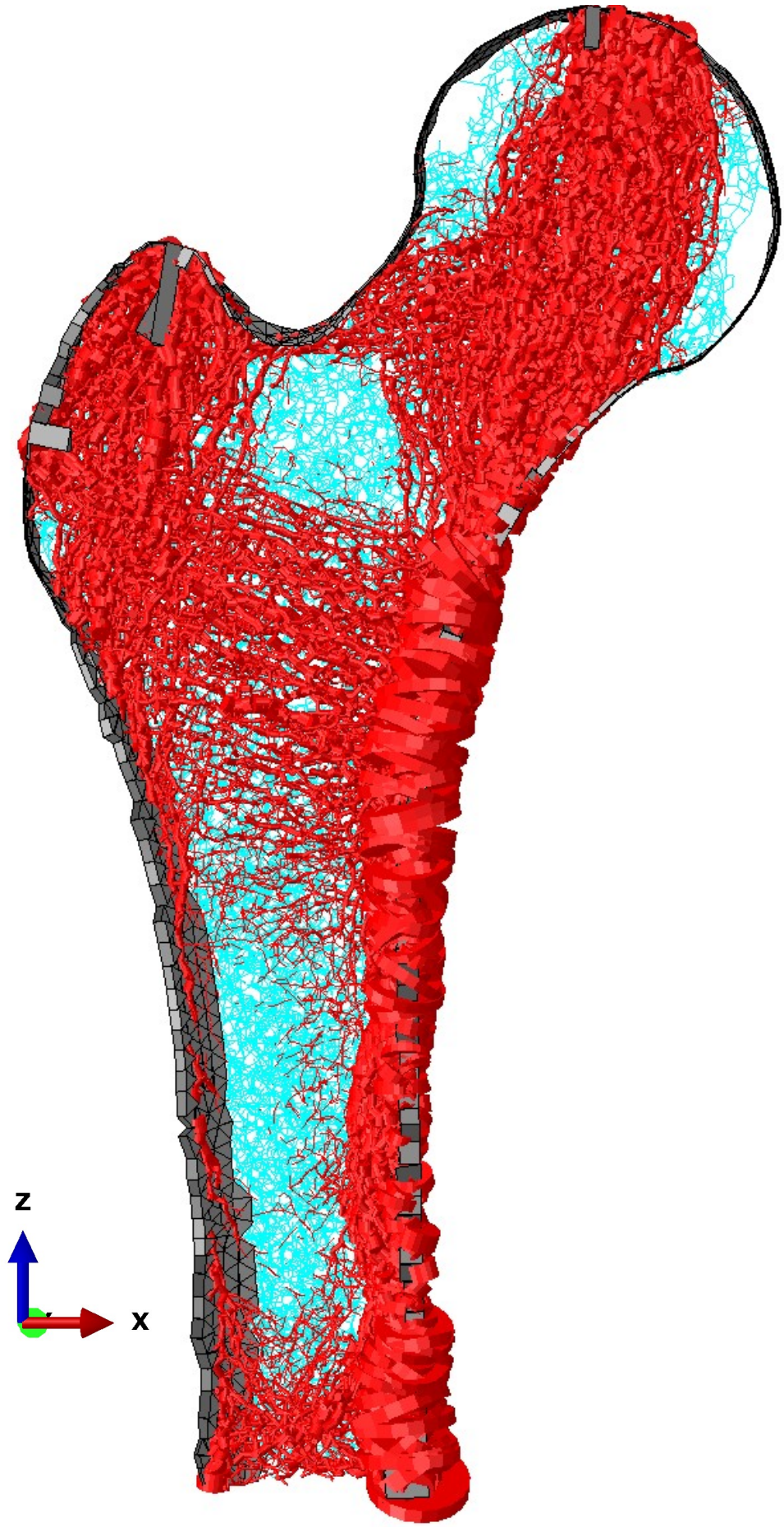


Figure 7.5: A 2mm thick slice through the converged NN14 model of the proximal femur showing trabecular and cortical architecture. Inactive elements with a radius of 0.5μm are omitted and the elements with the smallest active element radius of 25μm are shown in cyan.

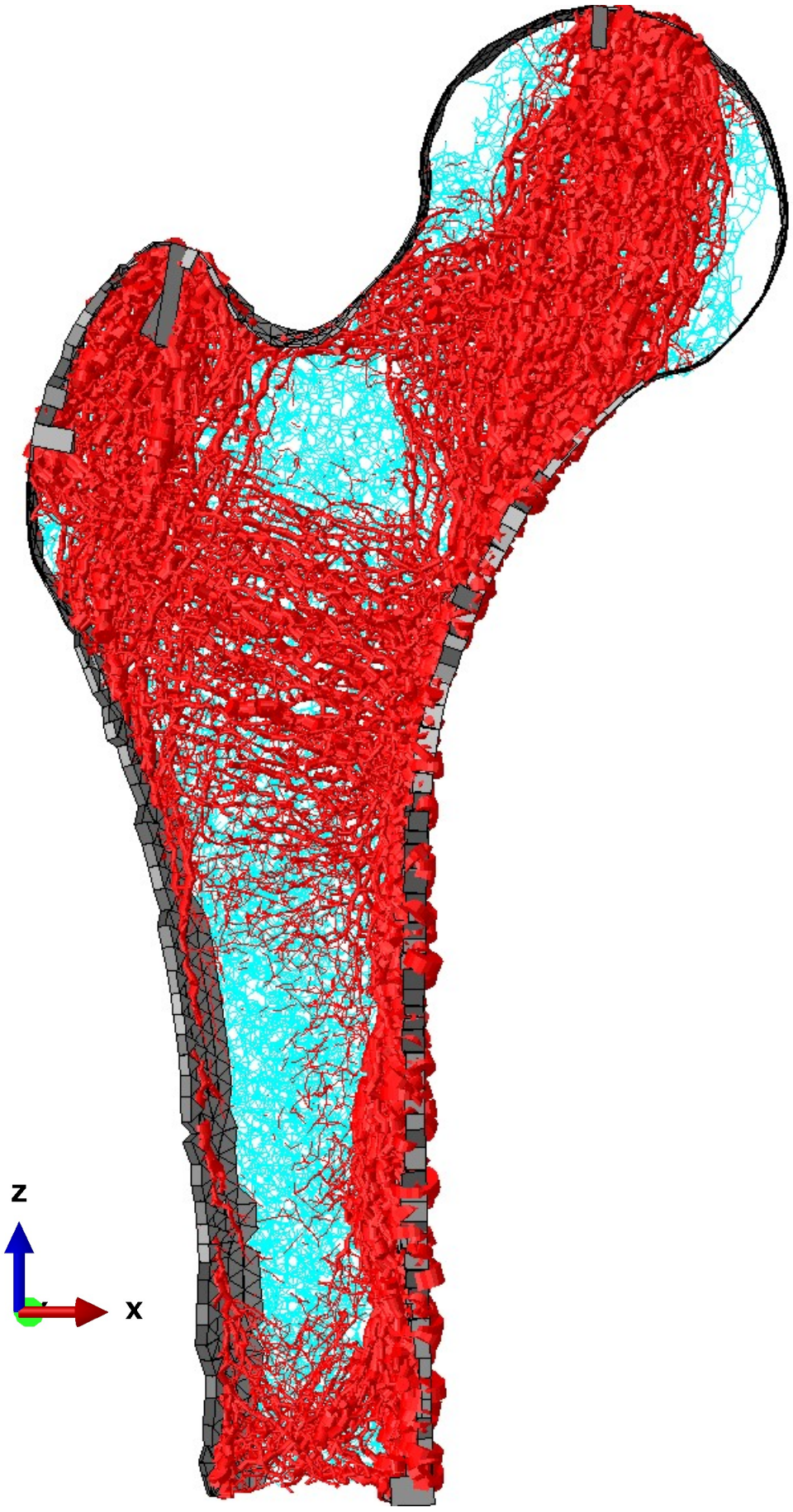


Figure 7.6: A 2mm thick slice through the converged NN14 model of the proximal femur showing trabecular and cortical architecture. Inactive elements with a radius of 0.5μm are omitted and the elements with the smallest active element radius of 25μm are shown in cyan. Elements with radii above 1.7mm are omitted.

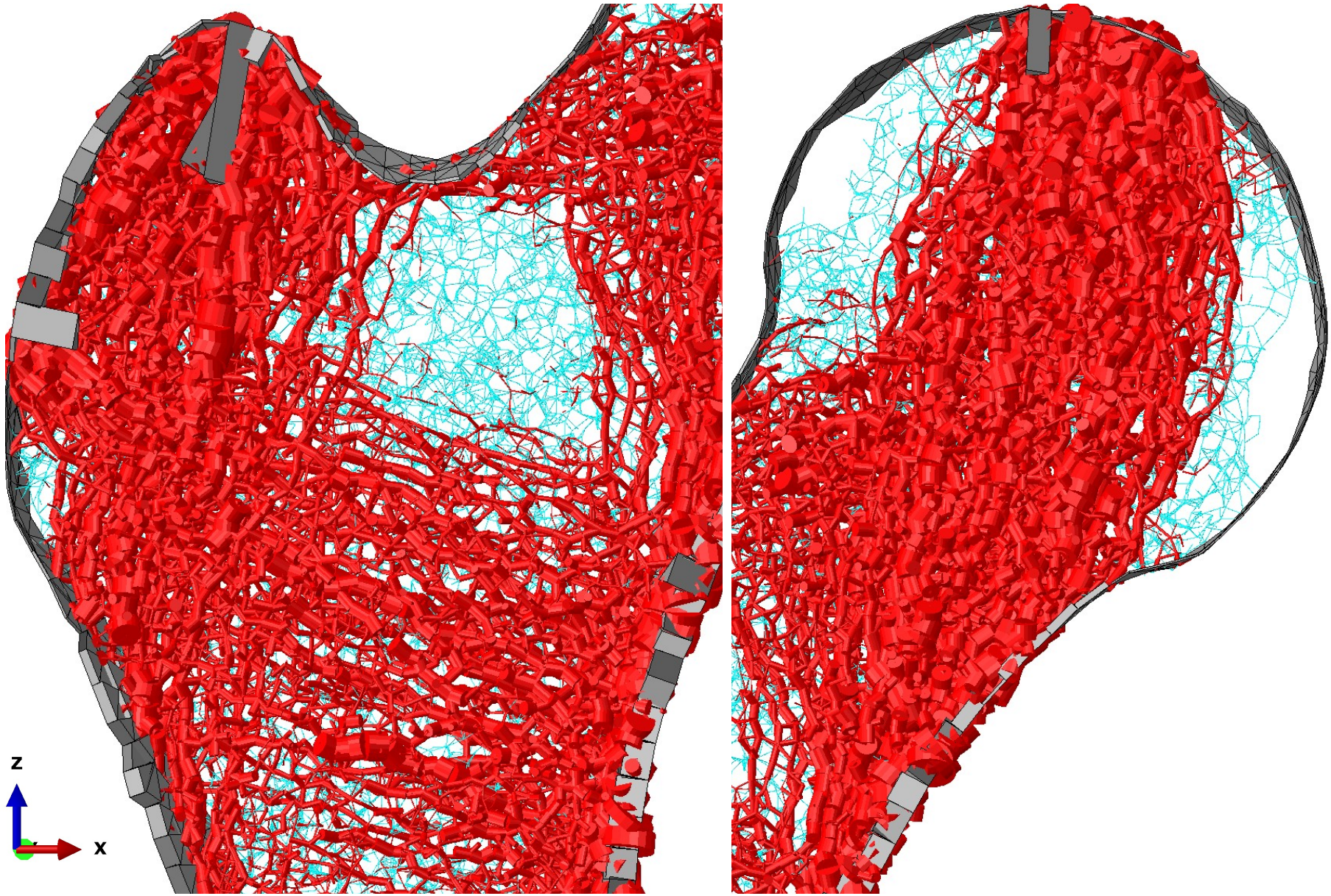
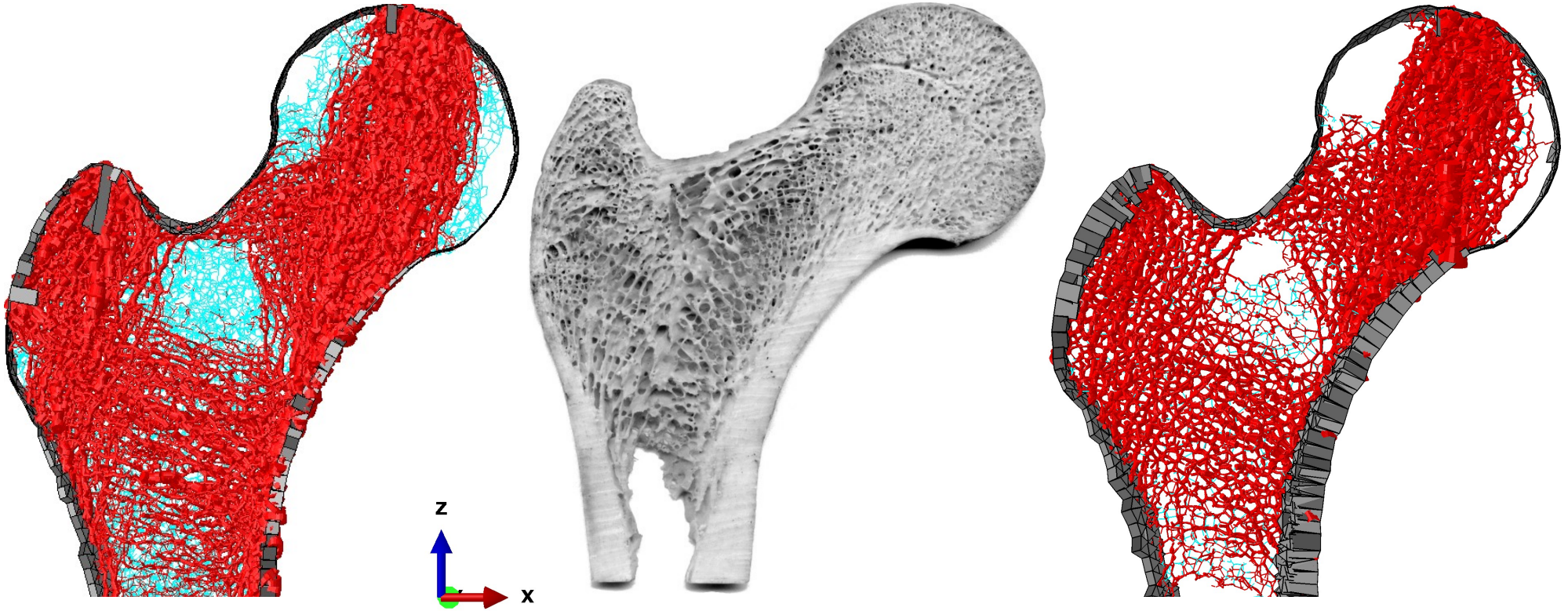


Figure 7.7: A close up of the converged NN14 model of proximal femur in Figure 7.5. Trabecular trajectories in the greater trochanter and the femoral head are shown with greater resolution. Ward's triangle is clearly defined. Inactive elements with a radius of 0.5μm are omitted and the elements with the smallest active element radius of 25 μm are shown in cyan.



a) Slice through the NN14 model

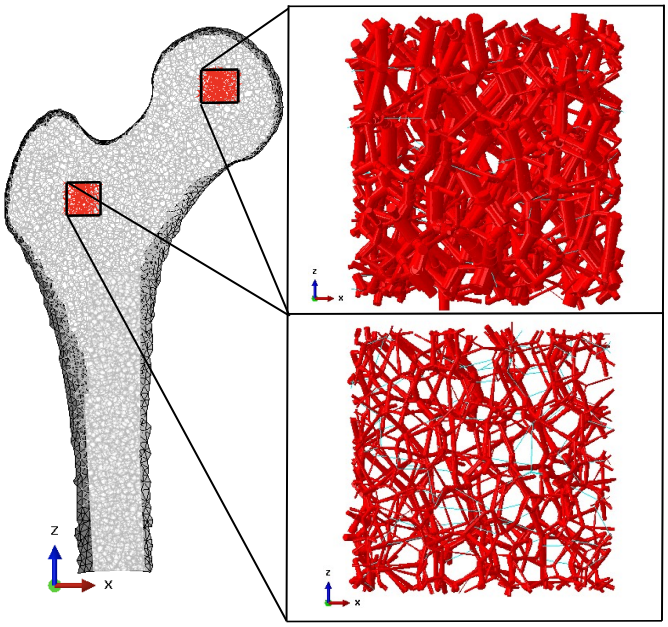
b) Photograph of a slice through the proximal femur

c) Slice through the Voronoi model

Figure 7.8: A comparison of proximal femur trabecular architecture predicted by the a) NN14 model and c) Voronoi model with the real proximal trabecular architecture in the b) photograph of the slice trough the bone. Inactive elements with a radius of 0.5μm are omitted and the elements with the smallest active element radius of 25 μm are shown in cyan.

Relative density and Young's moduli were derived from a 8mm x 8mm x 8mm cube model extracted from the centre of the femoral head as indicated in Figures 7.9 and 7.10 for the Voronoi and NN14 models respectively. Figure 7.11 presents plots of the E values for different orientations. The maximum predicted Young's moduli in both models from the femoral head, one from the NN14 and the the other form the Voronoi model, aligned with the model z direction. The Voronoi model predicted 5,716 MPa and the NN14 10,100MPa in this direction. The minimum modulii were similar with predicted values of 1,368MPa and 1,337MPa respectively. The predicted modulii in the y direction were somewhat larger in the Voronoi model. The opposite was the case in the greater trochanter where the Voronoi predicted larger modulii. The maximum of 1,158MPa in the Voronoi model was predicted in the orientation of 30° in the anticlockwise direction about the y axis. The direction of the maximum modulus was the same in the NN14 model but its value of 440MPa was three times lower.

The predicted relative density in the femoral head was about 0.9 in both models, except for one sample in the NN14 model with predicted relative density approaching unity. The trabecular volume was calculated by summing the product of element lengths and their area. This method gives rise to an overestimation of volume as it considers the material at joint nodes several times. This overestimation increases with greater NC and shorter MSL. A more realistic volume estimate for the cube samples, which is presented here, was made using a Rhinoceros/Grasshopper.

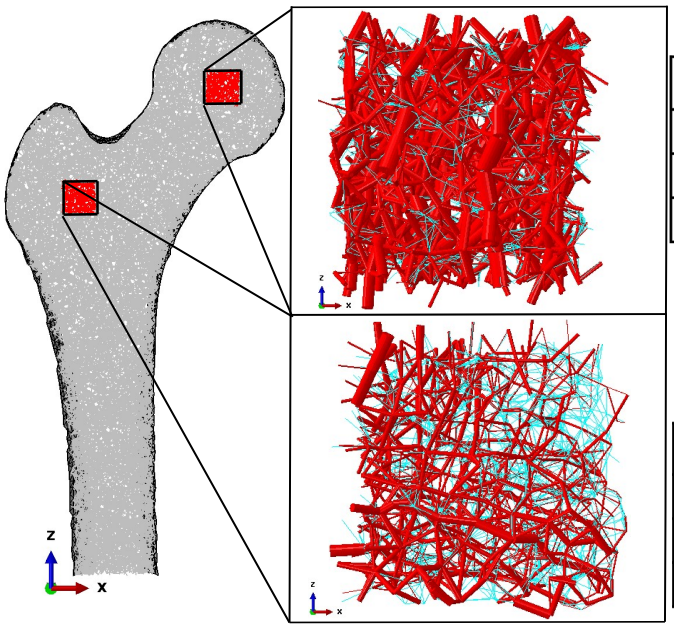


a) Slice through the femur b) Extracted cube models of trabeculae

	Young's Modulus [MPa]			
α [°]	$E_{x'}$	$E_{y'}$	$E_{z'}$	RD
0	1368	1247	5716	0.88
30	2051	1888	3811	0.92
-30	1891	1691	4012	0.92

	Young's Modulus [Mpa]			
α [°]	$E_{x'}$	$E_{y'}$	$E_{z'}$	RD
0	182	498	535	0.35
30	652	427	543	0.45
-30	457	496	1158	0.49

Figure 7.9: Young's modulus and relative density of trabeculae in the femoral head and the greater trochanter based on an 8mm x 8mm x 8mm cube sample extracted from the adapted Voronoi model as indicated in red on the slice. α is the angle between the femur model z axis and the cube model z' axis with anticlockwise direction about y axis being positive. Inactive elements with a radius of 0.5μm are omitted and the elements with the smallest active element radius of 25μm are shown in cyan. The cubes orientated at 30° and -30° from the model z axis were extracted at those orientations from the femur model and rotated to vertical in Abaqus for calculation of stiffness properties.



a) Slice through the femur b) Extracted cube models of trabeculae

	Young's Modulus [MPa]			
α [°]	$E_{x'}$	$E_{y'}$	$E_{z'}$	RD
0	1337	1073	10100	0.98
30	1895	834	2242	0.93
-30	1423	1126	8244	0.91

	Young's Modulus [MPa]			
α [°]	$E_{x'}$	$E_{y'}$	$E_{z'}$	RD
0	344	57	368	0.24
30	167	88	233	0.42
-30	349	55	440	0.28

Figure 7.10: Young's modulus and relative density of trabeculae in the femoral head and the greater trochanter based on an 8mm x 8mm x 8mm cube sample extracted from the adapted NN14 model as indicated in red on the slice. α is the angle between the femur model z axis and the cube model z' axis with anticlockwise direction about y axis being positive. Inactive elements with a radius of 0.5μm are omitted and the elements with the smallest active element radius of 25 μm are shown in cyan. The cubes orientated at 30° and -30° from the model z axis were extracted at those orientations from the femur model and rotated to vertical in Abaqus for calculation of stiffness properties.

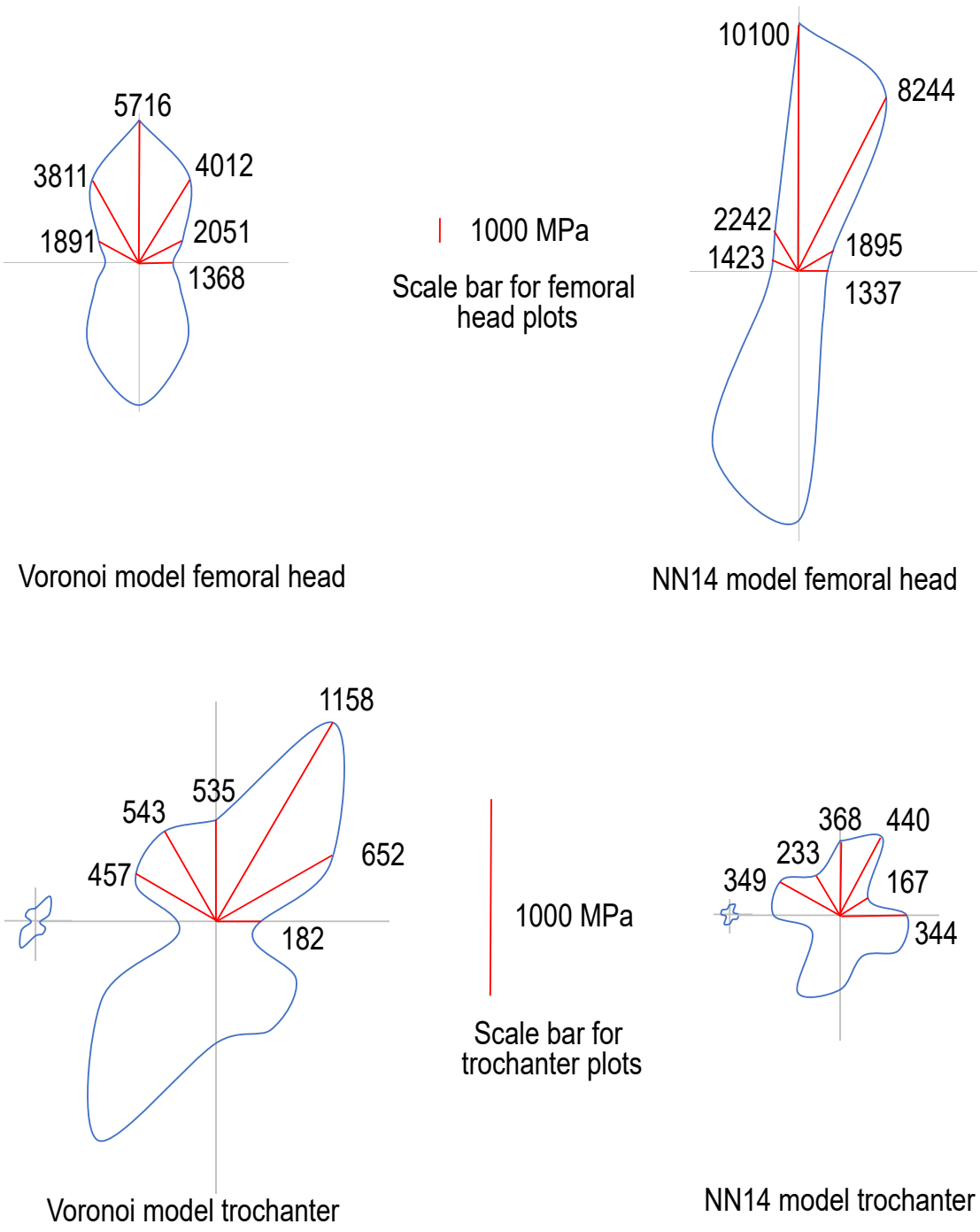


Figure 7.11: Plots of E values in different orientations in the femoral head and the greater trochanter as presented in Figures 7.9 and 7.10. Values are given at 30° intervals. For clarity greater trochanter plots are 8 times larger as indicated by the scale bars. The smaller plots to the left hand side of each greater trochanter plot are at the same scale as the femur head plots for ease of visual comparison.

The proximal femur is recognised as an anatomic site with high relative density (Hildebrand et al. (1999), Liu et al. (2006), Zhao et al. (2018)), high Young's Modulus (Hildebrand et al. (1999)) and higher proportion of plate like compared to rod like trabeculae (Hildebrand et al. (1999), Zhao et al. (2018), Kirby et al. (2020)). The reported relative density values are summarised in Table 7.1 and stiffness values in Table 7.2.

Mean RD	Min RD	Max RD	Source
0.26	0.12	0.48	Hildebrand et al. (1999)
0.23	0.15	0.33	Liu et al. (2006)
	0.12	0.44	Zhao et al. (2018)

Table 7.1: Proximal femur relative density (RD) reported in the literature.

Mean E_l	Min E_l	Max E_l	Mean E_h	Min E_h	Max E_h
739	277	1739	2177	1112	3104

Table 7.2: Proximal femur Young's modulii [MPa] reported by Liu et al. (2006). E_l denotes the modulus in the direction with the lowest values and E_h demotes the modulus in the direction with the highest values.

Baum et al. (2010) reported on the relative density variability within the femur. For the femoral head they report relative density and standard deviation of 0.56 and 0.14, for the neck 0.1 and 0.09 and for the greater trochanter 0.15 and 0.1. On this basis, the femoral head may be expected to be three to four times denser than the greater trochanter and 5 to 6 times denser than the neck.

The femoral head predicted relative density values are approximately twice as large as values from literature (Hildebrand et al. (1999), Liu et al. (2006), Zhao et al. (2018)). The Young's modulus predicted by the Voronoi model is almost twice of that predicted by the NN14 model and three times the maximum reported value. Some of these differences may be caused by the method of load application and by the lack of plate like trabeculae in models. This will be further addressed in the discussion section. The relative magnitude of predicted trabecular density in the greater trochanter in relation

to the femoral head compares well with the literature as it is between 2 and 4 times smaller.

7.3.2 Predicted trabecular topology

Table 7.3 presents the abundance of nodes with ANC between 3 and 5 and above 5 in the Voronoi model, while Table 7.4 presents the abundance of nodes with ANCs which are present in more than 5% of total nodes in the NN14 model. It is evident that neither the Voronoi nor the NN14 model predict the high abundance of 65% to 75% in ANC3 nodes reported by Reznikov et al. (2016). The Voronoi model predicts 60.8% of ANC4 nodes, while the imaging study reports 19% to 27% (Reznikov et al. (2016)). The NN14 model predicts a value of under 5% for both ANC3 and ANC4 nodes. The NN14 simulation predicts a larger than 80% proportion of nodes with ANC greater than 5 while the imaging study only reports 1.5% of these nodes (Reznikov et al. (2016)). The Voronoi model predicts 14.3% of these nodes.

Adapted NC	ANC=3	ANC=4	ANC=5	ANC>5
Proportion of total nodes	20.6%	60.8%	4.3%	14.3%

Table 7.3: Proportion of joint nodes with ANC=3, ANC=4, ANC=5 and ANC>5 in the Voronoi femur model at the end of adaptation simulations. Nodes which subdivide struts are excluded.

Adapted NC	ANC=5	ANC=6	ANC=7	ANC=8	ANC=9	ANC=10
Proportion of total nodes	8.5%	12.0%	16.0%	18%	15.6%	9.7%

Table 7.4: Proportion of joint nodes with ANCs which are present in more than 5% of total nodes.

Tables 7.5 and 7.6 present the mean, mode, standard deviation and minimum and maximum NC for the Voronoi and NN14 models. Reznikov et al. (2016) report a mean connectivity of around 3.2 to 3.4 and the Voronoi prediction is close with the predicted value of 4.0. However, it is evident that the simulation predicts a structure with predominant NC of 4 and not 3 which the Reznikov et al. (2016) study reports.

Mean	Mode	SD	Min	Max
4.00	4	0.84	3	12

Table 7.5: Predicted mean, mode, standard deviation (SD), minimum (Min) and maximum (Max) NC in the adapted Voronoi femur model.

Mean	Mode	SD	Min	Max
7.84	8	2.18	3	17

Table 7.6: Predicted mean, mode, standard deviation (SD), minimum (Min) and maximum (Max) NC in the adapted NN14 femur model.

Table 7.7 presents the predicted ITA values for nodes with NC of 3, 4 and 5 in the adapted Voronoi model. Table 7.8 presents the predicted ITA values for the nodes with five most represented NC in the adapted NN14 model. The mean ITAs predicted by the Voronoi model are closer to those reported by the imaging study (Reznikov et al. (2014*a*) than the NN14 model predictions.

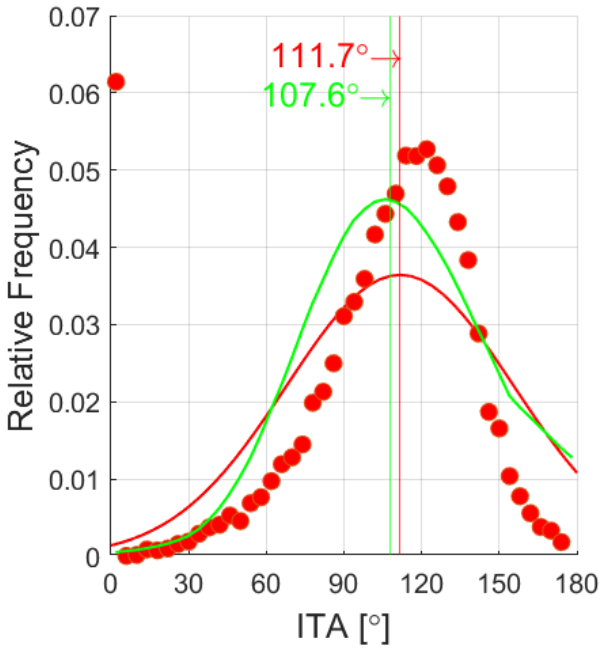
NC	Number of Nodes	Mean	SD	Min	Max
3	18718	111.9°	29.6°	0°	180°
4	55249	109.9°	28.7°	0°	180°
5	3890	101.6°	34.1°	0°	178°

Table 7.7: Predicted number of nodes, mean, standard deviation (SD), minimum (Min) and maximum (Max) ITA for given NC in the adapted Voronoi femur model.

NC	Number of Nodes	Mean	SD	Min	Max
5	3194	95.1°	38.8°	1.1°	179.5°
6	4743	94.0°	39.3°	0.9°	179.3°
7	6373	92.7°	34.1°	0.3°	179.7°
8	7730	92.0°	39.7°	0.4°	179.6°
9	6845	91.2°	40.1°	0.5°	179.2°

Table 7.8: Predicted number of nodes, mean, standard deviation (SD), minimum (Min) and maximum (Max) ITA for given NC in the adapted NN14 femur model.

Figure 7.12 presents the distribution of ITA angles in nodes with predicted NC of 4 in the Voronoi model as this is the only one with sufficient number of nodes which compares well withReznikov et al. (2016). The equivalent ITA distribution from Reznikov et al. (2016) is plotted for comparison.



Denotes the ITA distribution predicted by the simulation

Denotes the ITA distribution reported by Reznikov et al.(2016) .

Figure 7.12: Comparison of the Voronoi model predictions of ANC4 node ITA distribution with those reported by Reznikov et al. (2016). Red dots present the raw data, grouped into bins 4° wide, whilst the curves are fitted probability distributions.

Figure 7.13 presents the predicted strut radii distributions for both femur models.

Two distributions are presented for each model: one with all the active element sizes and the other excluding the smallest elements. A study of the lumbar spine reports a large abundance of smallest elements (Favier (2020), Favier et al. (2021)). Although this was successfully reduced in the cube model simulations reported in Chapters 4, 5 and 6 by reducing the minimum radius from 100μm to 25μm, an abundance of smallest elements persists in the femur simulations, particularly in the NN14 model. The omission of the smallest elements yields distributions closer to those reported in the imaging studies (Hildebrand & Rüegsegger (1997), Liu et al. (2008), Kirby et al. (2020)). The NN14 model predicts smaller mean values and a radii distribution which are closer to those reported in literature (Hildebrand & Rüegsegger (1997), Liu et al. (2008), Kirby et al. (2020)). The discussion section will consider the impact of the presence of both struts and plates the trabecular architecture on the predictions presented here.

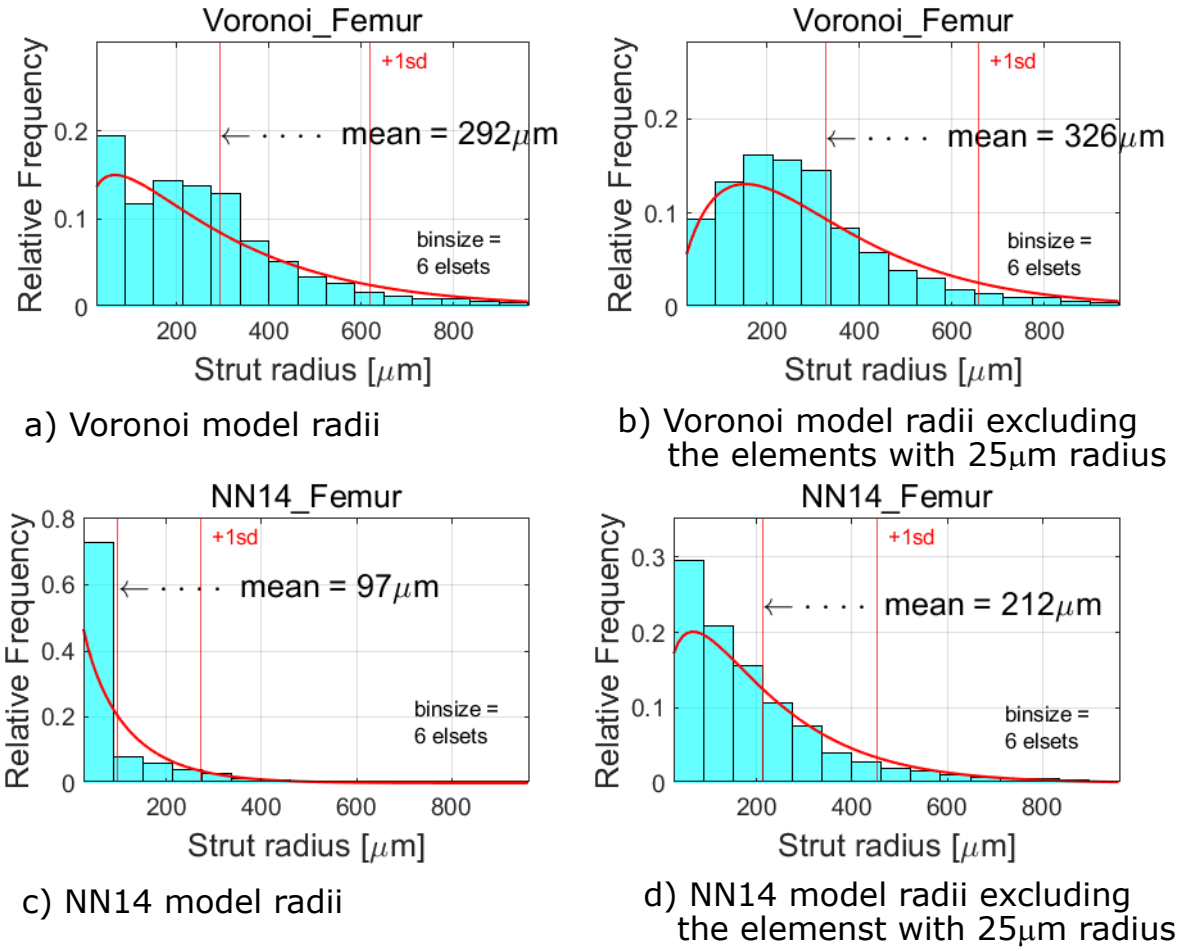


Figure 7.13: Comparison of the Voronoi and NN14 model radius distributions. Voronoi distributions are based on the mean radii of four elements comprising a strut and the NN14 of the radii for each struts as there were no subdivisions.

7.4 Discussion

To the best of the authors knowledge, the two proximal femur simulations presented in this chapter are the first attempt to achieve representative trabecular architecture at micro-scale in structural models. The Voronoi adaptation converged in 19h over 36 iterations on a standard workstation (Intel(R) Core(TM) i5-9500 CPU @ 3.00GHz RAM 32GB) while the NN14 simulation converged in 24h over 32 iterations on a different workstation (Intel(R) Xeon(R) CPU E5-2630 v3 @ 2.40GHz (2 processors) RAM 64GB). More memory was required to run the NN14 model due to a larger number of degrees of freedom due to the greater connectivity. Boyle & Kim (2011) developed a continuum micro-scale proximal femur model, utilising around 23.3 million elements at a 175μm resolution. Subjecting the model to a single combined load case they reported an adaptation run time of around 343 hours on a computing cluster. They do not report the cluster specification but they usually range from 1,000 to 10,000 processor cores with the memory range from 512GB to 1024GB (Dell (UK)). The adaptation in the Voronoi model was able to capture trabecular radius changes of 8μm along 175μm element section lengths. Four divisions of a strut with a 0.7mm MSL gives an average element length of 175μm. Therefore, the resolution achieved in the Voronoi model matches well with that used by the Boyle & Kim (2011) study at much greater computational efficiency.

Both the Voronoi and NN14 models predicted trabecular trajectories which correspond well with those recorded in the literature with Ward's triangle clearly visible (Singh et al. (1970), Kim et al. (2009)). The arching over the Ward's triangle under the femoral neck observed by Garden (1961) can also be seen in both models. Trajectories are marginally better defined in the NN14 model, which is particularly evident in the secondary compressive trabecular group where the majority of elements align in the mediolateral direction, with very few in the proximal to distal direction.

The total volumes of trabecular and cortical bone were found to be 47,537mm^3 and 19,736mm^3 respectively in the Voronoi model and 66,274mm^3 and 6,814mm^3 in the NN14 model. The NN14 model predicts a larger volume of trabecular bone and a smal-

ler volume of cortical bone, but an overall higher total bone volume. The trabecular volume is higher and cortical volume volume lower in the NN14 model compared to the Voronoi model. Due to the limitation in the NN14 model generation, a string of beam elements following the cortical outline are generated. These elements, shown in Figure 7.5 but omitted from Figure 7.6, are favoured by the adaptation algorithm intentionally as the trabecular bone reacts to a changing strain environment faster than the cortical bone. The total volume of these elements is 15,264mm^3 and adjusting the totals by this amount yields a trabecular volume of 51,011mm^3 and a cortical volume of 22,078mm^3. Amending the model to exclude these trabecular elements would not result in precisely these volumes but this simple calculation provides a reasonable guide. In addition, the trabecular bone volume is over predicted in both models due to the method used to calculate it by summing the product of element lengths and their area. This method considers the material at joint nodes several times, once for every element. This over-estimation increases with greater NC and shorter MSL. The more realistic volume of the femoral cube sample taken form the adapted Voronoi model (Figure 7.9) calculated by Rhinoceros/Grasshopper was 65% of that calculated by the method used for the whole femur. For the sample taken from the NN14 model this was 55%. These proportions depend heavily on the strut size and could not be applied wholesale to femur models. However, it is reasonable to assume that relative proportions are consistent and that the NN14 model trabecular volume is overestimated by 18% [100((65/55)-1)] more than the Voronoi trabecular volume. Making this adjustment would have resulted in the total trabecular volume in the Voronoi model being about 10% [100(1.18(47,537/51,011)-1)] greater than in the NN14 model.

The Voronoi model predicts larger moduli in the unloaded direction, the femur model y axis, as was the case in the cube models presented in Chapter 6. This predicts greater ability of the real bone to resists any out of plane loading that may be applied in the anterior to posterior direction. For instance, such loading may result from a fall or an impact.

The proximal femur is recognised as an anatomic site with high relative density (Hildebrand et al. (1999), Liu et al. (2006), Zhao et al. (2018)), high Young's Modulus (Hildebrand et al. (1999)) and higher proportion of plate like compared to rod like

trabeculae (Hildebrand et al. (1999), Zhao et al. (2018), Kirby et al. (2020)). The predicted whole bone stiffness was calculated by applying a unit load to the top of the femoral head and extracting the maximum deflection in the model z direction. Stiffness values of 3,600N/mm and 7,465N/mm were obtained for the Voronoi and NN14 models respectively. These are overestimates when compared to the mean of 1446N/mm and standard deviation of 446N/mm obtained from tests of 44 proximal femur samples (Patton et al. (2019)).

The Young;s modulus calculated for the femoral head cube samples extracted form the adapted models were found to be overestimated, with the Voronoi model predicting a maximum of 5,716MPa and the NN14 model 10,100MPa for the femoral head. The maximum reported stiffness for this anatomic site is 3104 MPa (Liu et al. (2006)).

The overprediction of trabecular volume and stiffness may be caused by the combination of the load application method and the reported presence of plate like trabeculae in the femoral head which were not modelled. Hildebrand et al. (1999) report a mean structural modelling index (SMI) of 0.46 for the femur, where the SMI varies from 0 for the ideal plate structure to 3 for the ideal rod structure. Furthermore, they report a mean SMI of 0.16 for the femoral head indicating that it is largely composed of plate like trabeculae. Zhao et al. (2018) report approximately three times as many plates as rods in the femur, with number density ranging from 10.2$/mm^3$ to 30.5$/mm^3$ for plates and 2.9$/mm^3$ to 11.2$/mm^3$ for rods. The joint contact force on the femoral head was applied as 24 point loads which provided some load spread. Nevertheless, the concentrated loads would have caused high strains locally and the adaption algorithm would have increased the stiffness in elements directly connected to load application nodes. The increased stiffness would have attracted even more load to these elements in the next iteration, further increasing their stiffness until an equilibrium was reached in subsequent iterations. It is likely that this process would have been less dramatic were plates and a layer of cartilage modelled at the top of femur to spread the load as was done in the study by Phillips et al. (2015). Another reason for high predicted stiffness may be related to the boundary conditions and this limitation maybe reduced by developing a model of the whole bone. The effect of plates on stiffness and volume is further addressed in the discussion of the trabecular thickness at the end of this section.

It is evident that neither the Voronoi nor the NN14 model predict the high abundance of NC3 reported by Reznikov et al. (2016) but the mean connectivity of 4.0 predicted by the Voronoi model is much closer to the study reported value of between 3.2 and 3.4 than the NN14 model mean predicted value of 7.48. It is hypothesised that the difference between the Voronoi model predicted connectivity and imaging study findings arises from the fact that the trabecular bone consists of both struts (rods) and plates (Liu et al. (2008), Zhao et al. (2018), Gibson & Ashby (1997)). It is not clear how Reznikov et al. (2016) consider plates in the skeletonization of the CT imaging data and the models used in this thesis consist only of struts. Such models require a larger number of struts than an equivalent one with a combination of struts and plates in order to achieve the same stiffness. A model with both types of trabecular elements would likely have a lower connectivity although it is also not clear how such connectivity might be evaluated.

Alsheghri et al. (2021) carried out an optimisation simulation of trabecular bone inspired by the investigation of trabecular bone's topology properties (Reznikov et al. 2014*a*, 2015, 2016). They created a random set of trabecular nodes by replicating real bone node density and separation from other nodes by using statistical data extracted from a CT image. Each of these nodes was connected to another 5 nodes to created a lattice of trabecular bone elements. The lattice was optimised by deleting or adding elements with the lowest stress until convergence was achieved. Three simulations were undertaken with different convergence criteria. One simulation was terminated when the most uniform stress state was achieved in all elements. Another was terminated when the predicted total length equalled that obtained form the CT image and the third when the number of trabeculae equalled the value obtained form the CT image. Their findings were that the predictions of connectivity and its abundance in all three different simulations matched the findings of their imaging investigations. The Alsheghri et al. (2021) study was based on Voronoi inspired lattice model as was one of the femur models in this thesis but unlike this thesis, the element sizes were not adapted, that is to say all elements remained the same size throughout the simulation. This thesis simulates adaptation based on a local target strain value, which is more likely to represent a local stimulus that bone adapts to, and both eliminates elements and varies their size.

The Voronoi model was found to predict mean NC of 4 and the ITAs of 111.9°, 109.9° and 101.6° for ANC3, ANC4 AND ANC5 nodes. This corresponds well with Reznikov et al. (2016) study and the idealised ITA angles. Whilst the increased dead zone wasn't implemented in the femur models based on the findings for the cube samples the mean NC would likely decrease to a value closer to real bone. In addition the trabecular volume would likely decrease with many elements in the femoral canal with low radii likely to be inactivated.

The radius predictions for NN14 simulation correspond better with the values of trabecular thickness recorded in the literature (Hildebrand & Rüegsegger (1997), Liu et al. (2008), Kirby et al. (2020)). The NN14 model is fundamentally a stretch dominated lattice and the adaptation simulation guides the model towards a more efficient structure with lower strut radii. The voronoi model as a bending dominated lattice is not as efficient resulting in larger strut radii.

Doube et al. (2011) suggest 460 μm as the maximum feasible thickness for a human trabecula. They arrive at this by noting that diffusion required for cellular metabolism limits the osteocytes in the human trabecula to a location no further than 230 μm from the bone surface (Lozupone (1985), Lozupone & Favia (1990)). However, this limit relates to the trabecular thickness in one direction, whereas the algorithm used in this thesis adapts trabecular radius in all directions. The existence of plates in trabecular structure is well documented (Hildebrand & Rüegsegger (1997), Liu et al. (2008), Kirby et al. (2020)) and it is feasible to hypothesise a strut which is thicker in one direction than the other as depicted in Figure 7.14.

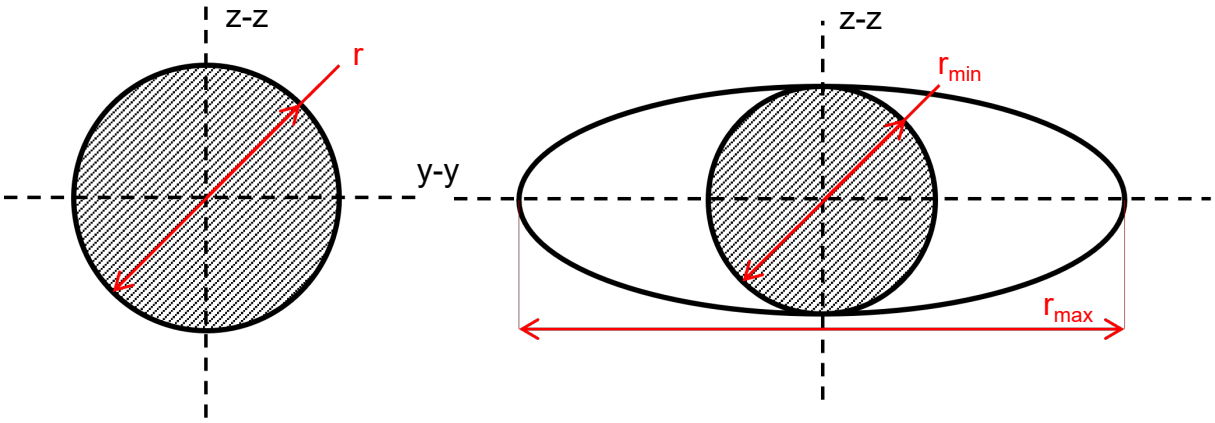
Making an assumption that the minor radius length is governed by the axial load, the maximum radius by bending as indicated in Figure 7.14 and that the maximum moment will always act about the $z-z$ axis, it is possible to calculate equivalent ellipse dimensions. For the adapted circular element, target strain is given by

$$\varepsilon_{target} = \frac{F_x}{EA_c} + \frac{M_{zz}}{EI_c} \tag{7.2}$$

and for the adapted elliptical section by

$$\varepsilon_{target} = \frac{F_x}{EA_e} + \frac{M_{zz}}{EI_{zz-e}} \tag{7.3}$$

where F_x is the axial force in the strut, $M_Z Z$ is the bending moment around $z-z$ axis, $A_c = \pi r^2$, $A_e = \pi r_{min} r_{max}$, $I_c = (\pi r^4)/4$, $I_{zz-e} = (\pi r_{max}^3 r_{min})/4$ and E is the Young's modulus. A_c is the area of a circular strut, A_e is the area of an elliptical strut, I_c is the circle second moment of area, I_{zz-e} is the ellipse second moment of area around zz axis, r, r_{max} and r_{min} are defined in Figure 7.14.



a) Strut at the end of adptation simulation

b) Equivalent eliptical strut

Figure 7.14: Evaluation of ellipse element radii to reproduce the capacity of a circular strut at the end of the adaptation simulation. In step 1 the minimum radius of the ellipse is calculated so that a circular strut with such radius is able to resist the axial load applied to the circular strut whilst limiting the strain to the target value. The major radius is then calculated so that combined axial force and moment do not exceed the target strain value.

One random element with a strut radius close to the mean radius was chosen from both the Voronoi and the NN14 simulations. Axial forces F_x and moments M_{zz} were extracted. The ellipse minimum radius r_{min} was calculated using $\varepsilon_{target} = F_x/E\pi r_{min}^2$. The ellipse maximum radius r_{max} was then calculated using $\varepsilon_{target} = M_{zz}/E\pi r_{min}^3 r_{min}$ substituting the r_{min} obtained from the previous step. The radii are presented in Table 7.9.

It is evident that mean minor radii remain below the limiting value reported by (Dorne & Lander 1985) whilst the mean maximum radii do not excessively exceed the circular radius. In addition, overall trabecular volume reduced from 47,537mm^3 to 39,275mm^3

in the Voronoi model and from 66,275mm^3 to 58,205 mm^3 in the NN14 model.

	Voronoi model			NN14 model		
	Circular strut	Elliptical strut		Circular strut	Elliptcal strut	
	r [μm]	r_{min} [μm]	r_{max}[μm]	r [μm]	r_{min} [μm]	r_{max}[μm]
Mean	292	162	436	97	60	125
SD	325	233	457	175	122	239

Table 7.9: Mean and standard deviation of element radii at the end of the adaptation simulation for circular and equivalent elliptical struts.

This approach does not take into account the axis the bending moment acts about, but it is likely that this would be within a narrow range of directions even if several load cases were to be considered. In the future, the adaptation algorithm could be amended to include this if not as a final but as an interim step towards accounting for plates in trabecular bone.

7.5 Conclusion

As was the case with the virtual cube bone samples in Chapters 4, 5 and 6 both the Voronoi and NN14 models were able to adequately predict the mechanical properties of bone at macro-scale. However the Voronoi model predictions of NC and ITA were much closer to those observed in imaging studies (Reznikov et al. 2014*a*, 2015, 2016). The representative prediction of trabecular bone thickness remains an issue but a potential approach utilising elliptical struts is presented which has the potential to address this. At the same time this approach ia step towards mimicking plate behaviour which may improve the NC and ITA predictions.

8

Discussion and conclusion

8.1 Summary

This thesis has advanced the existing bone structural modelling methodology. Its primary goal has been to achieve a close correspondence between the adapted model topology and that observed in micro-CT imaging studies, while maintaining agreement in predicted stiffness and relative density with macro-level continuum studies. To better understand trabecular bone behaviour and fulfil the thesis objectives, 960 near neighbour (NN) and 110 Voronoi scenarios, using in silico structural lattice models representing trabecular bone samples were studied. The simulations allowed adapted strut cross sectional radii to be varied along their length. To the author's knowledge, this is the first time that such a non-prismatic representation of trabecular bone has been attempted.

The first part of the thesis focused on the NN modelling approach and examined the influence of nominal node connectivity (NNC), mean strut length (MSL), joint fixity and loading on mechanical and topological predictions. A link between a lower NNC and lower stiffness, particularly in stretch dominated simulations, was established. Additionally, lower MSL simulations and those subjected to uniaxial loading exhibited a more significant rate of stiffness decline with reducing NNC. Trabecular bone volume, on the other hand, increased with decreasing NNC, with a higher rate of growth in bending simulations, high MSL, and triaxial loading simulations. This established a clear link between structural efficiency and nodal connectivity where high NNC simulations emerged as the most efficient. Small differences in stiffness and relative density predictions were noted between stretch and bending-dominated simulations exceeding an NNC of 8. A detailed examination of models with NNC of 8 and 6 revealed a transition from stretch-dominated to bending dominated behaviour between these two simulations. The Young's modulus and relative density predictions in different simulations spanned a considerable range, which aligned well with values from literature.

A relationship between the relative density of trabecular bone as a cellular solid and its Young's modulus (Equation 8.1), defined by Gibson & Ashby (1997), was explored.

$$E_i^* = \alpha E_s \bar{\rho}^\beta \tag{8.1}$$

where E_i^* is the Young's modulus of the cellular solid and E_s is the Young's modulus of the solid part. The subscript i can take a value of 1, 2 or 3 defining the three orthogonal directions. The relative density is defined by $\bar{\rho} = v_s/v_t$ where v_s is the solid part and v_t the total volume. α and β are constants dependant on the topology of the cellular solid.

A linear relationship between relative density and stiffness was identified in high NNC simulations both before and after adaptation. In contrast, and not surprisingly, higher values of exponent β were found in low NNC simulations. However, they were typically around 1.55 in unadapted NN04 simulations reducing to 1.4 after adaptation. This challenged the standard theory that low NC lattices exhibit bending dominated behaviour with exponent β values of around 2 (Gibson & Ashby (1982)). This unexpected result suggested that adaptation simulations guide lattices toward a more stretch-dominated behaviour, enhancing their overall efficiency. It is hypothesised that the disordered trabecular arrangements resulting from adaptation simulations, characterised by varying cross-sectional areas along individual elements and between different elements, offer potential advantages in terms of higher tolerance to damage and the ability to self-heal through bone remodelling.

Unexpectedly, a dependence of the modulus density relationships on the MSL has been identified. The simulations with shorter MSL have been found to be more efficient. It is hypothesised that this may be caused by shear deformations which are not considered in the simplified modulus density relationship developed by Gibson & Ashby (1997). This is supported by the finding that simulations with MSL of 0.7mm predict higher shear modulii than the ones with 1.5mm. Consequently, shear deflections make a larger contribution to overall displacements in 1.5mm MSL simulations leading to somewhat lower modulii for the same relative density.

The NN simulations used in this thesis were validated against continuum and previous structural models by examination of macro-scale strains in the virtual cube samples. Bending simulations consistently predicted strains within the adaptation algorithm's lazy zone. The strains in stretch simulations, particularly the low NNC and the uniaxial load-

ing ones, exceeded this range. This demonstrated that all high NNC simulations and low NNC simulations with fixed joint lattices globally behave as continuum models and corresponds with the finding that predictions of these simulations more closely match those in the literature.

The smallest mean predicted NC in NN06 to NN14 simulations was 5.5 and the predominance of nodes with ANC above 5 was larger than 50%. This resulted in an unfavourable comparison with the findings of imaging studies which report a mean NC of about 3.4 and predominance of nodes with NC above 5 of 1.5% (Reznikov et al. (2016)). Conversely, NN04 simulations closely approximated the reported nodal connectivity of real bone with predicted ANCs ranging from 3.4 to 4.8. Additionally, simulations indicated that the prevalence of ANC4 nodes aligns closely with the imaging study findings. However, discrepancies remain, particularly in prediction of ANC3 node prevalence.

The simulation predictions agreed with imaging studies finding that NC, apart from serving as a standalone metric, impacts the ITA. The idealised ITAs of 120°, 109.5° and 108° for ANC3, ANC4 and ANC5 nodes respectively were presented and it was shown that the optimal ITA tends towards 90 degrees as NC increases, resembling an orthotropic continuum. Differences in ITAs between simulations and imaging studies were identified, possibly due to the idealised conditions assumed in simulations and the absence of plate-like trabeculae in the models.

Furthermore, the predictions of mean trabecular thickness indicated that high NNC simulations more closely matched real trabecular bone thickness. These simulations were also found to exhibit a high right skew in diagrams of thickness distributions. This suggested a high prevalence of very small trabeculae which contradicted the findings for real bone. The mean thickness in low NNC simulations was higher but the skew was lower. It is hypothesised that the introduction of plate-like trabeculae in simulation models could potentially address these discrepancies and lead to a better representation of trabecular bone structure.

Overall, the first part of the thesis concluded that NN04 simulations presented the most suitable trabecular structural form candidates. However, challenges remain in ac-

curately representing the complex morphology of trabecular bone, which lead to consideration of an alternative to a NN04 model in the form of a Voronoi cell inspired lattice.

The comparison between Voronoi and NN04 simulations revealed similarities and differences in their predictions regarding the mechanical properties and topology of trabecular bone. Their ability to predict trabecular trajectories was evaluated through a directional index, derived by summing the products of the element vector component absolute values and their corresponding areas. Somewhat unexpectedly, a similar degree of directionality was found in both simulations. Adjustment of the dead zone threshold led to NN14 simulations displaying a greater degree of directionality than either Voronoi or NN04 simulations, however this needs to be explored further.

Both simulations predicted relative density and Young's modulus values that are comparable to those found in the literature and demonstrated a similar relationship between Young's modulus and relative density consistent with a bending-dominated lattice structure. However, Voronoi simulations tend to predict slightly less dense but stiffer trabecular architectures compared to NN04 simulations, resulting in slightly greater structural efficiency. Furthermore, there were slight variations in stiffnesses predicted in directions not aligned with the loading direction. Voronoi simulations display larger stiffness in these directions at 0.7mm MSL, while NN04 simulations do so at 1.5mm MSL. The stiffness in these directions was found to decrease with increasing MSL, but the rate of reduction was greater in Voronoi simulations.

Additionally, Voronoi simulations exhibit a closer resemblance to the topology of actual trabecular bone when compared to NN04 simulations, especially regarding mean NC predictions which are closer to those reported in imaging studies of real bone. The ITA predictions in Voronoi simulations are also closer to those theoretically expected and reported in literature for real bone, particularly for ANC4 and ANC5 nodes.

The task of predicting trabecular thickness which closely matches real bone remained challenging, with NN14 simulations showing the closest resemblance to actual bone. Voronoi, NN04 and NN14 simulations all tend to predict a large proportion of smallest radii elements and predict a mean radius which exceeds trabecular bone thickness.

Finally, the Voronoi and NN04 modelling of trabeculae were implemented on a proximal femur adaptation simulation. As was the case with the abstract cube bone samples in Chapters 4, 5 and 6 both the Voronoi and NN14 models were able to adequately predict the mechanical properties of bone at macro-scale. However, the Voronoi model predictions of NC and ITA were much closer to those observed in the imaging studies (Reznikov et al. 2014*a*, 2015, 2016). The representative prediction of trabecular bone thickness remains an issue but an approach utilising elliptical struts is presented which has the potential to address this. This approach has the ability to mimic plate behaviour which may improve the NC and ITA predictions.

8.2 Limitations and future work

Deficiencies and limitations of the bone adaptation simulations presented in this thesis have have been discussed in previous Chapters. This Section draws them together and suggests possible future enhancements.

Compared to micro-scale continuum finite element models, the mesoscale structural approach used prior to this research ensured computational efficiency with resolution sufficient to adequately represent trabecular trajectories. It could not represent individual trabeculae as strut lengths and radii were above the size of rod-like trabeculae and plate-like trabeculae were absent. Truss elements could only resist axial force. This thesis successfully enhanced this simulation approach by developing an algorithm which models bending behaviour using element lengths representative of actual trabeculae. However, limitations remain. Adjustment of the dead zone threshold led to NN14 simulations revealing a greater degree of directionality than any other simulation, which needs to be explored further. In addition an algorithm could be adjusted to allow the nodes to move in relation to the applied strains and thus achieve trajectory predictions which better match those observed in real bone (Villette & Phillips (2016)).

Implementation of the Voronoi modelling of the trabecular bone has achieved NC predictions closer to that of real bone, however differences remain. Some of the discrepancy between the modelling predictions and the imaging study findings may be

caused by the presence of plate like trabeculae. The modelling algorithm does not consider plates and it is not clear how they were considered in imaging studies. Future work will consider modelling plates and this is likely to reduce NC predictions.

Additionally, the predicted mechanical properties and topology of trabecular bone are influenced by the applied loading conditions. While 1.0 MPa used in the virtual cube samples is considered representative of trabecular bone loading in joint contact sites, different anatomical sites and loading environments may yield different predictions. This variability underscores the importance of considering specific loading conditions when interpreting simulation results. In the case of the femur model a single load case representative of the peak hip joint contact force during the stance phase of the walking cycle was considered. Consideration of more loading cases and load spreading would likely enhance the predictions.

The modelling framework developed in this thesis allows predictions of how bone adapts to its mechanical environment. The adaptation algorithm does not consider the physiological time needed for bone remodelling and only predicts the final remodelled state nor the frequency at which activities are performed. Both have been shown to influence bone remodelling (Turner et al. (1995), Turner (1998)), and future work could implement a remodelling rate and loading frequency to improve the simulation of the loading environment.

Another limitation related to the algorithm is related to the use of strain to drive the optimisation simulations. Considering the model scale, strain is an acceptable surrogate for the physiological phenomenon that takes place at the cellular level. However, modelling the cellular response to fluid motion, which has been proposed as a mechanistic driver for bone remodelling, would allow the investigation of trabecular bone behaviour at a different scale. This could be achieved with the use of meta-models developed by Villette & Phillips (2017).

8.3 Field of application

A trabecular bone model topology closely resembling real bone would be a step toward 3D printing of patient specific implants. The additive manufacturing techniques could be used to translate computational models developed in this thesis into printable structures. Using converged models at the end of the adaptation simulations would result in scaffolds with more biofidelic properties in terms of node connectivity, strut length in addition to mechanical properties of density and stiffness matching that of bone. Such scaffolds would allow vascular invasion and would behave sympathetically in load bearing with the healthy bone tissue. It is hoped that such implants would be better integrated within the bone tissue. Current scaffold based implants, which are based on high NC lattice models with uniform struts cross sections, are difficult to print and tend to loosen over time.

8.4 Conclusion

The modelling approach presented in this thesis contributes to a deeper understanding of trabecular bone architecture and could allow more productive collaborations with clinicians in the future. This efficient numerical tool could simulate patient specific bone behaviour under real loading conditions, particularly if combined with musculoskeletal modelling. This could inform clinical decisions. In addition, the models could allow study of clinical conditions such as osteoporosis.

The modelling methodology developed in this thesis, which is essentially an iterative optimisation, could be applied to civil and structural engineering design to minimise the amount of material used. The ability of the algorithm to produce non-prismatic sections could allow the material to be placed where its required further optimising designs. The algorithm used in the thesis divides individual members into four sections but there is no theoretical limit of how many sections could be used. Finally, the fact that the simulation predicts disordered lattices which appear to have an advantage in terms of damage tolerance, could hold an advantage in design of structures where robustness

or resistance to blast damage is a requirement.

References

Aamodt, A., Lund-Larsen, J., Eine, J., Andersen, E., Benum, P. & Husby, O. S. (1997), 'In vivo measurements show tensile axial strain in the proximal lateral aspect of the human femur', *Journal of Orthopaedic Research* **15**(6), 927–931.

Adachi, T., Tsubota, K.-i., Tomita, Y. & Hollister, S. J. (2001), 'Trabecular surface remodeling simulation for cancellous bone using microstructural voxel finite element models', *Journal of biomechanical engineering* **123**(5), 403–409.

Alsheghri, A., Reznikov, N., Piché, N., McKee, M. D., Tamimi, F. & Song, J. (2021), 'Optimization of 3d network topology for bioinspired design of stiff and lightweight bone-like structures', *Materials Science and Engineering: C* **123**, 112010.

Anderson, B., Jackson, J. & Sitharam, M. (1998), 'Descartes' rule of signs revisited', *The American Mathematical Monthly* **105**(5), 447–451.

Arabnia, H. R. & Tran, Q. N. (2015), *Emerging trends in computational biology, bioinformatics, and systems biology: algorithms and software tools*, Morgan Kaufmann.

Ashby, M. F. (2006), 'The properties of foams and lattices', *Philosophical Transactions of the Royal Society A: Mathematical, Physical and Engineering Sciences* **364**(1838), 15–30.

Atiyah, M. & Sutcliffe, P. (2003), 'Polyhedra in physics, chemistry and geometry'.

Baum, T., Carballido-Gamio, J., Huber, M., Müller, D., Monetti, R., Räth, C., Eckstein, F., Lochmüller, E., Majumdar, S., Rummeny, E. et al. (2010), 'Automated 3d trabecular bone structure analysis of the proximal femur—prediction of biomechanical strength by ct and dxa', *Osteoporosis international* **21**(9), 1553–1564.

Bayraktar, H. H., Morgan, E. F., Niebur, G. L., Morris, G. E., Wong, E. K. & Keaveny, T. M. (2004), 'Comparison of the elastic and yield properties of human femoral trabecular and cortical bone tissue', *Journal of biomechanics* **37**(1), 27–35.

Beaupré, G., Orr, T. & Carter, D. (1990), 'An approach for time-dependent bone modelling and remodelling-application: A preliminary remodeling simulation', *J. Orthopaed. Res* **8**(5), 662–670.

Ben-Zvi, Y., Reznikov, N., Shahar, R. & Weiner, S. (2017), '3d architecture of trabecular bone in the pig mandible and femur: inter-trabecular angle distributions', *Frontiers in Materials* **4**, 29.

Bergmann, G., Deuretzbacher, G., Heller, M., Graichen, F., Rohlmann, A., Strauss, J. & Duda, G. (2001), 'Hip contact forces and gait patterns from routine activities', *Journal of biomechanics* **34**(7), 859–871.

Bitsakos, C., Kerner, J., Fisher, I. & Amis, A. A. (2005), 'The effect of muscle loading on the simulation of bone remodelling in the proximal femur', *Journal of biomechanics* **38**(1), 133–139.

Boyle, C. & Kim, I. Y. (2011), 'Three-dimensional micro-level computational study of wolff's law via trabecular bone remodeling in the human proximal femur using design space topology optimization', *Journal of biomechanics* **44**(5), 935–942.

Brickley, M. & Howell, P. (1999), 'Measurement of changes in trabecular bone structure with age in an archaeological population', *Journal of Archaeological Science* **26**(2), 151–157.

BSE (2014), BS EN 1991-1-7:2006+A1:2014: Eurocode 1 — Actions on structures Part 1-7 - General actions — Accidental actions, Standard, BSI.

Burr, D. B. & Allen, M. R. (2019), *Basic and applied bone biology*, Academic Press, chapter 4.

Buxton, G. A. & Clarke, N. (2007), '"bending to stretching" transition in disordered networks', *Physical review letters* **98**(23), 238103.

Carter, D. (1982), 'The relationship between in vivo strains and cortical bone remodeling.', *Critical reviews in biomedical engineering* **8**(1), 1–28.

Carter, D., Fyhrie, D. & Whalen, R. (1987), 'Trabecular bone density and loading history: regulation of connective tissue biology by mechanical energy', *Journal of biomechanics* **20**(8), 785789–787794.

Carter, D., Orr, T. & Fyhrie, D. P. (1989), 'Relationships between loading history and femoral cancellous bone architecture', *Journal of biomechanics* **22**(3), 231–244.

Carter, D. R., Beaupré, G. S., Giori, N. J. & Helms, J. A. (1998), 'Mechanobiology of skeletal regeneration.', *Clinical orthopaedics and related research* **355**, S41–S55.

Carter, D. R. & Hayes, W. C. (1977), 'The compressive behavior of bone as a two-phase porous structure', *J Bone Joint Surg Am* **59**(7), 954–962.

Chen, L. & Xu, J.-c. (2004), 'Optimal delaunay triangulations', *Journal of Computational Mathematics* pp. 299–308.

Ciarelli, M., Goldstein, S., Kuhn, J., Cody, D. & Brown, M. (1991), 'Evaluation of orthogonal mechanical properties and density of human trabecular bone from the major metaphyseal regions with materials testing and computed tomography', *Journal of Orthopaedic Research* **9**(5), 674–682.

Claes, L. & Heigele, C. (1999), 'Magnitudes of local stress and strain along bony surfaces predict the course and type of fracture healing', *Journal of biomechanics* **32**(3), 255–266.

Clarke, B. (2008), 'Normal bone anatomy and physiology', *Clinical journal of the American Society of Nephrology* **3**(Supplement 3), S131–S139.

Cowin, S. & Hegedus, D. (1976), 'Bone remodeling i: theory of adaptive elasticity', *Journal of Elasticity* **6**(3), 313–326.

Culmann, K. (1866), 'Die graphische statik', *Mayer and Zeller, Zurich* .

Currey, J. D. (2012), 'The structure and mechanics of bone', *Journal of Materials Science* **47**, 41–54.

Deal, C. (2009), 'Potential new drug targets for osteoporosis', *Nature clinical practice Rheumatology* **5**(1), 20–27.

Dell(UK) (2024), 'Hpc solutions'.
URL: *https://shorturl.at/msPWZ*

Deshpande, V., Ashby, M. & Fleck, N. (2001), 'Foam topology: bending versus stretching dominated architectures', *Acta materialia* **49**(6), 1035–1040.

Dorne, H. & Lander, P. H. (1985), 'Spontaneous stress fractures of the femoral neck', *American journal of roentgenology* **144**(2), 343–347.

Doube, M., Kłosowski, M. M., Wiktorowicz-Conroy, A. M., Hutchinson, J. R. & Shefelbine, S. J. (2011), 'Trabecular bone scales allometrically in mammals and birds', *Proceedings of the Royal Society B: Biological Sciences* **278**(1721), 3067–3073.

Ducheyne, P. (2015), *Comprehensive biomaterials*, Vol. 1, Elsevier.

Favier, C. D. (2020), Combined musculoskeletal and finite element modelling of the lumbar spine and lower limbs, PhD thesis, Imperial College London.

Favier, C. D., McGregor, A. H. & Phillips, A. T. (2021), 'Maintaining bone health in the lumbar spine: Routine activities alone are not enough', *Frontiers in bioengineering and biotechnology* **9**.

Fenech, C. & Keaveny, T. (1999), 'A cellular solid criterion for predicting the axial-shear failure properties of bovine trabecular bone'.

Frost, H. M. (1996), 'Perspectives: a proposed general model of the (suggestions from a new skeletal-biologic paradigm)', *The anatomical record* **244**(2), 139–147.

Frost, H. M. (2003), 'Bone's mechanostat: a 2003 update', *The Anatomical Record Part A: Discoveries in Molecular, Cellular, and Evolutionary Biology* **275**(2), 1081–1101.

Fyhrie, D. & Carter, D. (1986), 'A unifying principle relating stress to trabecular bone morphology', *Journal of Orthopaedic Research* **4**(3), 304–317.

Gallois, J. & Japoit, T. (1925), 'Architecture interieure des vertebres', *Revue de Chirurgie* **63**, 688–708.

Garcia-Aznar, J. M., Rüberg, T. & Doblare, M. (2005), 'A bone remodelling model coupling microdamage growth and repair by 3d bmu-activity', *Biomechanics and modeling in mechanobiology* **4**(2-3), 147–167.

Garden, R. (1961), 'The structure and function of the proximal end of the femur', *The Journal of Bone & Joint Surgery British Volume* **43**(3), 576–589.

Geraldes, D. M. & Phillips, A. T. (2014), 'A comparative study of orthotropic and isotropic bone adaptation in the femur', *International journal for numerical methods in biomedical engineering* **30**(9), 873–889.

Gibson, I. & Ashby, M. F. (1982), 'The mechanics of three-dimensional cellular materials', *Proceedings of the royal society of London. A. Mathematical and physical sciences* **382**(1782), 43–59.

Gibson, L. J. (2005), 'Biomechanics of cellular solids', *Journal of biomechanics* **38**(3), 377–399.

Gibson, L. J. & Ashby, M. F. (1997), *Cellular Solids: Structure and Properties*, Cambridge Solid State Science Series, 2 edn, Cambridge University Press.

Gillespie, R. (1963), 'The valence-shell electron-pair repulsion (vsepr) theory of directed valency', *Journal of Chemical Education* **40**(6), 295.

Goldberg, M. (1974), 'Three infinite families of tetrahedral space-fillers', *Journal of Combinatorial Theory, Series A* **16**(3), 348–354.

Goldstein, S. A., Matthews, L. S., Kuhn, J. L. & Hollister, S. J. (1991), 'Trabecular bone remodeling: an experimental model', *Journal of biomechanics* **24**, 135–150.

Goulet, R. W., Goldstein, S. A., Ciarelli, M. J., Kuhn, J. L., Brown, M. & Feldkamp, L. (1994), 'The relationship between the structural and orthogonal compressive properties of trabecular bone', *Journal of biomechanics* **27**(4), 375–389.

Guo, X. & Kim, C. (2002), 'Mechanical consequence of trabecular bone loss and its treatment: a three-dimensional model simulation', *Bone* **30**(2), 404–411.

Hambli, R. (2013), 'Micro-ct finite element model and experimental validation of trabecular bone damage and fracture', *Bone* **56**(2), 363–374.

Harris, M. D., Anderson, A. E., Henak, C. R., Ellis, B. J., Peters, C. L. & Weiss, J. A. (2012), 'Finite element prediction of cartilage contact stresses in normal human hips', *Journal of Orthopaedic Research* **30**(7), 1133–1139.

Harvey, N. C., Glüer, C. C., Binkley, N., McCloskey, E., Brandi, M.-L., Cooper, C., Kendler, D., Lamy, O., Laslop, A., Camargos, B. M. et al. (2015), 'Trabecular bone score (tbs) as a new complementary approach for osteoporosis evaluation in clinical practice', *Bone* **78**, 216–224.

Hegedus, D. & Cowin, S. (1976), 'Bone remodeling ii: small strain adaptive elasticity', *Journal of elasticity* **6**(4), 337–352.

Helgason, B., Perilli, E., Schileo, E., Taddei, F., Brynjólfsson, S. & Viceconti, M. (2008), 'Mathematical relationships between bone density and mechanical properties: a literature review', *Clinical biomechanics* **23**(2), 135–146.

Heller, M., Bergmann, G., Kassi, J.-P., Claes, L., Haas, N. & Duda, G. (2005), 'Determination of muscle loading at the hip joint for use in pre-clinical testing', *Journal of biomechanics* **38**(5), 1155–1163.

Hildebrand, T., Laib, A., Müller, R., Dequeker, J. & Rüegsegger, P. (1999), 'Direct three-dimensional morphometric analysis of human cancellous bone: microstructural data from spine, femur, iliac crest, and calcaneus', *Journal of bone and mineral research* **14**(7), 1167–1174.

Hildebrand, T. & Rüegsegger, P. (1997), 'Quantification of bone microarchitecture with the structure model index', *Computer Methods in Biomechanics and Bio Medical Engineering* **1**(1), 15–23.

Hill, P. (1998), 'Bone remodelling', *British journal of orthodontics* **25**(2), 101–107.

Huiskes, R., Weinans, H., Grootenboer, H., Dalstra, M., Fudala, B. & Slooff, T. (1987), 'Adaptive bone-remodeling theory applied to prosthetic-design analysis', *Journal of biomechanics* **20**(11), 1135–1150.

Hutchinson, R. G. & Fleck, N. A. (2006), 'The structural performance of the periodic truss', *Journal of the Mechanics and Physics of Solids* **54**(4), 756–782.

Jang, I. G. & Kim, I. Y. (2008), 'Computational study of wolff's law with trabecular architecture in the human proximal femur using topology optimization', *Journal of biomechanics* **41**(11), 2353–2361.

Jensen, K., Mosekilde, L. & Mosekilde, L. (1990), 'A model of vertebral trabecular bone architecture and its mechanical properties', *Bone* **11**(6), 417–423.

Kaufmann, J., McGregor, A. & Phillips, A. (2021), A combined musculoskeletal and finite element modelling approach to investigating bone loss in transfemoral amputees, *in* 'Orthopaedic Proceedings', Vol. 103, The British Editorial Society of Bone & Joint Surgery, pp. 37–37.

Keaveny, T. M., Morgan, E. F., Niebur, G. L. & Yeh, O. C. (2001), 'Biomechanics of trabecular bone', *Annual review of biomedical engineering* **3**(1), 307–333.

Keaveny, T. M., Morgan, E. F., Yeh, O. C. et al. (2004), 'Bone mechanics', *Standard handbook of biomedical engineering and design* pp. 8–1.

Kim, H., Howard, G. & Cunningham, J. (2009), Do trabeculae of femoral head represent a structural optimum?, *in* '13th International Conference on Biomedical Engineering: ICBME 2008 3–6 December 2008 Singapore', Springer, pp. 1636–1639.

Kirby, M., Morshed, A. H., Gomez, J., Xiao, P., Hu, Y., Guo, X. E. & Wang, X. (2020), 'Three-dimensional rendering of trabecular bone microarchitecture using a probabilistic approach', *Biomechanics and modeling in mechanobiology* pp. 1–19.

Kontulainen, S., Sievänen, H., Kannus, P., Pasanen, M. & Vuori, I. (2003), 'Effect of long-term impact-loading on mass, size, and estimated strength of humerus and radius of female racquet-sports players: a peripheral quantitative computed tomography study between young and old starters and controls', *Journal of Bone and Mineral Research* **18**(2), 352–359.

Kular, J., Tickner, J., Chim, S. M. & Xu, J. (2012), 'An overview of the regulation of bone remodelling at the cellular level', *Clinical biochemistry* **45**(12), 863–873.

Kung, C. (2005), 'A possible unifying principle for mechanosensation', *Nature* **436**(7051), 647.

Laib, A., Newitt, D., Lu, Y. & Majumdar, S. (2002), 'New model-independent measures of trabecular bone structure applied to in vivo high-resolution mr images', *Osteoporosis International* **13**, 130–136.

Langdahl, B., Ferrari, S. & Dempster, D. W. (2016), 'Bone modeling and remodeling: potential as therapeutic targets for the treatment of osteoporosis', *Therapeutic advances in musculoskeletal disease* **8**(6), 225–235.

Lanyon, L., Hampson, W., Goodship, A. & Shah, J. (1975), 'Bone deformation recorded in vivo from strain gauges attached to the human tibial shaft', *Acta Orthopaedica Scandinavica* **46**(2), 256–268.

Legrand, E., Chappard, D., Pascaretti, C., Duquenne, M., Krebs, S., Rohmer, V., Basle, M.-F. & Audran, M. (2000), 'Trabecular bone microarchitecture, bone mineral density, and vertebral fractures in male osteoporosis', *Journal of Bone and Mineral Research* **15**(1), 13–19.

Lill, H., Hepp, P., Korner, J., Kassi, J.-P., Verheyden, A., Josten, C. & Duda, G. (2003), 'Proximal humeral fractures: how stiff should an implant be?', *Archives of orthopaedic and trauma surgery* **123**(2), 74–81.

Linde, F., Hvid, I. & Madsen, F. (1992), 'The effect of specimen geometry on the mechanical behaviour of trabecular bone specimens', *Journal of biomechanics* **25**(4), 359–368.

Liu, L., Kamm, P., García-Moreno, F., Banhart, J. & Pasini, D. (2017), 'Elastic and failure response of imperfect three-dimensional metallic lattices: the role of geometric defects induced by selective laser melting', *Journal of the Mechanics and Physics of Solids* **107**, 160–184.

Liu, X. S., Sajda, P., Saha, P. K., Wehrli, F. W., Bevill, G., Keaveny, T. M. & Guo, X. E. (2008), 'Complete volumetric decomposition of individual trabecular plates and rods and its morphological correlations with anisotropic elastic moduli in human trabecular bone', *Journal of Bone and Mineral Research* **23**(2), 223–235.

Liu, X. S., Sajda, P., Saha, P. K., Wehrli, F. W. & Guo, X. E. (2006), 'Quantification of the roles of trabecular microarchitecture and trabecular type in determining the elastic modulus of human trabecular bone', *Journal of Bone and Mineral Research* **21**(10), 1608–1617.

Lozupone, E. (1985), 'The structure of the trabeculae of cancellous bone. 1. the calcaneus.', *Anatomischer Anzeiger* **159**(1-5), 211–229.

Lozupone, E. & Favia, A. (1990), 'The structure of the trabeculae of cancellous bone. 2. long bones and mastoid', *Calcified tissue international* **46**, 367–372.

Luxner, M. H., Stampfl, J. & Pettermann, H. E. (2007), 'Numerical simulations of 3d open cell structures–influence of structural irregularities on elastoplasticity and deformation localization', *International Journal of Solids and Structures* **44**(9), 2990–3003.

Luxner, M. H., Woesz, A., Stampfl, J., Fratzl, P. & Pettermann, H. E. (2009), 'A finite element study on the effects of disorder in cellular structures', *Acta biomaterialia* **5**(1), 381–390.

Macchiarelli, R., Bondioli, L., Galichon, V. & Tobias, P. (1999), 'Hip bone trabecular architecture shows uniquely distinctive locomotor behaviour in south african australopithecines', *Journal of Human Evolution* **36**(2), 211–232.

Maconachie, T., Leary, M., Lozanovski, B., Zhang, X., Qian, M., Faruque, O. & Brandt, M. (2019), 'Slm lattice structures: Properties, performance, applications and challenges', *Materials & Design* **183**, 108137.

Marks, N., McKenzie, D., Pailthorpe, B., Bernasconi, M. & Parrinello, M. (1996), 'Microscopic structure of tetrahedral amorphous carbon', *Physical review letters* **76**(5), 768.

Maskery, I., Aboulkhair, N. T., Aremu, A., Tuck, C. & Ashcroft, I. (2017), 'Compressive failure modes and energy absorption in additively manufactured double gyroid lattices', *Additive Manufacturing* **16**, 24–29.

Maxwell, J. C. (1864), 'L. on the calculation of the equilibrium and stiffness of frames', *The London, Edinburgh, and Dublin Philosophical Magazine and Journal of Science* **27**(182), 294–299.

Mercer, C., He, M., Wang, R. & Evans, A. (2006), 'Mechanisms governing the inelastic deformation of cortical bone and application to trabecular bone', *Acta Biomaterialia* **2**(1), 59–68.

Mont, M. A. & Hungerford, D. S. (1995), 'Non-traumatic avascular necrosis of the femoral head.', *JBJS* **77**(3), 459–474.

Morgan, E. F., Bayraktar, H. H. & Keaveny, T. M. (2003), 'Trabecular bone modulus–density relationships depend on anatomic site', *Journal of biomechanics* **36**(7), 897–904.

Morgan, E. F. & Keaveny, T. M. (2001), 'Dependence of yield strain of human trabecular bone on anatomic site', *Journal of biomechanics* **34**(5), 569–577.

Morlock, M., Schneider, E., Bluhm, A., Vollmer, M., Bergmann, G., Müller, V. & Honl, M. (2001), 'Duration and frequency of every day activities in total hip patients', *Journal of biomechanics* **34**(7), 873–881.

Mosekilde, L. (1988), 'Age-related changes in vertebral trabecular bone architecture—assessed by a new method', *Bone* **9**(4), 247–250.

Nawathe, S., Nguyen, B. P., Barzanian, N., Akhlaghpour, H., Bouxsein, M. L. & Keaveny, T. M. (2015), 'Cortical and trabecular load sharing in the human femoral neck', *Journal of biomechanics* **48**(5), 816–822.

Nebot, E., Heimel, P., Tangl, S., Dockner, M., Patsch, J., Weber, G. W., Pretterklieber, M., Teschler-Nicola, M. & Pietschmann, P. (2019), 'Paget's disease of long bones: microstructural analyses of historical bone samples', *Calcified tissue international* **105**, 15–25.

OpenStax (2017), 'Anatomy & physiology'. Accessed: 2022-03-01.
URL: *https://openstax.org/books/anatomy-and-physiology/pages/1-introduction*

Pankaj, P. (2013), 'Patient-specific modelling of bone and bone-implant systems: the challenges', *International journal for numerical methods in biomedical engineering* **29**(2), 233–249.

Parfitt, A. M. (1994), 'Osteonal and hemi-osteonal remodeling: the spatial and temporal framework for signal traffic in adult human bone', *Journal of cellular biochemistry* **55**(3), 273–286.

Patton, D. M., Bigelow, E. M., Schlecht, S. H., Kohn, D. H., Bredbenner, T. L. & Jepsen, K. J. (2019), 'The relationship between whole bone stiffness and strength is age and sex dependent', *Journal of biomechanics* **83**, 125–133.

Pauwels, F. (1959), 'A new theory on the influence of mechanical stimuli on the differentiation of supporting tissue. the tenth contribution to the functional anatomy and causal morphology of the supporting structure.', *Zeitschrift fur Anatomie und Entwicklungsgeschichte* **121**, 478–515.

Pauwels, F. (1965), *Gesammelte abhandlungen zur funktionellen anatomie des bewegungsapparates*, Springer-Verlag.

Pauwels, F. (1980), *Biomechanics of the locomotor apparatus: contributions on the functional anatomy of the locomotor apparatus*, Springer Verlag.

Phillips, A. T. (2010), 'Coronal slice of the proximal femur. [photograph].'.

Phillips, A. T. (2012), 'Structural optimisation: biomechanics of the femur', *Proceedings of the Institution of Civil Engineers-Engineering and Computational Mechanics* **165**(2), 147–154.

Phillips, A. T., Villette, C. C. & Modenese, L. (2015), 'Femoral bone mesoscale structural architecture prediction using musculoskeletal and finite element modelling', *International Biomechanics* **2**(1), 43–61.

Prendergast, P. & Taylor, D. (1994), 'Prediction of bone adaptation using damage accumulation', *Journal of biomechanics* **27**(8), 1067–1076.

Reginster, J.-Y. & Burlet, N. (2006), 'Osteoporosis: a still increasing prevalence', *Bone* **38**(2), 4–9.

Reznikov, N., Alsheghri, A. A., Piché, N., Gendron, M., Desrosiers, C., Morozova, I., Siles, J. M. S., Gonzalez-Quevedo, D., Tamimi, I., Song, J. et al. (2020), 'Altered topological blueprint of trabecular bone associates with skeletal pathology in humans', *Bone reports* **12**, 100264.

Reznikov, N., Chase, H., Brumfeld, V., Shahar, R. & Weiner, S. (2015), 'The 3d structure of the collagen fibril network in human trabecular bone: Relation to trabecular organization', *Bone* **71**, 189–195.

Reznikov, N., Chase, H., Zvi, Y. B., Tarle, V., Singer, M., Brumfeld, V., Shahar, R. & Weiner, S. (2016), 'Inter-trabecular angle: a parameter of trabecular bone architecture in the human proximal femur that reveals underlying topological motifs', *Acta biomaterialia* **44**, 65–72.

Reznikov, N., Phillips, C., Cooke, M., Garbout, A., Ahmed, F. & Stevens, M. M. (2017), 'Functional adaptation of the calcaneus in historical foot binding', *Journal of Bone and Mineral Research* **32**(9), 1915–1925.

Reznikov, N., Shahar, R. & Weiner, S. (2014*a*), 'Bone hierarchical structure in three dimensions', *Acta biomaterialia* **10**(9), 3815–3826.

Reznikov, N., Shahar, R. & Weiner, S. (2014*b*), 'Three-dimensional structure of human lamellar bone: the presence of two different materials and new insights into the hierarchical organization', *Bone* **59**, 93–104.

Rho, J.-Y., Kuhn-Spearing, L. & Zioupos, P. (1998), 'Mechanical properties and the hierarchical structure of bone', *Medical engineering & physics* **20**(2), 92–102.

Rucci, N. (2008), 'Molecular biology of bone remodelling', *Clinical cases in mineral and bone metabolism* **5**(1), 49.

Salari, N., Ghasemi, H., Mohammadi, L., Behzadi, M. H., Rabieenia, E., Shohaimi, S. & Mohammadi, M. (2021), 'The global prevalence of osteoporosis in the world: a comprehensive systematic review and meta-analysis', *Journal of orthopaedic surgery and research* **16**, 1–20.

Seeman, E. (2013), 'Age-and menopause-related bone loss compromise cortical and trabecular microstructure', *Journals of Gerontology Series A: Biomedical Sciences and Medical Sciences* **68**(10), 1218–1225.

Shefelbine, S. J., Augat, P., Claes, L. & Simon, U. (2005), 'Trabecular bone fracture healing simulation with finite element analysis and fuzzy logic', *Journal of biomechanics* **38**(12), 2440–2450.

Singh, M., Nagrath, A. & Maini, P. (1970), 'Changes in trabecular pattern of the upper end of the femur as an index of osteoporosis', *JBJS* **52**(3), 457–467.

Skedros, J. G. & Baucom, S. L. (2007), 'Mathematical analysis of trabecular 'trajectories' in apparent trajectorial structures: the unfortunate historical emphasis on the human proximal femur', *Journal of theoretical biology* **244**(1), 15–45.

Stauber, M. & Müller, R. (2006), 'Volumetric spatial decomposition of trabecular bone into rods and plates—a new method for local bone morphometry', *Bone* **38**(4), 475–484.

Stephenson, P. & Seedhom, B. (1999), 'Cross-sectional geometry of the human femur in the mid-third region', *Proceedings of the Institution of Mechanical Engineers, Part H: Journal of Engineering in Medicine* **213**(2), 159–166.

Taddei, F., Balestri, M., Rimondi, E., Viceconti, M. & Manfrini, M. (2009), 'Tibia adaptation after fibula harvesting: an in vivo quantitative study', *Clinical Orthopaedics and Related Research®* **467**, 2149–2158.

Treece, G. M., Gee, A. H., Mayhew, P. & Poole, K. E. (2010), 'High resolution cortical bone thickness measurement from clinical ct data', *Medical image analysis* **14**(3), 276–290.

Tsubota, K.-i., Adachi, T. & Tomita, Y. (2002), 'Functional adaptation of cancellous bone in human proximal femur predicted by trabecular surface remodeling simulation toward uniform stress state', *Journal of biomechanics* **35**(12), 1541–1551.

Turner, C. H. (1998), 'Three Rules for Bone Adapatation to Mechanical Stimuli', *Bone* **23**(5), 399–407.

Turner, C. H., Owan, I. & Takano, Y. (1995), 'Mechanotransduction in bone: role of strain rate', *American Journal of Physiology-Endocrinology and Metabolism* **269**(3), E438–E442.

Turner, C. H., Rho, J., Takano, Y., Tsui, T. Y. & Pharr, G. M. (1999), 'The elastic properties of trabecular and cortical bone tissues are similar: results from two microscopic measurement techniques', *Journal of biomechanics* **32**(4), 437–441.

Vajjhala, S., Kraynik, A. & Gibson, L. (2000), 'A cellular solid model for modulus reduction due to resorption of trabeculae in bone', *J. Biomech. Eng.* **122**(5), 511–515.

van Lenthe, G. H., Stauber, M. & Müller, R. (2006), 'Specimen-specific beam models for fast and accurate prediction of human trabecular bone mechanical properties', *Bone* **39**(6), 1182–1189.

Verhulp, E., van Rietbergen, B. & Huiskes, R. (2006), 'Comparison of micro-level and continuum-level voxel models of the proximal femur', *Journal of biomechanics* **39**(16), 2951–2957.

Villette, C. C. & Phillips, A. T. (2016), 'Informing phenomenological structural bone remodelling with a mechanistic poroelastic model', *Biomechanics and modeling in mechanobiology* **15**(1), 69–82.

Villette, C. & Phillips, A. (2017), 'Microscale poroelastic metamodel for efficient mesoscale bone remodelling simulations', *Biomechanics and modeling in mechanobiology* **16**(6), 2077–2091.

Villette, C. & Phillips, A. (2018), 'Rate and age-dependent damage elasticity formulation for efficient hip fracture simulations', *Medical engineering & physics* **61**, 1–12.

von Meyer, G. (1867), 'Die architecture der spongiosa. archv fur anatomie.', *Physiologie und Wissenschanfiche Medizin.* **34**, 615–625.

Weaire, D. & Rivier, N. (1984), 'Soap, cells and statistics—random patterns in two dimensions', *Contemporary Physics* **25**(1), 59–99.

Whalen, R., Carter, D. & Steele, C. (1988), 'Influence of physical activity on the regulation of bone density', *Journal of biomechanics* **21**(10), 825–837.

Whyte, M. P. (2006), ‘Paget’s disease of bone’, *New England Journal of Medicine* **355**(6), 593–600.

Wolff, J. (1869), ‘Uber die bedeutung der architektur der spongiosen substanz’, *Zentralblatt fur die medizinische Wissenschaft* pp. 223–234.

Wu, Y. & Yang, L. (2020), ‘The effect of unit cell size and topology on tensile failure behavior of 2d lattice structures’, *International Journal of Mechanical Sciences* **170**, 105342.

Zaharie, D. T. & Phillips, A. (2018), ‘Pelvic construct prediction of trabecular and cortical bone structural architecture’, *Journal of biomechanical engineering* **140**(9).

Zhao, F., Kirby, M., Roy, A., Hu, Y., Guo, X. E. & Wang, X. (2018), ‘Commonality in the microarchitecture of trabecular bone: a preliminary study’, *Bone* **111**, 59–70.

Publications

Radukic, B. & Phillips, A. (2023), The role of the dead zone in predictions of trabecular bone topology and continuum level mechanical properties, *in* 'Orthopaedic Proceedings', Vol. 105, Bone & Joint, pp. 44–44.

A

Additional results appendix

NN nodal connectivity

Load	NNC	MSL = 0.7 mm				MSL = 1.0 mm				MSL = 1.5 mm			
		Bending simulations											
		Mean	Mode	SD	Max	Mean	Mode	SD	Max	Mean	Mode	SD	Max
Uniaxial	4	4	5	6	7	4	5	6	9	4	5	6	9
		46.5%	33.8%	14.3%	4.5%	46.5%	33.8%	14.3%	4.5%	46.5%	33.8%	14.3%	4.5%
	4*	14.0	15.0	16.0	17.0					14.0	15.0	16.0	17.0
		31.3%	24.5%	16.6%	9.7%					31.3%	24.5%	16.6%	9.7%
	6	6	7	8	9	6	7	8	9	6	7	8	9
		43.6%	33.1%	16.4%	5.3%	43.6%	33.1%	16.4%	5.3%	43.6%	33.1%	16.4%	5.3%
	8	8	9	10	11	8	9	10	11	8	9	10	11
		42.0%	30.9%	16.8%	6.5%	42.0%	30.9%	16.8%	6.5%	42.0%	30.9%	16.8%	6.5%
	10	10	11	12	13	10	11	12	13	10	11	12	13
		38.3%	28.9%	17.2%	8.5%	38.3%	28.9%	17.2%	8.5%	38.3%	28.9%	17.2%	8.5%
	12	13	14	15	16	13	14	15	16	13	14	15	16
		26.7%	17.2%	9.3%	4.0%	26.7%	17.2%	9.3%	4.0%	26.7%	17.2%	9.3%	4.0%
	14	14.0	15.0	16.0	17.0	14.0	15.0	16.0	17.0	14.0	15.0	16.0	17.0
		31.3%	24.5%	16.6%	9.7%	31.3%	24.5%	16.6%	9.7%	31.3%	24.5%	16.6%	9.7%
	14*	14	15	16	17					14	15	16	17
		31.3%	24.5%	16.6%	9.7%					31.3%	24.5%	16.6%	9.7%
Triaxial	4	4	5	6	7	4	5	6	9	4	5	6	9
		46.1%	33.6%	14.0%	4.3%	46.5%	33.8%	14.3%	4.5%	46.5%	33.8%	14.3%	4.5%
	4*	6	7	8	9					6	7	8	9
		43.4%	32.8%	16.2%	5.2%					43.6%	33.1%	16.4%	5.3%
	6	6	7	8	9	6	7	8	9	6	7	8	9
		43.4%	32.8%	16.2%	5.2%	43.6%	33.1%	16.4%	5.3%	43.6%	33.1%	16.4%	5.3%
	8	8	9	10	11	8	9	10	11	8	9	10	11
		41.9%	30.3%	16.6%	6.4%	42.0%	30.9%	16.8%	6.5%	42.0%	30.9%	16.8%	6.5%
	10	10	11	12	13	10	11	12	13	10	11	12	13
		37.7%	28.4%	17.0%	8.4%	38.3%	28.9%	17.2%	8.5%	38.3%	28.9%	17.2%	8.5%
	12	13	14	15	16	13	14	15	16	13	14	15	16
		26.6%	16.9%	9.2%	3.9%	26.7%	17.2%	9.3%	4.0%	26.7%	17.2%	9.3%	4.0%
	14	14	15	16	17	13	14	15	16	6	7	8	9
		31.2%	24.6%	16.6%	9.6%	26.7%	17.2%	9.3%	4.0%	43.6%	33.1%	16.4%	5.3%
	14*	14	15	16	17					14	15	16	17
		31.2%	24.6%	16.6%	9.6%					31.3%	24.5%	16.6%	9.7%
Uniaxial		Stretch simulations											
	6	6	7	8	9	6	7	8	9	6	7	8	9
		43.6%	33.1%	16.4%	5.3%	43.6%	33.1%	16.4%	5.3%	43.6%	33.1%	16.4%	5.3%
	6*	6	7	8	9					6	7	8	9
		43.4%	32.8%	16.2%	5.2%					43.6%	33.1%	16.4%	5.3%
	8	8	9	10	11	8	9	10	11	8	9	10	11
		42.0%	30.9%	16.8%	6.5%	42.0%	30.9%	16.8%	6.5%	42.0%	30.9%	16.8%	6.5%
	10	10	11	12	13	10	11	12	13	10	11	12	13
		38.3%	28.9%	17.2%	8.5%	38.3%	28.9%	17.2%	8.5%	38.3%	28.9%	17.2%	8.5%
	12	13	14	15	16	13	14	15	16	13	14	15	16
		26.7%	17.2%	9.3%	4.0%	26.7%	17.2%	9.3%	4.0%	26.7%	17.2%	9.3%	4.0%
	14	13	14	15	16	13	14	15	16	13	14	15	16
		26.7%	17.2%	9.3%	4.0%	26.7%	17.2%	9.3%	4.0%	26.7%	17.2%	9.3%	4.0%
	14*	14	15	16	17					14	15	16	17
		31.3%	24.5%	16.6%	9.7%					31.3%	24.5%	16.6%	9.7%
Triaxial	6	6	7	8	9	6	7	8	9	6	7	8	9
		43.6%	33.1%	16.4%	5.3%	43.6%	33.1%	16.4%	5.3%	43.6%	33.1%	16.4%	5.3%
	6*	6	7	8	9					6	7	8	9
		43.4%	32.8%	16.2%	5.2%					43.6%	33.1%	16.4%	5.3%
	8	8	9	10	11	8	9	10	11	8	9	10	11
		42.0%	30.9%	16.8%	6.5%	42.0%	30.9%	16.8%	6.5%	42.0%	30.9%	16.8%	6.5%
	10	10	11	12	13	10	11	12	13	10	11	12	13
		38.3%	28.9%	17.2%	8.5%	38.3%	28.9%	17.2%	8.5%	38.3%	28.9%	17.2%	8.5%
	12	13	14	15	16	13	14	15	16	13	14	15	16
		26.7%	17.2%	9.3%	4.0%	26.7%	17.2%	9.3%	4.0%	26.7%	17.2%	9.3%	4.0%
	14	13	14	15	16	13	14	15	16	13	14	15	16
		26.7%	17.2%	9.3%	4.0%	26.7%	17.2%	9.3%	4.0%	26.7%	17.2%	9.3%	4.0%
	14*	14	15	16	17					14	15	16	17
		31.3%	24.5%	16.6%	9.7%					31.3%	24.5%	16.6%	9.7%

Table A.1: Proportions of nodes with four most prevalent NC following adaptation simulations. Results are tabulated by the loading, initial NC and MSL. Each simulation entry gives NC on top and its proportion below. Results for simulation with dead zone at 250$\mu\varepsilon$ and 1000$\mu\varepsilon$ are shown in black and red respectively.

NN ITA

NC		MSL = 0.7 mm							MSL = 1.0 mm							MSL = 1.5 mm						
Initial	Adapted	Men	95\% CI		Median	SD	Min	Max	Mean	9a5\% CI		Median	SD	Min	Max	Mean	95\% CI		Median	SD	Min	Max
			Min	Max						Min	Max						Min	Max				
4	3	103.6	94.4	113.3	99.6	34.3	36.1	178.4	101.4	87.5	117.5	97.4	34.7	31.2	177.8	98.3	74.3	130.0	94.4	33.9	34.1	177.5
	4	99.0	94.9	103.3	95.4	33.0	24.6	179.6	97.5	90.7	104.7	93.8	32.9	29.3	178.8	96.7	85.9	108.8	92.9	33.1	16.7	179.2
	5	99.8	95.4	104.4	96.3	32.6	27.9	179.1	99.4	92.2	107.2	95.8	33.0	34.4	177.8	98.2	86.4	111.6	94.5	33.3	32.2	178.8
	6	99.4	93.1	106.2	95.9	32.8	34.2	179.2	99.6	90.0	110.3	96.0	33.2	30.6	177.6	98.4	83.2	116.5	94.7	33.5	31.6	179.1
	2	123.0	102.6	147.4	119.6	35.6	36.2	178.7								99.9	56.4	177.1	95.1	38.2	32.4	174.8
	3	105.6	98.4	113.4	102.1	33.5	29.6	179.6								101.0	82.1	124.4	97.3	33.8	34.1	179.0
	4	100.8	96.0	105.9	97.3	32.6	31.5	179.1								98.7	86.6	112.6	95.0	33.4	16.7	179.2
	5	100.6	94.2	107.4	97.2	32.2	32.8	179.1								100.1	85.2	117.6	96.6	32.7	32.5	179.1
6	4	97.4	90.7	104.4	93.2	34.8	10.8	178.4	95.2	85.2	106.4	90.9	35.0	9.2	178.7	92.2	75.4	112.7	87.8	35.0	17.7	179.0
	5	97.4	93.9	101.0	93.4	34.4	19.3	178.7	95.4	89.8	101.3	91.2	34.9	19.1	179.4	92.9	84.0	102.9	88.6	35.1	16.8	177.8
	6	96.4	93.9	98.9	92.3	34.4	11.2	179.7	95.7	91.6	100.1	91.6	34.6	14.5	179.9	93.7	86.7	101.2	89.4	34.9	14.8	178.8
	7	97.0	94.0	100.2	93.0	34.5	10.6	179.1	96.9	91.9	102.1	92.7	35.0	8.1	179.1	95.9	87.4	105.1	91.6	34.9	13.3	179.2
8	5	95.2	90.3	100.4	90.7	36.1	6.4	179.2	92.0	84.4	100.2	87.2	36.4	9.2	178.4	86.4	74.9	99.6	81.2	36.8	5.3	179.2
	6	95.3	92.4	98.4	90.9	35.7	7.6	179.5	93.3	88.6	98.3	88.7	36.1	8.7	178.7	90.0	82.0	98.8	85.2	36.3	6.2	178.8
	7	94.8	92.7	97.0	90.4	35.7	2.2	179.1	93.7	90.1	97.3	89.1	36.0	8.1	178.6	91.5	85.7	97.6	86.8	36.1	6.7	179.0
	8	94.9	92.9	96.9	90.4	35.8	7.6	179.7	94.7	91.4	98.1	90.1	36.1	5.4	179.3	93.4	87.6	99.5	88.7	36.5	14.7	178.4
10	7	93.9	91.5	96.3	89.1	36.9	0.3	179.4	92.3	88.4	96.4	87.4	37.2	6.6	179.1	89.6	83.3	96.4	84.3	38.1	2.0	179.2
	8	93.6	91.8	95.5	88.8	36.9	2.4	179.4	92.5	89.6	95.6	87.6	37.2	1.0	179.5	89.5	84.5	94.9	84.4	37.6	7.0	179.4
	9	93.8	92.1	95.5	89.0	36.9	2.3	179.5	92.7	90.0	95.5	87.8	37.2	1.0	179.1	89.8	85.0	94.7	84.6	37.6	1.2	179.1
	10	94.1	92.2	96.0	89.3	37.0	2.0	179.5	93.0	90.0	96.1	88.1	37.2	5.5	178.9	92.5	87.3	98.0	87.4	37.9	2.4	178.8
12	8	92.8	90.8	94.8	87.6	38.1	0.2	179.6	90.6	87.3	94.0	85.3	38.1	4.0	179.0	87.2	81.7	93.2	81.5	39.1	4.6	177.4
	9	92.7	91.1	94.3	87.6	37.9	0.2	179.8	91.4	88.8	94.1	86.1	38.5	0.2	179.4	89.4	84.9	94.1	83.8	38.7	2.1	178.9
	10	92.7	91.3	94.3	87.7	37.9	0.4	179.7	91.6	89.2	94.1	86.3	38.3	1.3	179.3	89.9	85.8	94.2	84.3	39.0	2.0	179.1
	11	92.8	91.3	94.5	87.7	38.0	1.7	179.9	92.3	89.9	94.8	87.0	38.3	0.8	178.9	91.0	87.0	95.2	85.6	38.7	2.4	179.4
14	9	92.3	90.7	94.0	86.9	39.2	1.8	179.8	90.5	87.7	93.4	84.8	39.5	0.9	179.2	87.3	82.5	92.4	81.2	40.0	2.6	179.1
	10	92.0	90.6	93.4	86.6	39.0	0.2	179.6	90.3	88.1	92.6	84.6	39.4	0.1	179.5	88.2	84.2	92.4	82.3	39.8	1.5	179.1
	11	92.3	90.9	93.6	86.8	38.9	0.3	179.9	91.1	89.0	93.3	85.5	39.2	0.2	179.8	88.3	84.7	92.1	82.5	39.7	1.3	179.0
	12	92.5	91.1	94.0	87.1	38.9	0.2	179.8	91.3	89.2	93.4	85.8	39.1	0.3	179.3	90.3	86.9	93.8	84.6	39.6	2.6	179.4
	2	123.8	110.7	138.6	112.6	65.3	3.3	178.7														
	3	103.5	98.3	109.0	95.3	50.7	3.2	179.8								92.8	74.4	115.7	84.8	47.5	7.4	177.2
	4	101.4	97.9	105.1	94.1	47.6	2.3	179.9								90.4	80.1	102.1	83.0	45.2	2.9	178.8
	5	98.9	95.6	102.3	91.9	45.9	2.3	179.8								90.6	82.7	99.3	83.3	44.9	2.1	179.1
	6															89.9	82.9	97.4	83.1	43.2	3.2	178.8

Table A.2: The ITA mean, 95 % Confidence intervals (CI), median, standard deviation(SD), minimum (min) and maximum (max) values for fixed joint lattice model simulations subjected to uniaxial loading. ITAs for four most prevalent NCs at the end of adaptation are presented. Dead zone of 250$\mu\varepsilon$ has been used except for simulations with * next to the NNC value which indicate that the dead zone of 1000$\mu\varepsilon$ has been used.

NC		MSL = 0.7 mm							MSL = 1.0 mm							MSL = 1.5 mm						
Initial	Adapted	Men	95\% CI		Median	SD	Min	Max	Mean	9a5\% CI		Median	SD	Min	Max	Mean	95\% CI		Median	SD	Min	Max
			Min	Max						Min	Max						Min	Max				
4	3	103.4	94.4	113.3	99.6	34.3	36.1	178.4	101.4	87.5	117.5	97.4	34.7	31.2	177.8	98.3	74.3	130.0	94.4	33.9	34.1	177.5
	4	99.0	94.9	103.3	95.4	33.0	24.6	179.6	97.5	90.7	104.7	93.8	32.9	29.3	178.8	96.7	85.9	108.8	92.9	33.1	16.7	179.2
	5	99.8	95.4	104.4	96.3	32.6	27.9	179.1	99.4	92.2	107.2	95.8	33.0	34.4	177.8	98.2	86.4	111.6	94.5	33.3	32.2	178.8
	6	99.4	93.1	106.2	95.9	32.8	34.2	179.2	99.6	90.0	110.3	96.0	33.2	30.6	177.6	98.4	83.2	116.5	94.7	33.5	31.6	179.1
	2	123.0	102.6	147.4	119.6	35.6	36.2	178.7								99.9	56.4	177.1	95.1	38.2	32.4	174.8
	3	105.6	98.4	113.4	102.1	33.5	29.6	179.6								101.0	82.1	124.4	97.3	33.8	34.1	179.0
	4	100.8	96.0	105.9	97.3	32.6	31.5	179.1								98.7	86.6	112.6	95.0	33.4	16.7	179.2
	5	100.6	94.2	107.4	97.2	32.2	32.8	179.1								100.1	85.2	117.6	96.6	32.7	32.5	179.1
6	4	97.4	90.7	104.4	93.2	34.8	10.8	178.4	95.2	85.2	106.4	90.9	35.0	9.2	178.7	92.2	75.4	112.7	87.8	35.0	17.7	179.0
	5	97.4	93.9	101.0	93.4	34.4	19.3	178.7	95.4	89.8	101.3	91.2	34.9	19.1	179.4	92.9	84.0	102.9	88.6	35.1	16.8	177.8
	6	96.4	93.9	98.9	92.3	34.4	11.2	179.7	95.7	91.6	100.1	91.6	34.6	14.5	179.9	93.7	86.7	101.2	89.4	34.9	14.8	178.8
	7	97.0	94.0	100.2	93.0	34.5	10.6	179.1	96.9	91.9	102.1	92.7	35.0	8.1	179.1	95.9	87.4	105.1	91.6	34.9	13.3	179.2
8	5	95.2	90.3	100.4	90.7	36.1	6.4	179.2	92.0	84.4	100.2	87.2	36.4	9.2	178.4	86.4	74.9	99.6	81.2	36.8	5.3	179.2
	6	95.3	92.4	98.4	90.9	35.7	7.6	179.5	93.3	88.6	98.3	88.7	36.1	8.7	178.7	90.0	82.0	98.8	85.2	36.3	6.2	178.8
	7	94.8	92.7	97.0	90.4	35.7	2.2	179.1	93.7	90.1	97.3	89.1	36.0	8.1	178.6	91.5	85.7	97.6	86.8	36.1	6.7	179.0
	8	94.9	92.9	96.9	90.4	35.8	7.6	179.7	94.7	91.4	98.1	90.1	36.1	5.4	179.3	93.4	87.6	99.5	88.7	36.5	14.7	178.4
10	7	93.9	91.5	96.3	89.1	36.9	0.3	179.4	92.3	88.4	96.4	87.4	37.2	6.6	179.1	89.6	83.3	96.4	84.3	38.1	2.0	179.2
	8	93.6	91.8	95.5	88.8	36.9	2.4	179.4	92.5	89.6	95.6	87.6	37.2	1.0	179.5	89.5	84.5	94.9	84.4	37.6	7.0	179.4
	9	93.8	92.1	95.5	89.0	36.9	2.3	179.5	92.7	90.0	95.5	87.8	37.2	1.0	179.1	89.8	85.0	94.7	84.6	37.6	1.2	179.1
	10	94.1	92.2	96.0	89.3	37.0	2.0	179.5	93.0	90.0	96.1	88.1	37.2	5.5	178.9	92.5	87.3	98.0	87.4	37.9	2.4	178.8
12	8	92.8	90.8	94.8	87.6	38.1	0.2	179.6	90.6	87.3	94.0	85.3	38.1	4.0	179.0	87.2	81.7	93.2	81.5	39.1	4.6	177.4
	9	92.7	91.1	94.3	87.6	37.9	0.2	179.8	91.4	88.8	94.1	86.1	38.5	0.2	179.4	89.4	84.9	94.1	83.8	38.7	2.1	178.9
	10	92.7	91.3	94.3	87.7	37.9	0.4	179.7	91.6	89.2	94.1	86.3	38.3	1.3	179.3	89.9	85.8	94.2	84.3	39.0	2.0	179.1
	11	92.8	91.3	94.5	87.7	38.0	1.7	179.9	92.3	89.9	94.8	87.0	38.3	0.8	178.9	91.0	87.0	95.2	85.6	38.7	2.4	179.4
14	9	92.3	90.7	94.0	86.9	39.2	1.8	179.8	90.5	87.7	93.4	84.8	39.5	0.9	179.2	87.3	82.5	92.4	81.2	40.0	2.6	179.1
	10	92.0	90.6	93.4	86.6	39.0	0.2	179.6	90.3	88.1	92.6	84.6	39.4	0.1	179.5	88.2	84.2	92.4	82.3	39.8	1.5	179.1
	11	92.3	90.9	93.6	86.8	38.9	0.3	179.9	91.1	89.0	93.3	85.5	39.2	0.2	179.8	88.3	84.7	92.1	82.5	39.7	1.3	179.0
	12	92.5	91.1	94.0	87.1	38.9	0.2	179.8	91.3	89.2	93.4	85.8	39.1	0.3	179.3	90.3	86.9	93.8	84.6	39.6	2.6	179.4
	2	123.8	110.7	138.6	112.6	65.3	3.3	178.7														
	3	103.5	98.3	109.0	95.3	50.7	3.2	179.8								92.8	74.4	115.7	84.8	47.5	7.4	177.2
	4	101.4	97.9	105.1	94.1	47.6	2.3	179.9								90.4	80.1	102.1	83.0	45.2	2.9	178.8
	5	98.9	95.6	102.3	91.9	45.9	2.3	179.8								90.6	82.7	99.3	83.3	44.9	2.1	179.1
	6															89.9	82.9	97.4	83.1	43.2	3.2	178.8

Table A.3: The ITA mean, 95 % Confidence intervals (CI), median, standard deviation(SD), minimum (min) and maximum (max) values for fixed joint lattice model simulations subjected to triaxial loading. ITAs for four most prevalent NCs at the end of adaptation are presented. Dead zone of 250$\mu\varepsilon$ has been used except for simulations with * next to the NNC value which indicate that the dead zone of 1000$\mu\varepsilon$ has been used.

NC		MSL = 0.7 mm							MSL = 1.0 mm							MSL = 1.5 mm						
Initial	Adapted	Mean	95\% CI		Median	SD	Min	Max	Mean	95\% CI		Median	SD	Min	Max	Mean	95\% CI		Median	SD	Min	Max
			Min	Max						Min	Max						Min	Max				
6	5	95.9	91.8	100.2	91.9	34.3	11.2	179.6	93.3	86.3	100.9	89.2	34.2	19.1	178.0	90.1	79.2	102.5	85.8	34.2	16.8	177.4
	6	95.8	93.5	98.1	91.8	34.2	10.8	179.7	94.6	90.9	98.5	90.5	34.4	8.1	179.9	92.4	86.1	99.1	88.1	34.7	14.8	179.2
	7	97.0	94.6	99.6	93.0	34.3	9.1	179.5	96.6	92.6	100.8	92.5	34.8	16.7	179.1	95.4	88.5	102.9	91.1	35.2	13.6	177.5
	8	97.0	93.6	100.5	92.9	34.6	20.4	179.5	96.7	91.5	102.1	92.5	35.0	21.6	179.2	96.4	88.4	105.1	92.1	35.3	19.0	178.3
	4	96.1	90.5	102.0	92.0	34.5	21.2	178.5								88.5	72.5	108.1	84.0	34.6	17.7	177.5
	5	96.7	93.5	100.0	92.7	34.4	9.1	178.8								92.3	83.1	102.4	87.9	35.2	23.3	178.8
	6	96.9	94.2	99.6	92.9	34.2	17.9	179.6								93.5	86.8	100.7	89.3	34.5	14.8	179.0
	7	97.4	94.0	101.0	93.4	34.4	23.7	179.5								96.7	88.5	105.5	92.4	35.2	15.8	179.1
8	6	94.5	92.4	96.6	90.0	35.6	3.5	179.5	91.3	85.6	97.5	86.7	35.8	5.4	178.6	87.7	79.4	96.8	82.8	35.9	7.0	179.0
	7	94.8	93.0	96.6	90.4	35.7	6.0	179.9	93.0	89.5	96.6	88.4	35.9	6.0	178.7	91.3	85.3	97.7	86.5	36.3	5.3	178.3
	8	95.6	93.4	97.8	91.1	35.9	4.8	179.5	94.1	91.2	97.0	89.5	35.9	6.0	179.1	91.5	86.4	97.0	86.7	36.4	5.0	177.7
	9	95.4	92.2	98.7	90.9	36.2	2.0	179.4	94.8	91.3	98.4	90.2	36.3	6.4	179.2	94.4	88.3	100.9	89.7	36.6	7.3	179.1
10	7	93.4	90.7	96.2	88.6	37.0	2.2	179.3	91.0	86.3	96.0	86.0	37.2	11.8	179.1	87.3	80.2	95.0	82.0	37.6	5.4	178.3
	8	93.3	91.5	95.2	88.5	36.9	1.7	179.5	91.6	88.5	94.8	86.7	37.1	1.0	179.8	88.3	83.2	93.8	83.2	37.2	1.2	179.1
	9	93.6	92.0	95.1	88.8	36.8	2.0	179.7	92.5	90.0	95.0	87.6	37.0	2.2	179.3	90.3	85.9	94.9	85.2	37.5	2.0	179.4
	10	94.1	92.4	95.7	89.3	36.9	3.5	179.9	93.1	90.5	95.8	88.2	37.1	1.0	179.2	91.9	87.4	96.6	86.7	37.9	1.3	179.1
12	8	92.1	89.9	94.4	86.9	37.9	0.2	179.5														
	9	92.6	91.0	94.2	87.5	37.9	2.5	179.6	90.7	88.0	93.5	85.4	38.2	0.2	179.3	87.9	83.2	92.8	82.4	38.1	2.0	177.8
	10	92.9	91.5	94.3	87.8	37.7	1.7	179.9	91.2	88.9	93.5	85.9	38.1	1.8	179.8	89.0	85.1	93.1	83.6	38.4	2.6	179.1
	11	93.0	91.6	94.5	88.0	37.8	2.0	179.8	92.3	90.1	94.5	87.1	38.2	0.2	179.5	90.8	87.1	94.7	85.4	38.7	2.4	179.0
	12								92.9	90.5	95.3	87.7	38.2	0.8	179.3	91.9	87.8	96.2	86.5	38.8	3.3	179.7
14	9	91.9	90.1	93.7	86.4	39.0	1.6	179.7														
	10	92.0	90.6	93.4	86.6	38.7	0.4	179.6	90.4	88.0	92.9	84.9	39.2	0.1	179.3	87.4	83.1	91.8	81.5	39.4	2.5	178.8
	11	92.2	90.9	93.4	86.8	38.7	0.2	179.9	90.3	88.3	92.4	84.7	39.1	0.5	179.5	88.1	84.7	91.6	82.3	39.4	1.6	179.1
	12	92.5	91.2	93.8	87.1	38.8	0.2	179.8	91.3	89.4	93.2	85.8	39.0	0.3	179.4	89.7	86.4	93.0	84.0	39.4	2.1	179.4
	13								91.9	89.9	94.0	86.4	39.0	0.5	179.7	90.5	87.1	94.1	84.9	39.5	1.3	179.0
	4	93.9	89.7	98.4	87.6	42.5	4.0	179.6								91.3	80.1	104.1	84.1	44.7	2.9	178.8
	5	95.6	92.7	98.5	89.5	42.1	0.2	179.9								90.9	82.0	100.7	84.3	42.9	3.1	179.0
	6	95.1	92.8	97.5	89.2	41.2	2.1	179.5								90.1	81.5	99.6	83.5	42.7	6.2	178.8
	7	94.8	92.6	97.0	88.9	40.9	2.7	179.8								87.0	78.8	96.1	80.6	41.2	2.0	178.1

Table A.4: The ITA mean, 95 % Confidence intervals (CI), median, standard deviation(SD), minimum (min) and maximum (max) values for pinned joint lattice model simulations subjected to uniaxial loading. ITAs for four most prevalent NCs at the end of adaptation are presented. Dead zone of 250$\mu\varepsilon$ has been used except for simulations with * next to the NNC value which indicate that the dead zone of 1000$\mu\varepsilon$ has been used.

NC		MSL = 0.7 mm							MSL = 1.0 mm							MSL = 1.5 mm						
Initial	Adapted	Mean	95\% CI		Median	SD	Min	Max	Mean	95\% CI		Median	SD	Min	Max	Mean	95\% CI		Median	SD	Min	Max
			Min	Max						Min	Max						Min	Max				
6	6	94.3	92.3	96.4	90.2	34.2	7.2	179.2	92.2	88.8	95.7	88.0	34.3	5.0	179.9	88.5	83.0	94.4	84.1	34.3	12.3	179.0
	7	96.7	94.6	98.8	92.6	34.3	9.7	179.7	95.9	92.5	99.5	91.8	34.7	4.2	179.1	94.6	88.8	100.7	90.3	35.1	13.6	179.2
	8	97.0	94.5	99.6	92.9	34.6	9.1	179.5	96.6	92.6	100.7	92.4	35.0	8.1	179.2	95.8	89.4	102.7	91.5	35.5	9.9	178.8
	9	96.7	92.9	100.8	92.6	35.0	23.6	179.2	96.7	90.8	102.9	92.4	35.3	21.6	178.2	96.4	87.2	106.6	92.1	35.4	13.3	179.1
	5	92.6	85.6	100.3	88.3	34.9	11.2	178.9														
	6	94.9	92.9	97.1	90.9	34.1	10.8	179.6								89.8	84.2	95.7	85.4	34.3	16.3	179.0
	7	97.0	94.9	99.2	93.0	34.3	14.5	179.7								95.0	89.0	101.4	90.7	35.0	14.8	179.2
	8	97.1	94.5	99.9	93.1	34.6	9.1	179.5								96.1	89.6	103.1	91.8	35.4	13.2	178.8
	9															96.6	86.9	107.3	92.3	35.2	16.9	179.1
8	8	92.6	91.2	94.0	88.1	35.5	2.2	179.7	90.3	88.0	92.7	85.7	35.7	4.2	179.9	85.8	82.0	89.7	80.9	35.5	4.4	179.2
	9	95.1	93.6	96.6	90.7	35.7	4.8	179.6	94.0	91.6	96.5	89.5	36.1	5.0	179.2	92.3	88.1	96.7	87.6	36.5	5.0	178.8
	10	95.4	93.7	97.3	91.0	36.0	6.0	179.9	95.1	92.3	98.1	90.6	36.2	5.7	179.8	93.9	89.3	98.7	89.2	36.8	5.3	178.8
	11	95.3	92.8	98.0	90.8	36.4	5.0	179.1	95.0	91.3	98.8	90.3	36.6	6.9	179.1	95.0	89.1	101.4	90.3	36.7	13.2	179.1
10	10	91.3	90.2	92.3	86.4	36.6	0.7	179.7	88.7	87.0	90.5	83.7	36.8	0.1	179.9	84.6	81.8	87.6	79.4	36.9	0.9	179.1
	11	93.8	92.7	95.0	89.1	36.8	0.9	179.7	92.9	91.0	94.8	88.0	37.1	2.2	179.8	90.5	87.3	93.8	85.3	37.6	1.2	179.0
	12	94.4	93.1	95.8	89.6	37.0	2.0	179.9	93.9	91.8	96.1	89.0	37.4	1.2	179.7	92.7	89.2	96.4	87.6	37.9	1.3	179.4
	13	94.5	92.8	96.3	89.7	37.3	3.0	179.6	94.2	91.5	96.9	89.3	37.5	1.0	179.3	93.7	89.4	98.1	88.6	38.2	5.0	179.1
12	12	90.6	89.8	91.5	85.5	37.5	0.2	179.8	88.0	86.6	89.4	82.7	37.8	0.1	179.9	83.7	81.4	86.1	78.1	37.7	1.6	179.2
	13	92.9	92.0	93.8	87.9	37.7	0.9	179.9	91.7	90.2	93.2	86.5	38.0	0.1	179.8	89.6	86.9	92.3	84.1	38.5	2.1	179.4
	14	93.7	92.6	94.8	88.6	37.9	0.3	179.8	93.1	91.4	94.9	88.0	38.2	0.2	179.8	91.7	88.8	94.7	86.4	38.7	3.1	179.7
	15	93.8	92.4	95.1	88.7	38.2	0.2	179.4	93.6	91.5	95.7	88.4	38.4	2.5	179.3	92.7	89.4	96.1	87.3	38.9	1.3	178.9
14	14	90.3	89.5	91.0	84.9	38.3	0.1	179.9	87.9	86.7	89.1	82.3	38.6	0.1	179.8	82.7	80.6	84.7	76.8	38.4	1.5	179.2
	15	92.2	91.5	93.0	86.9	38.5	0.2	179.8	91.2	89.9	92.5	85.7	38.8	0.1	179.9	88.7	86.5	91.0	83.0	39.1	1.4	179.4
	16	93.2	92.3	94.1	87.9	38.6	0.2	179.6	92.5	91.1	94.0	87.1	38.9	0.3	179.8	91.3	88.9	93.8	85.7	39.4	1.2	179.2
	17	93.3	92.2	94.4	88.0	38.8	0.3	179.9	92.9	91.3	94.7	87.5	39.0	2.1	179.8	92.4	89.7	95.1	86.8	39.5	1.3	179.4
	6	96.5	93.3	99.7	91.2	39.3	1.7	179.8														
	7	96.1	93.6	98.6	91.0	38.7	0.3	179.8														
	8	95.8	93.8	97.9	90.7	38.4	1.7	179.9														
	9	95.7	93.8	97.6	90.7	38.0	2.3	179.4														
	10															87.9	84.1	92.0	82.0	39.7	1.5	179.2
	11															90.3	87.0	93.6	84.6	39.3	1.4	179.0
	12															90.9	87.8	94.2	85.3	39.3	1.3	179.1
	13															92.2	88.9	95.7	86.7	39.3	1.6	178.8

Table A.5: The ITA mean, 95 % Confidence intervals (CI), median, standard deviation(SD), minimum (min) and maximum (max) values for pinned joint lattice model simulations subjected to triaxial loading. ITAs for four most prevalent NCs at the end of adaptation are presented.Dead zone of 250$\mu\varepsilon$ has been used except for simulations with * next to the NNC value which indicate that the dead zone of 1000$\mu\varepsilon$ has been used.

ITA probability distribution (PD)

Matlab Statistics and Machine Learning Toolbox was used to fit the Gamma distribution to radius and ITA data. The type of probability distribution was chosen by evaluating the goodness of fit for the Normal, Weibull and Gamma distributions using the mean squared error (MSE), normalised root mean squared error (NRSME) and normalised mean squared error (NMSE) cost functions in Matlab. The evaluation was performed on two simulations, one with low mean strut length with low connectivity and one one on high mean strut length with high connectivity.

Cost function	NN06_B_0.7_1 Simulation Distribution type			NN12_S_1.5_3 Simulation Distribution type		
	Normal	Weibull	Gamma	Normal	Weibull	Gamma
MSE	0.0014	0.0014	0.0014	0.0010	0.0010	0.0010
NRMSE	12.47	11.26	10.32	7.45	7.45	7.25
NMSE	155.60	126.76	106.59	55.46	55.52	52.50

(a) Strut radius

Cost function	NN06_B_0.7_1 Simulation Distribution type			NN12_S_1.5_1 Simulation Distribution type		
	Normal	Weibull	Gamma	Normal	Weibull	Gamma
MSE	0.0010	0.0010	0.0010	0.0014	0.0014	0.0013
NRSME	8.41	8.91	7.99	8.72	8.95	7.78
NMSE	70.74	79.40	63.78	76.12	80.19	60.50

(b) ITA

Table A.6: Goodness of fit between radius and ITA data extracted from simulations and the probability distributions fitted to this data. The table presents goodness of fit for three probability distributions of 2 separate simulations tested with squared error (MSE), normalised root mean squared error (NRSME) and normalised mean squared error (NMSE) cost functions. Lower numbers indicate better fit where 0 is the perfect fit.

The goodness of fit results presented in Table A.6 show very little difference between the three distributions of radius and ITA data when using the MSE cost function, but begin to emerge with the NRSME function. Gamma distribution is clearly the best fit when considering the NSME function. It is worth noting that whilst neither of the NRSME and NMSE are close to zero it is the relative difference that leads to the choice of the Gamma distribution.

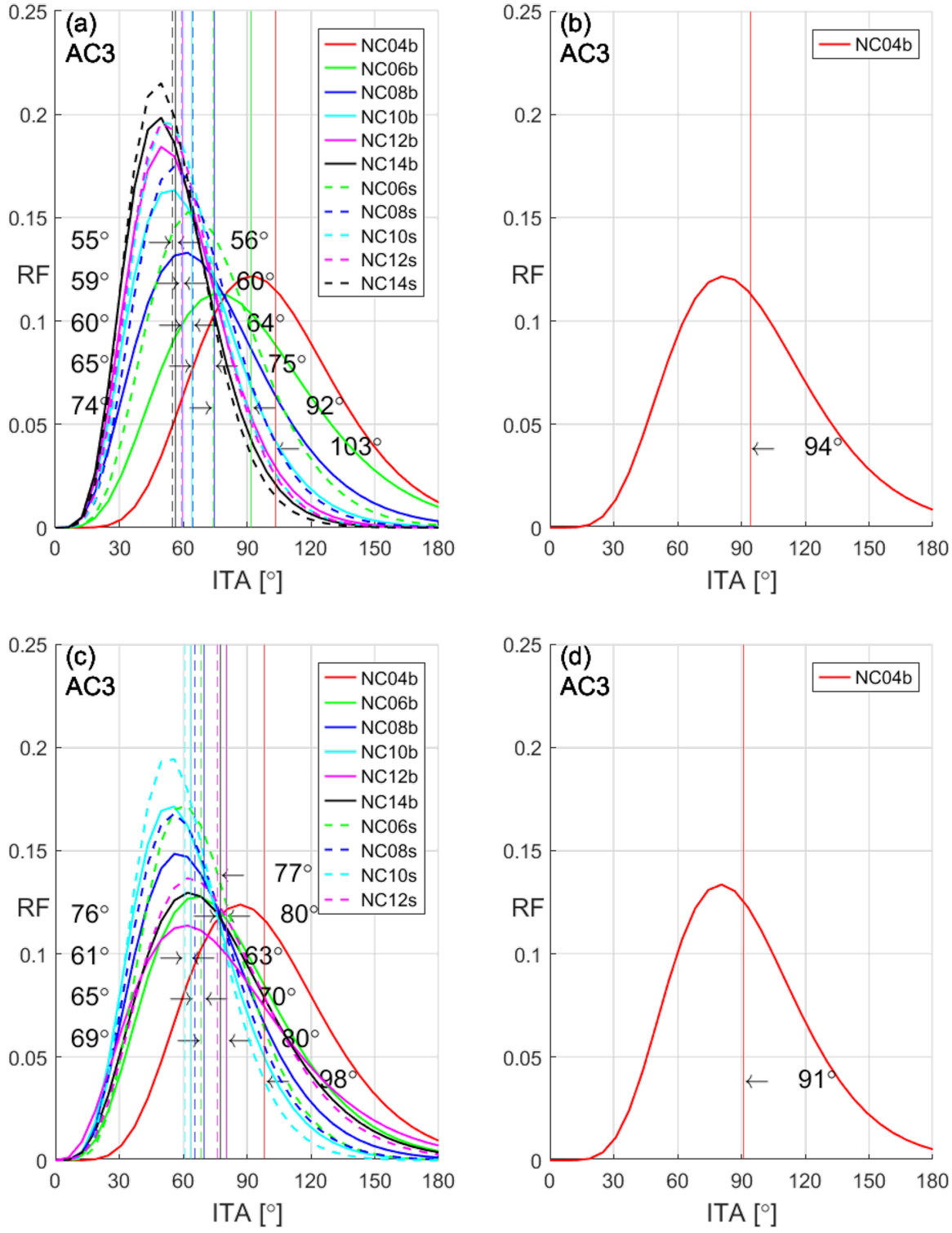


Figure A.1: ITA probability distribution (PD) for actual connectivity (AC) of 3 following adaptations simulations. Distribution plots are derived from mean values of five different models for each nominal connectivity as shown in the legend where b signifies bending and s stretch simulations. Mean ITA for each distribution is indicated by a vertical line and annotated with the corresponding value. (a) and (b) show distributions for simulations using the mean strut length of 0.7mm subjected to triaxial and uniaxial loading scenarios respectively. (c) and (d) show equivalent plots for mean strut length of 1.5mm

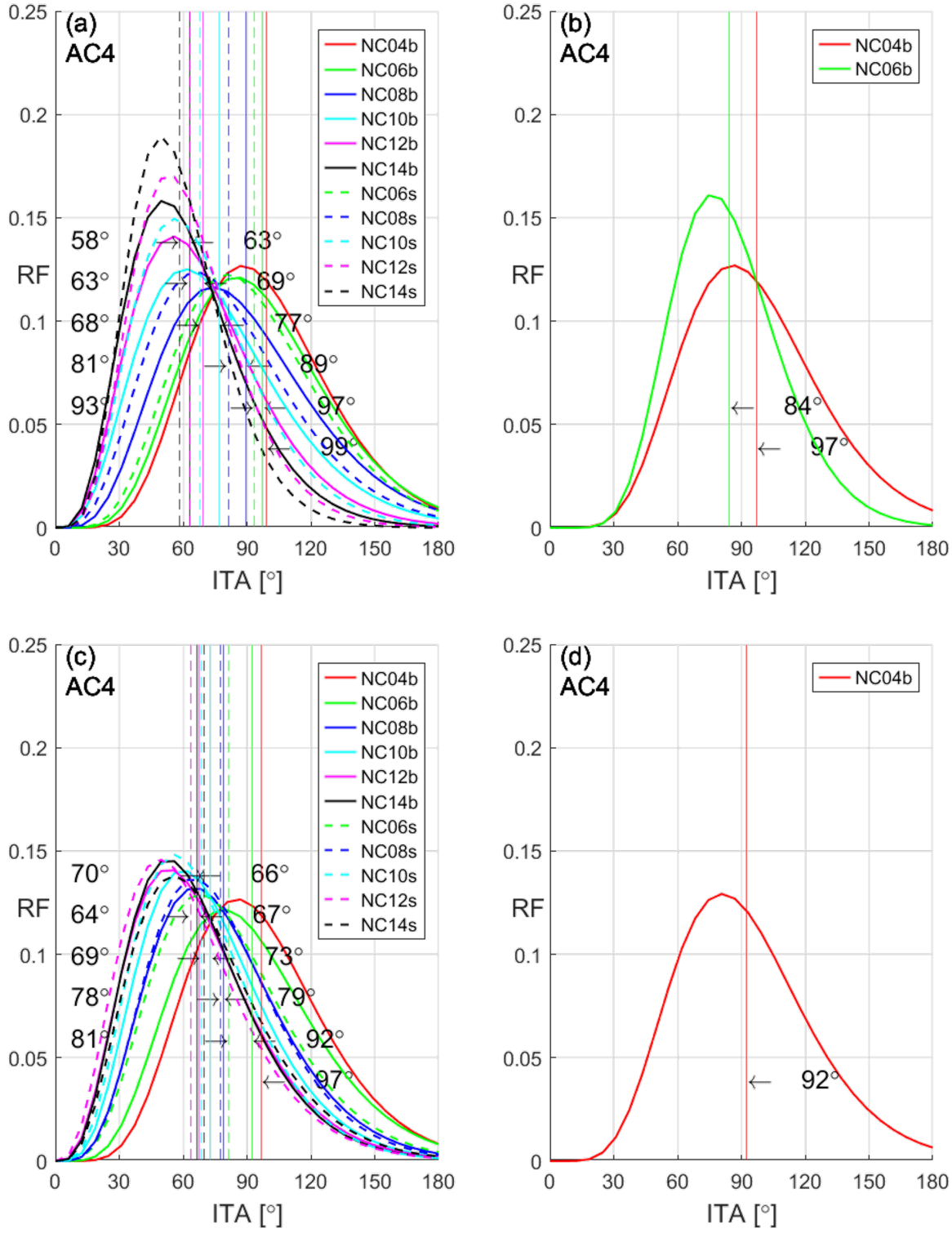


Figure A.2: ITA probability distribution (PD) for actual connectivity (AC) of 4 following adaptations simulations. Distribution plots are derived from mean values of five different models for each nominal connectivity as shown in the legend where b signifies bending and s stretch simulations. Mean ITA for each distribution is indicated by a vertical line and annotated with the corresponding value. (a) and (b) show distributions for simulations using the mean strut length of 0.7mm subjected to triaxial and uniaxial loading scenarios respectively. (c) and (d) show equivalent plots for mean strut length of 1.5mm

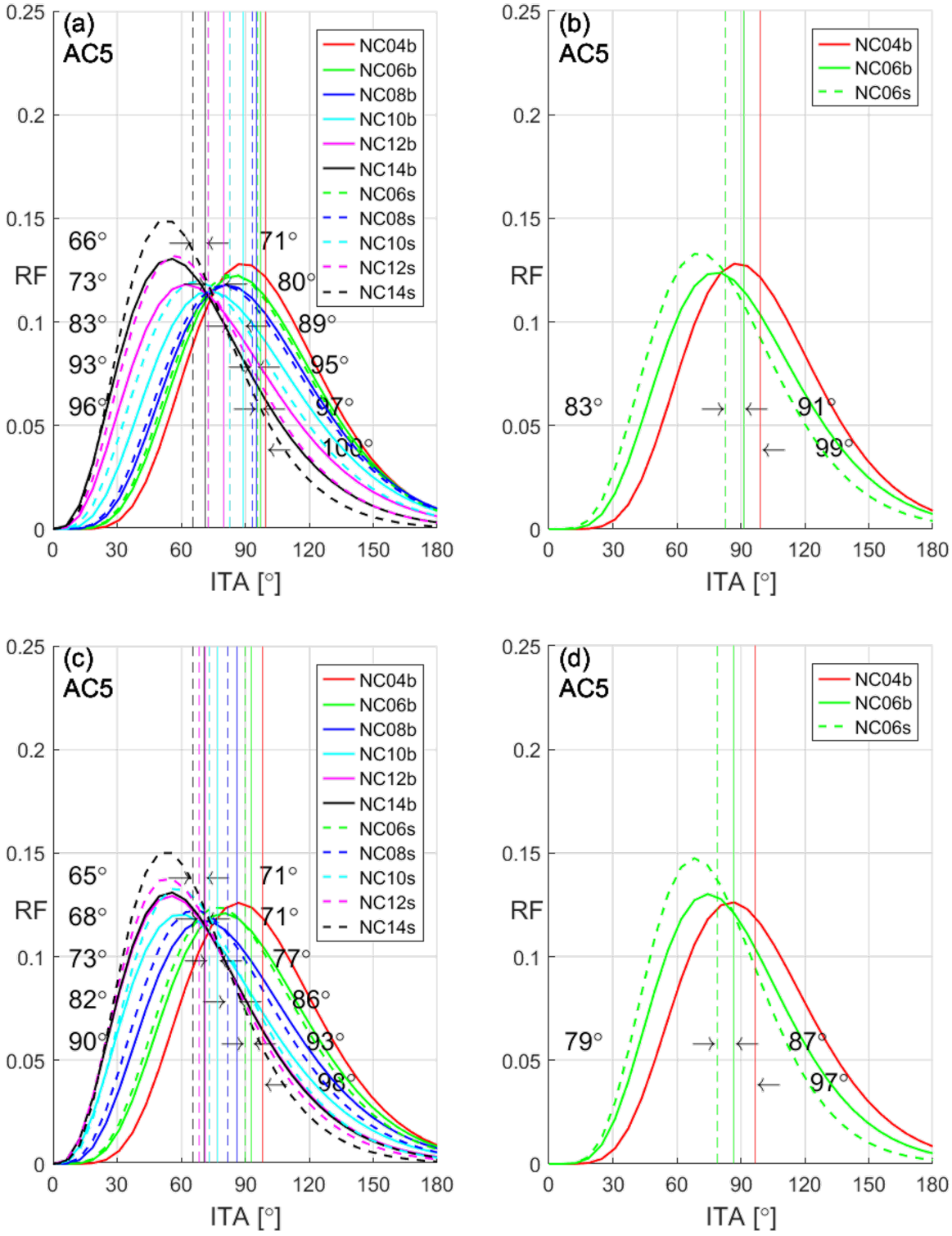


Figure A.3: ITA probability distribution (PD) for actual connectivity (AC) of 5 following adaptations simulations. Distribution plots are derived from mean values of five different models for each nominal connectivity as shown in the legend where b signifies bending and s stretch simulations. Mean ITA for each distribution is indicated by a vertical line and annotated with the corresponding value. (a) and (b) show distributions for simulations using the mean strut length of 0.7mm subjected to triaxial and uniaxial loading scenarios respectively. (c) and (d) show equivalent plots for mean strut length of 1.5mm

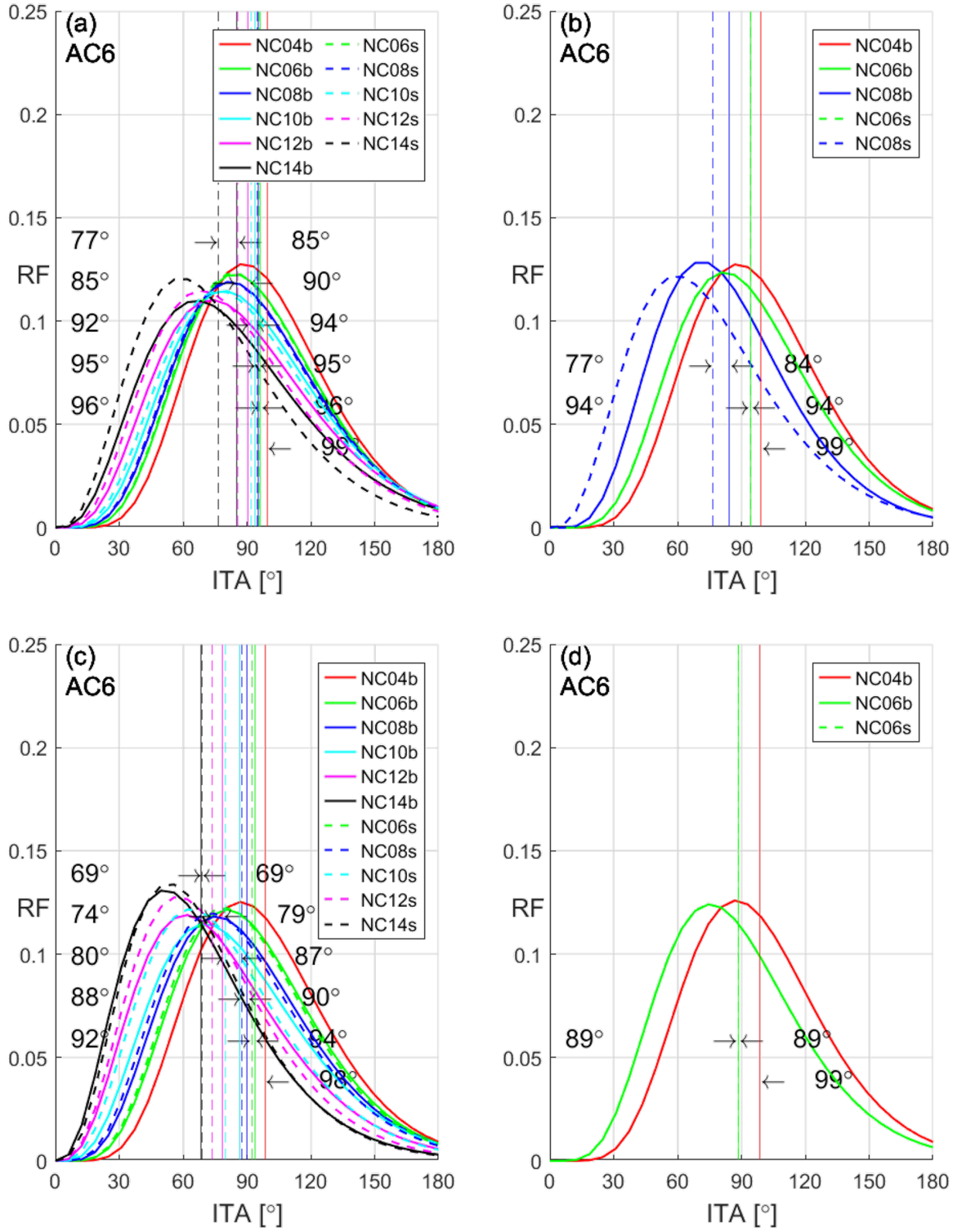


Figure A.4: ITA probability distribution (PD) for actual connectivity (AC) of 6 following adaptations simulations. Distribution plots are derived from mean values of five different models for each nominal connectivity as shown in the legend where b signifies bending and s stretch simulations. Mean ITA for each distribution is indicated by a vertical line and annotated with the corresponding value. (a) and (b) show distributions for simulations using the mean strut length of 0.7mm subjected to triaxial and uniaxial loading scenarios respectively. (c) and (d) show equivalent plots for mean strut length of 1.5mm

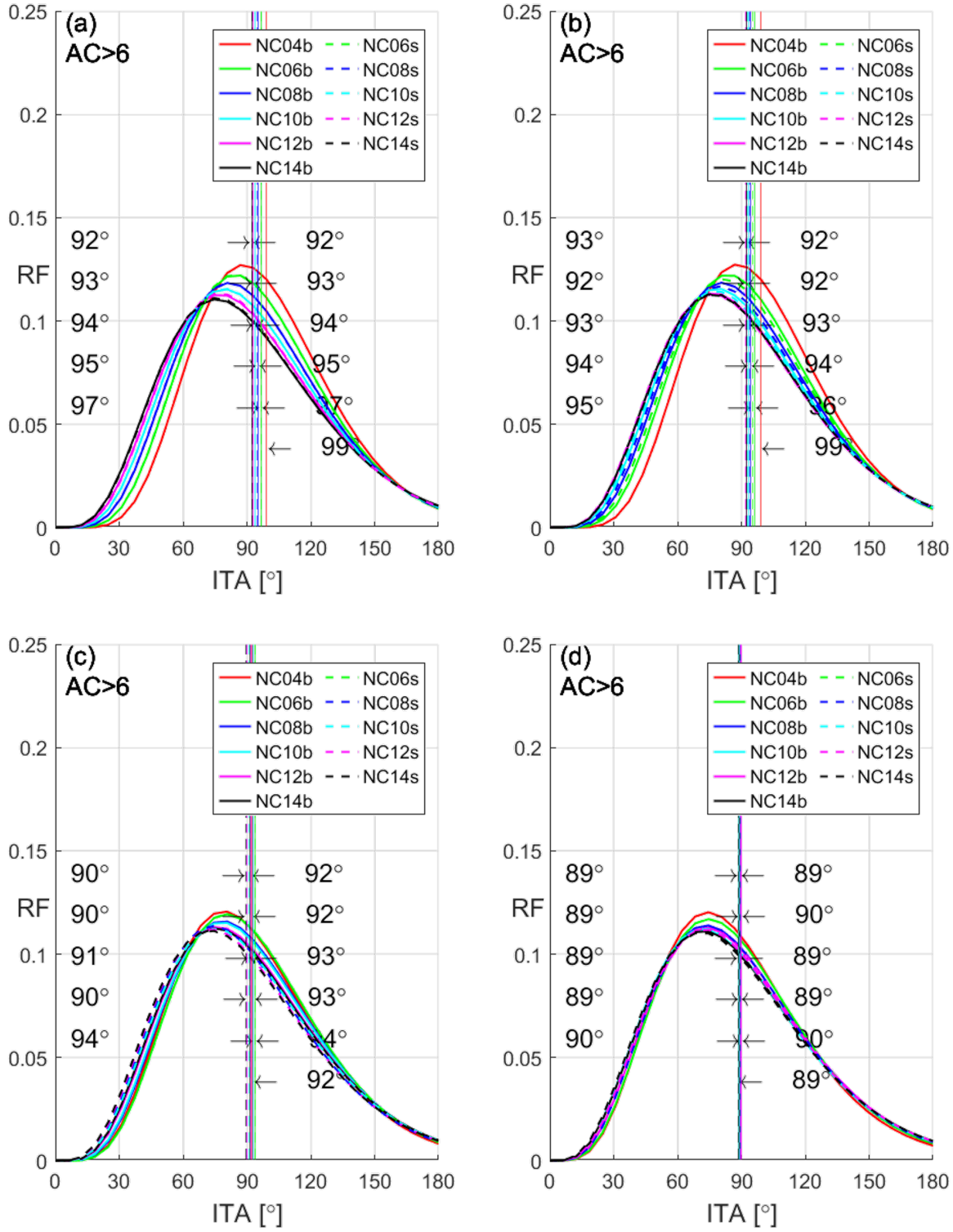


Figure A.5: ITA probability distribution (PD) for all actual connectivity (AC) of above 6 following adaptations simulations. Distribution plots are derived from mean values of five different models for each nominal connectivity as shown in the legend where b signifies bending and s stretch simulations. Mean ITA for each distribution is indicated by a vertical line and annotated with the corresponding value. (a) and (b) show distributions for simulations using the mean strut length of 0.7mm subjected to triaxial and uniaxial loading scenarios respectively. (c) and (d) show equivalent plots for mean strut length of 1.5mm

Radii distribution plots

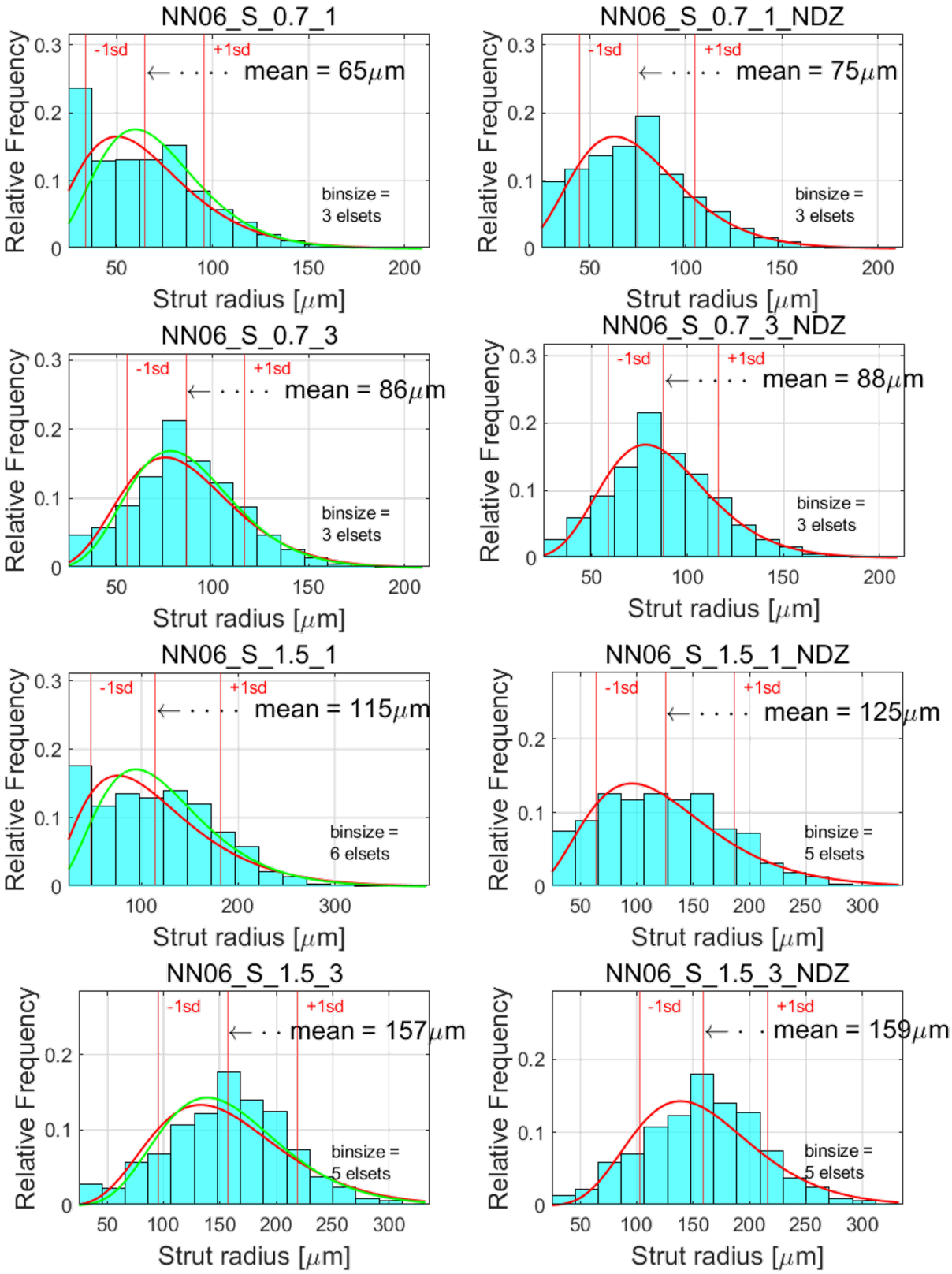


Figure A.6: Comparison of 5 model mean strut radii distributions for low connectivity stretch simulations with and without dead zone. Each diagram is annotated with the simulation name identifying the mean strut length and the loading scenario. Each bar represents a number of strut radii element sets which are also annotated on diagrams.

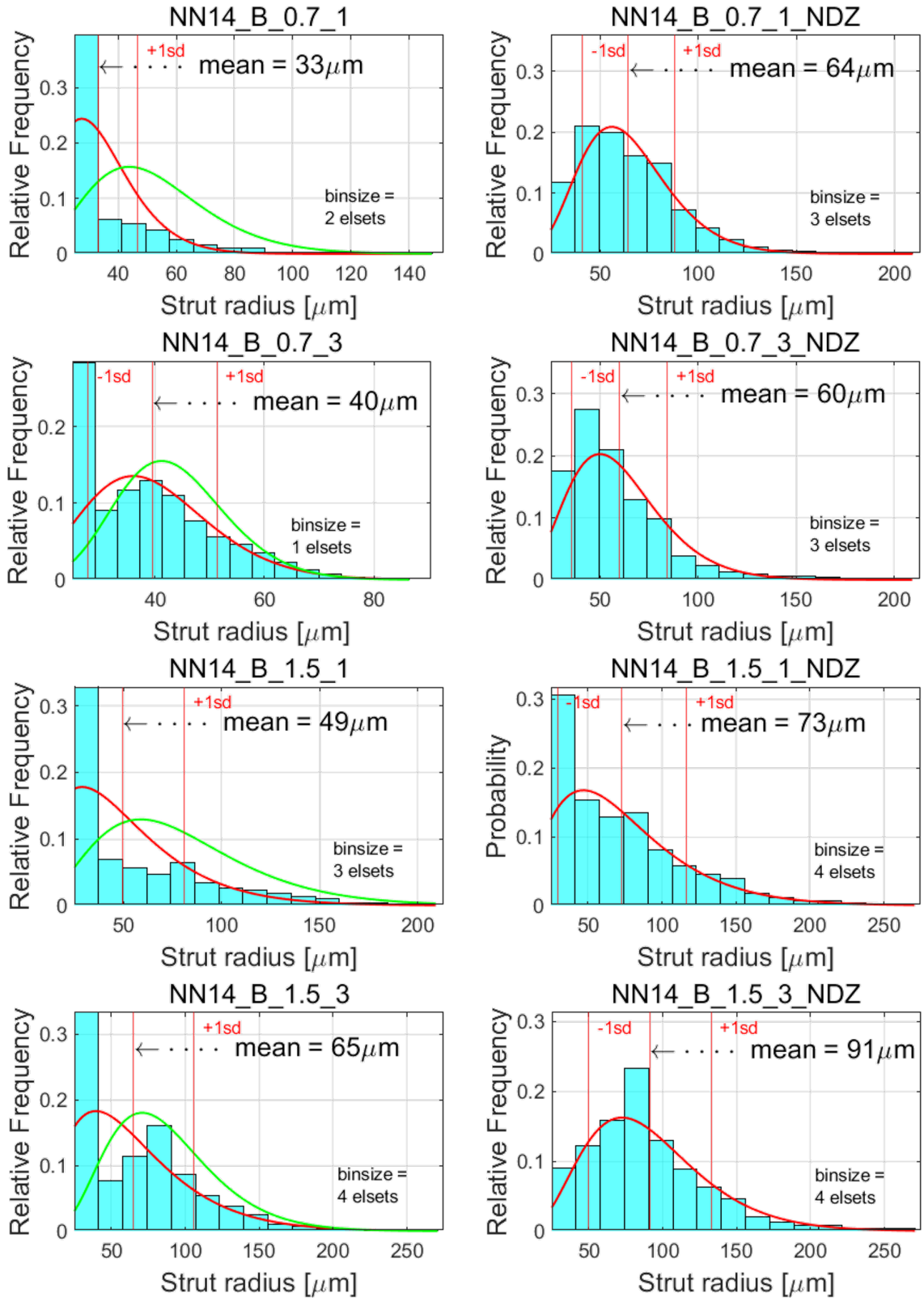


Figure A.7: Comparison of 5 model mean strut radii distributions for high connectivity bending simulations with and without dead zone. Each diagram is annotated with the simulation name identifying the mean strut length and the loading scenario. Each bar represent a number of strut radii element sets which are also annotated on diagrams.

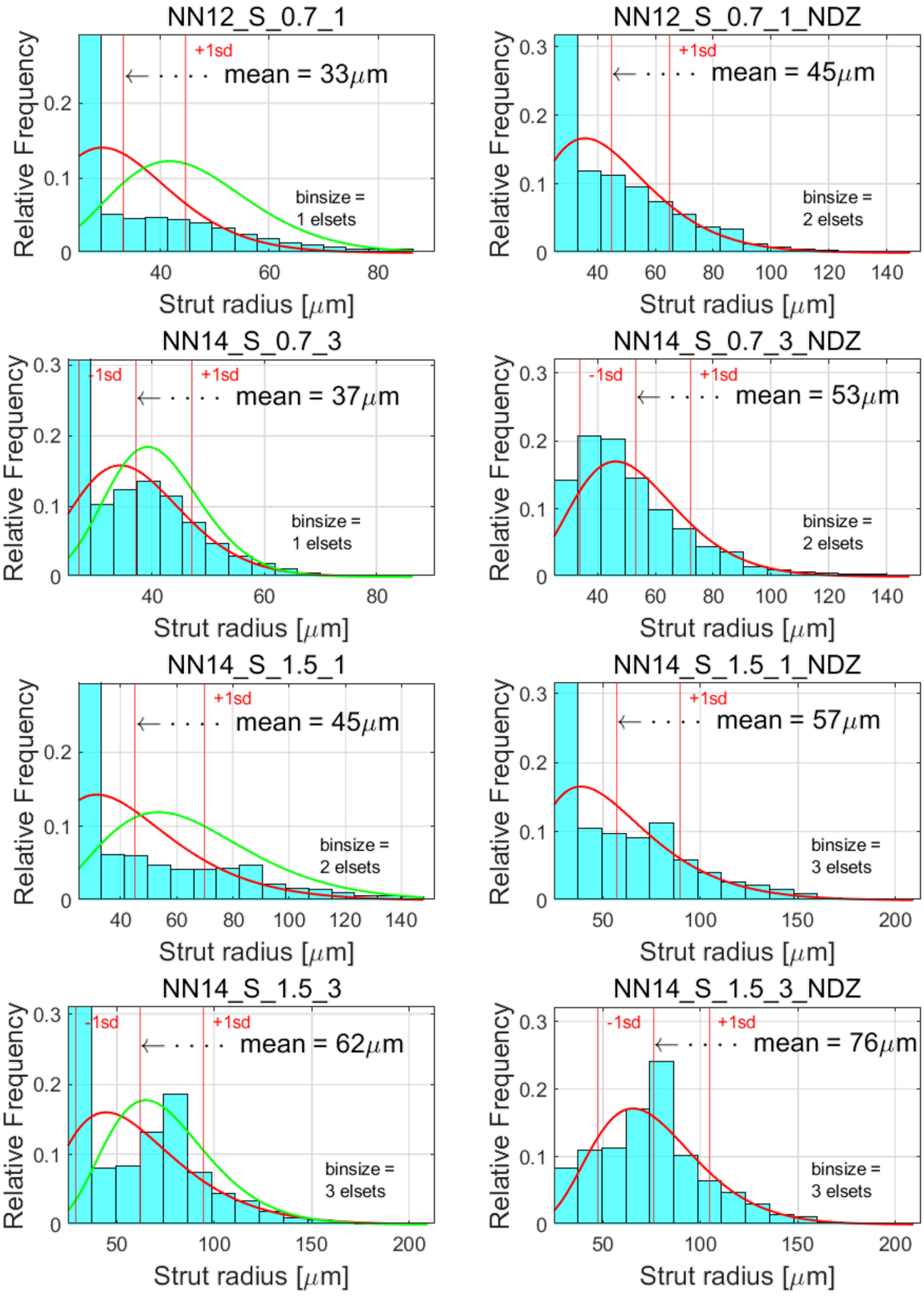


Figure A.8: Comparison of 5 model mean strut radii distributions for high connectivity stretch simulations with and without dead zone. Each diagram is annotated with the simulation name identifying the mean strut length and the loading scenario. Each bar represents a number of strut radii element sets which are also annotated on diagrams.

B

Digital appendix

Key analysis and scripting files can be accessed in the digital appendix:

BranimirRadukic-PhD-Digital Appendix